

Università Degli Studi di Milano



Corso di Dottorato di Ricerca
in Scienze e Tecnologie Chimiche

Dipartimento di Chimica

“CHEMICAL PARADIGMS SEEN THROUGH CHARGE DENSITY DESCRIPTOR LENSES”

CHIM/02

Tesi di Dottorato di Ricerca di:
Gabriele Saleh
R09023

Tutor: Leonardo Lo Presti
Co-Tutor: Carlo Gatti

Coordinatore del Corso di Dottorato: Prof. Emanuela Licandro

Anno Accademico 2013/2014

Table of contents

Chapter I: Introduction	4
1.1 CHEMICAL DESCRIPTORS AND ELECTRON DENSITY	5
1.2 THE MULTIPOLAR MODEL	6
1.3 THE QUANTUM THEORY OF ATOMS IN MOLECULES	8
REFERENCES.....	10
Chapter II: Non-Covalent interactions description	11
2.1 INTRODUCTION	12
2.2 THE NCI DESCRIPTOR.....	14
2.2.1 THE REDUCED DENSITY GRADIENT	15
2.2.2 THE QUANTITY $\rho(r)*\text{sign}\lambda_2$	16
2.3 APPLICATION OF THE NCI DESCRIPTOR TO EXPERIMENTAL, THEORETICAL AND IAM ELECTRON DENSITY: METHODS.....	17
2.3.1 TEST CASES	18
2.4 APPLICATION OF THE NCI DESCRIPTOR TO EXPERIMENTAL ELECTRON DENSITY DISTRIBUTION: RESULTS	21
2.4.1 OPERATIONAL CHOICES	21
2.4.2 AUSTDIOL	22
2.4.3 BENZENE	27
2.4.4 FAMOTIDINE	29
2.4.5 CONCLUSIONS	33
2.5 COMPARISON BETWEEN EXPERIMENTAL AND THEORETICAL RESULTS	35
2.5.1 VAN DER WAALS INTERACTIONS	35
2.5.2 HYDROGEN BONDS AND C-H...C INTERACTIONS	36
2.5.3 INTERACTIONS INVOLVING π ELECTRONS	38
2.5.4 SULPHUR-SULPHUR INTERACTIONS	40
2.5.5 CONCLUSIONS	42
2.6 'NCI DESCRIPTOR' APPLIED TO INDEPENDENT ATOM MODEL.....	42
2.6.1 INDEPENDENT ATOM MODEL AND INFORMATION THEORY	43
2.6.2 AIM OF THE WORK AND OPERATIONAL PROCEDURE	45
2.6.3 COMPARISON OF RDG vs ED PLOTS FOR IAM AND EXPERIMENTAL ED: THE CASE OF BENZENE	46
2.6.4 RESULTS FOR BENZENE	50
2.6.5 RESULTS FOR AUSTDIOL.....	53

2.6.6 RESULTS FOR FAMOTIDINE	58
2.6.7 CONCLUSIONS	62
2.7 'NCImilano' A CODE FOR THE STUDY OF NON-COVALENT INTERACTIONS BASED ON THE ELECTRON DENSITY	65
2.7.1 PROPERTIES FROM THE WAVEFUNCTION	66
2.7.2 TOPOND TO CUBE CONVERSION	67
2.7.3 RDG, $\rho^* \text{sign}(\lambda_2)$ AND ABRAMOV'S ENERGIES	68
REFERENCES	70
Chapter III: Using the Source Function to detect electron delocalization effects	74
3.1 INTRODUCTION	75
3.1.1 ELECTRON LOCALIZATION/DELOCALIZATION FROM THE WAVEFUNCTION	76
3.1.2 ELECTRON LOCALIZATION/DELOCALIZATION THROUGH THE ELECTRON DENSITY DISTRIBUTION	78
3.1.3 THE SOURCE FUNCTION AND ITS USE TO DETECT ELECTRON DELOCALIZATION	80
3.2 TEST CASES: DESCRIPTION, MULTIPOLAR REFINEMENT, <i>AB-INITIO</i> CALCULATIONS AND SOURCE FUNCTION EVALUATION	82
3.2.1 CHOSEN TEST CASES AND REASONS BEHIND THE CHOICE	82
3.2.2 MULTIPOLAR MODEL	84
3.2.3 THEORETICAL CALCULATIONS	87
3.2.4 BASIN INTEGRATION AND SOURCE FUNCTION EVALUATION	87
3.3 RESULTS	89
3.3.1 BENZENE	89
3.3.2 NAPHTHALENE	91
3.3.3 8'-BENZHYDRYLIDENEAMINO-1,1'-BINAPHTYL-2-OL	94
3.4 CONCLUSIONS AND OUTLOOKS	102
REFERENCES	104
Chapter IV: chemical bonding in coordination polymers $M(\text{HCOO})_2(\text{H}_2\text{O})_2$ [M=Co,Cu] ...	107
1.1 INTRODUCTION	108
4.1.1 COORDINATION POLYMERS	108
4.1.2 3d METAL FORMATE DIHYDRATE $M(\text{HCOO})_2(\text{H}_2\text{O})_2$: STRUCTURE AND MAGNETIC ORDERING	109
4.2 CRYSTALLIZATION AND X-RAY DIFFRACTION: OBTAINING THE EXPERIMENTAL ELECTRON DENSITY OF $\text{Co}(\text{HCOO})_2(\text{H}_2\text{O})_2$ AND $\text{Cu}(\text{HCOO})_2(\text{H}_2\text{O})_2$	110
4.2.1 FROM SYNTHESIS TO FINAL DIFFRACTION PATTERN: EXPERIMENTAL PROCEDURE	110
4.2.2 MULTIPOLAR REFINEMENT OF $\text{Cu}(\text{HCOO})_2(\text{H}_2\text{O})_2$	112
4.2.3 MULTIPOLAR REFINEMENT OF $\text{Co}(\text{HCOO})_2(\text{H}_2\text{O})_2$	115
4.3 EXPERIMENTAL RESULTS	117
4.3.1 $\text{Co}(\text{HCOO})_2(\text{H}_2\text{O})_2$	117
4.3.2 $\text{Cu}(\text{HCOO})_2(\text{H}_2\text{O})_2$	123

4.4 THORETICAL CALCULATIONS: OUTLOOKS AND PRELIMINARY RESULTS	128
4.5 CONCLUSIONS	132
REFERENCES.....	133
V Concluding remarks	135
ACKNOWLEDGMENTS (RINGRAZIAMENTI).....	138

Chapter I: Introduction

1.1 CHEMICAL DESCRIPTORS AND ELECTRON DENSITY

The advent of quantum mechanics has had without any doubts a great impact on the whole scientific world, since it entirely revolutionized the approach to the study of microscopic properties. Regarding chemistry, the first and probably most important step towards the introduction of a quantum approach is represented by the work of Heitler and London [1], who showed that the chemical bond could be explained using Schrödinger's wave mechanics. Because of that, the possibility of reducing chemical concepts to mere physical laws have been tantalizing for many scientists and philosophers [2]. This reductionist viewpoint can be summarized in a famous provocative statement reported in the opening of a book written by Henry Eyring *et al.* [3]: "In so far as quantum mechanics is correct, chemical questions are problems in applied mathematics." Notwithstanding those efforts, modern philosophers (and hopefully also a great part of the modern scientific community) have argued an anti-reductionist standpoint [2,4], not only for the practical mathematical/computational difficulties which hamper a full reduction of chemistry to physics but, more importantly, because a true understanding of chemical phenomena cannot be achieved without invoking the -although often not rigorously defined- chemical paradigms (one example above all: the Lewis theory of chemical bonding [5]). The latter are important not only for the theoretical community which investigate them, but also for experimentalists, since chemical paradigms form nowadays the basis of chemical thinking, ultimately defining the language used by chemists to communicate, discuss and understand their discoveries. On the theoretical side, over the past decades there has been a considerable effort in trying to put such chemical paradigms on firm theoretical basis* by means of quantum mechanics. This is customarily done by introducing 'chemical descriptors', *i.e.* theoretical tools and procedures which allow one to retrieve from the -often too mathematically complex- wavefunction a description close to the classical chemical thinking. The wavefunction is indeed by definition the quantum-mechanical object which enclose all the properties of the system. A particularly interesting subset of descriptors is represented by the ones based on the Electron Density (ED) distribution, whose features will be discussed in the last part of this paragraph.

The main focus of this thesis is the exploration of new applications of ED-based descriptors for the investigation of several chemical paradigms. The property of ED of being a measurable quantity (see *infra*) will be fully exploited by comparing experimentally and theoretically derived results throughout the thesis. In addition, chapter IV is devoted to the application of several ED-based descriptors to the study of chemical bonding in coordination polymers, therefore demonstrating the impact that this kind of research may have on 'real-life' chemistry.

ED (eq. 1.1) represents the probability of finding an electron at the position \mathbf{r} independently from the position of the other electrons and independently from the spin of all the electron of the system

$$\rho(\mathbf{r}; \mathbf{R}) = \int \psi^*(\mathbf{r}_1, \mathbf{r}_2, \dots, \mathbf{r}_N; \mathbf{R}) \psi(\mathbf{r}_1, \mathbf{r}_2, \dots, \mathbf{r}_N; \mathbf{R}) d\mathbf{s}_1 d\mathbf{r}_2, d\mathbf{s}_2 \dots d\mathbf{s}_N, d\mathbf{r}_N \quad \text{eq. 1.1}$$

where ψ represents the wavefunction, \mathbf{r}_i and \mathbf{s}_i are the space and spin coordinates of the i -th electron and \mathbf{R} is the position of nuclei[†]. There are several reasons which make this quantity particularly interesting for the study of chemical phenomena. From its definition it results clear that ED is a quantity defined in real space,

* note that there is a profound difference between the reductionist viewpoint which aim at abandoning the chemical paradigms, and the attempt to put the latter on quantum-mechanical basis

[†] Eq. 1.1 is valid in the Born-Oppenheimer approximation, which considers the nuclei 'frozen' and electrons moving in the field created by nuclei in their fixed positions. This approximation is completely reasonable for most of the systems at equilibrium, where the motion of nuclei is several order of magnitude slower with respect to the one of electrons.

therefore being much more easy to deal with, compared to the wavefunction*. At the same time, the famous Hohenberg and Kohn theorem [6] demonstrated that the external potential† of a system is uniquely determined by its ED distribution. Since the external potential uniquely determines the wavefunction of a system, it follows that all the properties of a system can be determined by its ED distribution only. It must be pointed out, however, that the ED-properties relationship presented above is demonstrated only from a formal point of view, while an operative approach to exactly obtain the properties of a system from the ED does not exist (yet). Nevertheless, there are many approaches which can be used to associate chemical concepts to certain features of the ED distribution. They are the so-called ED-based descriptors cited above. Among them, The Quantum Theory of Atoms in Molecules (QTAIM [7]) is the most widespread. In the process of discussing new ED-based approaches in the rest of the thesis, QTAIM will be considered as the terms of comparison, to highlight advantages, disadvantages and complementarities between QTAIM and other ED-based approaches. A brief overview of the main features of QTAIM is given in section 1.3. Another very important advantage in the use of ED-based chemical descriptors lies in the fact that ED is not only a quantum mechanical observable (see eq. 1.1), but it is also a measurable quantity. In particular, ED distribution can be obtained -under several approximations- from X-ray diffraction experiment. This is because the structure factors which are measured in an X-ray diffraction experiment are the Fourier transform of the ED distribution (eq. 1.2).

$$F_{hkl} = \int_{V_{cell}} \langle \rho(\mathbf{r}) \rangle e^{2\pi i \mathbf{H} \cdot \mathbf{r}} d\mathbf{r} \quad \text{eq. 1.2}$$

where h, k, l are the so-called Miller indices which define vectors \mathbf{H} in the reciprocal space[8]. The process of obtaining accurate and reliable structure factors from an X-ray diffraction experiment involves a complicate experimental setup as well as many mathematical elaboration steps of the measured intensity and a complete explanation is beyond the scope of this dissertation. The interested reader is referred to [8]. It will be only pointed out here that low temperature and good quality crystals (*i.e.* of appreciable volume, completely free of twinning phenomena and without a significant number of defects) are essential factors to obtain a reliable ED distribution from experiment. There exist several approaches to obtain the ED distribution from X-ray diffraction data [9], but we will consider only the ‘multipolar model’ approach, which is certainly the most widespread. A brief overview of such approach will be given in the next section.

1.2 THE MULTIPOLAR MODEL

Although, due to the fact that structure factors are the Fourier transform of ED distribution (eq. 1.2), it is possible in principle to obtain the latter from an inverse transform, the practical implementation of this procedure is hampered by many limitations. In particular, the oscillations introduced by the truncation of the series (only a finite number of structure factors can be measured) and the impossibility of measuring the phases of the structure factors (only the module $|F|$ can be obtained) are the two issues which make the evaluation of ED distribution through the inverse Fourier transform not feasible. In the ‘multipolar model approach’ introduced by Hansen and Coppens [10], the electron density is expressed through atom centered multipolar expansion (eq. 1.3).

* The wavefunction, even in its simplified Born-Oppenheimer form, is instead a $3N$ -dimensional object, where N is the number of electrons

† except for a constant

$$\rho(\mathbf{r}) = \sum_{i=1}^{N \text{ atoms}} \rho_i(\mathbf{r} - \mathbf{r}_i) \quad \text{eq. 1.3a}$$

$$\rho_i(\mathbf{r}) = P_{i,\text{core}} \rho_{i,\text{core}}(\mathbf{r}) + k_i^3 P_{i,\text{valence}} \rho_{i,\text{valence}}(k\mathbf{r}) + \sum_{l,m} k'_i{}^3 R_{il}^3(k'\mathbf{r}) P_{ilm\pm} y_{lm\pm}\left(\frac{\mathbf{r}}{r}\right) \quad \text{eq.1.3b}$$

where y_{lm} are spherical harmonics centered on i -th atom of the unit cell and derived from atomic orbitals having angular quantum number l and magnetic number m . R_{il} is the radial part of the multipoles centered on the i -th atom and having angular momentum l . Usually the multipoles up to the hexadecapole (*i.e.* $l_{\text{max}}=4$) level are considered, but different choices are obviously possible. k and k' (for spherical and deformation density, respectively) are factors included to modify the radial dependence of the multipoles according to the ED distribution of the system under investigation. Indeed, they are parameters included in the least-squares procedure (see *infra*). $\rho_{i,\text{core}}$ and $\rho_{i,\text{valence}}$ are the electron density distribution derived from the core and valence density of isolated atoms. P are the population parameters which are included in the least-square procedure (see *infra*).

Basically, eq. 1.3 expresses the ED distribution with function centered on each atom which are composed by a spherical part, taken from the ED distribution of isolated atoms, and a deformation part, which is included in order to take into account the deformation of ED caused by the presence of chemical interactions. From a practical point of view, the ED distribution of a crystal is obtained through a least-squares procedure in which the population parameters P (and the k parameters for very accurate datasets) are varied in order to minimize (in the least-squares sense) the difference between the structure factors measured from experiment and the ones calculated from the multipolar expansion, the latter being convoluted with the thermal parameters (usually expressed as ellipsoids, the so-called Anisotropic Displacement Parameters, ADP [8]) which account for the thermal motion of atoms. Besides P and k parameters reported in eq. 1.3, also atomic positions and thermal parameters are refined in the least-squares procedure. As a final note regarding the latter, it must be pointed out that in the multipolar model, the atom-centered ED distribution is supposed to rigidly follow atoms when, due to the thermal motion, they are displaced from their equilibrium position. Although this is a rather heavy approximation, it is justified for low-temperature experiments, where the thermal motion of atoms is drastically reduced.

Before concluding this section about the multipolar model, some quantities used in the rest of the thesis to discuss the quality of the model and/or the data set must be introduced. In the expressions reported in the following, F_c and F_o will be the structure factors calculated from the model and measured from experiment, respectively. w instead, are the weight associated to each structure factor in the least-squares procedure. Usually they are taken as the inverse of the square of the estimated standard uncertainty (u.s.d.), *i.e.* $w=1/\sigma(F)$, but other choices may be done depending of the specific dataset considered.

The parameters which will be thoroughly used are the following:

- $R_{int} = \frac{\sum |F_o^2 - F_c^2(\text{mean})|}{\sum F_o^2} \quad \text{eq. 1.4}$

is an estimation of the precision of the dataset. Since, depending on the crystal space group, reflection having certain Miller indices are supposed to have identical intensities, the deviation from the average (the " $F_o^2(\text{mean})$ " in the equation) gives an estimation of the average error in the measurement.

- $wR_2 = \sqrt{\frac{\sum w(F_o^2 - F_c^2)^2}{\sum w(F_o^2)^2}} \quad \text{eq. 1.5}$

is simply a measure of the extent to which the multipolar model is able to fit the measured data, as can be easily seen from the expression.

$$\bullet \quad \text{Goof} = \sqrt{\frac{\sum w(F_o^2 - F_c^2)^2}{N_{ref} - N_{par}}} \quad \text{eq. 1.6}$$

it gives an overall estimation of the quality of the multipolar model. It should be as close as possible to 1.

Finally, the residual density, *i.e.* the Fourier transform of the difference between observed and calculated structure factors will be also considered as a measure of the extent to which the multipolar model has been successful in describing the features of ED distribution measured from the data. Significant residuals may also indicate a bad quality of the dataset.

1.3 THE QUANTUM THEORY OF ATOMS IN MOLECULES

In this section, an overview of the most important aspect of QTAIM [7] will be given. As the name suggests, the main characteristic of this theory is the possibility of partitioning molecules (and crystals) into atomic regions. Obviously, QTAIM is not the sole method for the partitioning of properties and real space into atomic contributions, but it is the only one truly rooted in quantum mechanics (see *infra*). The boundaries among atoms are defined by the so-called zero-flux surfaces, *i.e.* the ensemble of points fulfilling eq. 1.7

$$\nabla\rho(\mathbf{r}) \cdot \mathbf{n}(\mathbf{r}) = 0 \quad \text{eq. 1.7}$$

where $\nabla\rho(\mathbf{r})$ is the ED-gradient and $\mathbf{n}(\mathbf{r})$ is the vector normal to the surface. It can be demonstrated that the atomic regions defined through zero-flux surfaces are non-overlapping and exhaustive (*i.e.* the whole space is included into zero-flux surfaces*). More importantly, the atomic basins built by means of equation 1.7 are defined as 'proper open systems', since their properties are "defined by quantum mechanics" [7]. Although here the quantum mechanical implications for the atomic basins defined above will not be discussed, it is important to point out that, through such definition, all the properties of a system (volume, charge, electrostatic moments, energy, etc.) can be partitioned into atomic contributions.

Another important aspect of QTAIM is represented by the so-called 'Critical Points' (CPs), *i.e.* points where the ED gradient vanishes. Critical points are labeled as (m,n) where m , the rank of the CP, is the number of ED curvatures (*i.e.* eigenvalues of the Hessian matrix) different from zero, while n is the sum of the sign of the curvatures. The CPs of a system at equilibrium are all (with just a few exceptions, not encountered in the systems investigated in this thesis) of rank three. Therefore, there exist four types of CPs, each of which is univocally associated with a structural feature of the system:

- $(3,-3)$ are maxima in the ED distribution and are found in the position of nuclei (with a few exceptions, see *infra*). Since all the gradient lines terminate at these maxima, they are also called attractors.
- $(3,+3)$ are minima in ED and are found in the cages, *i.e.* in regions enclosed by rings
- $(3,+1)$ are saddle points which are found at the center of rings (they are therefore called Ring Critical Points, RCP), the latter being defined by bond paths (see *infra*)
- $(3,-1)$ saddle critical points called Bond Critical Points (BCPs)

The latter kind of critical points are particularly important since they are related to chemical interactions. Because of that, they deserve some comments. A BCP is the minimum on the Bond Path (BP) *i.e.* a gradient

* Note that the condition reported in eq. 1.7 is fulfilled also to infinity

line joining two (3,-3) critical points* where ED is maximally concentrated with respect to any direction perpendicular to it. BPs appear wherever a chemist would draw a chemical bond (not only for covalent ones, see chapter II and IV). The inverse relationship is unfortunately not that straightforward: there are many cases in which BPs are found among atoms whose interaction would be classified as repulsive in many chemistry textbooks (*e.g.* BPs are often found among anions in a crystal [11] or among positively charged hydrogen atoms [12]). Because of that, an intense debate have taken place in literature (see, for example, refs. 12 and 13). We will not enter into the merit of such (sophistic) discussion, and in the rest of the thesis we will limit ourselves to use QTAIM as a reference descriptor for interactions and point out those cases where an alternative approach is needed.

For the sake of completeness, a note about (3,-3) critical points and atomic basins is in order here. There are a few documented cases where ED maxima [14] (and associated zero-flux basins) were found in points where there are no nuclei. They are the so-called non-nuclear attractor. However, the occurrence of these topological entities is very rare and it was not encountered in any of the systems investigated in this thesis.

* In some special cases, the so-called catastrophe points, BPs may join topological entities different from (3,-3) CPs. These, however, which are very particular situations which are never met in this thesis

REFERENCES

- [1] W. Heitler, F. London, *Zeitschrift für Physik*, (1927) 44, 455
- [2] M. L. Harris *Studies in History and Philosophy of Science* (2008) 39, 78
- [3] H. Eyring, J. Walter, G. E. Kimball “*Quantum Chemistry*” (1944) John Wiley and Sons, Inc.
- [4] A. I. Woody *Philosophy of science* (proceedings) (2000) 67, S612
- [5] G. N. Lewis *J. Am. Chem. Soc.* (1916) 33, 762–785.
- [6] P. Hohenberg, W. Kohn, *Phys. Rev.* (1964) B864, 136
- [7] R. F. W. Bader (1990) *Atoms In Molecules: A Quantum Theory* Oxford: Clarendon Press
- [8] Giacovazzo, C., Monaco, H. L., Artioli, G., Viterbo, D., Ferraris, G., Gilli, G., Zanotti, G., Catti, M. (2002) *Foundamentals of Crystallography. Secon Edition*. Edited by C. Giacovazzo. New York: Oxford University Press
- [9] C. Gatti and P. Macchi (Eds.), *Modern Charge Density Analysis*, Springer, Dordrecht-Heidelberg-London- New York, 2012
- [10] N. K. Hansen, P. Coppens. *Acta Cryst.* (1978) A34, 909.
- [11] see, for example: Y. V. Nelyubina, K. A. Lyssenko, V. Y. Kotov M. Y. Antipin *J. Phys. Chem. A* (2008) 112 (37), 8790
- [12] J. Poater, M. Solà, F. M. Bickelhaupt. *Chem. Eur. J.* (2006) 12(10), 2889
- [13] R. F. W. Bader *Chem Eur. J.* (2006) 12(10), 2896
- [14] see, for example: C. Gatti, P. Fantucci, G. Pacchioni *Theor. Chim. Acta* (1987) 72, 433

Chapter II: Non- Covalent interactions description

2.1 INTRODUCTION

Non-covalent Interactions (NCIs) can be defined as those interactions which do not involve electron sharing to a significant extent. The investigation of this kind of interactions can be traced back to 1873, when J. D. van der Waals was studying the behavior of gases [1] and realized that the simple ideal gas model often fails due to many effects, among which the (non-covalent) attraction between gas atoms/molecules. Nowadays, NCIs play an essential role in several branches of chemistry, like biochemistry [2], crystal engineering [3], polymorphism [4], molecular recognition [5], and self-assembly [6]. Therefore the concept of NCIs has an outstanding role in chemistry since the understanding of NCI has been inherently bound to the development of chemistry itself.

For the very fact that NCIs have been studied for very long time, many ways have been proposed to categorize the various kind of interactions. A commonly employed classification is the one built by considering how the wavefunction of two interacting fragments is *perturbed* when they come close to one another from infinite distance (Perturbation Theory approach [7], hereinafter PT) or, in other words, by considering which is the dominant contribution to the interaction energy* for a given non-covalent complex. Being defined in terms of wavefunction, this kind of approach is rooted in quantum mechanics. The formalism used to define the various contribution is beyond the scope of this dissertation: the interested reader can find a complete explanation in ref. 7. In the PT framework, NCIs are classified as follow[†]:

- **Electrostatic interaction.** It is the interaction energy calculated considering the unperturbed ED distribution of the two fragments in the geometry they have in the dimer.
- **Induction.** It represents the contribution to interaction energy due to the deformation of ED distribution of one fragment caused by the proximity of the other fragment.
- **Dispersion (also called London forces).** Although it is often conveniently described as due to the interaction between instantaneous multipoles in the ED distribution of the two interacting fragments, dispersion energy is purely quantum phenomenon and is due to electron correlation. It is important to point out that, differently from induction, this contribution is *always present* when two ED distribution are interacting.

For the majority of NCIs, however, all the contributions reported in the classification above play an important role. Moreover, in some cases, NCIs take place between fragments of the same molecule (intramolecular NCIs) and, therefore, the separation into fragments is not possible anymore, at least not unambiguously. For these reasons, the classification based on perturbation theory is often of little use for a chemist, who usually need an -albeit more empirical- classification which is based on observations and which allows explanation (and prediction) of the chemical consequences (*i.e.* molecular geometry, interaction energy, etc.) caused by the presence of a given NCI. In this work, rather than the classification

*The interaction energy for a molecular dimer is defined as: $E_{\text{int}} = E_{\text{AB}} - E_{\text{A}} - E_{\text{B}}$, where E_{AB} is the (electronic) energy of the dimer, while E_{A} and E_{B} are the energy of the separated fragments A and B *in the same geometry they have in the dimer*. When the calculation is not done at the complete basis set limit, the correction for basis set superposition error must be taken into account

[†] the interaction energy can be (almost) exactly decomposed into the terms reported in the following list only when the two fragments are not too close to each other at equilibrium geometry. When this condition is not fulfilled, *e.g.* in the case of strongly interacting dimers, the terms arising from the antisymmetrization of the whole wavefunction must be taken into account.

above reported, based on a model of increasingly interacting wavefunctions for a complex and of the corresponding total energy changes), NCI will be classified using the nomenclature by which chemists normally design such interactions. Being essentially based on the kind of atoms involved in the NCI, the list of NCI is in continuous growth. In the following, a list of the NCI types most frequently considered in this work is reported:

- **Hydrogen Bonds (HBs).** It is probably the most ubiquitous, strong and frequently studied type of NCI. A recent definition of hydrogen bond was proposed in 2011: “The hydrogen bond is an attractive interaction between a hydrogen atom from a molecule or a molecular fragment X–H in which X is more electronegative than H, and an atom or a group of atoms in the same or a different molecule, in which there is evidence of bond formation” [8]. It is necessary to point out that, in some special cases (*e.g.* the so called “resonant assisted HBs” [9]), this kind of interaction is cannot be considered anymore as a purely non-covalent one as it involves a partial covalent contribution.
- **C–H \cdots π interaction.** This kind of interaction shares many similarities with HBs (interaction between a hydrogen atom and a group of atoms, which in this case is the fragment bearing the π electronic cloud) but, at the same time, is characterized by different behavior (*e.g.* it lacks the strong directionality which characterizes HBs). For this reason there is a debate in literature regarding whether to consider it as a ‘conventional hydrogen bond’ [10] or whether, instead, label it as a particular kind of NCI [11]. As a matter of fact, C–H \cdots π interactions play an outstanding role in many important chemical phenomena such as biological interactions [12] and in the determination of crystal packing [13]. Therefore, this kind of interaction will be investigated in the present dissertation within the ‘NCI descriptor’ framework and will be defined as C–H \cdots π , without considering the matter of whether they are real HBs or not.
- **Van der Waals interactions.** The term ‘van der Waals’ is used in literature with different meanings. According to IUPAC [14], in this dissertation it will be used to indicate the following kind of interactions: dipole-dipole (or higher order multipole), dipole-induced dipole and dispersion forces.
- **Sulphur-Sulphur interaction.** This kind of NCI, although known since long time [15] is not significantly considered in literature. It takes place between divalent Sulphur atoms, as Sulphur is able to act as both nucleophile and electrophile, depending on interaction geometry. A more detailed description will be given in paragraph 2.4, when ‘NCI descriptor’ picture of this kind of interaction will be presented.

The list above reported is obviously far from being complete and many other kind of NCIs, such as halogen bonds [16], agostic interactions [17], $\pi\cdots\pi$ stacking [18] etc. are important in many chemical phenomena.

Despite their recognized important role, the mechanisms leading to the appearance of a given NCI as well as the interplay among the various type of NCIs is still far from being fully understood. Considering the experimental point of view, it must be pointed out that most of the features of non-covalent complexes are not directly observable. Nevertheless, there are several techniques which allows one to investigate NCIs. The experimental methods used for the study NCIs range from the ‘classical’ spectroscopic ones, such as infrared and Raman spectroscopy to the more modern and sophisticated methods like the zero electron kinetic energy [19] and the resonance-enhanced multiphoton ionization [20]. However, experimental techniques usually provides only evidence of the *presence* of a given non-covalent complex (at best they can give an estimation of interaction energy) and, although the combination of several experimental outcomes may lead a scientist to draw some rules about the behavior of certain classes of compounds, it cannot be denied that theoretical approaches are necessary to obtain a more complete explanation of the

mechanism leading to the NCIs formation. On the other hand, very accurate calculations are needed for these kinds of investigations. . . Indeed, dispersion energy often plays a fundamental role in the stabilization of non-covalent complexes. Therefore, any accurate theoretical investigation of NCIs cannot leave dispersion out of consideration. On the other hand, the dispersion energy can only be retrieved when explicitly correlated wavefunctions, *i.e.* the ones obtained from computationally expensive methods such as Configuration Interaction or Coupled Cluster, are used (the dispersion-corrected DFT Hamiltonians [21] represent an exception, but the reliability of such techniques is still under debate [22]). For what explained so far, it becomes clear that the systematic investigation of NCIs can be carried out only nowadays, due, on the experimental side, to the development of new accurate techniques and, from the computational point of view, to the remarkable increase in the performance of modern computers. As a result, NCI investigation is experiencing a tremendous growing in the last decade and this topic is thus of central interest for modern science.

Single-Crystal X-Ray Diffraction (SCXRD) plays a truly central role in the investigation of NCIs as the crystal packing is mostly dictated by non-covalent forces [23] and, therefore, crystals are ideal supramolecular entities for the study of NCIs. As explained in chapter 1, Electron Density (ED) distribution brings the advantage of allowing the study of NCIs experimentally and theoretically on the same ground. It is clear, therefore, that the possibility of studying this kind of interaction using ED distribution only represents an important step for the investigation of NCIs.

An NCIs descriptor entirely based on ED distribution has been proposed in 2010 by Johnson *et al.* [24]. We have applied it *for the first time* to experimentally derived ED distribution [25]. Moreover we have carried out a systematic comparison between experimental results and: i) results obtained from fully periodical calculation [25], ii) the NCIs picture offered by the Quantum Theory of Atoms in Molecules, [26] and iii) the results obtained from Independent Atom Model [27].

In section 2.2 the main characteristics of the so called “NCI descriptor” will be explained, while in part 2.3 an overview regarding the application of this descriptor carried out in our group will be given. Results of such investigation will be reported in paragraphs 2.4, 2.5 and 2.6, while in section 2.7 the features of the code developed in our group to apply the NCI descriptor to experimental as well as theoretical ED distribution will be briefly summarized.

2.2 THE NCI DESCRIPTOR

The so called ‘NCI descriptor’ has been introduced by Johnson *et al.* in 2010 [24]. The main breakthrough of this descriptor lies in its ability to allow one to obtain a chemically meaningful and easy-to-catch pictorial visualization of NCIs. Another interesting aspect of this descriptor is the fact that it exploits quantities which can be obtained from the ED distribution only, therefore leading to the advantages of ED-based descriptors highlighted in the introduction. The two quantities which are exploited in the ‘NCI descriptor’ are the Reduced Density Gradient (RDG) and the quantity $\rho(\mathbf{r}) \cdot \text{sign} \lambda_2$ (where λ_2 is the second greatest eigenvalue of the ED Hessian matrix). In particular, low-value RDG isosurfaces in low-ED regions are used to detect the presence of NCIs, while the quantity $\rho(\mathbf{r}) \cdot \text{sign} \lambda_2$ is mapped onto RDG isosurfaces to characterize the different interactions. In the following two paragraphs, a more detailed description of these quantities is given.

2.2.1 THE REDUCED DENSITY GRADIENT

The origin of RDG is to be sought in the Density Functional Theory (DFT) framework [28]. In such theory, the Hamiltonian –which is formally exact- is written in the following form:

$$E = T_S + \int \rho(\mathbf{r})V_{ext}d\mathbf{r} + \frac{1}{2} \int \int \frac{\rho(\mathbf{r}_1)\rho(\mathbf{r}_2)}{r_{12}} d\mathbf{r}_1 d\mathbf{r}_2 + \frac{1}{2} \int \int \frac{\rho(\mathbf{r}_1)h_{XC}(\mathbf{r}_1;\mathbf{r}_2)}{r_{12}} d\mathbf{r}_1 d\mathbf{r}_2 \quad \text{eq.2.1}$$

Details of the model behind such expression are beyond the scope of this dissertation: the interested reader can find the details of the derivation of DFT Hamiltonian in ref 28. What is important for the present discussion is the last term, called ‘exchange correlation term’, E_{XC} . Its exact analytic form is not known, and there exist many techniques to approximate it. The simplest approximating method is called ‘Local Density Approximation’ (LDA). LDA is based on the model of ‘homogeneous electron gas’, and, in the framework of such approximation, the term $h_{xc}(r1;r2)$ is written in the form:

$$E_{XC}^{LDA}[\rho] = \int \rho(\mathbf{r}) \varepsilon_{XC}(\rho(\mathbf{r}))d\mathbf{r} \quad \text{eq. 2.2}$$

As can be seen from eq. 2.2, in LDA the exchange correlation term depends on ED only. A step forward with respect to this simple model is done by considering the deviation of the ED from homogeneity, *i.e.* the ε term is not anymore a function of ED only, but also of its gradient(which is null everywhere for a homogeneous electron gas).For practical reasons, however, the inclusion of ED gradient in such equations, is formulated in term of RDG, which is the true argument of GGA exchange-correlation part, rather than the ED gradient itself. The definition of RDG is reported in equation 2.3,

$$s(\mathbf{r}) = \frac{1}{2(3\pi^2)^{1/3}} \frac{|\nabla\rho(\mathbf{r})|}{\rho(\mathbf{r})^{4/3}} \quad \text{eq. 2.3}$$

where $s(\mathbf{r})$ is the RDG evaluated at the point \mathbf{r} , while $\nabla\rho$ represents the ED gradient. Because of the 4/3 power of ED, the denominator has the same dimension of the ED gradient and as a result RDG is dimensionless. In general, this quantity represents the deviation of the ED distribution from the ‘homogeneous electron gas’ model and, therefore, it is to be understood as a local inhomogeneity parameter [28]. It is clear, from the discussion reported above, that the understanding of the general behaviour of RDG is of vital importance for the improvement of GGA functionals. Because of this, RDG has been deeply investigated in the past, with the aim of improving existing exchange-correlation functionals [29]. In particular, several quantities related to exchange-correlation functional were evaluated for a number of real physical systems, including isolated atoms, molecules, and crystals. A number of important results were obtained from such investigations. The most important for the present discussion is that the energy-averaged RDG (as defined in ref 29b) diminishes in passing from atoms to molecule and from molecules to crystal. This implies that low-RDG values can be associated to chemical interactions. Moreover, there is a straightforward connection with QTAIM: by looking at eq 2.3, one can immediately see that wherever a critical point is present, RDG must go to zero and, being ED a continuous function (with the exception of nuclear cusps), RDG must be low in the neighbourhoods of the CP as well.

In order to better understand why and how RDG isosurfaces can be used to detect NCIs, it is instructive to consider plots of RDG VS ED for a simple system: the benzene molecular crystal (the reader is referred to paragraph 2.3.1 for the details regarding how ED distribution of this system has been obtained). In figure 2.1a, such plot for a molecule of benzene extracted from the crystal (*i.e.* considering only the multipoles centred on the atoms belonging to such molecule) is reported. The space considered to calculate the RDG and ED has been chosen so that it encloses some C-C and C-H bonds (two and three, respectively) and the

region far away from the nuclei. From such plot, it can be seen that RDG assumes low values in the region around $2 \text{ e}/\text{\AA}^3$, that is the regions associated to covalent bonds, eventually going to zero at the C-C and C-H BCPs. On the contrary, in the region far from nuclei, where the ED is exponentially decaying, RDG assumes large values, due to the fact that the term $\rho(\mathbf{r})^{4/3}$ goes to zero faster than $\nabla\rho$. Figure 2.1b shows an analogue plot within the same volume enclosing, this time, a pair of molecules extracted from the crystal, so that intermolecular contacts can be detected. Note that, at variance with the reference molecule, the second one is entirely contained within the cube (see inset). Besides those related to intramolecular covalent interactions, four new spikes (three of which at lower ED values are nearly superimposed) appear in the low-ED/low-RDG region of this plot. These spikes, whose building points are relative to the region between the two interacting molecules, are the signature of NCIs. Although the appearance of low-RDG/low-ED spikes associated to NCIs has been demonstrated here for a molecular pair of benzene molecular crystal, this behaviour is completely general: whenever two (or more) molecules are close to each other, *i.e.* when they are somehow interacting, such peaks appear [24,25,27,38].

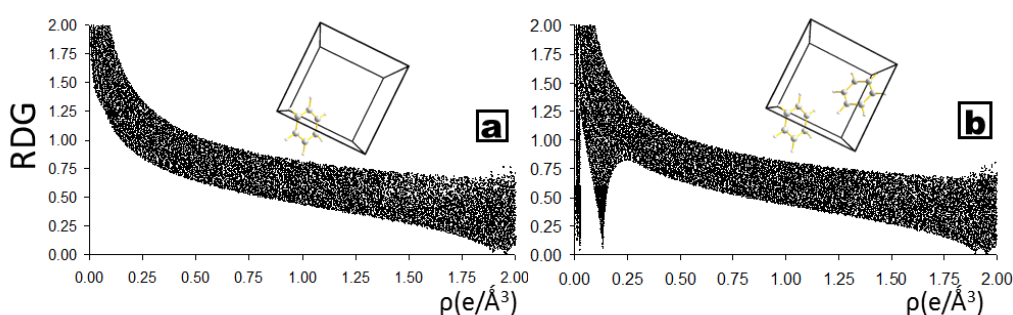


Figure 2.1 Plots of RDG VS ED. a) Molecule of benzene extracted from crystal b) molecular pair of benzene extracted from crystal. In the inset of each picture the position of the cube in which properties were evaluated with respect to the molecule(s) is shown

From the discussion above, it should be clear how low-RDG isosurfaces can be used for NCI investigation. RDG assumes low values in the region associated with both covalent and non-covalent interactions. Since the latter are characterized by ED far lower than the former, by building low-RDG isosurfaces in low-ED regions it is possible to detect the presence of NCIs. Many examples of such isosurfaces can be found in paragraph 2.4, 2.5 and 2.6.

Although, as it will be explained in section 2.4, the shape of RDG isosurfaces already contains information on the type of interaction, the possibility of mapping a quantity onto isosurfaces is certainly helpful to gain more insights into the various kinds of NCIs. In the original formulation of ‘NCI descriptor’, the quantity used is $\rho(\mathbf{r}) \cdot \text{sign}\lambda_2$. In the next paragraph details regarding the definition and significance of such quantity are given.

2.2.2 THE QUANTITY $\rho(\mathbf{r}) \cdot \text{sign}\lambda_2$

To better distinguish the nature of the various interactions and to rank their strength, Johnson *et al.* [24] proposed to map the quantity $\rho(\mathbf{r}) \cdot \text{sign}\lambda_2$ onto RDG isosurfaces. This quantity was somehow ‘borrowed’ from QTAIM, since in the latter the value of ED and its curvatures at the BCP are usually correlated with the strength and the type of the interactions. In the ‘NCI descriptor’, in fact, $\rho(\mathbf{r})$ mapped onto isosurfaces is considered as a measure of the strength of interactions, exactly as it is usually done in QTAIM for BCPs.

Regarding the curvatures, in QTAIM framework the sign of the ED laplacian (*i.e.* the sum of the eigenvalues of ED Hessian matrix) at BCPs is often used to distinguish between covalent and non-covalent interactions (although many exceptions to this classification can be found [30]). On the other hand, ED laplacian is of little use to classify NCIs since for this kind of interactions it is always positive and often very small. Therefore, Johnson *et al.* proposed the use of only the second greatest eigenvalue of ED Hessian matrix, which is labeled as λ_2 . They showed, for a number of simple molecular dimers, how the sign of λ_2 mapped onto RDG isosurfaces relative to NCIs can be directly translated into chemically meaningful concepts. In particular, λ_2 is negative for those interactions which are usually considered as attractive, *e.g.* hydrogen bonding, while it assumes positive values for non-bonded contacts (*e.g.* steric clashes). Hence, the sign of λ_2 can be used to distinguish the former from the latter.

Despite it has been shown that the sign of λ_2 has some direct correlation with what a chemist would consider as an attractive interaction or a non-bonded contact (the latter being also defined, in the seminal work on 'NCI descriptor', as 'steric crowding'), a note of caution is in order here. As well-known from physics, and as pointed out quite recently by Bader [31], in a system at equilibrium there are no net repulsive or attractive forces acting on the nuclei. Nevertheless, the identification of attractive and repulsive interactions has always been part of many chemical models, from the simplest ones which are taught to undergraduate students (*e.g.* concepts such as 'steric crowding' or 'ring tension') to the more advanced theories in which the interaction energy is decomposed into attractive and repulsive contributions [32]. Therefore one can say that such partitioning is, in a sense, part of chemistry itself. In the discussion presented in paragraph 2.3, the classification based on the sign of λ_2 , in accordance with the 'NCI descriptor' framework, will be used, and for some cases the parallelism with attractive and repulsive interactions will be discussed.

2.3 APPLICATION OF THE NCI DESCRIPTOR TO EXPERIMENTAL, THEORETICAL AND IAM ELECTRON DENSITY: METHODS

In this paragraph, the work realized in our lab concerning the application of the 'NCI descriptor' will be presented, while the discussion of the results is given in the subsequent sections.

The main aim of our investigation, started in 2012, was to apply the 'NCI descriptor' to experimentally derived ED. Despite two years had passed since the original proposal of the 'NCI descriptor' [24], the (numerous) applications reported in literature were all relative to theoretically derived ED, mostly *in vacuo*. Extending its use to ED derived from X-ray diffraction experiments would pave the way for popularizing this tool within the crystallographers community. In particular, such investigation is important to shed light on limits and advantages of multipolar ED distribution when used for the study of NCIs in the 'NCI descriptor' framework. Moreover, to carry out this investigation, we developed a Fortran90 code [33] able to calculate all the quantities needed to apply the 'NCI descriptor' starting from ED-distribution obtained from experimental and theoretical (both periodical and *in vacuo*) ED. We provided, in this way, a new powerful tool for the experimentally-based investigation of NCIs. Furthermore, we implemented in such code several additional features, *e.g.* the calculation of quantities directly from the wavefunction. Details regarding the code are reported in paragraph 2.7.

In our work, the 'NCI descriptor' was applied to the ED distribution of three molecular crystals (see paragraph 2.3.1) obtained through low-temperature single-crystal X-ray diffraction. As stated in section 2.1,

molecular crystals are composed of molecules held together by NCIs and, for this reason, they can be considered as suitable supramolecular entities to study NCI. More importantly, X-ray diffraction experiments carried out on crystals are, the only way to obtain experimental ED distribution in the bulk.

For all the investigated systems, we performed a least squares multipolar refinement against datasets taken from literature. In particular, we adopted the formalism of Hansen & Coppens [34] using the code XD2006 [35]. Details of the multipolar refinement are reported in the next paragraphs, along with an overview of the three crystal systems investigated. To assess the reliability of experimental picture, we also compared it with the theoretical one (see section 2.5), obtained through fully-periodical DFT calculations performed at the experimentally-determined geometry. In particular, B3LYP hybrid functional [36], combined with 6-311G** basis set [37] has been employed.

Another important step of our investigation on 'NCI descriptor' regards the use of Independent Atom Model (IAM) ED distribution. Slightly after the 'NCI descriptor' was introduced, it was stated [38] that the results obtained from IAM-ED are qualitatively equivalent to the ones obtained from SCF calculations. To explore to which extent this is true, we carried out a systematic comparison between isosurfaces obtained with multipolar and IAM ED [27]. Details and results of this investigation are reported in paragraph 2.6.

2.3.1 TEST CASES

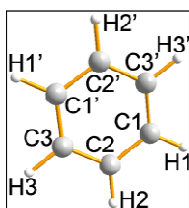
In order to apply the 'NCI descriptor' to experimentally derived ED of molecular crystals, we explored the crystallographic literature looking for systems to be used as test cases. The quest was, in particular, to find some molecular crystals whose NCIs are variegated enough to cover a broad range of interactions types, from the strong to the weak ones. In addition, we tried to include substances which crystallize in different crystal forms (polymorphs), so as to make it possible to compare NCIs in the two different crystal systems. Most importantly, to be suitable for the a reliable determination of ED distribution, the datasets had to be available and fulfill the following requirement:

1. Being measured at temperature not higher than 100 K
2. Containing almost all the measurable reflections (completeness above 99%) up to a high resolution (at least 1.1 \AA^{-1} in $\sin\theta/\lambda$)
3. Having a good precision, which is usually measured, for X-ray diffraction datasets, as the average difference among reflections which, due to crystal symmetry, are supposed to have the same intensity. One of the most commonly used index is called R_{int} (defined in chapter I and in ref. 39) and we wanted it to be lower than 4%
4. Not being affected by systematic errors
5. Having a good agreement with the published multipolar model, *i.e.* being accurate. This can be checked by verifying the featurelessness of the residual density map. Moreover, the R_{F} parameter, which is a commonly used index in crystallography to measure the agreement between calculated and measured structure factors, should be as low as possible. We looked for values lower than 3%.

Eventually, we found three crystal systems able to fulfill all the requirements reported above. Such set is formed by the three following compounds: austdiol [40], benzene [41] and famotidine [42], the latter being able to crystallize in two different crystal forms, whose accurate structure factors have been measured. In the next paragraphs, some details regarding the crystal packing, multipolar model and periodical calculations will be reported.

BENZENE.

Benzene (Scheme 2.1) molecular crystal was chosen as a prototype of system characterized by interactions involving π electrons.



Scheme 2.1. Atom labels for benzene. The primed ones refer to inversion-related atoms. The 'ball and stick models' of molecular structure in this and all the following pictures were produced using the software 'Diamond' [43].

It crystallizes, below 270 K, in the centrosymmetric *Pbca* space group, with half a molecule in the asymmetric unit and four molecules or, equivalently, four unique pairs of molecules in the unit cell. The crystal packing of aromatic and polyaromatic compounds was largely investigated by Desiraju and Gavezzotti [44], who classified the typical packing motif in crystalline benzene as a herringbone structure, which was found to maximize the number of C-H \cdots π and C-H \cdots C interactions. This feature is clearly reflected by the NCI descriptor (see paragraph 3.3).

Single-crystal X-ray and neutron diffraction experiments were carried out by Bürgi et al. [41]. The X-ray diffraction data set has been used in the present work to obtain multipolar populations. In particular, all multipole populations up to $l=4$ and $l=2$ were refined for Carbon and Hydrogen atoms, respectively. Only the Anisotropic Displacement Parameters (ADPs) of Carbon atoms were refined, as positional and thermal parameters came from accurate X-ray and neutron estimates. It should be noted, however, that our final C thermal parameters are equal to those previously published within 3 s.u. and differ, on average, by less than 1.5%. Moreover, we also refined radial expansion/contraction parameters (k -values) for the multipoles of all atoms. The same constraints used in the original paper were applied: the monopole population of each hydrogen atom and its bonded carbon were constrained to sum up to 5.0 electrons*, so that each C-H moiety was neutral, and only one $k = k'$ parameter was refined for H atoms. For all the Carbon atoms, only one k and k' values were refined independently. According with 41, only data with $I/\sigma(I) > 2$ were included in the least-squared procedure. Final agreement indices are reported in Table 2.1.

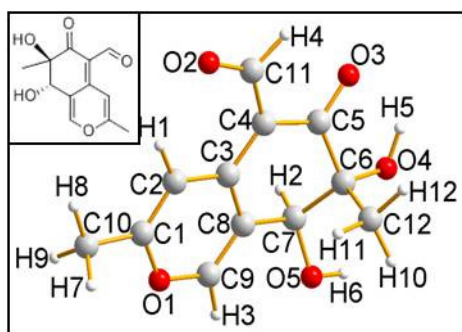
Table 2.1 Final agreement indices of the multipole refinements for the investigated molecular crystals

	AUSTDIOL	BENZENE	FAMOTIDINE (A)	FAMOTIDINE(B)
space group	$P2_12_12$	<i>Pbca</i>	$P2_1/c$	$P2_1/n$
refined against	F^2	F^2	F	F
$R_w(F)$	0.0245	0.0499	0.0205	0.0201
$R_w(F^2)$	0.0485	0.0258	0.0413	0.0400
$R(F)$	0.0375	0.0168	0.0325	0.0331
$R(F^2)$	0.0241	0.0337	0.0220	0.0261
Gof	1.2251	1.0435	1.0896	1.0175

AUSTDIOL. Austdiol (Scheme 2.2) is a fungal metabolite which crystallizes in the unusual space group $P2_12_12$ as a consequence of the coexistence of two main packing patterns in the bulk. In the a,b crystal plane, molecules are held together by a network of Hydrogen Bonds (HBs), while in the direction perpendicular to such planes van der Waals forces are the main forces which hold molecules together (see

* Note that the monopole population include the number of valence electrons only (4 electrons for C and 1 for H)

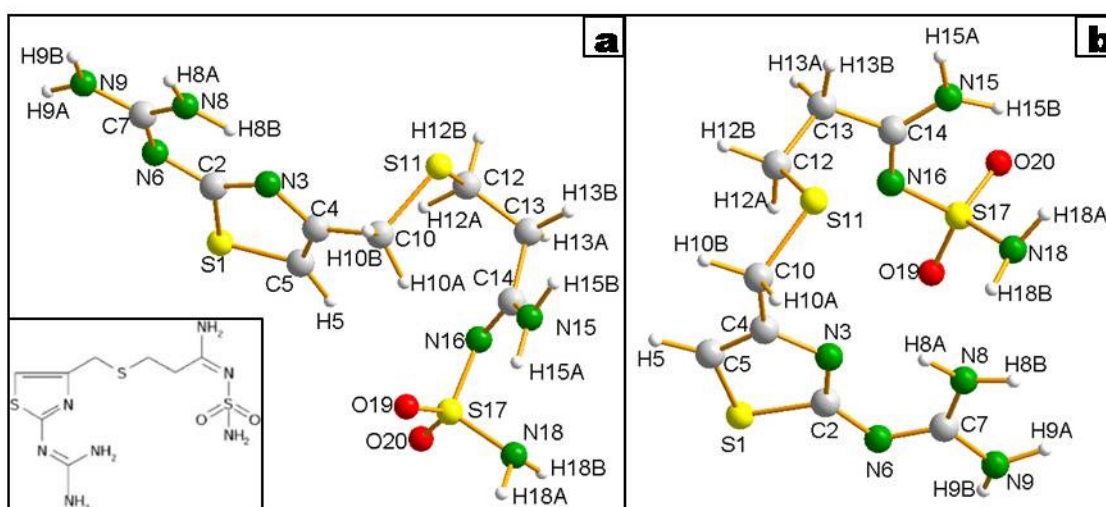
infra). This system is therefore characterized by the presence of many HBs of different strength and van der Waals interactions, making it a suitable test cases to investigate these interactions in the 'NCI descriptor' framework.



Scheme 2.2 Atom labels and chemical scheme (topleft inset) of the fungal metabolite Austdiol.

Austdiol crystal structure and charge density were deeply investigated by Destro et al. [40]. The coordinates and the anisotropic displacement parameters (ADP's) of all non-hydrogen atoms were refined. Positional and thermal parameters of the H atoms were on the contrary kept fixed at their best-estimate values. As concerns the k-parameters, they were not refined in the original paper and we kept them fixed to the standard values computed by XD2006. In any case, we judged that the final ED model was satisfactory enough (see also Table 2.1) to reliably apply the RDG-based NCI descriptor.

FAMOTIDINE. Famotidine (Scheme 2.3) is an antiulcer drug. This crystal system was chosen as test case for two reasons. First, because it is a molecule containing many different functional groups and rich in heteroatoms, and as such it is able to give rise to many different kind of NCIs (see paragraph 2.4). In addition, this molecule is able to crystallize in two different crystal forms and accurate X-ray diffraction datasets have been measured for both polymorphs by Overgaard et al. [42]. Therefore it allows one to investigate the different kinds of NCIs which takes places in the two different polymorphs.



Scheme 2.3a) molecular conformation of polymorph A of famotidine; b) same as a), for polymorph B. Bottom left inset: chemical scheme of famotidine.

Regarding the multipolar refinement, the same refinement strategy was employed for both polymorphs. The atomic positions, thermal motion (isotropic for hydrogen, anisotropic for C, N, O and S) and multipole populations up to $l=0$ for hydrogen and to $l=4$ for all other atoms were initially refined. Then, the H atoms were placed at idealized positions on the basis of the neutron-based Allen's estimates [45] and kept fixed in the following refinement steps. Subsequently, the dipole populations of H atoms were also refined and their ADP's were computed by means of the SHADE2 server [46]. Within this approach, the TLS rigid-body contribution is estimated on the basis of a somewhat arbitrary fragmentation of the molecule in one or more 'rigid body' moieties. We tried different fragmentation schemes, and eventually we chose to consider the molecule as a whole for the TLS calculation. Indeed, the agreement between calculated and observed rigid-body thermal parameters was satisfactory, with wR values as large as 0.127 for polymorph A and 0.167 for polymorph B, both being perfectly comparable with other SHADE2 test cases reported in ref. [47]. Eventually, we tried to perform a radial scaling refinement. Due to the flatness, in this system, of the least-squares weighted error function with respect to k and k' , the convergence criterion was far to be satisfied even after 100 cycles. Therefore, as in the original paper,[42] we performed a block-refinement by optimizing multipole populations at fixed k -parameters, and then k -parameters at fixed multipole coefficients. We considered that convergence was satisfactory when both the parameter classes change by less than one their own s.u.. This procedure took 8 steps for polymorph A and 7 steps for polymorph B. Eventually, as it was suggested [48] that the standard atomic expansion employed by XD2006 for S is not the optimal choice to describe the deformation part of the ED for the sulphur atom, we modified such expansion as suggested in the original work. It should be stressed that the Hirshfeld rigid bond test [49] was always satisfied for all the covalent bonds within the investigated systems.

2.4 APPLICATION OF THE NCI DESCRIPTOR TO EXPERIMENTAL ELECTRON DENSITY DISTRIBUTION: RESULTS

2.4.1 OPERATIONAL CHOICES

From an operational point of view, the NCI descriptor has been separately applied to a series of molecular pairs extracted from the crystal. This strategy implies that the contribution due to the multipoles centred on atoms belonging to the rest of the unit cell is ignored in reconstructing the multipole ED within each pair. In the Hansen–Coppens formalism[34] implemented in the XD program package, [35] the ED at each point \mathbf{r} can therefore be partitioned as follows (Eq. 2.4)

$$\rho(\mathbf{r}) = \rho_A(\mathbf{r}) + \Delta\rho(\mathbf{r}) \quad \text{eq. 2.4}$$

where $\rho_A(\mathbf{r})$ is the contribution of a certain (group of)atom(s) or molecule(s) A and $\Delta\rho$ is that arising from the multipoles centered on the remaining atoms in the unit cell. In general, as the radial part of the multipole functions decays exponentially with $|\mathbf{r}|$, [34] the direct contribution of an atom M, located at \mathbf{r}_M , to the ED at \mathbf{r} is negligible whenever the $|\mathbf{r}-\mathbf{r}_M|$ distance is significantly greater than the covalent radius of M. Accordingly, the main features of ED in the space between a pair of nearest neighbor molecules depend almost exclusively on their (composing) pseudoatoms. We found that this condition was always satisfied in the present work, the only exception being that of a single benzene molecular pair (see below).

Therefore, NCI analysis can in general be safely performed on a molecular pair extracted from the crystal, the effect of the crystalline matrix being properly and indirectly included in the multipole expansion of the molecular pair pseudoatoms.

As explained in the paragraph 2.2.1, the RDG isosurfaces relative to covalent and non-covalent interactions appear in regions of space characterized by very different ED values. To investigate NCIs only, RDG has to be evaluated in regions having ED lower than a certain value. The most suited cutoffs were selected by examining the ED/RDG plots case by case. For all the results presented in this chapter, a cutoff of 0.05 au ($=0.337 \text{ e}\cdot\text{\AA}^{-3}$) was adopted. The same colour scale was employed for all isosurfaces which will be presented in paragraph 2.5, ranging from -0.03 (red) to 0.035 (violet) au.

Another choice to be made regards the RDG isovalue to build isosurfaces. Selecting a reasonable RDG isovalue is, usually, not a problematic issue being customarily set at more or less half of the highest RDG values of the points in the spikes observed in the RDG/ED plot. The only rule of thumb seems that the same RDG value should be used when comparing to each other the various NCI, both in the same or in different systems, provided a single method was employed to obtain the various ED's. Otherwise, different RDG values are seemingly required to compare on similar grounds the RDG-based results for differently computed ED (*e.g.* from wavefunction, multipole), although this may be a delicate and debatable assumption when contrasting the performance of "true" ED's against that of the Independent Atom Model (IAM) ED. For true ED's, the main effect of different methods on the $s(\mathbf{r})$ vs. $\rho(\mathbf{r})$ diagram is a shift of peaks, thus, in order to obtain comparable images just a shift of cutoffs is needed. This can be related to the fact that $s(\mathbf{r})$ roughly behaves like $\rho^{-1/3}$ (see eq. 3 in Ref.38), so that the effect of the method on the density is directly followed by the RDG. In their seminal paper, Johnson *et al.* used RDG values among 0.4 and 0.7 for true ED's. For experimentally derived isosurfaces, the isovalue of 0.6 will be used for all the isosurfaces. For what concerns the *ab-initio* and IAM isosurfaces, the matter of what is the best isovalue will be discussed in the relative sections, *i.e.* 2.5 and 2.6, respectively.

2.4.2 AUSTDIOL

Within the *ab* crystal plane of Austdiol molecular crystal, the molecules are held together by relatively strong O-H \cdots O HBs involving a hydroxyl, a keto and an aldehyde groups (see Fig. 2.2a). Therefore, an overall zigzag ribbon [40] HB pattern is generated along the *a* axis. At the same time, such a pattern forces each pair of molecules in the *ab* plane to be C_2 symmetry-related, and therefore excludes the possibility of a third 2_1 axis parallel to *c* to exist. Rather, different molecular layers along *c* are connected by considerably weaker CH \cdots O HBs (see Fig. 2.4a). According to ref. 40, only those H \cdots O contacts for which the Koch and Popelier criteria [50] are satisfied were considered as true HBs in the present work. This system was chosen as test case with the aim of investigating the experimentally derived results of 'NCI descriptor' when HBs and van der Waals interactions are considered.

Table 2.2 Geometrical and topological features of some intermolecular and intramolecular X-H...O contacts (X=C,O) of Austdiol.

Bond [figure number] ^a	$\rho_{\text{BCP}}(\text{e}/\text{\AA}^3)^{\text{b}}$	$\nabla^2\rho_{\text{BCP}}(\text{e}/\text{\AA}^5)^{\text{b}}$	$d_{\text{H}\cdots\text{O}}(\text{\AA})$	angle XHO(deg)
Intermolecular				
O5-H6...O4 ^c [2.2b]	0.14(4)	1.34(6)	2.023	153.2
O4-H5...O3 ^d [2.2d]	0.09(4)	1.11(5)	2.114	158.4
C9-H3...O2 ^e [2.2c]	0.13(3)	1.40(4)	2.174	150.7
C11-H4...O5 ^f [2.2c]	0.05(2)	0.56(1)	2.519	154.1
C12-H11...O2 ^g [2.4b]	0.05(3)	0.83(2)	2.443	163.4
C10-H7...O3 ^g [2.4b]	0.04(3)	0.41(1)	2.544	166.9
C12-H11...O1 ^h [2.4b]	0.03(1)	0.33(<1)	2.979	116.9
Intramolecular				
C9-H3...O5 [2.2c]	no BCP	no BCP ⁱ	2.461	92.1
C2-H1...O2 [2.3a]	0.11(3)	2.00(3)	2.145	121.8
C11-H4...O3 [2.3b]	no BCP	no BCP ⁱ	2.359	100.5
O4-H5...O3 [2.3c,2.2d]	no BCP	no BCP ⁱ	2.052	116.9

a) The labels reported in square brackets in column 1 refer to the figures where the corresponding RDG-based NCI iso-surfaces are portrayed.

b) Electron and Laplacian density values standard uncertainties (s.u.) are given in parentheses. The s.u. on the Laplacian are well known to be underestimated using XD2006. The s.u. on the geometrical parameters cannot be correctly estimated since the hydrogen positions were not refined; however, the s.u. on $d_{\text{H}\cdots\text{O}}$ should be roughly 0.001 Å while the ones on the angle in the order of 0.1 (see Ref.40).

c) At -X, 1-Y, Z ; d) At 1-X, 1-Y, Z ; e) At -1+X, Y, Z ; f) At 1+X, Y, Z ; g) At -0.5+X, 0.5-Y, -Z ; h) At 0.5+X, 0.5-Y, -Z.

i) $\lambda_2 < 0$ at the midpoint of the H...O vector.

The isosurfaces relative to some of the relevant inter- and intramolecular X-H...O (X=C,O) contacts of Austdiol are shown in Figures 2.2 and 2.3, respectively, while Table 2.2 reports their corresponding geometrical and topological features. Figure 2.4 displays iso-surfaces relative to three weak C-H...O intermolecular interactions along *c*.

Intermolecular hydrogen bonds

Johnson *et al.* showed that relatively strong HBs, such as those formed in water and formic acid dimers, result in disc-shaped, contracted RDG iso-surfaces with $\lambda_2 < 0$ curvatures. [24] Figures 2.2b-d display the RDG surfaces as computed from the experimental ED for the quite strong intermolecular H...O HBs in the (*a*,*b*) plane of the unit cell of Austdiol (Fig. 2.2a). Some disc-shaped, negative-valued RDG iso-surfaces are indeed recognizable (Figures 2.2b-d), together with more complex ones arising from the formation of cyclic H-bonded patterns due to the crystal packing. This is in particular the case for the H5...O3 interaction (Fig. 2.2d), where a green-blue surface winds in the free space between two C_2 symmetry-related molecules. Indeed, the two facing O3 atoms are linked through a BP, producing therefore an RDG isosurface containing the BCP, the two corresponding RCPs, and even an *intramolecular* O4-H5...O3 contact per molecule (see section below). The other important O-H...O bond is the H6...O4 one (Fig. 2.2b). Again, the couple of symmetry-related HBs are characterized by disc-shaped, $\lambda_2 < 0$ surfaces. On the other hand, the third green surface visible between them is the signature of the ring critical point. At variance with the RCP-related surface within the benzene ring, it is quite elongated, possibly as a result of the much smaller symmetry in the ring in the present case and of the fact that the internuclear axes related to 1,4 (O4...O5) or higher "topological" non-bonded contacts (1,5: O5...O5, O4...O4, H6...H6) either do not intersect or do so in different points.

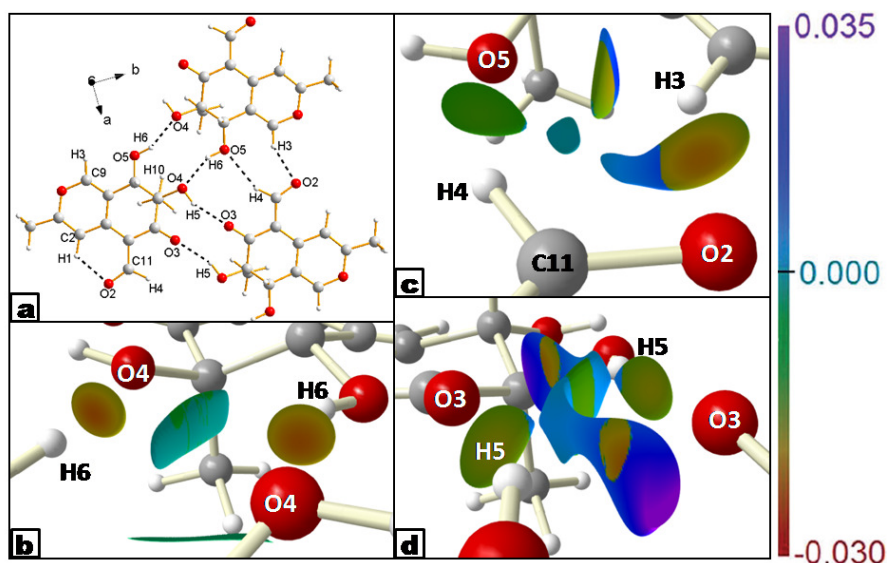


Figure 2.2 a) Inter- (black) and intra- (blue) Hydrogen bond network in the (a,b) plane of Austdiol. All the interactions marked in this panel are shown as corresponding RDG iso-surfaces in Figure 2.2 and 2.3. b-d) RDG-based NCI iso-surfaces for X-H \cdots O (X=C,O) contacts of Austdiol. The color scale for $ED^* \text{sign} \lambda_2$ (e/au) is shown on the right. The iso-surfaces in this and the following Figures have been drawn with the software Molliso [82]

The C9-H3 \cdots O2 contact is worth of being discussed separately (Fig. 2.2c), as it is quite short (Table 2.2) and it was estimated to bear strength comparable with that of the above described OH \cdots O bonds. [40] Such an evidence is recovered in the NCI framework: the corresponding signed isosurface, and in particular its negative part, looks similar to those discussed above for the OH \cdots O HBs, even though it is not as well shaped because of the presence of a non-bonded contact involving C11 and H3 atoms in symmetry-related molecules.

Intramolecular hydrogen bonds

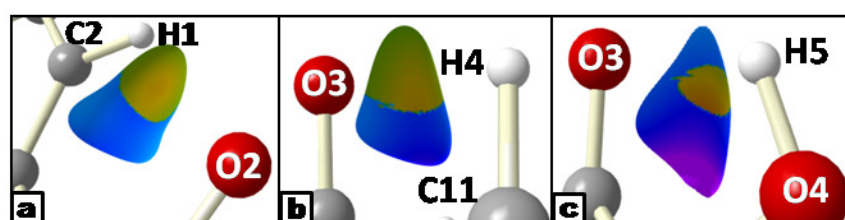


Figure 2.3. RDG-based NCI iso-surfaces for selected X-H \cdots O (X=C,O) intra-molecular contacts of Austdiol. See Fig. 2.2 for the molecular geometry (2.2a) and the color legend

As concerns the intramolecular H \cdots O contacts, that are certainly important in determining the molecular conformation observed in the bulk, a BP was found only for the C2-H1 \cdots O2 interaction. On the contrary, a RDG iso-surface depicts each of the six unique intramolecular H \cdots O contacts, no matter a BP is present or not (three iso-surfaces for non-bonded contacts are shown in Fig. 2.3b-c and 2.2c). Interestingly, the RDG iso-surface of the C2-H1 \cdots O2 HB (Figure 2.3a) is characterized by two well-defined regions of positive and negative λ_2 , respectively, due to the presence of a ring critical point near (0.61 Å apart) the HB BCP. This was expected on the basis of the ED topology in a cycle when a bond is significantly weaker than the others. [26] It should be stressed, however, that RDG iso-surfaces provide a similar picture also for the remaining non bonded intramolecular C-H \cdots O contacts, including those in Figures 2.3b and 2.2c. In general, the

farther the hydrogen from the oxygen is, the more the CHO angle is bent, the smaller is the $\lambda_2 < 0$ zone onto the isosurface. However, such a trend is not neat and, also, not always respected. The simultaneous involvement of the H and of the acceptor O atoms also in significant intermolecular interactions (this is the case of H4, H5, H6, O2, O3, O4, O5 atoms in Austdiol) may complicate the picture and affects the shape and the relative fractions of positive and negative signed RDG iso-surfaces for the intramolecular interactions besides what is expected on the basis of the geometry of the intramolecular CH \cdots O interaction only. This external perturbation results particularly evident in the case of the two intramolecular O-H \cdots O non bonded contacts. For instance, the O4-H5 \cdots O3 interaction (Table 2.2 and Figure 2.3c) shows a larger iso-surface, almost completely characterized by positive λ_2 . The H5 atom is also contemporarily involved in a strong, almost linear, intermolecular O-H \cdots O contact with the same O atom type, O3, but belonging to another molecule (Table 2.2). Interestingly, the O4-H5 \cdots O3 contact forms a BP in the gas-phase, *i.e.* when no intermolecular interactions compete for stronger HBs. In this context, the RDG-based NCI descriptor may be useful to highlight the environment effects on the relative strength and nature of such contacts.

Van der Waals interactions

Van der Waals and, in particular, dispersion interactions are known to be difficult to be properly modelled both *in vacuo*[51] and in molecular crystals.[52,53,54] These interactions are due to time-dependent perturbations of the ED and imply correlations among distant electrons. Therefore, they cannot be correctly taken into account by ground state adiabatic methods, such as standard DFT theory, where the exchange-correlation potential is estimated on the basis of a finite number of the static ED derivatives.[54,55] Moreover, dispersion interactions are inherently non-local in nature, as they correlate the *overall* charge density distributions of individual molecular moieties to each other. [56] Even though dispersion forces do not significantly affect ED,[57] they play an important role in lowering the overall interaction energy of the system.[53] The ability of the NCI descriptor to highlight subtle intra- and intermolecular density features typically associated to dispersion interactions was discussed in detail in Ref.24. Indeed, in complexes like methane dimer, large and almost flat iso-surfaces appeared in regions characterized by very low and almost constant ED values. It was also demonstrated there that MP2/6-311++G** calculations produce virtually identical NCI iso-surfaces as the B3LYP/6-31G* ones, despite the different interaction energy estimates of these two methods. [24]

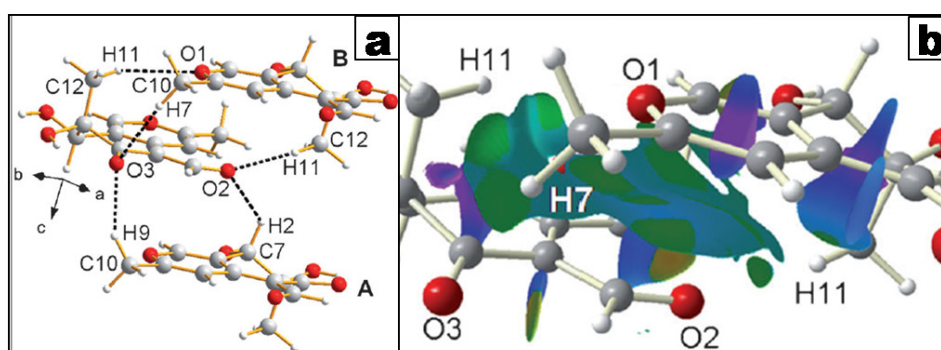


Figure 2.4 RDG representation of NCI for Austdiol along the *c* axis. See Table 2.2 for the symmetry operations relating the showed molecules. *a*) Crystal packing along the *c* direction; *b*) RDG-based NCI iso-surfaces for the ‘B’ molecular pair, formed by the central molecule and the upper one in panel *a*).

As concerns the experimental ED of Austdiol, quite large RDG iso-surfaces were found for the two unique neighbouring molecular pairs along the *c* direction (structure in Fig. 2.4a; signed-RDG iso-surfaces are

shown in Fig. 2.4b and, for the sake of space, only for the molecular pair labeled as 'B' in Fig. 2.4a). Three C-H \cdots O bonded contacts, based on the BP criterion, hold together the molecular pair in Fig. 2.4b. Two of such contacts (*i.e.* C12-H11 \cdots O1 and C10-H7 \cdots O3) are very weak and the first one was even found [40] not to satisfy the Koch and Popelier criteria [50] for hydrogen bonding. Indeed, they are not recognizable through specific RDG iso-surfaces. Rather, a single, broad van der Waals-like iso-surface has merged with and encompasses the two slightly negative, diffuse and not disc-shaped regions around the BCPs of the two interactions. This behaviour may be explained in terms of the marginal difference between a closed-shell dispersive interaction and an extremely weak and long C-H \cdots O bond. Moreover, the ED is relatively flat in this region. Therefore, the λ_2 eigenvalue is always very close to zero and its sign turns out to be quite indeterminate. This implies that both positive and negative values are present when the $\rho(\mathbf{r})\cdot\text{sign}(\lambda_2)$ quantity is mapped onto the RDG iso-surface. Figure 3.4b also displays a clearly recognizable disc-shaped RDG iso-surface for the C12-H11 \cdots O2 intermolecular hydrogen bond that connects neighbouring molecules outside the (*a,b*) plane (*i.e.* at different heights along *c*). Actually, in this case, besides the comparatively short HB bond length (Table 2.2), it occurs that the H \cdots O direction is almost parallel to the molecular layers in the (*a,b*) plane and the HB takes place in a region where the non-directional purely steric-dispersive interactions are not playing the dominant role.

In general, the electronic excitations causing dispersive interactions are *always* present, but the characteristic large and flat RDG iso-surfaces associated to such interactions emerge only if stronger interactions (such as, for example, OH \cdots O, but also strong CH \cdots O hydrogen bonds) are not simultaneously acting within the same region of space. Moreover, strictly speaking, purely dispersive, van der Waals interactions are always *attractive*. Yet, in Figure 2.4b the $\text{sign}(\lambda_2)$ quantity is positive throughout vast areas of the RDG isosurfaces. According with the interpretation of the NCI descriptor,[24] this indicates that (several) atoms are in "nonbonded" contact (closed-shell interactions), but, clearly, it does not also imply that the overall interaction revealed by the RDG iso-surface is destabilizing. Note that the NCI descriptor explores the behavior of the RDG in a specific region, whereas the interaction energy is the result of a balance involving forces which effectively operate in a larger portion of space. Moreover, the observed crystal packing is the outcome of a subtle competition among different energy contributions, and there is always a certain degree of arbitrariness in partitioning the overall cohesive energy of a crystal in 'stabilizing' and 'repulsive' terms*. As reminded by Bader,[58,59] there are no net attractive or repulsive forces acting on a field-free quantum system at the equilibrium, as in that case the overall balance of the quantum-mechanical Eherenfest and Feynman forces (acting respectively on electrons and nuclei) is exactly zero. In conclusion, the so-called 'van der Waals-like' large and flat RDG iso-surfaces above described should be considered as tools to highlight those regions of space characterized by steric crowding and dispersive interaction balance, rather than as a way to 'see' or 'localize' van der Waals, dispersive interactions in the bulk, which by their very nature are neither local nor static. Another word of warning concerns the soundness of the energy classifications proposed for the signed RDG iso-surfaces [24] when they enclose regions of flat and low X-ray-derived ED's, particularly prone to both random and systematic experimental errors.

From the results presented here for Austdiol, it emerges that a one-to-one inverse correlation seems to exist among the directionality (and the strength) of specific non-covalent interactions and the surface/volume ratio of the corresponding RDG iso-surface. In particular, the stronger is the NCI, the

* Actually, the former is the only true quantum mechanical observable, whereas individual attractive and repulsive energy terms are not. In principle, any quantum mechanical or classical energy partitioning that retrieves the overall cohesive energy is valid. Therefore, there is no universal agreement on what recipe should be employed to highlight specific dispersive and steric contributions to the total energy.

smaller and more disc-shaped the RDG surface appears in the real space, at the same time being characterized by more negative $\rho(\mathbf{r}) \cdot \text{sign}(\lambda_2)$ values (see also Ref.38 and 24).

2.4.3 BENZENE

Table 2.3 reports the topological properties of the intermolecular BCPs found for each unique molecular pair of benzene molecular crystal, whereas Figures 2.5 and 2.6 show the corresponding RDG iso-surfaces for the pair I and II-IV, respectively. As concerns the pair I, NCI iso-surfaces (Fig. 2.5a) are associated to two intermolecular bond paths (Fig. 2.5b).

Table 2.3. Geometrical and topological (BCP) data for intermolecular C-H...C and C-H...H interactions in the benzene crystal.^{a,b}

bond [figure number]	$\rho(e/\text{\AA}^3)$	$\nabla^2\rho(e/\text{\AA}^5)$	$d_{\text{H}\cdots\text{C}}(\text{\AA})$
C3...H2 ^c [5a]	0.030(4)	0.256(1)	3.065
C1...H3 ^c [5a]	0.042(6)	0.371(2)	2.862
C1...H3 ^d [6a]	0.016(5)	0.235(1)	2.955
H2...H1 ^e [6a]	0.018(4)	0.275(1)	2.638
H3...H2 ^f [6b]	0.013(5)	0.238(1)	2.548
C3...H1 ^f [6b]	0.024(4)	0.241(1)	2.934
C3...C2 ^g [6c]	0.001(<1)	0.008(<1)	5.295

a) The labels reported in square brackets in column 1 refer to the figures where the corresponding RDG-based NCI iso-surfaces are portrayed.

b) Electron and Laplacian density values s.u. are given in parentheses.

c) At -0.5-X, -Y, -0.5+Z

d) At -X, 0.5+Y, 0.5-Z

e) At +X, 0.5-Y, 0.5+Z

f) At -0.5-X, -0.5+Y, +Z

g) At -1-X, -Y, -Z. The BCP was recovered by using only the multipoles of the two molecules (see text)

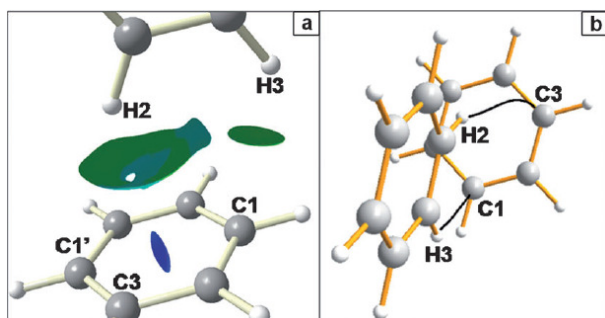


Figure 2.5. See Fig. 2.2 for the color legend. a) RDG-based NCI iso-surfaces for the molecular pair I in the benzene crystal. b) Intermolecular bond paths for the same molecular pair.

These two BPs link C3 and C1 with H2 and H3 atoms at -0.5 -x, -y, -0.5+z. From the QTAIM perspective, this should indicate two well-defined CH...C interactions. However, the H2...C3 BP is significantly bent, due to the fact that the BP points towards the (3,-1) critical point of the C3-C4 covalent bond and then suddenly deviates towards the (3,-3) nuclear C3 attractor (Fig. 2.5b). Moreover, the H2 atom is roughly equidistant from all the carbon atoms belonging to the other molecule of the pair, as the $d_{\text{H}\cdots\text{C}}$ distances range from 3.065 Å (H2...C3) up to 3.109 Å (H2...C1). All these features, typical of systems showing CH... π interactions, [60] suggest that H2 should in fact similarly interact with all the carbon atoms of the symmetry-related molecule, giving rise to a C-H... π attractive contact involving the whole π -electron cloud of the facing aromatic ring. Indeed, the RDG-based NCI descriptor (Fig. 2.5a) gives rise to a donut-like-shaped, large iso-

surface that, from the viewpoint of the H2 hydrogen atom, covers almost entirely the hydrocarbon ring of the other molecule. This picture clearly clashes against the one provided by the BP analysis, which is found to privilege the interaction of the H with just one single atom of the ring.* However, the $\rho(\mathbf{r})\cdot\text{sign}(\lambda_2)$ quantity is slightly more negative (light green zone of the surface in Fig. 2.5a) between H2 and its nearest carbon atom (C3), somewhat mirroring the presence of the BP connecting these two specific atoms. It is worth noting that the RDG iso-surface looks to some extent similar to the broad surfaces that were associated to the steric/dispersive interactions in Austdiol (see Section 2.4.2 above): in fact, C-H $\cdots\pi$ interactions are essentially dispersive in nature. [60] Nonetheless, the surfaces associated to CH $\cdots\pi$ and 'pure' van der Waals-like interactions differ in that the former appear more localized in space, owing to their clear association to the dispersive interactions arising from the π system.

The signed RDG iso-surfaces of the other CH \cdots C interaction (H3 \cdots C1) look instead much smaller, disc-shaped, and only slightly negative. All these features comply with a conventional, very weak HB, as anticipated by the largely asymmetric location of H3 with respect to the ring atoms of the other molecule in the pair and by the almost straight BP and density properties at the BCP. The RDG-based NCI and BP pictures nicely match in this case.

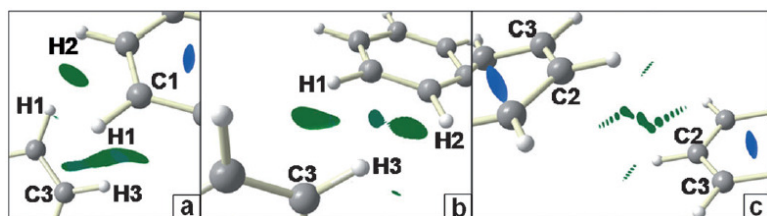


Figure 2.6. RDG iso-surfaces for the molecular pairs II (a), III(b), and IV(c) in the benzene crystal. a) Contacts H1 \cdots H2, C1 \cdots H3. b) Contacts H3 \cdots H2, C3 \cdots H1. c) C3 \cdots C2. See Fig. 2.2 for the color legend and Table 2.3 for the symmetry operations.

In both the molecular pairs II and III (Fig. 2.6a-b) two similar BPs are present. One links an Hydrogen to a Carbon atom (CH \cdots C contact), whereas the other connects two Hydrogen atoms. The shape of the RDG iso-surface associated to the first BP for the molecular pair III resembles those found for intermolecular HBs in Austdiol (see Section 2.4.2 above) and in benzene pair I, although in this case it appears slightly broader in space, while the iso-surface relative to the same contact in molecular pair II is definitely more elongated. This shape could likely be the result of C1-H1 and C3-H3 bonds facing each other. Nearly disc-shaped iso-surfaces were found also for the H \cdots H contacts. In general, all the surfaces associated to H \cdots C and H \cdots H contacts in Fig. 2.6a-b are relatively broad and bear signed $\rho(\mathbf{r})$ values quite close to zero, although negative. In other words, they signal weakly attractive interactions, only partly localized between the atom pairs that give rise to the QTAIM BP's. The iso-surfaces look somewhat intermediate between the 'van der Waals-like' and 'HB' ones, as it could reasonably be inferred on the basis that weakly dispersive interactions should play a significant role in almost apolar H \cdots C and H \cdots H contacts.†

The CH \cdots C interactions in Fig. 2.6a and 2.6b are formally equivalent to a very weak HB, as they follow the trend sketched above on going from relatively strong (OH \cdots O) to weak (CH \cdots O) HB interactions (see Section

* Though not recovered, a set of six more or less bent, inequivalent H \cdots C bond paths, would have clearly been a topologically possible alternative outcome.

† Monopole net charges on the unique H atoms are all positive and equal among each other within one standard deviation. Bader's net charges for the unique H atoms are all positive and range from 0.085 (H2) to 0.122 (H1) up to 0.145 (H3) electrons

2.4.2 above). Nevertheless, it should also be remembered that RDG iso-surfaces and BPs depend to some extent on the whole set of the interactions present in a system. In the case of the BP this may, for instance, be revealed by the Source Function contributions of the various atoms to the ED at each point of the BP. [61] Analogously, the smaller or larger size of the RDG iso-surfaces provide an insight on the more or less local character of an interaction, respectively. It is thus not granted that the broad, dark green surfaces between H and C in Fig. 2.6a and 2.6b be *exclusively* due to the interaction between the two facing atoms. Eventually, the molecular pair IV (Fig. 2.6c) deserves specific comments. In such a pair, the centres of mass of the two molecules are 6.78 Å far apart (see also Table 2.3). When the multipole ED for this pair extracted from the crystal is considered, two intermolecular C...C BP's are found between the C2 atom of the reference molecule and the C3 atom at -x, -y, 1-z, and *vice-versa*. The corresponding BCPs have a very low ED (Table 2.3). In the RDG-based approach, a broad and low-ED valued iso-surface appears, representing therefore some kind of very weak, although attractive interaction (based on the λ_2 sign). The latter could be interpreted as a sort of dispersive-driven $\pi\cdots\pi$ interaction among the lateral Carbons of the two molecules. However, when also the multipoles of the neighbouring molecules are considered, *i.e.* when the same analysis is performed in the bulk, both the BP's and the RDG iso-surfaces disappear. This implies that the $\Delta\rho$ term in equation (2.4) is no longer negligible and follows from the fact that the two molecules are quite far apart from each other. Indeed, in this case the relative contribution to ED in the intermolecular region due other molecules in the unit cell increases at expense of that due to the multipoles belonging to pair IV. In particular, when the multipoles associated to the $\Delta\rho$ term are considered, the quantity $|\nabla\rho(\mathbf{r})|$ in equation (2.3) increases more than the ED itself, rising the RDG values well above the value used for defining the RDG iso-surface.* A possible explanation of this behaviour may reside on that, even though a very weak $\pi\cdots\pi$ interaction may take place in pair IV, it is negligible with respect to other stronger interactions (CH... π , dispersive) present in the benzene crystal. Interestingly, similar RDG iso-surfaces appear when they are computed on a quantum-mechanical ED of an isolated benzene molecular pair at the same crystal geometry, whereas they are no longer present when the fully periodical ED is considered (see paragraph 2.5). All this agrees with the conclusions drawn above for Austdiol as for the conditions which are required to make the RDG iso-surfaces related to van der Waals interactions visible and even with Literature findings.[44]At the same time, what we found provides evidence that the NCI features displayed in Fig. 2.6c are likely not due to the artefacts of the multipole model.

2.4.4 FAMOTIDINE

Famotidine (Scheme 2.3) is an heteroatom-rich antiulcer drug. Two different polymorphs of this compound are known [62] to date (P2₁/c and P2₁/n), that differ from each other in both their crystal packing and molecular conformation. Indeed, the form A, which is the thermodynamically stable one, adopts an 'elongated' conformation, while the kinetically favoured modification B has a folded 'hairpin' geometry. Most of the intermolecular interactions in both polymorphs are alike to the HBs and van der Waals-like contacts that were already discussed for Austdiol (Section 2.4.2) and benzene (Section 2.4.3). In this Section, therefore, we will mainly focus on the NCI results regarding interaction types not yet analysed, *i.e.* NH...N HBs and other relevant interactions involving π -electrons or sulphur-atoms.

* For example, considering the intermolecular BCPs in the isolated pair geometry as the reference points, the ED increases from 0.00061 to 0.00280 e/Å³ on passing from the isolated pair to the crystal, whereas the ED gradient goes from 0 to 0.0062 e/Å⁴. In the latter case, the RDG becomes as large as 2.54, well above the 0.6 isovalue (see Section 3.1) adopted in this work.

Both the A and B polymorphs show an intramolecular N-H \cdots N BP among a guanidinic -NH₂ group as H-donor and the thiazole N atom as H-acceptor. The topological features of the BCP indicates that this HB is the strongest among all the hydrogen bonds considered so far. In fact, it may be classified as a Resonance-Assisted HB. [63] Interestingly, the topological descriptors for this interaction are different on going from the form A to the form B (see Table 2.4). In particular, this HB is significantly stronger in the polymorph B, as the H \cdots N distance undergoes a \approx 4 % shortening and the ED at the BCP increases by \approx 28 % (see Table 2.4). In general, from the QTAIM perspective, strong (but still mainly electrostatic) HBs show a larger contraction of ED towards the BP and from the BCP towards the nuclei with respect to weaker ones. This is reflected in higher negative values for the λ_1 and λ_2 density curvatures (related to the directions of maximal charge decrease perpendicular to the BP at BCP) and in higher positive value for the λ_3 curvature along the BP at BCP, as it is indeed the case for the interaction here considered.

Table 2.4. Geometrical and bond critical point properties of the intramolecular N-H \cdots N interaction for the two polymorphs A and B of famotidine.

	A H8B \cdots N3	B H8A \cdots N3
$\rho(e/\text{\AA}^3)$	0.18(2)	0.23(3)
$\nabla^2\rho(e/\text{\AA}^5)$	3.52(4)	3.62(5)
$d_{\text{H}\cdots\text{N}}(\text{\AA})$	1.928	1.853
angle NHN(deg)	130.6	131.2
λ_1	-0.99	-1.19
λ_2	-0.59	-0.93
λ_3	5.09	5.74
$d_{\text{BCP-RCP}}(\text{\AA})^a$	0.839	0.830

a) distance from BCP to the nearest ring critical point (RCP)

The RDG iso-surfaces for this NH \cdots N interaction in both polymorphs are reported in Figure 2.7. In this case the region with negative λ_2 value is more disc-like shaped and contracted in space with respect to those found for the intramolecular HBs in Austdiol (see Section 2.4.2 above).

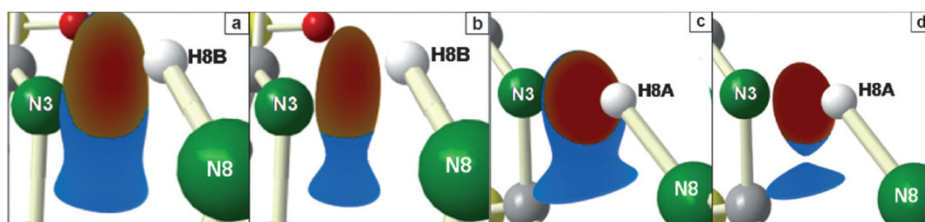


Figure 2.7. N-H \cdots N intramolecular H-bonds in famotidine. See Fig. 2.2 for the $\rho(\mathbf{r})\text{sign}(\lambda_2)$ color legend. a) Polymorph A, reduced density gradient $s(\mathbf{r}) = 0.6$; b) Polymorph A, $s(\mathbf{r}) = 0.45$; c) polymorph B, $s(\mathbf{r}) = 0.6$; d) Polymorph B, $s(\mathbf{r}) = 0.45$

This effect is particularly evident for the B form, when compared to that for the A (Fig. 2.7). As discussed above for Austdiol and Famotidine, these features correlate with the HB strength and again the QTAIM and RDG scenarios are mutually supporting each other. The ED contraction commented above is larger in the B form and the $|\nabla\rho(\mathbf{r})|/\rho(\mathbf{r})^{4/3}$ ratio, due to the larger λ_i ($i=1-3$) magnitudes (especially λ_2), changes more rapidly, thus yielding smaller RDG-isovalue domains in such form. This can be in fact seen also from the smaller negative- λ_2 region found in the polymorph B. The contraction of the RDG surface as a function of

the HB strength becomes even clearer if the RDG isovalue is diminished from 0.6 to 0.45 (Figure 2.7). Reducing such value may result in a splitting of the original higher iso-surface value RDG domain, in sub-domains. This is typically the case when the original domain encompasses more than one critical point in the density. There will be a given, lower RDG value where the RDG domains associated to the two critical points will start to separate. The process is reminiscent of the Electron Localization Function analysis where, by continuously increasing the ELF isovalue from 0 up to 1, the initial reducible basin containing all the 3-dimensional attractors of a given system progressively splits up into its component irreducible domains, each of them containing just one ELF local maximum. [64] Diminishing the RDG iso-value to 0.45 yields a splitting of the original RDG = 0.60 iso-surface domain in two sub domains only in polymorph B, one domain being related to the BCP and the other to the RCP.

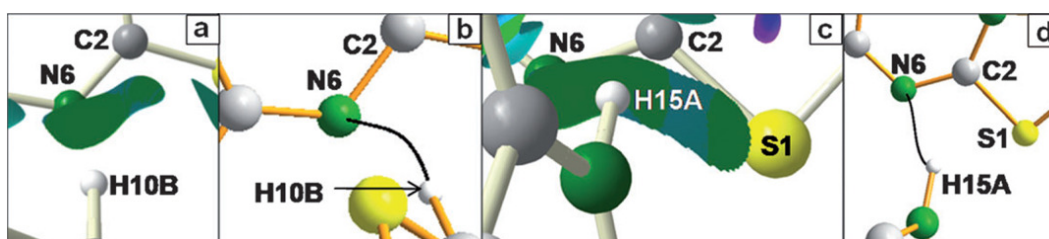


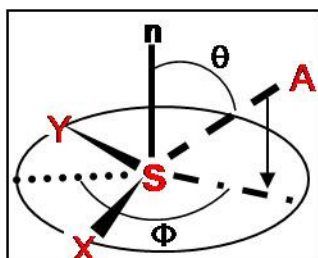
Figure 2.8. RDG-based NCI iso-surfaces and bond paths for two intermolecular H-bonds of famotidine (polymorph A). See Fig. 2.2 for the color legend. *a-b*) C-H... π interaction involving the N=C bond at $1-x, 0.5+y, 1.5-z$ and the corresponding H10B...N6 bond path; *c-d*) Same as *a-b*), for the interaction between H15A and the atoms N6, C2 and S1 at $x, 0.5-y, 0.5+z$. Only the H15A...N6 bond path is observed.

Figure 2.8a shows a CH... π -type intermolecular interaction (similar to those found in benzene) for the polymorph A. In this case, however, only a single bond, namely N6-C2, conjugated with the thiazole system*, acts as acceptor in the CH... π contact. In other words, this CH... π interaction appears to be more localized with respect to those involving the entire aromatic ring in benzene (Section 2.4.3). In any case, both the QTAIM and the NCI descriptor approaches provide evidences of the existence of such an interaction. As concerns QTAIM, the BP relating H10B and N6 atoms points towards the covalent N6-C2 BCP and then deviates to reach the N6 attractor (Fig. 2.8b). The NCI descriptor, on the other hand, shows a typical low-ED RDG iso-surface among the hydrogen atom and the conjugated bond. Interestingly, at variance with similar surfaces detected for benzene, that shown in Fig. 2.8a is relatively constricted in space, as it does not extend far away from the N6-C2 bond. An NH... π interaction scheme is found in another molecular pair of the same polymorph A (see Fig. 2.8c). The QTAIM picture clearly indicates a HB between H15A and N6, with an almost straight BP connecting the two atoms (see Fig. 2.8d). The NCI descriptor, instead, suggests a more delocalized, through-space interaction somewhat relating the H15A atom with both S1-C2 and C2-N6 bonds. In this case, the RDG iso-surface probably bears contributions arising from different interaction types. Therefore, it is difficult to disentangle the contribution due to the NH...N HB evidenced by QTAIM from other, less localized and somewhat more subtle interactions. The theoretically-derived RDG iso-surfaces for these interactions (see section 2.5) are anyhow markedly similar to those obtained from the multipole ED. In the present example, the joint RDG-NCI and QTAIM approach is more informative with respect to either of the two, as at least two different interaction types (NH...N HB and a possible NH... π interaction), coexisting in the same region of space, can be distinguished.

NCI involving Sulphur atoms have been studied for a long time, as, due to its large van der Waals radius and relatively high polarizability, Sulphur is able to set up several interactions with its local environment in

* the N6-C2 bond is much shorter than the neutron-estimated [45] value for a single bond (1.488 Å) and slightly longer than both the neighbouring N6-C7 bond (1.339 Å) and the neutron-estimate for a double (1.336 Å) N-C bond

organic crystals [see, *e.g.* Ref. 65]. In 1977, Rosenfield *et al.*[15] systematically investigated the geometrical preferences of the non-covalent contacts involving divalent Sulphur atoms and within the sum of the van der Waals radii of the interacting chemical species. In particular, they considered the polar coordinates ϕ and ϑ with respect to the vector normal to the X-S-Y plane as defined in scheme 4 as possible approaching angles.



Scheme 2.4. Geometrical parameters for the S...A contact. X and Y are the atoms covalently bonded to the sulphur. θ is the angle between the normal \mathbf{n} to the YSX plane and the interacting atom A. ϕ is the angle between the projection of the vector SA onto such plane and the line bisecting the YSX angle.

They concluded that $\vartheta < 40^\circ$ for the electrophilic species, whereas the nucleophilic ones approach Sulphur with $60^\circ \leq \vartheta \leq 90^\circ$ and $110^\circ \leq \phi \leq 140^\circ$ (*i.e.* the nucleophile tends to lie almost in the X-S-Y plane, and preferably along the X-S or the Y-S directions). In Famotidine, only the former type of contacts is relevant, with Hydrogen acting as the electrophilic species. The corresponding RDG iso-surfaces for the form A and B are reported in Fig. 2.9a-b and 2.9c-d, respectively (S1-H13A is not shown).

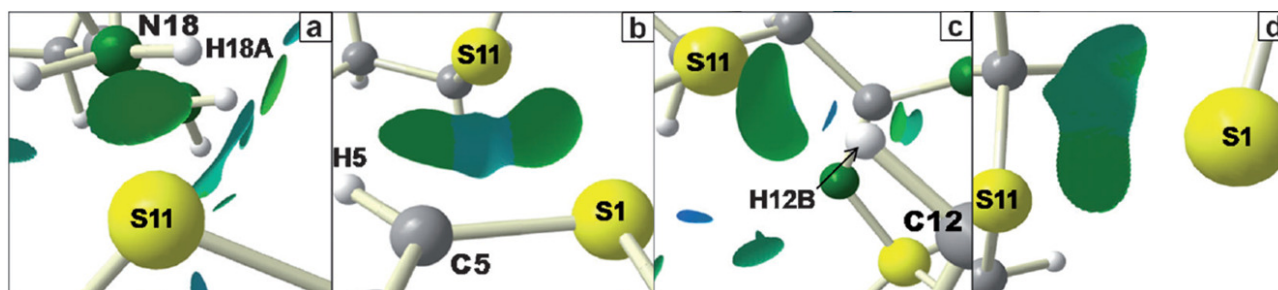


Figure 2.9 RDG-based NCI surfaces for intermolecular interactions involving Sulphur atoms in famotidine polymorph A, a-b), and B, c-d). See Fig. 2.2 for the color legend and Table 2.5 for the labeling of the interactions here shown in the various panels.

Nevertheless, as S atoms may behave either as nucleophiles or electrophiles, they can set up NCI in a key-lock mechanism even with other sulphur atoms. Fig.2.9b and 2.9d show just contacts of this type in polymorphs A and B, respectively. In the form A, S11 is linked through BP's with both H5 and S1, giving rise, therefore, to a unique, broad iso-surface characterized by $\rho(\mathbf{r}) \cdot \text{sign}(\lambda_2)$ close to zero and that contains the two BCPs and the RCP. Interestingly, however, the signed surface is negative in the regions between S11 and H5, and S1 and S11 (Fig. 2.9b), *i.e.* where the S...H and the S...S contacts are likely to be attractive. By reducing the RDG isovalue, this NCI iso-surface domain will necessarily split in three separate small domains, each associated to a critical point and with the two related to BCPs likely bearing only a negative $\rho(\mathbf{r}) \cdot \text{sign}(\lambda_2)$ value on their iso-surfaces.

Table 2.5 Intermolecular BCPs involving sulphur atoms in famotidine.^{a,b}

bond [polymorph, Figure number]	$\rho(\text{e}/\text{\AA}^3)$	$\nabla^2\rho(\text{e}/\text{\AA}^5)$	θ (deg)	Φ (deg)
S1...H13A ^c [A]	0.031(1)	0.514(4)	42,7	116,5
H18A...S11 ^d [A, 9a]	0.047(8)	0.603(4)	3,4	89,4
S1...S11 ^e [A, 9b]	0.031(2)	0.359(2)	(82,3 / 71,1) ^h	(125,6 / 162,0) ^h
H5...S11 ^e [A, 9b]	0.024(5)	0.306(2)	70,1	177,5
S11...H12B ^f [B, 9c]	0.019(1)	0.332(6)	74,9	119,8
S1...S11 ^g [B, 9d]	0.008(<1)	0.115(<1)	(47,8 / 70,2) ^h	(154,0 / 156,2) ^h

a) Labels reported in square brackets in column 1 refer to the polymorph, form A or B, where the contact was found and to the Figure where the corresponding RDG iso-surface is shown.

b) Angles reported in the last two columns are defined in Scheme 2.4.

c) At $-X, 0.5+Y, 1.5-Z$

d) At $X, 0.5-Y, 0.5+Z$

e) At $X, 1+Y, Z$

f) At $X, 1+Y, Z$

g) At $0.5+X, 0.5-Y, 0.5+Z$

h) For the S...S contact the first (second) entry refers to the polar coordinates (reference system in Scheme 2.4) of the first (second) atom listed in column 1

As for the QTAIM picture, it should be noted that all the intermolecular contacts above described give rise to BP's, whose topological features are reported in Table 2.5 together with the ϕ and ϑ parameters. When S...H contacts are taken into account, the smaller is the ϑ angle, the higher is the ED at the BCP and, therefore, the stronger is the bond. It is interesting to note that on passing from weaker to stronger S...H. interactions, the shape of the RDG iso-surface changes from van der Waals-like (broad in space and in a case with zones exhibiting both $\lambda_2 > 0$ and $\lambda_2 < 0$, Fig. 2.9b-c) to HB-like (disc-shaped, $\lambda_2 < 0$, Fig. 2.9a).

The same considerations hold true also for the S...S contacts. Indeed, in the form A, S11 lies in the ideal 'nucleophilic position' with respect to S1 ($\vartheta = 82.3^\circ$ and $\phi = 125.6^\circ$, Table 2.5). On the contrary, in the form B, the ϑ angle is fairly below (47.8°) and the ϕ angle (154.0°) slightly above the $60-90^\circ$ and the $110-140^\circ$ ranges retrieved in classical nucleophilic approach to the reference Sulphur atom. RDG iso-surfaces mirror these arrangements, since the S...S contact gives rise to a disc-shaped negative surface in polymorph A, whereas in the form B the analogue RDG surface appears definitely more spread in space. In any case, the agreement between the experimentally- and theoretically-derived pictures is excellent for this kind of NCI (see paragraph 2.5).

In conclusion, this last test case confirms that the stronger is the NCI, the smallest is the surface/volume ratio of the RDG iso-surface (and the most negative is the signed-ED mapped on it). Therefore, such ratio could be taken as a qualitative criterion to rank on a relative (energy) scale interactions between the same kind of atoms (but in different environments and with different geometries) or, to some extent, also interactions between different atomic pairs in various chemical and structural situations. We recently developed a software which allows the user to evaluate properties integrated over the RDG isosurfaces, hence including their volume (see section 2.7)

2.4.5 CONCLUSIONS

In the previous sections, the results of the application of the 'NCI descriptor' to experimentally derived ED distributions have been illustrated. More in detail, such descriptor was applied to three molecular crystals, whose ED distribution was obtained from single-crystal, low-temperature X-ray diffraction experiments. It was demonstrated that such descriptor is able to dissect some of the most typical competing intra- and intermolecular interactions leading to the observed molecular packing. It was also explored in detail to what extent the RDG-based NCI descriptor provides a complementary picture to that offered by QTAIM. In

the latter, the presence of a BP unequivocally highlights a stabilizing interaction, as the ED is homeomorphic with respect to the corresponding virial field.[66] However, this picture is quite often too localized and unavoidably discontinuous (yes/no). Quite recently, it was proposed [67] that the presence of a BP essentially signals privileged exchange path channels among topological atoms. Instead, the NCI descriptor, analogously to other continuous descriptors like the localization/delocalization indices or the Source Function is able to visibly reflect the simultaneous occurrence of competing exchange path channels, rather than to single out just one or (in some special cases) few dominant channels for electron exchange. For instance, the RDG descriptor depicts the case of inherently delocalized interactions (*e.g.*, C-H $\cdots\pi$ interactions in benzene) in terms of extended, largely flat, $s(\mathbf{r})$ iso-surfaces, in contrast to the bond path analysis which provides instead a fairly localized description of such interaction. However, when the RDG-iso-surface domain contains more than one critical point in the electron density, the RDG-NCI and QTAIM pictures can be brought to a closer correspondence by progressively lowering the s isovalue, until the original RDG-domain splits into its irreducible components. The hierarchy of the sequential splitting, along with the RDG value(s) at which such splitting realizes, brings further precious insight. Even more interesting are, perhaps, those cases where the QTAIM predicts a localized interaction, while the corresponding RDG iso-surface remains fairly broad and apparently related to more than one atomic pair interaction, regardless of the chosen RDG isovalue. In such cases, the delocalized nature of the interaction is particularly evident, since it emerges as an intrinsic feature of the interaction. Conversely, comparing RDG iso-surfaces characterized by a given, suitable, RDG isovalue, allows for a qualitative ranking of the interaction strength. Stronger interactions are characterized by small, disc-shaped RDG domains, whereas weaker and weaker interactions are progressively denoted by broader, multiform RDG domains, and possibly including more than one critical point (at least in the cases here considered).

In other works, the RDG descriptor has been applied, with reasonable success, also to the IAM ED's. [24,38] A key-point concerns the extent and kind of information about NCIs which is missing and that which is instead already stored and hidden in IAM thanks to the structural knowledge inherent to the model and the cumulative frozen electron distribution of the system's composing atoms. This relevant issue will be explored in section 2.6.

To assess the reliability of the experimental results presented above, it is important to have a comparison between experimental and theoretical results. In particular, a comparison of the results presented in section 2.4 with the ones from fully-periodical calculation is necessary to shed light on the limits of the multipolar model when used to build 'NCI descriptor' isosurfaces. Such comparison has been carried out by our group and the results are presented in the next session.

2.5 COMPARISON BETWEEN EXPERIMENTAL AND THEORETICAL RESULTS

In this section, the isosurfaces obtained from experimental EDs will be compared with the isosurfaces derived from periodic wavefunctions (B3LYP/6-311G**). In particular, single-point calculations were performed at the geometry obtained from experiment with the code CRYSTAL06 [68]. From the resulting wavefunction, grid files of ρ and $\nabla\rho$ were calculated using the code TOPOND [69] and given as input to the code developed in our lab (detailed description of the features of such code can be found in paragraph 2.7) to obtain grid files of $\rho(\mathbf{r}) \cdot \text{sign} \lambda_2$ and RDG.

As explained before, in the process of building ‘NCI descriptor’ isosurfaces, the same isovalue should be used to compare different interactions, not to introduce any bias. However, this holds true only when the interactions to be compared are obtained using the same method, as in paragraph 2.4, where the value 0.6 was used for all the interactions investigated, being them obtained all from experimental ED, adopting multipole model ED representations of comparable quality and using the same multipole model framework and code (Hansen-Coppens model within XD2006 [34,35]). In the present case, however, some systematic differences between theoretical and experimental ED distribution emerged. In particular, we found RDG to be systematically higher in intermolecular regions when experimental ED is considered. This is particularly true when weak interactions are considered. As can be seen for BCPs in Tables 2.6-2.9, for such kind of interactions ED at BCPs is generally lower for experimental ED, and this is probably the reason why RDG is higher with respect to theoretical ED distribution (see eq. 2.3). Because of this, it is reasonable to use a lower RDG value to build isosurfaces for theoretically derived ED. In particular, we looked for the value which gives on average the best match between experimental and theoretical isosurfaces, and we found it to be around 0.4 (while for experimental ED the value of 0.6 was used).

However, independently from the RDG isovalue, a little disagreement between the experimental and theoretical RDG-derived NCI description is anticipated, since the difference $\rho(\mathbf{r})_{\text{periodic, theo}} - \rho(\mathbf{r})_{\text{multipole, expt}}$ is clearly not constant for each point \mathbf{r} and it is likely to be greater, on percentage, when small $\rho(\mathbf{r})$ values are considered.

Regarding the operative point of view, it must be pointed out that, while for experimental ED the use of atom-centered multipoles allows a ‘natural’ partition of ED into molecular pairs contributions (as described in section 2.4.1), for theoretically derived ED distribution such partitioning is not straightforward. Therefore, to single out the isosurfaces relative to a given molecular pair, a spatial cutoff (see section 2.7) was applied. Nevertheless, when considering a molecular pair, some isosurfaces relative to the interaction with neighboring molecules might be still present, making the images more complicated to be interpreted and also making the comparison with experimental picture less straightforward.

In the following, the agreement between experimental and theoretical isosurfaces will be discussed separately for the different kind of interactions, and comparison of ED at BCPs will also be presented and discussed. Regarding the pictures, results using both 0.6 and 0.4 isosurfaces will be shown for theoretical ED distribution.

2.5.1 VAN DER WAALS INTERACTIONS

In figure 2.10 the theoretically derived isosurfaces for the van der Waals interaction in Ausitdiol are shown. From such picture, it can be seen that there is a good agreement between experimental and theoretical

picture, both when 0.4 and 0.6 isovalues are considered (the use of the latter isovalue, however, leads to a better agreement).

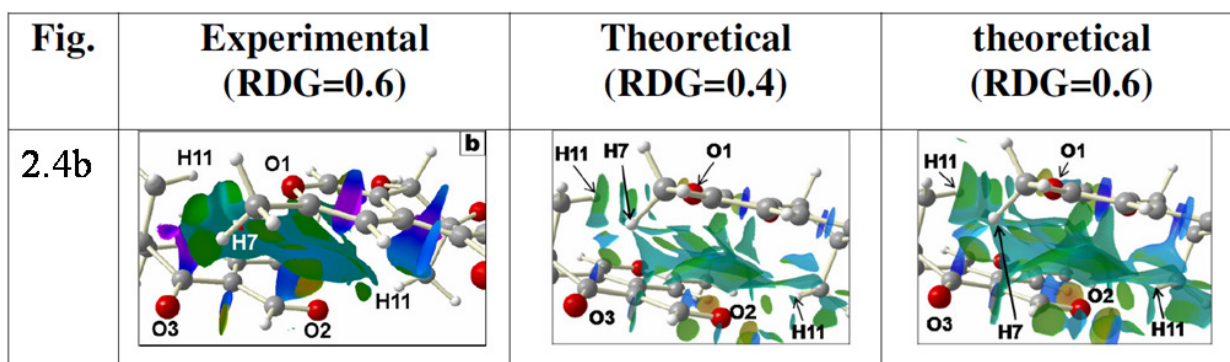


Figure 2.10 RDG-based NCI iso-surfaces as obtained from periodic wavefunctions and using different RDG $s(r)$ isovalues (0.4 and 0.6). The corresponding experimental iso-surfaces (RDG $s(r)$ =0.6) are also shown, with, on the left, the indication of the Figure number where they were shown in the paragraph 2.4

This also means that, for this very interaction, the isovalue does not significantly alter the picture of the interaction itself (provided a reasonable value is used), although the shape of the isosurface differs significantly. However, an important difference emerges here: the HB H7...O3, whose experimentally derived RDG iso-surface cannot be distinguished from the broad one associated to van der Waals interactions (Section 2.4.2), exhibits, in the theoretical case, a disc-shaped and well recognizable RDGs iso-surface, *i.e.* more similar to those of the relatively strong intramolecular HBs of Austdiol. On the other hand, this difference cannot be ascribed to the ‘NCI descriptor’ picture: the ‘strengthening’ of this HB is just a consequence of the increase of the ED at BCP in the theoretical model (see table 2.6) and the ‘NCI descriptor’ merely reflects this fact.

Table 2.6 Intermolecular BCPs for the molecular pair reported in Fig. 2.10. ED BCP is reported for theoretical (first column) and experimental (second column) ED distribution

bond	$\rho_{\text{BCP}}(\text{e}/\text{\AA}^3)$ exp.	$\rho_{\text{BCP}}(\text{e}/\text{\AA}^3)$ theor.	$d_{\text{H}\cdots\text{O}}(\text{\AA})$	angle XHO(deg)
C(12)-H(11)···O(1) ^a	0.03(1)	0.025	2.979	116.9
C(12)-H(11)···O(2) ^b	0.05(3)	0.058	2.443	163.4
C(10)-H(7)···O(3) ^b	0.04(3)	0.054	2.544	166.9

^a At 0.5+x, 0.5-y, -z. ^b At -0.5+x, 0.5-y

2.5.2 HYDROGEN BONDS AND C-H···C INTERACTIONS

As stated previously, weak interactions are likely to lead to a greater disagreement between experiment and theory. This not only because for this kind of interactions the ED difference is higher in percentage (see Table 2.7), but also because the ED curvatures -which define how fast $\nabla\rho$ grows and therefore how extended in space the isosurfaces will be- are even more subject to casual errors when ED is low. In other words, theoretical and experimental NCI pictures show, on average, different degree of similarity depending on the interaction strength. This difference can be clearly seen when HBs are considered, since, in the present work, a broad range of HBs was considered, from the strong O-H···O to the weak C-H···C HBs (although the latter are usually not considered as true HBs). Theoretical and experimental NCI isosurfaces

for HBs and C-H...C interactions are reported in Fig. 2.11. The HBs of Austiol can be considered to have a strength which is somehow in between the strong RAHB found for Famotidine and the weak C-H...C interactions. For O-H...O and C-H...O interactions the overall agreement is good for all the investigated HBs, especially if 0.4 isosurfaces are considered. It is however worth to be noted that, at odd with experimental picture, for theoretical ED distribution the use of 0.4 isovalue for the C2-H1...O2 HB (which is the only intramolecular HB for Austdiol which is characterized by the presence of a bond path, see section 2.4.2) produces an isosurface whose shape is clearly distinguishable from the H...O contact which does not give rise to any intramolecular bond path.

The situation is to some extent different for the isosurfaces associated to C-H...C contacts of benzene. Being these interactions very weak, the chosen isovalue significantly affects the shape of isosurfaces and a scaling of such value must be used to fully match theoretical and experimental picture, as can be seen by comparing 0.4 and 0.6 theoretical isosurfaces in Figure 2.11. In general, the 0.6 isovalue is clearly too high when theoretical ED distribution is considered. Indeed, the use of such isovalue leads to big and extended isosurfaces spreading throughout the intermolecular region, therefore not allowing to have a clear picture of the various interactions. What said above for C-H...C contacts holds true for all the weak interactions considered in the present investigation, as explained in the paragraphs 2.5.3 and 2.5.4.

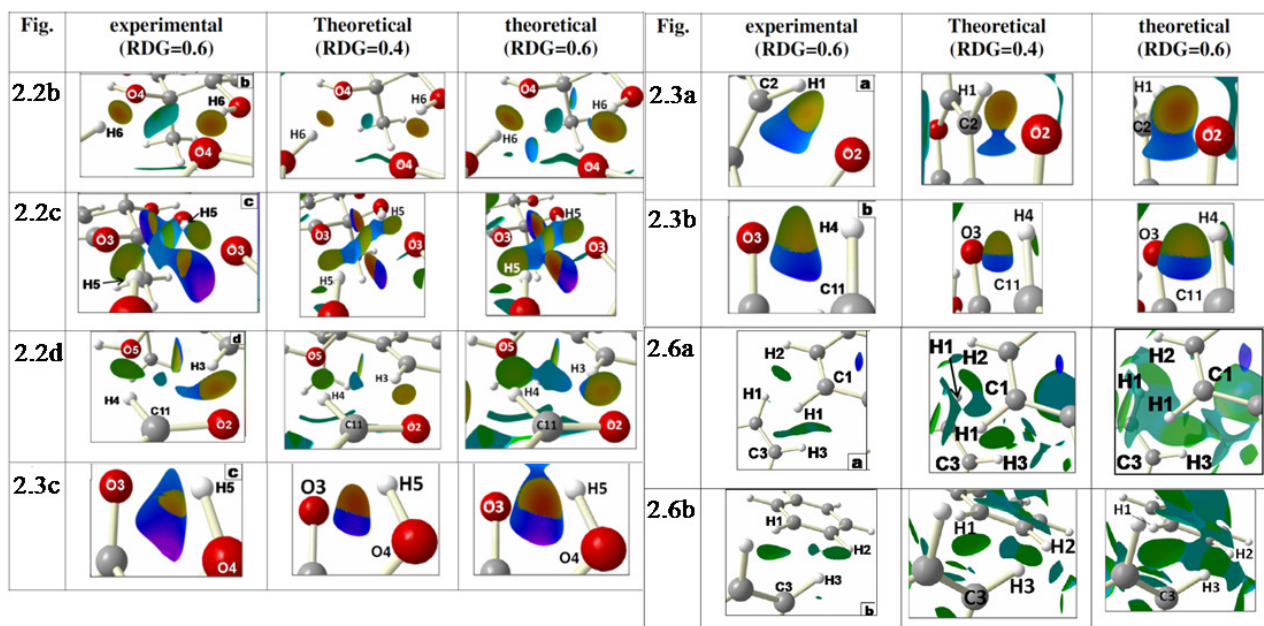


Figure 2.11 RDG-based NCI iso-surfaces as obtained from periodic wavefunctions and using different RDG $s(r)$ isovalues (0.4 and 0.6). The corresponding experimental iso-surfaces (RDG $s(r)$ =0.6) are also shown, with, on the left, the indication of the Figure number where they were shown in the paragraph 2.4

Being the intramolecular HB of Famotidine a strong NCI, it deserves a separate discussion. In this case, the agreement improves when the same isovalue (0.6) is used to build theoretical and experimental isosurfaces (figure 2.12). However, it must be pointed out that for the strong interactions the change of RDG isovalue alters the shape of isosurfaces much less than it does for weak interactions. Therefore, the agreement between experimental and theoretical picture is good even when slightly different RDG isovalues are used.

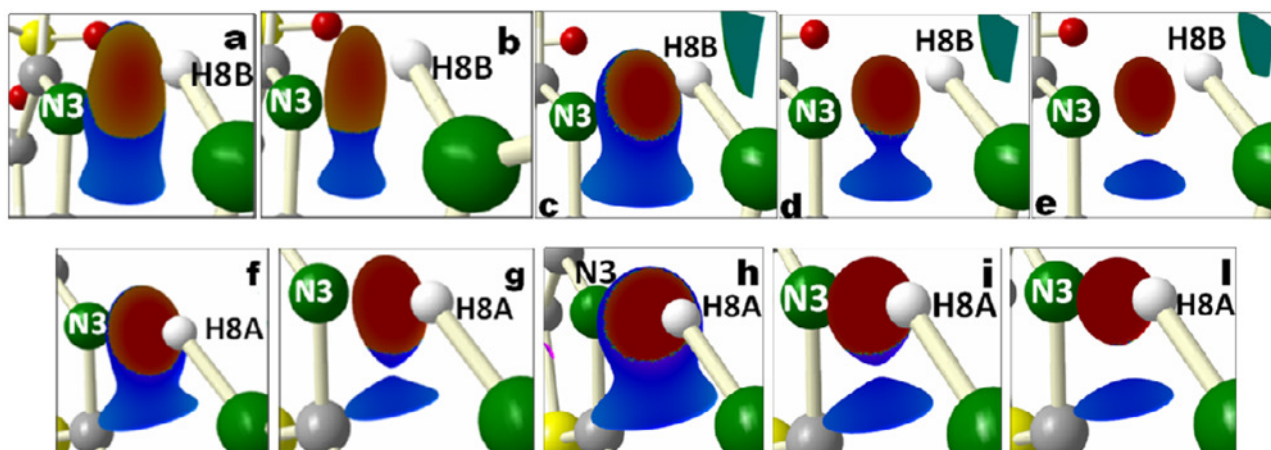


Figure 2.12 RDG-based NCI iso-surfaces for the intramolecular RAHB of famotidine (compare with Fig. 2.7 in the main text). a) Polymorph A, experimental, $s(r) = 0.6$; b) Polymorph A, experimental, $s(r) = 0.45$; c) polymorph A, theoretical, $s(r) = 0.6$; d) Polymorph A, theoretical, $s(r) = 0.45$; e) Polymorph A, theoretical, $s(r) = 0.4$; f) Polymorph B, experimental, $s(r) = 0.6$; g) Polymorph B, experimental, $s(r) = 0.45$; h) Polymorph B, theoretical, $s(r) = 0.6$; i) Polymorph B, theoretical, $s(r) = 0.45$; l) Polymorph B, theoretical, $s(r) = 0.4$.

Table 2.7 Intermolecular and intramolecular geometrical features and ED at BCP (experimental and theoretical) for some X-H \cdots O contacts (X=C,O) of austdiol (upper part of the table) and benzene (lower part of the table).

bond	$\rho_{\text{BCP}}(\text{e}/\text{\AA}^3)$ exp.	$\rho_{\text{BCP}}(\text{e}/\text{\AA}^3)$ theor.	$d_{\text{H}\cdots\text{O}}(\text{\AA})$	angle XHO(deg) ^g
AUSTDIOL				
Intermolecular				
C(10)-H(9) \cdots O(3) ^a	0.03(4)	0.067	2.420	150.5
C(9)-H(3) \cdots O(2) ^b	0.13(3)	0.116	2.174	150.7
C(11)-H(4) \cdots O(5) ^c	0.05(2)	0.058	2.519	154.1
O(4)-H(5) \cdots O(3) ^d	0.09(4)	0.095	2.114	158.4
O(5)-H(6) \cdots O(4) ^e	0.14(4)	0.133	2.023	153.2
Intramolecular				
C(2)-H(1) \cdots O(2)	0.11(3)	0.138	2.145	121.8
C(11)-H(4) \cdots O(3)	no BCP	no BCP	2.359	100.5
O(4)-H(5) \cdots O(3)	no BCP	no BCP	2.052	116.9
O(5)-H(6) \cdots O(4)	no BCP	no BCP	2.589	102.2
C(9)-H(3) \cdots O(5)	no BCP	no BCP	2.461	92.1
C(12)-H(10) \cdots O(5)	no BCP	no BCP	2.668	92.6
BENZENE				
C(3) \cdots H(2) ^h	0.030(4)	0.029	3.065	-
C(1) \cdots H(3) ^h	0.042(6)	0.036	2.862	-

S.u. in parentheses. For austdiol, the s.u. on the geometrical parameter cannot be correctly estimated since the hydrogen positions were not refined; however, the s.u. on $d_{\text{H}\cdots\text{O}}$ should be around of 0.001 \AA while the ones on the angle roughly 0.1 (see original paper on austdiol). ^a At $-0.5+x, 0.5-y, 1-z$ ^b At $-1+x, y, z$. ^c At $1+x, y, z$. ^d At $1-x, 1-y, z$. ^e At $-x, 1-y, z$. ^f At $-0.5-x, -y, -0.5+z$

^g angles are reported only for the XH \cdots O contacts, since for CH \cdots C contacts this geometrical parameter is not really relevant

2.5.3 INTERACTIONS INVOLVING π ELECTRONS

In figure 2.13 the theoretically derived isosurfaces for $H\cdots\pi$ interactions of Famotidine are reported.

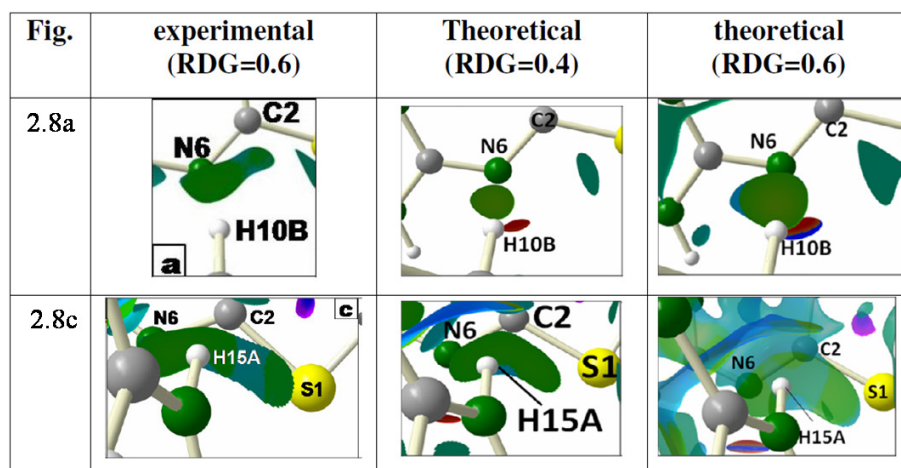


Figure 2.13 RDG-based NCI iso-surfaces as obtained from periodic wavefunctions and using different RDG $s(r)$ isovalues (0.4 and 0.6). The corresponding experimental iso-surfaces (RDG $s(r)$ =0.6) are also shown, with, on the left, the indication of the Figure number where they were shown in the paragraph 2.4

Regarding the $N-H\cdots\pi$ interaction involving the atom H15A, an excellent agreement was found (although, being this a weak interaction, 0.4 isovalue has to be used for theoretical ED). The situation is radically different for the $C-H\cdots\pi$ interaction (H10B \cdots N6): while in the experimental picture this interaction is described as a $C-H\cdots\pi$ one, theoretical isosurface simply indicates an HB between H10B and N6. In this case the difference is not simply in the shape of isosurfaces, but in the description of the interaction itself: $C-H\cdots\pi$ VS HB. This strong disagreement is probably caused by an inadequate description of hydrogen thermal motion, which in turn leads to artefacts in the static ED distribution obtained from experiment. Indeed, as explained in paragraph 2.3, the hydrogen thermal motion of Famotidine has been obtained by a TLS model in which the whole molecule of was considered as a unique rigid body, since all the attempts to fragment the molecules into independent rigid bodies failed. Nevertheless, as it can be seen from its structure (scheme 2.3), Famotidine is a quite flexible molecule and the choice of treating it as a rigid body might lead to an unsatisfactory description of thermal motion for a few H atoms. Yet, the disagreement between experimental and theoretical picture might also indicate inadequacies of the DFT functional that hamper a truly accurate description of the low-ED regions in this system. Certainly, such discrepancy deserves further investigation in the future.

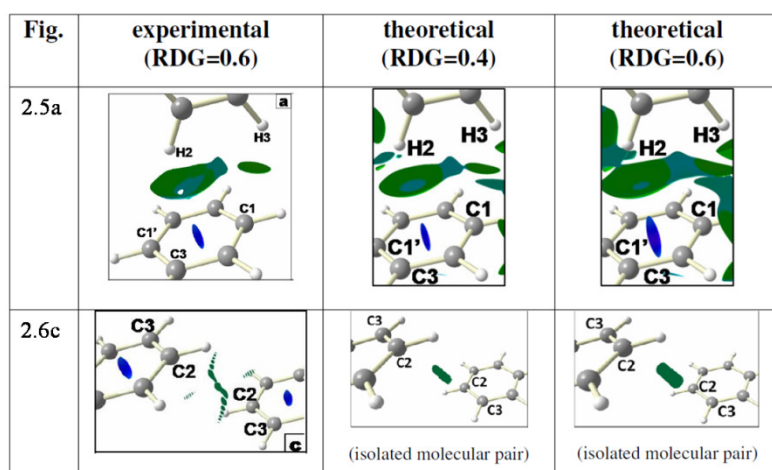


Figure 2.14 RDG-based NCI iso-surfaces as obtained from periodic wavefunctions and using different RDG $s(r)$ isovalues (0.4 and 0.6). The corresponding experimental iso-surfaces (RDG $s(r)$ =0.6) are also shown, with, on the left, the indication of the Figure number where they were shown in the paragraph 2.4

Table 2.8 Geometrical features and ED at BCP (experimental and theoretical) for intermolecular C-H...C and C-H...H BCP for benzene

bond	$\rho_{\text{BCP}}(\text{e}/\text{\AA}^3)$ exptl.	$\rho_{\text{BCP}}(\text{e}/\text{\AA}^3)$ theor.	$d_{\text{H}\cdots\text{O}}(\text{\AA})$
C(1)···H(3) ^a	0.016(5)	0.033	2.955
H(2)···H(1) ^b	0.018(4)	0.024	2.638
H(3)···H(2) ^c	0.013(5)	0.024	2.548
C(3)···H(1) ^c	0.024(4)	0.032	2.934

^aAt $-x, 0.5+y, 0.5-z$. ^bAt $x, 0.5-y, 0.5+z$. ^cAt $-0.5-x, -0.5+y, z$

The C-H... π interaction of benzene is reported in figure 2.14, while the theoretically and experimentally derived topological properties at corresponding BCPs can be found in table 2.8. In this case a remarkable agreement between experiment and theory is obtained. In particular, the discrimination between C-H... π and C-H...C interaction obtained from experimental picture is recovered when theoretical ED distribution is considered (0.4 isovalue). Regarding the molecular pair IV of benzene, it was illustrated in paragraph 2.4.3 that the isosurface between the two molecules disappears when the contribution of neighbouring molecules is taken into account. Accordingly, no isosurfaces between the two molecules of molecular pair IV were found in periodical calculation. On the contrary, when the calculation (B3LYP/6-311++G**) is performed considering only the molecular pair *in vacuo* (freezing the two molecules at the crystal geometry), an isosurface similar to the one reported in Figure 2.6c is found. The isosurface obtained through *in vacuo* calculation is less fragmented and characterized by a higher ED. This fact can be interpreted as the results of the absence of other competing interactions: in this case the π clouds of the two molecules polarized towards each other as a result of their van der Waals interaction.

2.5.4 SULPHUR-SULPHUR INTERACTIONS

Figure 2.15 reports the 'NCI descriptor' isosurfaces obtained from theoretical ED distribution, while the ED at BCP along with ϕ and ϑ angles (as defined in paragraph 2.4.4) are reported in Table 2.9.

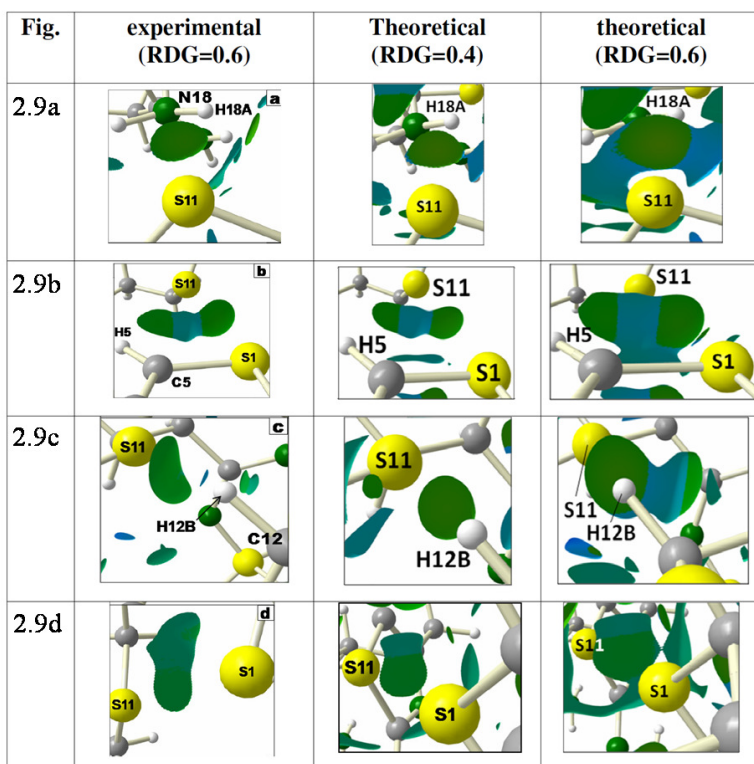


Figure 2.15 RDG-based NCI iso-surfaces as obtained from periodic wavefunctions and using different RDG $s(r)$ isovalues (0.4 and 0.6). The corresponding experimental iso-surfaces (RDG $s(r)$ =0.6) are also shown, with, on the left, the indication of the Figure number where they were shown in the paragraph 2.4

Sulphur-Sulphur NCIs found in both polymorphs of Famotidine can be classified as weak interactions (this can be seen from the low ED value at the corresponding BCPs, reported in Table 2.9). For this kind of interactions, the same considerations reported for weak C-H...C interactions of benzene holds true. What need to be pointed out is that, also for S...S interactions an excellent agreement is found when 0.4 RDG isosurfaces are considered.

Table 2.9. Experimental and theoretical ED for the investigated BCP of famotidine.

Bond [polymorph]	$\rho_{\text{BCP}}(\text{e}/\text{\AA}^3)$ exptl.	$\rho_{\text{BCP}}(\text{e}/\text{\AA}^3)$ theor.	θ (deg)	Φ (deg)
S(1)...H(13A) ^a [A]	0.031(1)	0.047	42,7	116,5
H(18A)...S(11) ^b [A]	0.047(8)	0.060	3,4	89,4
S(1)...S(11) ^c [A]	0.031(2)	0.039	82,3 / 71,1•	125,6 / 162,0•
H(5)...S(11) ^c [A]	0.024(5)	0.030	70,1	177,5
S(1)...S(11) ^d [B]	0.008(<1)	0.015	47,8 / 70,2•	154,0 / 156,2•
S(11)...H(12B) ^e [B]	0.019(1)	0.049	74,9	119,8
H(8B)-N(3) ^f [A]	0.18(2)	0.215	-	-
H(8A)-N(3) ^f [B]	0.23(3)	0.258	-	-

In the first column, the letter in square parenthesis refers to the polymorph in which the contact was found. The angles reported in the last two columns for the sulphur involving contacts are defined in Scheme 2.4 . ^a At $-x, 0.5+y, 1.5-z$ ^b At $x, 0.5-y, 0.5+z$ ^c At $x, 1+y, z$ ^d $0.5+x, 0.5-y, 0.5+z$ ^e At $x, 1+y, z$ ^f intramolecular contact. For the S...S contacts, the first number represents the θ and Φ angles in the reference system (as defined in scheme 4 of the main text) centered on the first S atom of the first column (*i.e.* the angles of the second sulphur atom with respect to the first), while the second number refers to the reference system centered on the second S atom.

2.5.5 CONCLUSIONS

In this paragraph the comparison between the theoretical and experimental results of 'NCI descriptor' has been presented. In general, theoretical ED is characterized by lower RDG value (in low ED regions) with respect to experimental one. Therefore a scaling of RDG isovalue (0.4 VS 0.6) is required to fully match the two pictures. This is especially true for weak interactions, while for relatively strong ones, the same isovalue can be used for both theoretical and experimental results. At the same time, when a reasonable RDG value is used, strong interactions are less affected by the isovalue used to build isosurfaces. Therefore, the use of RDG=0.4 isosurfaces for theoretical ED distributions gives an overall excellent agreement with experimental RDG=0.6 isosurfaces. The only exception to what said so far regards one interaction in Famotidine, which is described as a C-H... π interaction in the experimental picture while an isosurface relative to a conventional HB appears when theoretical ED distribution is considered. This is likely to be due to an inadequate description of hydrogen thermal motion in Famotidine but further investigations are needed to clarify the true origin of this discrepancy.

The investigation presented in this and the previous paragraphs (2.4 and 2.5) represents the first application of 'NCI descriptor' to experimentally derived ED distribution. The overall excellent agreement between experimental and theoretical description of NCIs in the 'NCI descriptor' framework lead us to conclude that the experimental picture obtained in the present investigation is certainly reliable. Therefore it can be stated that the 'NCI descriptor' can be successfully applied to ED distribution obtained from single-crystal X-ray diffraction experiments through the use of multipolar model, provided the model itself (including therefore the deconvolution of static ED from thermal motion) is built in an accurate fashion.

2.6 'NCI DESCRIPTOR' APPLIED TO INDEPENDENT ATOM MODEL

In this paragraph, we present the results of 'NCI descriptor' when applied to ED distribution obtained from Independent Atom Model (IAM, also called 'promolecular density') ED distribution. The latter is obtained by superimposing the spherical, neutral atomic densities centered at the (experimental) best estimates of the atomic positions. In particular, a detailed comparison between the 'NCI descriptor' picture obtained from IAM and the one obtained from experimental ED will be presented.

This investigation originated from the fact that Johnson et al. [24] and Contreras-Garcia et al. [38] already noted that the IAM ED is able, in principle, to recover at least the main NCI features with respect to the corresponding "true" (*ab-initio*) ED. Indeed, it was reported that "results at the self-consistent and promolecular [*i.e.* IAM] levels are qualitatively equivalent for all of the cases considered" [38]. If true, this would represent a great advantage for the study of NCIs, since to build promolecular density neither quantum mechanical calculations nor experimental data are required and, in general, the promolecular ED distribution can be obtained at extremely low computational cost. This in turn, would allow to investigate NCIs in very big systems as, for example, the ones considered in NCI-driven biochemical processes, such as protein folding, drug-receptor interaction, etc..

The fact that IAM might be able to recover most of the features of the NCIs is disturbing but should not necessarily be seen as a complete failure of the descriptor. This topic will be explored in the next session, where the role of IAM in the so-called 'information theory' will be highlighted.

2.6.1 INDEPENDENT ATOM MODEL AND INFORMATION THEORY

The application of the 'NCI descriptor' using the IAM density rather than the ED deformed by bonding, raises the interesting question of the role of this missing information on the RDG-NCI analysis. Indeed some residual information on NCI should be naturally stored and hidden into the IAM density, given the structural (atomic positions) and electronic (the cumulative frozen electron distribution of the system's composing atoms) knowledge intrinsic to such model density. For instance, it is well-known that the energy densities at the hydrogen-bond (H-bond) bond critical points (BCP's) are in general well-described by the promolecular model [70,71], in agreement with the observation that the effect of the crystal environment on the IAM density appears to be minimum just at the BCP's [71]. Indeed, Spackman demonstrated that the "essential behaviour exhibited by multipolar refined electron densities for X-H...O contacts (X=O, N, C) can be described remarkably well by the superposition of realistic spherical electron densities for O and H atoms and the separation between them" [70]. In particular, he showed that a simple two-atom model accounts for the observed exponential dependence, on the H...O distance, of both the kinetic and potential energies densities at the H-bond BCPs, a result raising the question "whether present experimental results differ from a simple reference model, that is the promolecular density, for weak interactions"[70]. A detailed analysis by Gatti *et al.* [71] on a molecular crystal, containing a large number of different C-H...O contacts and using both experimental and periodic *ab-initio* electron densities, showed that the above mentioned topological features of the H...O contacts at BCPs were indeed essentially reproduced by both the corresponding promolecular densities, but less much so for the electron density values at such points. In some cases, even qualitative topological changes, were observed, *i.e.* lack of some BCPs in the IAM densities which were instead present in the "true" reference densities. As an overall result of its study, Gatti *et al.* [71] found that, regardless of their experimental or theoretical origin, the differences between promolecular and crystal densities seem to be generally minimized close to the intermolecular surfaces and to bond critical points, whereas the two densities may considerably differ (well) inside the atomic basins of the O and H atoms involved in the intermolecular interactions.

Generally speaking, it is well known that the molecular or crystalline electron density $\rho(\mathbf{r})$ is, on average, only slightly modified relative to the promolecular distribution, $\rho_{IAM}(\mathbf{r})$ [72]. The amount of local reconstruction, $|\Delta\rho(\mathbf{r})| = |\rho(\mathbf{r}) - \rho_{IAM}(\mathbf{r})|$ is much smaller than either $\rho(\mathbf{r})$ or $\rho_{IAM}(\mathbf{r})$ and the ratio $\Delta\rho(\mathbf{r})/\rho(\mathbf{r})$ is usually small in the regions of greater energy relevance, *i.e.* close to the nuclei [72]. The largest *relative* changes are known to be those occurring in the bonding (intra- and intermolecular) regions, namely those where BCPs occur and where the associated RDG isosurfaces are located.

Nalewajski [72] and Nalewajski *et al* [73, 74] have shown a remarkable similarity between the portrait of functions related to the density difference $\Delta\rho(\mathbf{r})$ and that of local probes based on information theory, providing a semi-quantitative information-theoretic interpretation of the density difference plots. Such result endorses a special physical significance to the study of $\Delta\rho(\mathbf{r})$ and, indirectly, to that of other descriptors related to $\Delta\rho(\mathbf{r})$, as is the case of the present investigation. In particular they found that

$$\Delta\chi(\mathbf{r}) = \rho(\mathbf{r}) I[w(\mathbf{r})] \cong \Delta\rho(\mathbf{r}) \quad w(\mathbf{r}) \approx \Delta\rho(\mathbf{r}) \quad \text{eq. 2.5}$$

where $\Delta\chi(\mathbf{r})$ is the density of the *Kullback-Leibler divergence* $\Delta\Xi$ [75] (also called information divergence, information gain or relative entropy),

$$\Delta\Xi = \int \Delta\chi(\mathbf{r}) \, d\mathbf{r} = \int \rho(\mathbf{r}) \ln [\rho(\mathbf{r})/\rho_{IAM}(\mathbf{r})] \, d\mathbf{r} \quad \text{eq. 2.6}$$

measuring, in the present case, the local ($\Delta\chi(\mathbf{r})$) and average ($\Delta\Xi$) *information distance* between the molecular and the promolecular IAM density, while $I[w(\mathbf{r})]$ represents the *surprisal function* [72,74] of the local *enhancement factor* $w(\mathbf{r})$ of the density probability function,

$$I[w(\mathbf{r})] = \ln w(\mathbf{r}) = \ln [\rho(\mathbf{r})/\rho_{IAM}(\mathbf{r})] \quad \text{eq 2.7.}$$

The approximations in Eq. 2.6 were obtained [72,73,74] by expanding the molecular *surprisal* $I[w(\mathbf{r})]$ around $w(\mathbf{r}) = 1$ to first-order in the relative displacement of the electron density

$$I[w(\mathbf{r})] = \ln [\rho(\mathbf{r})/\rho_{IAM}(\mathbf{r})] = \ln \{ [\rho_{IAM}(\mathbf{r}) + \Delta\rho(\mathbf{r})] / \rho_{IAM}(\mathbf{r}) \} \cong \Delta\rho(\mathbf{r}) / \rho_{IAM}(\mathbf{r}) \approx \Delta\rho(\mathbf{r}) / \rho(\mathbf{r}) \quad \text{eq. 2.8.}$$

Likewise, Nalewajski [72] and Nalewajski *et al.* [76] analysed the Shannon entropy-displacement density, that yields the local difference between the true density S_p and the IAM density S_{IAM} Shannon entropies[77],

$$h(\mathbf{r}) = -\rho(\mathbf{r})\ln \rho(\mathbf{r}) + \rho_{IAM}(\mathbf{r})\ln \rho_{IAM}(\mathbf{r}) \quad \text{eq. 2.9}$$

where a negative value of $h(\mathbf{r})$ denotes a decrease in the local uncertainty in the molecule, relative to the promolecule, the opposite being true for a positive $h(\mathbf{r})$ value. Maps of $h(\mathbf{r})$ thus provide local changes of the entropy/information content upon bonding [72]. On average, formation of chemical bonds leads to a decrease of the degree of uncertainty compared to that present in the promolecular distribution, as the electron distribution of the bonded atoms increases its “structure” because of the presence of the remaining atoms, but locally the opposite can be true [72]. For instance, the formation of a covalent bond leads to an increase in the electron uncertainty in the bonding region, as due to the inflow of electrons in such region. Analysis of local Shannon entropies over QTAIM atomic basins reveals that increases and decreases of atomic entropies may occur upon bonding, with high charge transfer between atoms (ionic bonds) causing in general an entropy decrease [72,78]. In a number of examples, Nalewajski [72] could also show that, despite an often close similarity, the entropy difference plots, when compared to the corresponding $\Delta\rho(\mathbf{r})$ diagrams, lead usually to a more detailed representation of the reorganization of the electronic structure relative to the free atoms in the promolecule.

Based on what discussed above, it could seem natural and advisable to link the RDG differences (on passing from IAM to the “true” ED) to quantities related to information theory. However, the RDG (a dimensionless quantity) is neither a probability distribution (it cannot be normalized to unity since it goes to infinity far from the nuclei), nor it would provide a unique value, regardless of the kind of analysed ED, when integrated over only the regions where it is limited. Despite this fundamental warning, one can still define, just for the purpose of a qualitative insight, an information-distance-like density function $\Delta\sigma(\mathbf{r})$ between the molecular and the promolecular RDG $s(\mathbf{r})$ densities,

$$\Delta\sigma(\mathbf{r}) = s(\mathbf{r}) \ln \left[\frac{s(\mathbf{r})}{s_{IAM}(\mathbf{r})} \right] = s(\mathbf{r}) \ln \left[\frac{\nabla\rho}{\rho^{4/3}} \cdot \frac{\rho_{IAM}^{4/3}}{\nabla\rho_{IAM}} \right] = s(\mathbf{r}) \left[\ln \frac{\nabla\rho}{\nabla\rho_{IAM}} + \frac{4}{3} \ln \frac{\rho_{IAM}}{\rho} \right] \quad \text{eq. 2.10.}$$

Since low $s(\mathbf{r})$ regions are customarily investigated in the RDG-based descriptor analysis, $\Delta\sigma(\mathbf{r})$ are also expected to be small in these regions (Eq. 2.10), provided the term in parenthesis is not significantly large (and points too close to the CPs are avoided). More interestingly, for covalent intramolecular bonds one expects $(\rho_{IAM} / \rho) \ll 1$ in the regions between the nuclei because the ED is being accumulated in such regions upon bonding. Conversely, $(\nabla\rho / \nabla\rho_{IAM})$ should be much closer to 1 there, for the electron density increase upon bonding is compensated for by the density becoming more smoothly distributed in the bonding region. As a result, $\Delta\sigma(\mathbf{r})$ is expected to be negative in these regions. The RDG based on the molecular density should, therefore, assume lower values than the IAM-RDG and the corresponding RDG isosurfaces should extend more in space since $\nabla\rho/\rho$ changes less rapidly than $\nabla\rho_{IAM}/\rho_{IAM}$. A negative $\Delta\sigma(\mathbf{r})$

value may be associated to an information decrease in the bonding regions in the BCP neighbourhoods, as due to the electron density (and its gradient) becoming there more uniformly distributed. To this respect, it is worth noting the parallel between this hypothesized behaviour of $\Delta\sigma(\mathbf{r})$ in the bonding regions and that found mapping the Shannon entropy-displacement density in the same regions.

On the other hand, when the RDG isosurfaces for the NCI are investigated one awaits for $(\rho_{IAM}/\rho) \gg 1$ and for $(\nabla\rho/\nabla\rho_{IAM})$ being comparatively much less affected and closer to 1. These interactions have typically large closed-shell character and being dominated by the requirements of the Pauli exclusion principle, lead to a contraction of the density away from the interatomic surface towards each of the interacting nuclei [26]. As a result, the ED at and close to the associated BCP's, is generally smaller in magnitude for the "true" densities than is for the IAM model. The ED curvatures at BCP will also generally decrease because of the significant ED decrease with respect to the IAM model, but comparatively (much) less so than ρ because of the mentioned density contraction towards the nuclei. The same consideration holds true for the ED gradient, apart, obviously, from the BCP position. One then anticipates $\Delta\sigma(\mathbf{r})$ to be positive rather than negative in the regions associated to not too energetically strong NCI. The RDG based on the molecular (crystalline) density should there assume higher values than the IAM-RDG and the corresponding RDG isosurfaces should be somewhat less extended in space since the crystalline electron density will be more "structured" and less uniform than the unperturbed IAM density for these closed-shell intermolecular interactions. Therefore, $\nabla\rho/\rho$ is expected to change more rapidly than $\nabla\rho_{IAM}/\rho_{IAM}$. Then, the positive $\Delta\sigma(\mathbf{r})$ value may be associated in this case to an *information gain*, due to the electron density (and its gradient) becoming comparatively less uniformly distributed.

To conclude the qualitative analysis discussed in this paragraph, one should not forget that, upon bonding, a more or less significant displacement of the critical point (BCP, RCP) positions may occur. This clearly complicates the simple picture outlined thus far, because the RDG isosurfaces will be accordingly displaced and will, therefore, sample (slightly) different ED and ED gradient regions.

2.6.2 AIM OF THE WORK AND OPERATIONAL PROCEDURE

In the present study, the IAM ability to recover the NCIs features, discussed at the beginning of the session 2.6, will be investigated [27]. In particular, a detailed comparison between isosurfaces resulting from experimental and promolecular ED will be carried out. The aim is to reveal, quantify and possibly rationalize the recovered similarities and discrepancies, and focussing on the analysis of X-ray experimental densities and their IAM counterpart. In addition, the results of the RDG-NCI investigations are compared and/or supplemented with those obtained from classical QTAIM topological indicators on the same EDs. The combined analysis should not only reveal how the two descriptors may fruitfully complement each other, but can also provide quantitative and interpretive keys as for the changes of the RDG-NCI description using either of the two ED's. In general, such analysis is expected to also highlight those deformations of the promolecular density, arising from chemical bonding and packing environment, that are fairly delocalized in nature and not restricted to special points (BCP's) of the $\rho(\mathbf{r})$ distribution, where instead, they often reach their magnitude minima [71]. Since RDG-NCI isosurfaces for weak interactions are rather diffuse in nature, their shapes should significantly be affected by such deformations. Comparisons of RDG isosurfaces obtained with the IAM and the true densities should visibly reveal the effect.

The systems used to carry out the comparison are the same investigated in the previous sections of this chapter, namely: Austdiol, Benzene and Famotidine. The comparison will be carried out between the isosurfaces obtained from experimental ED (presented in section 2.4) and the ones from promolecular ED. The latter are obtained through the code XD2006 [35] by not considering neither atomic charges (*i.e.*

monopoles populations are set equal to the charge of the atoms to which they belong) nor the deformation of ED due to the multipoles (*i.e.* the population of the multipoles having $l \geq 1$ will be set to zero). The geometry used to build the promolecular density is obviously the one obtained from experiment. As for the investigation reported in paragraph 2.4, ρ and $\nabla\rho$ grid files were obtained through XD2006, while RDG and $\rho \cdot \text{sign}(\lambda_2)$ grid files were calculated with 'NCImilano', the program developed in our lab [33]. Detailed description of the features of such code are given in section 2.7.

As already discussed in Section 2.5, when comparing RDG isosurfaces obtained with different methods the question arises as to what isovalue should be chosen to make an unbiased and, at the same time, meaningful comparison. Basically, two options seem convenient. The first is to use the same RDG isovalue for the two EDs, so as to make the least-biased comparison between the resulting isosurfaces. A second one is to select different isovalues for the two derived RDGs distributions, so as to compensate for the different ED values and curvatures close to CPs and make the resulting RDG isosurfaces as close as possible. The underlying purpose of this second option, when using IAM EDs, is that of finding those "optimal" conditions that would enable one to get RDG isosurfaces for very large (biological) systems at a very low computational cost and without introducing large departures from the description one would obtain using a "real" ED. In the following, results obtained using both options will be discussed. An s isovalue of 0.6 and of 0.4 for the multipole and the IAM RDGs were respectively adopted when selecting the second option. The lower isovalue for the case of the IAM density is simply explained by its less *structured* nature and by its higher ED values in the regions of interest to NCI (see paragraph 2.6.3).

Another choice to be made concerns the cutoff to be used on $\rho(\mathbf{r})$ when mapping the $\rho(\mathbf{r}) \cdot \text{sign}(\lambda_2)$ quantity onto each RDG iso-surface. As done for results presented in sections 2.4 and 2.5, a single range [-0.05 au ($-0.337 \text{ e} \cdot \text{\AA}^{-3}$) $< \rho(\mathbf{r}) \cdot \text{sign}(\lambda_2) < 0.05 \text{ au}$ ($+0.337 \text{ e} \cdot \text{\AA}^{-3}$)] will be used throughout. The same colour scale was employed for all isosurfaces which will be presented in paragraph 2.4 and 2.5, ranging from -0.03 (red) to 0.035 (violet) au.

2.6.3 COMPARISON OF RDG vs ED PLOTS FOR IAM AND EXPERIMENTAL ED: THE CASE OF BENZENE

Johnson *et al.* [24] and Contreras-García *et al.* [38] have examined plots of RDG versus ρ showing that they provide clear fingerprints of molecular interactions. In paragraph 2.4 it was shown that similar capabilities hold also true when multipolar experimental ED's are considered. Here such results are compared, for the case of benzene crystal, with the ones obtained using the corresponding IAM ED (left and right column, respectively in Fig. 2.16). This will enable us to explore whether the qualitative predictions made in paragraph 2.6.1 on the RDG differences when using the "true" or the IAM ED's are verified.

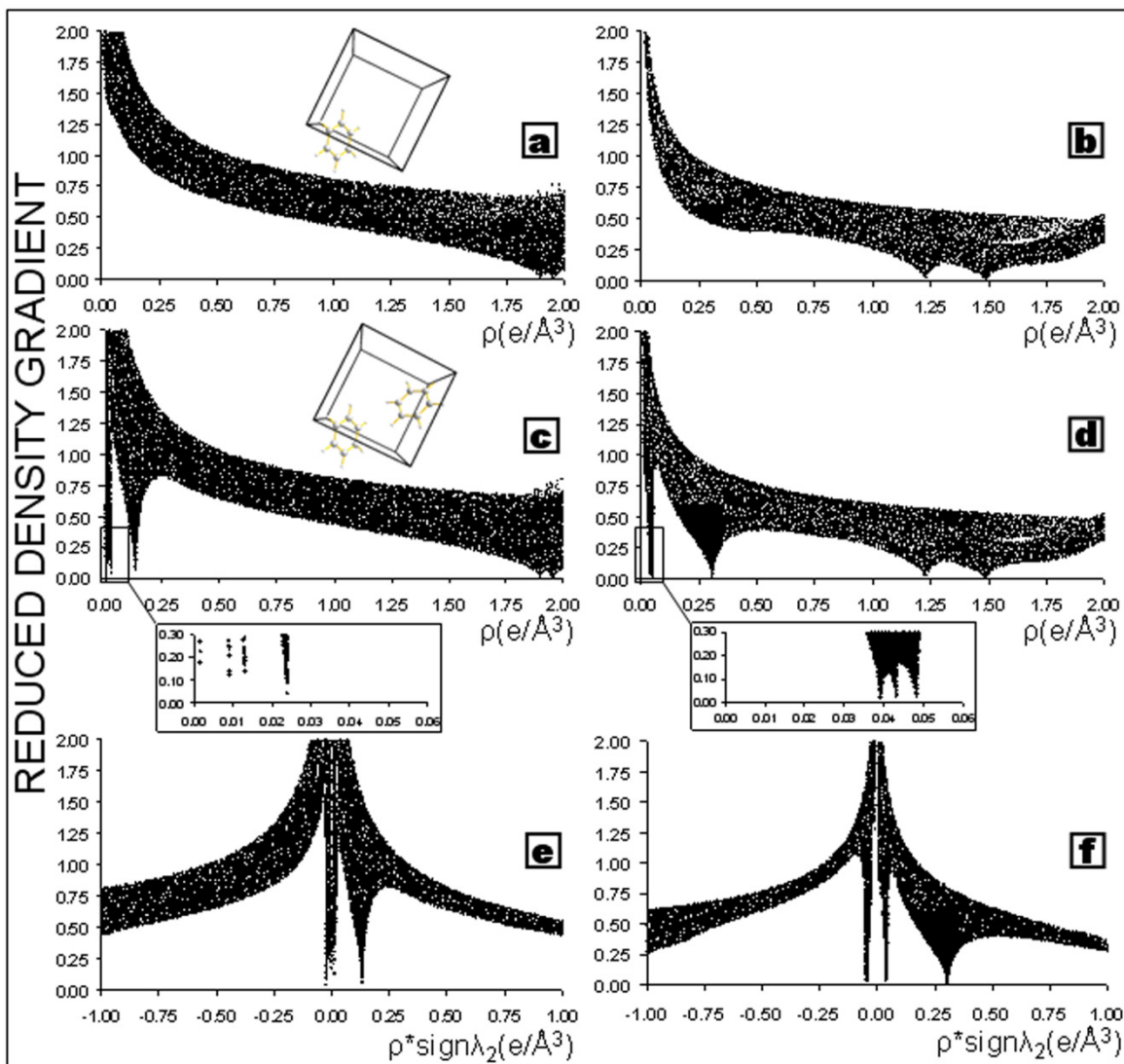


Figure 2.16. ρ vs RDG plots for *a)* *isolated* benzene (part of one molecule extracted from crystal, as represented in the inset) using the multipole electron density (ED); *b)* same as in panel *a)* but using the IAM ED; *c)* and *d)* The same *a)* and *b)*, respectively, but for two molecules of benzene at crystal geometry (see inset). The enlargements at low electron density values below panels *c)* and *d)* allow to distinguish the RDG spikes relative to the different intermolecular interactions and to the intermolecular ring critical point; *e)* and *f)* are the same as *c)* and *d)* but multiplying the corresponding ED by the sign of λ_2 . Molecular graphics in this and other Figures have been drawn with the software Diamond [43]

In Figure 2.16a (top left) and 2.16b (top right) ED and RDG are plotted within a cubic volume enclosing just three C-H and two C-C bonds of one reference benzene molecule extracted from the crystal (see the inset in figure 2.16a). This is the simple case of an isolated molecule (figure 2.16a), though with its own ED polarized by the crystalline environment. The RDG approaches low values in the regions of covalent bonds and reaches a value of zero at the BCP positions. Comparison of Fig. 2.16a and 2.16b shows that the BCP's occur, as expected, at lower ED values for the IAM density and that the spikes for C-H (lower ED value) and C-C interactions are definitely more separated for that density. Particularly interesting is the difference of the RDG distributions around the BCP's density values in the two cases. The spikes of the IAM-RDG are definitely sharper, with RDG varying much faster with respect to the ED. On the other hand the RDG spikes of the 'true' density distribution are less evident since the RDG varies much less rapidly and is much less "structured" around the BCP densities. Indeed for C-H and C-C bonds the ED value at BCP is about 50%

larger than for the IAM density, while the value of the λ_3 curvature of the electron density parallel to the bond path is almost alike in the two EDs (see Table 2.10). The different shape of the RDG spikes in Fig. 2.16a and 2.16b match perfectly the anticipations made in paragraph 2.6.1 as for the behavior of $\Delta\sigma$ for covalent interactions. The general trend of RDG vs ρ far from the BCP density values was already described in paragraph 2.4 and is not commented here further. It is only worth noting that visible differences emerge for the two EDs, though the qualitative trend is reasonably similar.

Figure 2.16c and 2.16d show analogue plots within the same cubic volume for a *pair* of neighboring benzene molecules extracted from the crystal. At variance with the reference molecule, the second one is almost entirely contained within the cube (see inset in Fig. 2.16c) so that some intermolecular contacts can be detected. Besides those related to intramolecular covalent interactions, four new spikes (three of which at lower ED values are nearly superimposed, see *infra*) appear in the low-ED/low-RDG region of both plots.* As shown by Johnson *et al.* [24] they are the distinctive feature of non-covalent interactions, as, according with equation 2.3, $s(\mathbf{r}) \rightarrow 0$ when $|\nabla\rho(\mathbf{r})| \rightarrow 0$. The three spikes at very low ED, clearly visible in the enlargements of Figures 2.16c and 2.16d, correspond to C \cdots H (at slightly higher ED) and H \cdots H NCIs and to an intermolecular RCP (Table 2.10), while that at much higher ED value is the sign of the RCP of the benzene molecule fully contained in the cubic volume (the spike relative to the reference molecule lies instead out of such volume).† Note that all four spikes occur at definitely lower ED values for the “true” density (about half of the corresponding IAM density values). In addition, the spike of the benzene molecule RCP is clearly sharper for the multipolar density, since the RDG varies more rapidly, as a consequence of the lower ED and higher or comparable ED curvatures at RCP for that density (see Table 2.10). It is a bit more difficult to compare, from figures 2.16c and 2.16d, the shape of spikes associated to the intermolecular NCI and RCP, also because the C \cdots H and H \cdots H interactions, and the RCP, have all very similar CP electron density values at the IAM level. However, if the corresponding figure enlargements at low ED are inspected, the RDG is clearly varying more rapidly for the multipole density also in this case, because the corresponding ED values are, as mentioned above, at least twice (three times) as low as the IAM values at BCPs (RCP). On the other hand, the ED curvatures (Table 2.10) are comparatively not as lowered (though smaller in magnitude because of the lower ED values).‡ In overall, it is worth noting that the different shape of the NCI RDG spikes in Fig. 2.16c and 2.16d match the anticipations made in paragraph 2.5.1 for the behavior of $\Delta\sigma$ also in the case of the closed-shell non-covalent interactions.

* The additional fifth spike at the lowest ED value in the enlargement of Figure 2.16c (and missing in the enlargement of Figure 2.16d) relates to only three RDG points and it is not associated to any CP. It is thus ignored in the present discussion.

† The presence of an ED critical point is *not* strictly required for the appearing of a RDG spike in the ED/RDG plot. The RDG-based NCI descriptor is potentially able to detect both the stabilizing, pair-specific chemical bond interactions (those with a bond path in QTAIM) and other through-space, somewhat elusive, not necessarily stabilizing interactions (without an associated bond path).

‡ The NCI spikes, in the case of the multipole density, are so sharp to become hardly visible in their region approaching RDG=0. This is due to the very small number of points representing that region in the multipole density – another indication of the faster RDG rise for the multipole density close to the NCI BCPs.

Table 2.10 Geometrical and topological (BCP) data for some intramolecular, all intermolecular (C-H...C and C-H...H, C...C) interactions and for some RCPs in the benzene crystal.^{a,b}

CP (Figure number) ^c	$\rho(\text{e}/\text{\AA}^3)$	$\nabla^2\rho(\text{e}/\text{\AA}^5)$	λ_1	λ_2	λ_3	$d_{\text{BCP}}(\text{\AA})^d$
<i>Intramolecular bonds</i>						
C(1)-C(2) [1a-1b]	2.24(1)	-19.99(4)	-15.99	-15.61	11.61	0.704
	1.48(2)	-2.364(72)	-7.02	-6.8	11.46	0.698
C(1)-H(1) [1a-1b]	1.96(3)	-22.50(1)	-19.2	-18.7	15.41	0.725
	1.23(2)	-4.37(8)	-9.42	-9.3	14.35	0.743
<i>Ring Critical Points (RCP)</i>						
Intramolecular [1c-1f]	0.131	3.7	-0.56	1.71	2.56	
	0.306	3.0	-0.86	1.94	0.25	
Intermolecular [1c-1f]	0.009	0.3	-0.03	0.05	0.25	
	0.039	0.4	-0.08	0.07	0.40	
<i>Intermolecular interactions</i>						
H(3)...H(2) ^e [1c-1f] [3a-d]	0.013(5)	0.238(1)	-0.05	-0.03	0.32	1.294 (2.548)
	0.043(<1)	0.388(<1)	-0.11	-0.07	0.57	1.268
C(3)...H(1) ^e [1c-1f] [3a-d]	0.024(4)	0.241(1)	-0.08	-0.06	0.38	1.773 (2.934)
	0.048(<1)	0.462(<1)	-0.11	-0.06	0.64	1.722
C(1)...H(3) ^f Not shown in Figures	0.016(5)	0.235(1)	-0.06	-0.02	0.32	1.797 (2.955)
	0.047(1)	0.455(<1)	-0.10	-0.07	0.62	1.7141
H(2)...H(1) ^g Not shown in Figures	0.018(4)	0.275(1)	-0.06	-0.04	0.37	1.390 (2.638)
	0.039(2)	0.365(<1)	-0.09	-0.07	0.52	1.3764
C(3)...H(2) ^h [2a-b;2d-e]	0.030(4)	0.256(1)	-0.10	-0.01	0.37	1.853 (3.065)
	0.045(<1)	0.458(<1)	-0.02	0.00	0.49	1.896
C(1)...H(3) ^h [2a-b;2d-e]	0.042(6)	0.371(2)	-0.15	-0.11	0.63	1.706 (2.862)
	0.053(<1)	0.504(<1)	-0.12	-0.09	0.71	1.650
C(3)...C(2) ⁱ [4a-d]	0.001(<1)	0.008(<1)	0.00	0.00	0.01	2.662 (5.295)
	0.002(<1)	0.018(<1)	0.00	0.00	0.02	2.652

a) for each entry the first row refers to the multipole ED and the second row to the IAM ED.

b) Electron and Laplacian density values s.u. are given in parentheses.

c) The labels reported in square brackets in column 1 refer to the figures where the corresponding RDG vs ρ plots or NCI isosurfaces are portrayed.

d) BCP distance from the first atom in column 1 (in parentheses the bond distance in \AA)

e) At $-0.5-X, -0.5+Y, +Z$

f) At $-X, 0.5+Y, 0.5-Z$

g) At $+X, 0.5-Y, 0.5+Z$

h) At $-0.5-X, -Y, -0.5+Z$

i) At $-1-X, -Y, -Z$. The BCP was recovered by using only the multipoles of the two molecules (see text)

Finally, the multipolar (fig. 2.16e) and the IAM (fig. 2.16f) RDG are plotted against $\rho(\mathbf{r})\cdot\text{sign}(\lambda_2)$ to discriminate between the supposedly attractive and the so-called non-bonded interactions (see Section

2.2.2 above). Only the spikes relative to NCI are represented in these figures. As expected, two of the three spikes at lower EDs values in fig. 2.16c and 2.16d, shift towards negative signed-ED values, being associated to BCPs ($\lambda_2 < 0$) and, therefore, denoting interactions somewhat attractive in nature. The remaining spike, as well as that associated to the RCP ($\lambda_2 > 0$) of the benzene molecule fully contained in the examined cubic volume, have instead a positive signed-ED value, in agreement to their non-bonded interaction nature. The larger $|\rho(\mathbf{r}) \cdot \text{sign}(\lambda_2)|$ magnitude for the IAM density is clearly evident from comparison of Fig. 2.16e and 2.16f, as well as the larger separation between intermolecular NCI and intermolecular RCP peaks for such density. The greater sharpness of the multipole RDG peaks (and the associated lack of representative points when approaching RDG=0) becomes also more evident in these RDG vs $\rho(\mathbf{r}) \cdot \text{sign}(\lambda_2)$ plots.

2.6.4 RESULTS FOR BENZENE

In this paragraph the comparison between IAM and experimental RDG isosurfaces for benzene molecular crystal will be discussed.

Table 2.10 reports the topological properties of the multipolar and IAM electron density intermolecular BCP's found for each unique molecular pair. Figures 2.17, 2.18 and 2.19, on the other hand, show the corresponding RDG iso-surfaces for pairs I, III and IV, respectively. The displayed surfaces correspond for all figures to isovalues 0.4 (left) and 0.6 (middle, figure 2.17 and right, figures 2.18 and 2.19) and to multipole (top row) and IAM (bottom row) EDs.

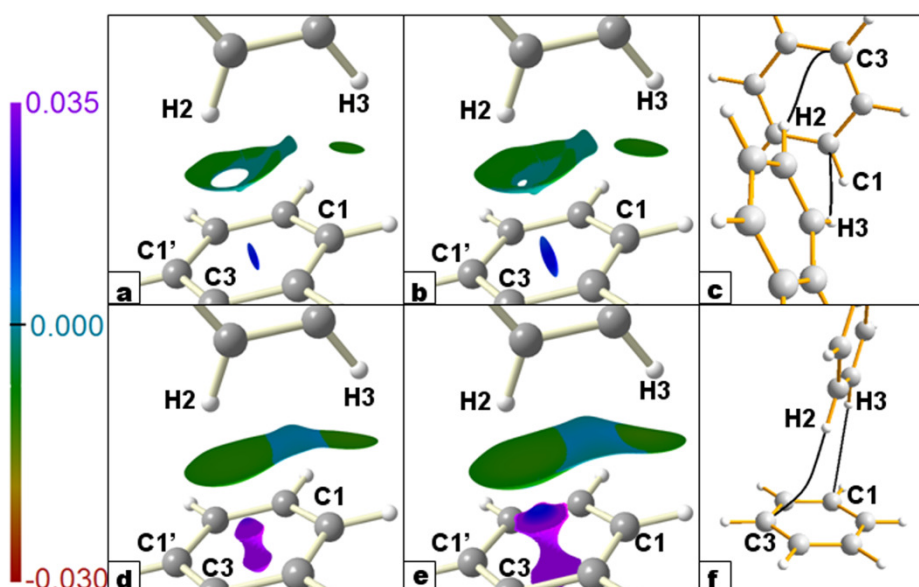


Figure 2.17. *a-b*) RDG-based NCI isosurfaces for the molecular pair I in the benzene crystal using the multipole Electron Density (ED) and the $s=0.4$ (*a*) and the $s=0.6$ (*b*) RDG isovalue. Panels *d* and *e* are the same as panels *a* and *b*, respectively, but for the IAM ED. In panels *c* and *f* the bond paths associated to the RDG isosurfaces displayed on the same row are shown. The color scale for $\rho \cdot \text{sign}(\lambda_2)$ (e/au) is shown on the left. The isosurfaces in this and the following figures have been drawn with the software Molliso [82].

The RDG isosurfaces for pair I are associated to two intermolecular bond paths (Figure 2.17: panel c, multipole ED; f, IAM ED) that link H2 and H3 with the C3 and C1 atoms belonging to the molecule at $-0.5-x, -y, 0.5-z$. The different nature of these two interactions is already suggested by the portrait of their bond paths (BPs). The C1...H3 BP is essentially straight while the H2...C3 BP is significantly bent. At the multipolar

level, the latter BP points towards the (3,-1) critical point of the C3-C1' covalent bond and then suddenly deviates towards the C3 nucleus, whereas at the IAM level it initially directs to the center of the benzene ring and then ends up at C3. The RDG isosurfaces magnify all these differences, and discussion about them was already reported in paragraph 2.4.3. Here it will only be added that the different shape of the two isosurfaces associated with C-H \cdots π and C-H \cdots C (the former being more extended in space, reflecting the more delocalized character of C-H \cdots π interaction, as discussed in paragraph 2.4.3) agrees with the λ_1 and λ_2 eigenvalues at the BCPs associated with the two interactions. Indeed, for C-H \cdots C the eigenvalues are similar in value (Table 2.10), at variance with those for the C-H \cdots π interaction that are not only smaller, but significantly different between each other, one being one order of magnitude smaller and very close to zero (this is likely the cause of the extended size of the associated RDG isosurface). When the RDG-signed isosurfaces derived from the IAM model are analyzed important differences emerge. As expected (see discussion in Section 2.6.1 and 2.6.3), the surfaces are more extended in size (they even merge, both at $s=0.4$ and 0.6), more flat and featureless (compare Figures 2.17a-b with 2.17d-e). Differences persist regardless the comparison is made (same s value or different s values to match the two descriptions as closely as possible). Indeed, the differences between multipolar and IAM isosurfaces at a given s value are larger than the differences between the multipolar (or the IAM) isosurfaces at the two analyzed isovalues. The description using the multipolar ED, reveals itself as clearly superior, as it more neatly distinguishes the nature of the two interactions. Note that at the IAM level (Table 2.10) the values of the λ_1 and λ_2 eigenvalues for the H2 \cdots C3 interaction are very close to zero and much more alike to each other, which explains why the associated RDG isosurface shape changes with respect to the multipolar description and loses important structural features, like concavity and the hole at its center. The different route followed by the multipolar and IAM BPs is also clearly mirrored by the differences in the RDG isosurfaces of the corresponding interactions.

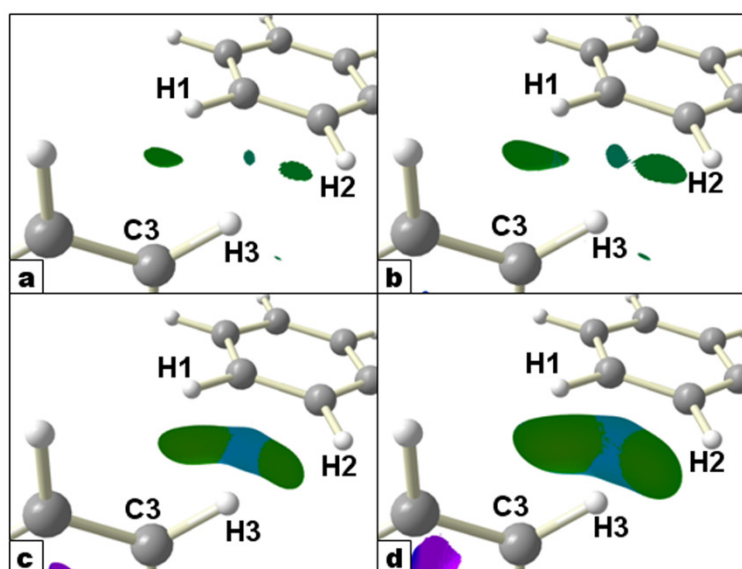


Figure 2.18. RDG-based NCI isosurfaces for the molecular pair III in the benzene crystal using the multipole (top row, panels a and b) and the IAM (bottom row, panels c and d) Electron Densities. See Fig. 2.17 for the signed ρ color legend. The left panels refer to the $s=0.4$ and those on the right to the $s=0.6$ RDG isovalue.

In both the molecular pairs II and III two similar BPs are present (Table 2-10). One links an Hydrogen to a Carbon atom (C-H \cdots C contact), whereas the other connects two Hydrogen atoms. Discussion on such interactions was already reported elsewhere in paragraph 2.4. The shape of the RDG iso-surface associated

to the first BP in the molecular pair III (Fig. 2.17) resembles that found for the intermolecular hydrogen bond in benzene pair I, although the surface is a bit broader, as anticipated by the electron density and curvatures at BCP being somewhat smaller. A nearly disc-shaped and slightly negative signed iso-surface is also found for the H \cdots H contact. Both interactions are characterized by small ED values and signal weakly attractive interactions. Differences between the multipole and the IAM model RDG isosurfaces are similar to those discussed in Figure 2.17 and need not to be commented any further.

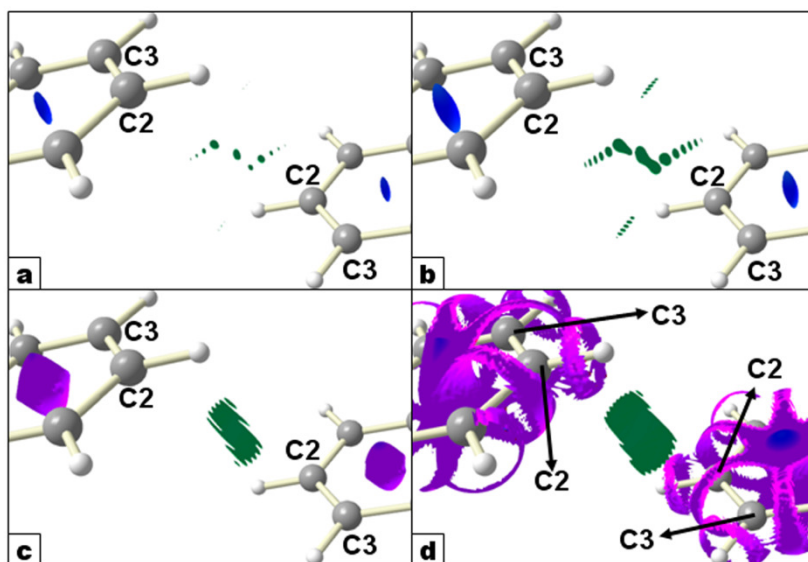


Figure 2.19 RDG-based NCI isosurfaces for the molecular pair IV in the benzene crystal using the multipole (top row, panels a and b) and the IAM (bottom row, panels c and d) Electron Densities. The left panels refer to the $s=0.4$ and those on the right to the $s=0.6$ RDG isovalue. See Fig. 2.17 for the signed ρ color legend and Table 1 for the symmetry operations relating the labeled atoms.

In the molecular pair IV (Figure 2.19) the two molecules lie quite far apart. When the multipolar ED for this pair extracted from the crystal is considered, two intermolecular C \cdots C BP's are found between the C2 atom of the reference molecule and the C3 atom at $-x, -y, -1-z$, and vice-versa. The ED at BCPs is negligible and all the density curvatures at this point are almost zero (Table 2.10). Accordingly, in the multipolar RDG-based approach, broad and low-ED valued iso-surfaces appear (Figure 2.10a-b), but they are also significantly more structured. They represent some kind of very weak, attractive interaction (based on the λ_2 sign), due to dispersive-driven $\pi\cdots\pi$ interaction among the lateral Carbons of the two molecules. The corresponding IAM isosurfaces are located similarly in space* and have similar $\rho(r)*\text{sign}\lambda_2$, but are much broader and different in shape, being almost structureless.†

*The violet RDG isosurfaces wrapping the two benzene molecules for the IAM case at $s=0.6$ (Figure 2.17d) are due to the fact that by using this high s isovalue one is actually enclosing RDG regions that do not belong to the RDG spikes (Figure 2.10).

†It was already reported in paragraph 2.4 and 2.5 (for experimental and theoretical results, respectively) that when the same analysis is performed in the bulk, *i.e.* when also the multipole ED contributions of the neighbouring molecules are considered, both the BP's and the NCI iso-surfaces of these very weak $\pi\cdots\pi$ interactions disappear. The same occurs with the IAM model. If the molecules of a pair are quite far apart, as in the present case, the contribution to the ED in the intermolecular region due to other molecules in the unit cell may become non negligible. In such a case, changes in the shape of RDG isosurfaces, or even their disappearance, may be envisaged. It appears that the $\pi\cdots\pi$ interaction taking place in pair IV, is too weak to survive the competition with other stronger interactions (CH $\cdots\pi$, dispersive) present in the benzene crystal.

2.6.5 RESULTS FOR AUSTDIOL

In this paragraph, there will be presented a few representative interactions of Austdiol to explore how these isosurfaces are modified using the IAM model ED (a full discussion of the NCIs for this system are reported in paragraph 2.4). Table 2.11 compares the topological properties of the multipolar and IAM electron density BCP's found for the investigated contacts. Figures 2.20-2.21 display the corresponding RDG iso-surfaces for intermolecular interactions within the (a,b) plane, Figures 2.22-2.23 those for two intramolecular contacts and Figure 9 shows iso-surfaces relative to three weak C-H...O intermolecular interactions along c. As for benzene, in all these figures the displayed surfaces correspond to isovalues 0.4 (left) and 0.6 (right) and to multipole (first row) and IAM (second row) ED's.

Table 2.11. Geometrical and topological features of some intermolecular and intramolecular X-H...O contacts (X=C,O) of Austdiol.^{a,b}

CP (Figure number) ^c	$\rho(e/\text{\AA}^3)$	$\nabla^2\rho(e/\text{\AA}^5)$	λ_1	λ_2	λ_3	$d_{\text{BCP}}(\text{\AA})^d$
<i>Intramolecular bonds</i>						
C(2)-H(1)...O(2) [7a-d]	0.11(3)	2.00(3)	-0.43	-0.33	2.77	0.879 (2.145)
	0.166(1)	1.78(1)	-0.59	-0.38	2.75	0.908
C(11)-H(4)...O(3) [8a-d]	no BCP for both electron densities					(2.359)
<i>Intermolecular interactions</i>						
O(5)-H(6)...O(4) ^e [5a-d]	0.14(4)	1.34(6)	-0.75	-0.71	2.81	0.784 (2.023)
	0.18(2)	2.00(2)	-0.78	-0.76	3.54	0.822
C(9)-H(3)...O(2) ^f [6a-d]	0.13(3)	1.40(4)	-0.68	-0.45	2.53	0.866 (2.174)
	0.14(<1)	1.57(<1)	-0.54	-0.43	2.54	0.903
C(11)-H(4)...O(5) ^g [6a-d]	0.05(2)	0.56(1)	-0.26	-0.18	0.99	1.083 (2.519)
	0.07(1)	0.79(1)	-0.21	-0.18	1.18	1.106
C(12)-H(11)...O(2) ^h [9a-d]	0.05(3)	0.83(2)	-0.22	-0.15	1.19	1.025 (2.443)
	0.07(<1)	0.90(<1)	-0.25	-0.24	1.39	1.067
C(10)-H(7)...O(3) ^h [9a-d]	0.04(3)	0.41(1)	-0.11	-0.07	0.59	1.122 (2.544)
	0.07(<1)	0.78(<1)	-0.19	-0.15	1.12	1.108
C(12)-H(11)...O(1) ⁱ [9a-d]	0.03(1)	0.33(<1)	-0.07	-0.05	0.45	1.409 (2.979)
	0.03(1)	0.38(<1)	-0.06	-0.04	0.49	1.399

a) for each entry the first row refers to the multipole ED and the second row to the IAM ED.

b) Electron and Laplacian density values s.u. are given in parentheses.

c) The labels reported in square brackets in column 1 refer to the figures where the corresponding NCI isosurfaces are portrayed.

d) BCP distance from the first atom in column 1 (in parentheses the bond distance in Å)

e) At $-X, 1-Y, Z$

f) At $-1+X, Y, Z$

g) At $1+X, Y, Z$

h) At $-0.5+X, 0.5-Y, -Z$

i) At $0.5+X, 0.5-Y, -Z$

Figure 2.20 displays HB surfaces for two symmetry-related intermolecular $\text{H}\cdots\text{O}$ HB's ($\text{O5-H6}\cdots\text{O4}$, $d_{\text{H}\cdots\text{O}} = 2.023 \text{ \AA}$) in the (a,b) plane of the unit cell of Austdiol. Being relatively strong HB's, they are characterized by disc-shaped, $\lambda_2 < 0$ surfaces, while the third green surface visible between them is the signature of the ring critical point.

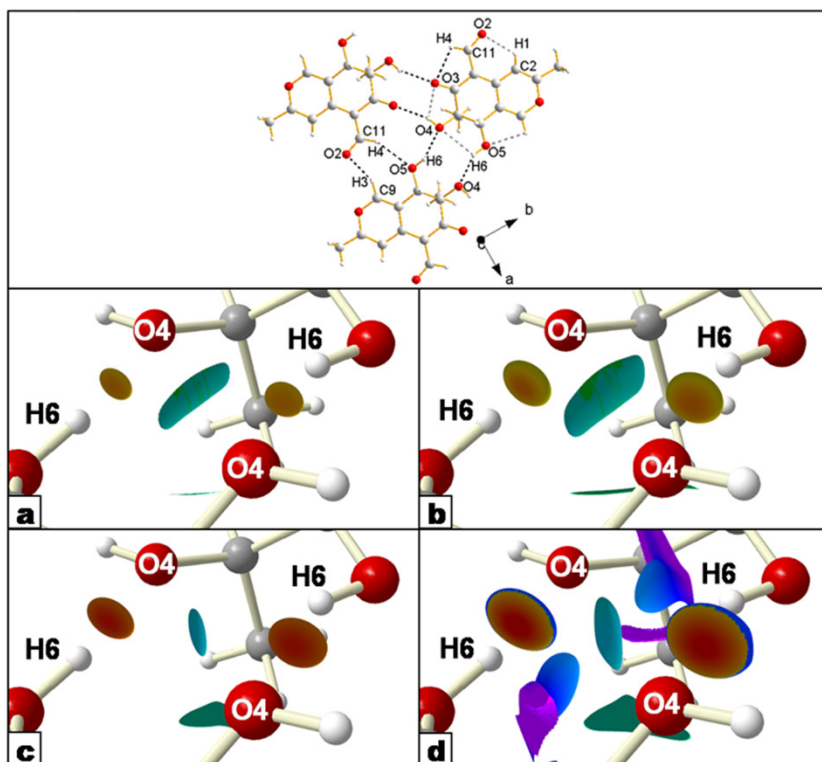


Figure 2.20. RDG-based NCI isosurfaces for two symmetry-related intermolecular $\text{OH}\cdots\text{O}$ HBs in the (a,b) plane of the Austdiol using the multipole (middle row, panels a and b) and the IAM (bottom row, panels c and d) Electron Densities. The left panels refer to the $s=0.4$ and those on the right to the $s=0.6$ RDG isovalue. See Fig. 2.17 for the signed ρ color legend and Table 2.11 for the symmetry operations relating the labeled atoms. In the top panel, the atom-atom contacts in the (a,b) plane of the Austdiol are shown. Those with a bond path by a dotted black line and those without a bond path by a dotted gray line.

As expected, the RDG-IAM isosurface related to the HB's is more extended in size and bears more negative $\rho(\mathbf{r}) \cdot \text{sign} \lambda_2$ values, because of the larger ED value at and in the close neighbourhood of the BCP. The shape of this surface at $s=0.4$ is very much alike that for the multipole density at $s=0.6$, though the "colour" of the two surfaces differs. At $s=0.6$, however, the RDG-IAM surface displays a large, positive, blue annular ring at its border, which is not at all visible in the multipole-derived surfaces and which is likely the result of a different description of the interactions between facing atoms in the ring. For the multipole density and differently from what observed for benzene ring (Figure 2.19a-b), the surface is quite elongated, possibly as a result of the much smaller symmetry in the ring in the present case and of the fact that the internuclear axes related to 1,4 ($\text{O4}\cdots\text{O5}$) or higher "topological" non-bonded contacts (1,5 : $\text{O5}\cdots\text{O5}$, $\text{O4}\cdots\text{O4}$, $\text{H6}\cdots\text{H6}$) either do not intersect or do so in different points. This peculiar feature is not due to a specific bias of the multipole model, since it was also observed in the corresponding RDG isosurface derived from the periodic

ab-initio ED (see paragraph 2.5). Conversely, in the IAM-RDG picture, this isosurface either resembles ($s=0.4$, Fig. 2.20c) that for the ring critical point in benzene or looks ($s=0.6$, Fig. 2.20d) quite differently in location, extension and “colour”. Interactions among facing atoms in the ring are described as very weak and negligibly attractive or repulsive by the multipole model, while they are clearly closed-shell and repulsive (in terms of λ_2) at the IAM level.

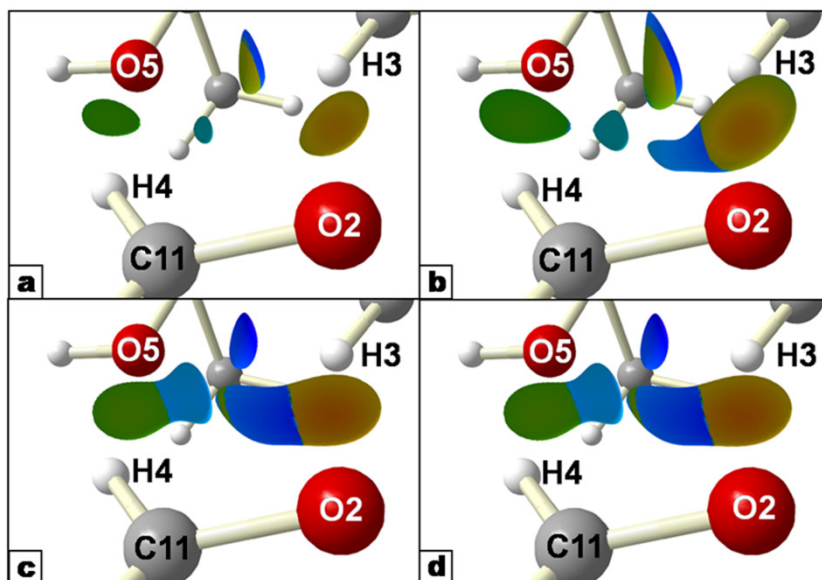


Figure 2.21. RDG-based NCI isosurfaces for two C-H \cdots O HBs (C9-H3 \cdots O2 and C11-H4 \cdots O5) in the (a,b) plane of the Austdiol using the multipole (top row, panels a and b) and the IAM (bottom row, panels c and d) Electron Densities. The left panels refer to the $s=0.4$ and those on the right to the $s=0.6$ RDG isovalue. See Fig. 2.17 for the signed ρ color legend and Table 2.11 for the symmetry operations relating the labeled atoms.

The signed-RDG isosurfaces for two C-H \cdots O HBs (C9-H3 \cdots O2 and C11-H4 \cdots O5) are displayed in Figure 2.21. The former is a very short C-H \cdots O HBs ($d_{\text{H}\cdots\text{O}} = 2.174 \text{ \AA}$) whose strength was estimated to be comparable with that of the OH \cdots O bonds in this system [40]. Accordingly, the corresponding signed iso-surface (multipole-RDG) looks similar in color to that discussed earlier for the OH \cdots O HB's. However, due to the presence of a non-bonded contact involving C11 and H3 atoms in symmetry-related molecules, it is not as well disc-shaped as for O5-H6 \cdots O4. At $s=0.6$ it even displays a positive part, clearly signaling the C11 \cdots H3 contact. The RDG-IAM description of the C9-H3 \cdots O2 interaction is qualitatively similar, though with much broader isosurfaces, as expected. The non-bonded C11 \cdots H3 contact is already evident at $s=0.4$: even at this lower s value, the RDG isosurfaces of the two C-H \cdots O HBs are close to merge, while the multipole-derived isosurfaces remain clearly distinct even at $s=0.6$. This provides a further evidence that the IAM model yields, in general, less structured RDG-NCI isosurfaces. Though weaker and longer ($d_{\text{H}\cdots\text{O}} = 2.519 \text{ \AA}$), the C11-H4 \cdots O5 bond has a clearer disc-shaped isosurface than C9-H3 \cdots O2, due to the lack of perturbing non bonded contacts. However, the different colors of the two surfaces re-establish the correct relative order of HB strength. Also for C11-H4 \cdots O5, the IAM description yields a broader, not disc-shaped RDG isosurface, with a significantly large positive part even at the lower s value.

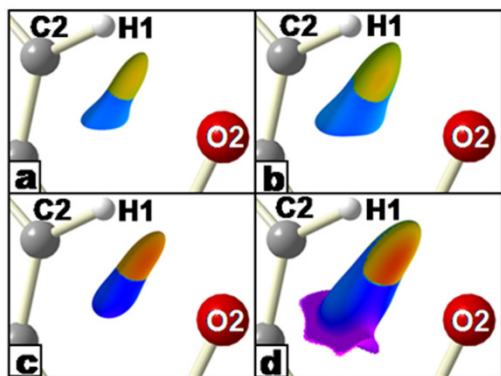


Figure 2.22. RDG-based NCI isosurfaces for a “bonded” (a bond path present) intramolecular C-H \cdots O contact of Austdiol using the multipole (top row, panels a and b) and the IAM (bottom row, panels c and d) Electron Densities. The left panels refer to the $s=0.4$ and those on the right to the $s=0.6$ RDG isovalue. See Fig. 2.17 for the signed ρ color legend.

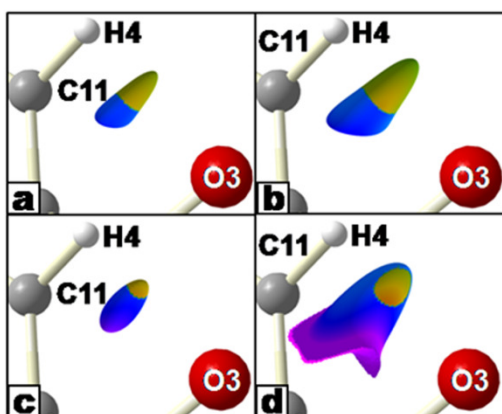


Figure 2.23. RDG-based NCI isosurfaces for a “non bonded” (no bond path) intramolecular C-H \cdots O contact of Austdiol using the multipole (top row, panels a and b) and the IAM (bottom row, panels c and d) Electron Densities. The left panels refer to the $s=0.4$ and those on the right to the $s=0.6$ RDG isovalue. See Fig. 2 for the signed ρ color legend.

The RDG-based NCI isosurfaces for the X-H \cdots O (X=C,O) intra-molecular contacts of Austdiol, have been carefully investigated in paragraph 2.4.2. Such contacts play an important role in determining the molecular conformation observed in the bulk and, despite a BP was only observed for the C2-H1 \cdots O2 one, RDG isosurfaces depicting each of the six unique intramolecular H \cdots O contacts were found. They are all characterized by small XHO angles (in the 92 $^\circ$ -122 $^\circ$ range) and their RDG isosurfaces at multipolar level are characterized by two well-defined regions of positive and negative λ_2 , respectively. The latter region extends towards the interior of the five or six-membered ring formed by the X-H \cdots O contact. To see how the description of such contacts is affected replacing the multipolar with the IAM ED, just a couple of them (Table 2.11) will be considered in the following discussion. Figure 2.22 displays RDG isosurfaces for the C2-H1 \cdots O2 contact, having an associated BP (Table 2.11), and Figure 2.23 for the slightly longer and more bent (101 $^\circ$ vs 122 $^\circ$) C11-H4 \cdots O3 contact, with no BP. In both cases it looks like the IAM model is able to qualitatively reproduce the features of the multipole-RDG isosurfaces, with the positive part of the surface increasing significantly its weight with respect to the multipole description, especially for the non bonded contact (Figure 2.23).

Van der Waals and, in particular, dispersion interactions are due to time-dependent perturbations of the ED, involving correlations among distant electrons. The discussion about the physical ground of such interactions was reported in paragraph 2.3. There, it was showed that quite large RDG iso-surfaces

exhibiting analogue characteristics to those observed by Johnson et al. [24] on methane come into view for the two unique neighboring molecular pairs along *c* in austdiol. The ED is relatively flat in the intermolecular region, the λ_2 curvature is close to zero and therefore quite indeterminate, so that both slightly positive or moderately negative regions were observed on the signed RDG iso-surface. The issue that is going to be investigated in this session is whether such features are adequately reproduced also when analyzed through the IAM model.

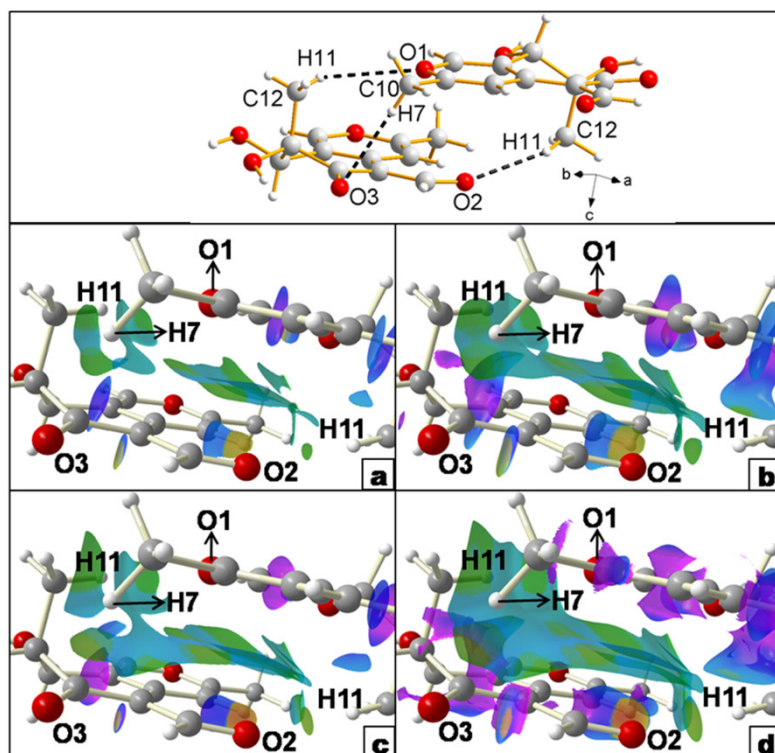


Figure 2.24. Austdiol: RDG-based NCI isosurfaces for one of the two unique molecular pairs along *c*, using the multipole (middle row, panels a and b) and the IAM (bottom row, panels c and d) Electron Densities. The left panels refer to the $s=0.4$ and those on the right to the $s=0.6$ RDG isovalue. There are two very weak and one moderately weak intermolecular $\text{CH}\cdots\text{O}$ interactions between the two molecules. See Fig. 2.17 for the signed p color legend and Table 2.11 for the symmetry operations relating the labeled atoms. In the top panel, the structure of the molecular pair and the $\text{CH}\cdots\text{O}$ interactions with a bond path are shown.

Figure 2.24 shows the signed-RDG isosurfaces for one of the two unique molecular pairs along *c* (see the structure in the top panel of the Figure, corresponding to the molecular pair labeled as B in Fig. 2.4). From a comparison of the isosurfaces in the Figure, it is immediate to conclude that the IAM model fairly mirrors the multipole density representation. When compared at the same s isovalue, the IAM-RDG isosurface appears broader and less structured as anticipated by the discussion in paragraph 2.6.1, but the IAM-RDG $s=0.4$ and the multipole $s=0.6$ isosurfaces match each other significantly.

Three $\text{C-H}\cdots\text{O}$ bonded contacts, based on the BP criterion, held together the molecular pair in Fig. 2.23, besides the van der Waals and dispersive interactions. Two of such contacts (*i.e.* $\text{C12-H11}\cdots\text{O1}$ and $\text{C10-H7}\cdots\text{O3}$) are very weak and the first was even found [40] not to satisfy the Koch and Popelier criteria [50] for hydrogen bonding. Indeed, they are not recognizable through specific RDG isosurfaces. Already at the multipole level and at the lower represented s value (Fig. 2.24a), a single, broad van der Waals-like isosurface has merged with and encompasses the two slightly negative, diffuse and not disc-shaped regions around the BCPs of the two interactions. This behavior may be explained in terms of the marginal

difference between a closed-shell dispersive interaction and an extremely weak and long C-H...O bond. In the IAM-RDG picture the signs of these two HB interactions become even more less evident.

Figure 2.24 also displays, at the multipolar level, a clearly recognizable disc-shaped RDG iso-surface for the C12-H11...O2 intermolecular HB. In this case, besides the comparatively shorter HB length (Table 2.11), it occurs that the H...O direction is almost parallel to the molecular layers in the (a,b) plane where the non-directional purely steric-dispersive interactions are not playing a dominant role. At the IAM level, the isosurfaces ($s=0.4$ and 0.6) for this stronger intermolecular H-bond are broader and less clearly distinct from the large RDG van der Waals-like isosurface lying in between the two molecules.

2.6.6 RESULTS FOR FAMOTIDINE

As already pointed out in section 2.4.4, Famotidine is an heteroatom-rich antiulcer drug, known to crystallize in two polymorphs differing in crystal packing and molecular conformation. The features of experimentally derived NCI isosurfaces were already discussed in section 2.3.4. Here the discussion will mainly focus on the comparison with IAM isosurfaces. Since most of the intermolecular interactions in both polymorphs are HBs and van der Waals-like contacts, closely resembling those discussed for benzene and Austdiol, here only the interactions distinctive of famotidine will be discussed (as done in section 2.3.4), like the XH...N (X=N,C) HBs, the NH...S and S...S contacts and those involving to various extent the π -electrons. Moreover, the analysis reported here will be limited to a few representative examples (table 2.12) of these peculiar interactions and only for those in the form A. RDG isosurfaces for famotidine are displayed in Figures 2.25-2.28, following the same convention (top multipole, bottom IAM; left $s=0.4$, right or middle, $s=0.6$) adopted for Figures 2.17-2.24.

Table 2.12. Geometrical and topological features of some intermolecular interactions in famotidine.^{a,b}

CP (Figure number) ^c	$\rho(\text{e}/\text{\AA}^3)$	$\nabla^2\rho(\text{e}/\text{\AA}^5)$	λ_1	λ_2	λ_3	$d_{\text{BCP}}(\text{\AA})^d$
<i>X-H...N (X=C,N) and N-H...C intermolecular (delocalized) HBs</i>						
N(6)...H(10B)C(10) ^e [10a-f]	0.03(2) 0.08(<1)	0.68(1) 0.80(<1)	-0.12 -0.22	-0.08 -0.16	0.87 1.18	1.637 (2.555) 1.478
N(15)(H15A)...N(6) ^f [11a-c]	0.037(7) no bcp no bcp 0.07(5)	0.39(<1) - - 0.65(3)	-0.15 - - -0.15	-0.08 - - -0.07	0.61 - - 0.88	1.152 (2.801) - (2.729) 1.133
N(15)(H15A)...C(2) ^f [11d-f]						
<i>N-H...S and S...S intermolecular contacts</i>						
N(18)H(18A)...S(11) ^g [12a-d]	0.047(8) 0.073(5)	0.603(4) 0.676(3)	-0.17 -0.17	-0.12 -0.13	0.89 0.98	1.098 (2.847) 1.138
S(1)...S(11) ^h [13a-d]	0.031(2) 0.047(2)	0.359(2) 0.458(1)	-0.08 -0.09	-0.07 -0.07	0.50 0.62	1.790 (3.664) 1.842
C(5)H(5)...S(11) ^h [13a-d]	0.024(5) no bcp	0.306(2) -	-0.09 -	-0.07 -	0.62 -	1.326 (3.215) -

a) for each entry the first row refers to the multipole ED and the second row to the IAM ED.

b) Electron and Laplacian density values s.u. are given in parentheses.

c) The labels reported in square brackets in column 1 refer to the figures where the corresponding NCI isosurfaces are portrayed.

d) BCP distance from the first atom in column 1 (in parentheses the bond distance in \AA)

e) At 1-X, 1/2+Y, 3/2-Z

f) At X, 1/2-Y, 1/2+Z

g) At X, 0.5-Y, 0.5+Z

h) At X, 1+Y, Z

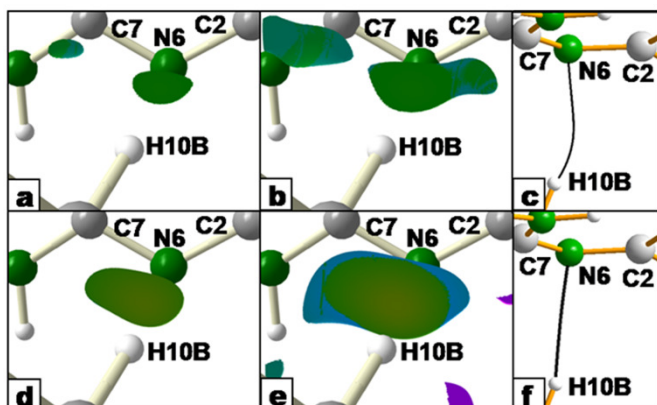


Figure 2.25. Famotidine : RDG-based NCI isosurfaces for the intermolecular interaction associated to the bond path involving H10B and N6 atoms using the multipole (top row, panels a and b) and the IAM (bottom row, panels d and e) Electron Densities. The left panels refer to the $s=0.4$ and those in the middle to the $s=0.6$ RDG isovalue. In panels c and f the bond paths associated to the RDG isosurfaces displayed on the same row are shown. The RDG picture reveals that it is more a C-H $\cdots\pi$ rather than an hydrogen bond interaction in nature (see text). See Fig. 2.17 for the signed pcolor legend and Table 2.12 for the symmetry operations relating the labeled atoms.

The intermolecular interaction associated to the BP involving the H10B and N6 atoms. In the multipolar ED this BP is significantly bent. It points initially towards the N6-C2 midpoint and then deviates to reach the N6 attractor (Figure 2.25c), while the corresponding IAM BP is almost a straight line, just slightly bent in the opposite direction, towards C7. (Figure 2.25f). At variance with what suggested by the formal bonding scheme shown in Scheme 2.3, the N6-C2 bond is conjugated (see discussion in paragraph 2.3.4) and may act as a π -acceptor in C-H $\cdots\pi$ in interactions. The other competing scheme of bonding would be through a standard HB interaction between H10B and the lone pair (if present and suitably oriented) on the N6 atom. At the multipolar level (Figure 2.25a-b), the RDG isosurface is already significantly extended even at $s=0.4$, which seems to rule out the hypothesis of a conventional H-bond (compare for instance with the RDG isosurface for the OH \cdots O bond in Austdiol, Fig. 2.20) and becomes much more so at $s=0.6$. Its shape denotes the presence of a CH $\cdots\pi$ interaction involving the π -cloud of both N-C bonds and in particular that of the N6-C2 bond, in agreement with the initial direction of the H10B-N6 BP. The lack of a non bonded maximum around N6 directed towards the H, that is of a (3,-3) CP in the minus ED Laplacian distribution [26], corroborates the CH $\cdots\pi$ description of the intermolecular interaction involving H10B. The corresponding IAM-RDG isosurfaces (Figure 2.25d-e) are much broader and suggest a preferential interaction of H10B with the π -cloud of the N6-C7 rather than that of the N6-C6 bond, again in accord with the different BP initial orientation for the IAM density. Interestingly, though different in size, the RDG isosurfaces for the periodic *ab-initio* ED show this same preference (see paragraph 2.5). We are in doubt of whether such discrepancy is the result of subtle systematic errors/statistical noise affecting the experimental structure factor amplitudes, or if it rather points at some inadequacies of the DFT functional model (and a fortiori of the IAM approach) in providing an accurate description of the low-ED regions relevant for this CH $\cdots\pi$ contact.

Interesting differences between the multipole and the IAM description are observed for another CH $\cdots\pi$ interaction involving the H15A atom in a different molecular pair of the polymorph A. As shown in Figure 2.26, an almost straight BP connects H15A and N6 using the multipole ED (Figure 2.26c), whilst the IAM

density describes H15A linked to the C2 rather than to the N6 atom, though with a similarly straight BP (Figure 2.26f).*

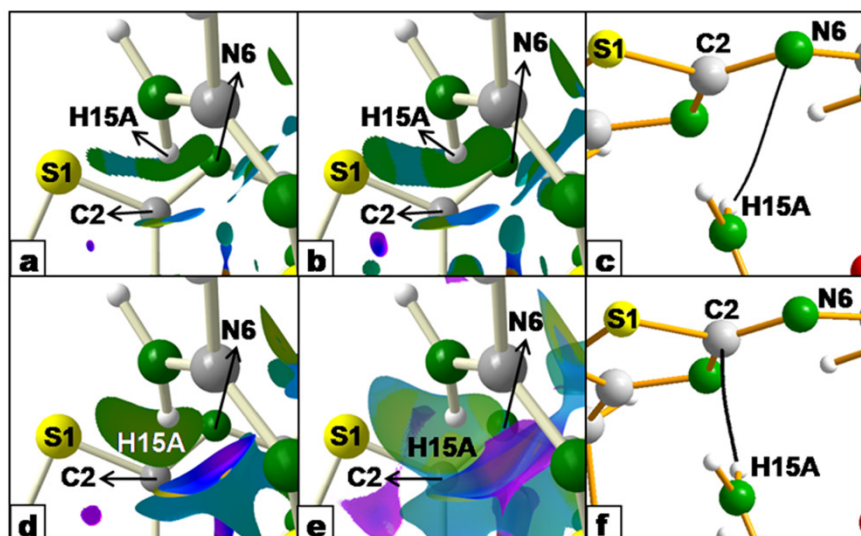


Figure 2.26. Famotidine : RDG-based NCI isosurfaces for the intermolecular interaction associated to the bond path involving H15A and N6 atoms, using the multipole electron density (ED), or H15A and C2 atoms using the IAM ED (see text). Top row, panels *a* and *b*): multipole-RDG and bottom row, panels *d* and *e*, multipole-IAM Electron Densities. The left panels refer to the $s=0.4$ and those in the middle to the $s=0.6$ RDG isovalue. In panels *c* and *f* the bond paths associated to the RDG isosurfaces displayed on the same row are shown. The RDG picture reveals a complex multi-center interaction. See Fig. 2.17 for the signed ρ color legend and Table 2.12 for the symmetry operations relating the labeled atoms.

The RDG-NCI descriptor, instead, suggests for both EDs quite a delocalized interaction between the H atom and the electron density distribution of the C2-N6 and S1-C2 bonds. The observed discrepancy in the BP terminus for the IAM and multipole ED is mirrored in their RDG isosurfaces, the one obtained from IAM being preferentially extended towards the S1 atom and that from the multipole ED towards the N6 atom. Noticeable, but still moderate differences in the preferential extension of the RDG isosurfaces reflect in a completely distinct BP description, as it is inherent to the “yes/no” language of the topological approach [67,79]. The RDG iso-surfaces in Fig. 2.26 are likely the result of contributions coming from different interaction types (NH \cdots N or NH \cdots C localized HBs, evidenced by the BP criterion, along with the more delocalized CH \cdots π interactions revealed by the RDG-NCI analysis), as also suggested by the similar internuclear distances between H15A and the N6 (2.801 Å), C2 (2.729 Å) and S1 (2.988 Å) atoms. The IAM signed-RDG isosurfaces when compared to those for the multipole ED (Figure 2.26d-e vs Figure 2.26a-b) are much broader, less well oriented along the C2-N6 and S1-C2 bonds and fairly less structured in terms of their “colour”. For instance, at $s=0.4$, the multipole RDG isosurface changes “colour”, becoming positive in the central part of the S-C bond, whereas it keeps to be moderately negative along the whole C2-N6 bond, denoting that the interaction of H15A is of (higher) CH \cdots π character with C2 and N6 and of more localized HB character with S1 (and C2). This “colour” structure is lost in the corresponding ($s=0.4$) IAM-RDG isosurface.

* At the periodic *ab-initio* level the same result as for the multipole ED is obtained in this case (see section 2.5).

Due to its large van der Waals radius and relatively high polarizability, Sulphur may set up several interactions with its local crystalline environment (see e.g. Ref. [15,65]). Divalent S atoms may behave either as nucleophiles or electrophiles [15]. Figure 2.27 and 2.28 display examples of such interactions in terms of their RDG isosurfaces.

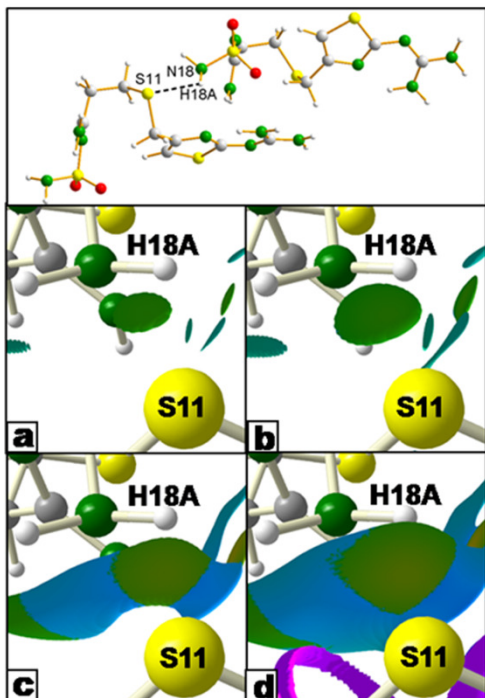


Figure 2.27 Famotidine, polymorph A: RDG-based NCI isosurfaces for the strongest intermolecular NH \cdots S interaction, using the multipole (middle row, panels a and b) and the IAM (bottom row, panels c and d) Electron Densities. The left panels refer to the $s=0.4$ and those on the right to the $s=0.6$ RDG isovalue. See Fig. 2.17 for the signed p color legend and Table 2.12 for the symmetry operations relating the labeled atoms. In the top panel, the structure of the studied molecular pair and the NH \cdots S interaction associated to the displayed RDG isosurfaces are shown.

In section 2.4.4 it was shown that on passing from weaker to stronger S \cdots H interactions, the shape of the RDG iso-surface changes from van der Waals-like (broad in space, with zones exhibiting both $\lambda_2 > 0$ and $\lambda_2 < 0$) to HB-like (disc-shaped, $\lambda_2 < 0$). We examine here (Figure 2.26) the RDG isosurfaces for the strongest XH \cdots S bond [N(18)H(18A) \cdots S(11)] in famotidine using the multipole (Figure 2.27 a-b) or the IAM ED (Figure 2.27 c-d). Both EDs find a BCP between the H and the S atoms. As due to the much higher ED value at BCP and similar density curvatures at the same point, the signed IAM RDG isosurfaces are broader, much less disc-shaped in their negatively “coloured” part and merged with the larger isosurface related to the overall interaction between the two molecules in the molecular pair. The NCI picture offered by the two EDs differs notably even when the comparison is favorably made between the RDG isosurface at lower s for the IAM and that at the higher s value for the multipole ED (Figure 2.27c vs 2.27b).

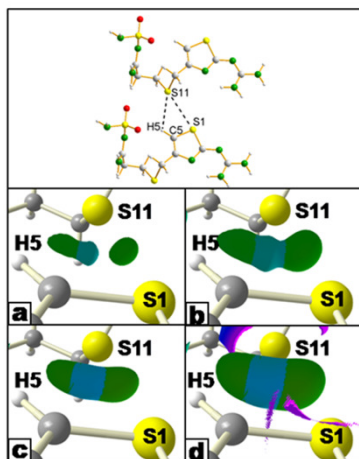


Figure 2.28. Famotidine, polymorph A: RDG-based NCI isosurfaces for the intermolecular C5H5...S and the S1...S11 interactions, using the multipole (middle row, panels a and b) and the IAM (bottom row, panels c and d) Electron Densities. The left panels refer to the $s=0.4$ and those on the right to the $s=0.6$ RDG isovalue. See Fig. 2.17 for the signed ρ color legend and Table 2.12 for the symmetry operations relating the labeled atoms. In the top panel, the structure of the studied molecular pair and the interactions associated to the displayed EDG isosurfaces are shown.

As for the multipole description of the polymorph A, S11 is linked through BP's with both H5 and S1, giving rise, at the higher s isovalue, to a unique, broad isosurface characterized by $\rho(r) \cdot \text{sign}(\lambda_2) \approx 0$ that contains the two BCP's and the RCP (Figure 2.28). This surface is moderately negative in the regions between the linked atoms where the S...H and the S...S contacts are likely to be attractive. At the lower s isovalue the NCI isosurface splits in two separate domains, one including the S11...S1 BCP and the other both the RCP and the H5...S1 BCP (as these two CP's have a similar and lower ED value than the S11...S1 BCP). At the IAM level, the H5...S BCP is missing and the RDG isosurface is already broad at $s=0.4$. It extends over the regions of the H5...S1 and S11...S1 contacts and has less structure but alternate "colors" as for the multipole ED.

2.6.7 CONCLUSIONS

The present work originates from a very important observation made by Johnson et al. [24] and Contreras-García et al. [38] in their seminal papers on the RDG-based NCI descriptor. Namely, that the IAM-ED is able, in principle, to recover at least the main NCI features that are unveiled using the corresponding aspherical (multipolar) molecular density. Were this true to a significant extent and for a variety of situations encompassing the diverse kind of NCI classes, it would naturally classify the proposed NCI descriptor as a very promising tool for the rationalization of such interactions in large molecules of biological interest.

In this study, a magnifying lens is used to observe and analyse in more detail the kind of information on the NCI that is lost and the one that is saved when the IAM ED replaces the "true" ED in the descriptor. In particular, it was done so for the case of the X-ray derived multipolar density and the corresponding IAM ED model.

By comparing the plots of the RDG vs the ED value for the two kinds of electron density in the benzene crystal, we could easily anticipate the main qualitative differences expected for the RDG isosurfaces relative to covalent and non covalent interactions, no matter they are intermolecular or intramolecular. In the case of the former, one awaits more contracted and less smooth isosurfaces using the IAM rather than the multipolar ED, while for the latter interactions exactly the opposite is expected to be true. Focusing the visual analysis only on the NCI isosurfaces, it was indeed found that those obtained from the IAM ED are invariably more extended in size, generally smoother and significantly less structured. This result appears as

a quite general outcome, because of the universal reasons underlying the sketched differences. Indeed, it holds true for all the three organic crystals considered in this work. More in detail, when NCI are considered, one awaits for $\nabla\rho/\rho$ to change more rapidly than $\nabla\rho_{\text{IAM}}/\rho_{\text{IAM}}$. Actually, these interactions have typically large closed-shell character, leading to a contraction of the density towards each of the interacting nuclei (hence increasing RDG for the “true” density), whereas $\nabla\rho$ is comparatively less affected and more alike in the two ED’s because the ED removal from the internuclear region (which would generally decrease also $\nabla\rho$) is partly paid off by the “true” density becoming there less smoothly distributed than the IAM ED. On the contrary, for covalent bonds one expects $\nabla\rho/\rho$ to change less rapidly than the $\nabla\rho_{\text{IAM}}/\rho_{\text{IAM}}$ ratio. In fact, electron density is being accumulated in the regions between nuclei for covalent bonding (hence decreasing RDG for the “true” density) whilst $\nabla\rho$ is comparatively less affected and more alike in the two ED’s, as the ED increase upon bonding (which would generally enhance also $\nabla\rho$) is partly compensated for by the density becoming more smoothly distributed in the bonding region.

Comparing the RDG associated to different ED’s also involves the delicate point of how to select the best isosurfaces for the least biased comparison. We made the choice to either use the same RDG isovalue or to adopt a suitable fixed value for each of the two ED’s so as to match as closely as possible their resulting RDG isosurfaces. Though a bit cumbersome, such procedure was indeed worth doing. It was generally found that the isosurfaces for the two EDs at a given isovalue differ more than the isosurfaces for the same ED at significantly different ($s = 0.4$ and 0.6) isovalues. This is an important result, because it alleviates the arbitrariness of the selection of a specific RDG isovalue when making comparison among isosurfaces derived from different EDs. Said in other words, it appears that there is not too much space to closely match two NCI isosurfaces (by selecting a specific isovalue for each surface), if the underlying ED’s is behaving in a significantly different manner in the molecular region of interest. Clearly, the need to select a different isovalue to get the best match, represents already a meaningful difference, and one whose origin (higher and lower ED value for covalent and non covalent interactions, respectively) has been adequately clarified by our investigation. We noticed that differences in the RDG isosurfaces may involve many different features, including global shape, size, colour(s), curvatures (convexity/concavity), etc. and whose combination results in the characteristic “structure” of the surface, with IAM-derived isosurfaces being generally less structured. As a valuable help to explore such differences, and when the isosurfaces correspond to RDG domains associated to more than one CP, one could find the RDG isovalue at which the (various) RDG domains become irreducible (*i.e.* when they start to contain only one CP in the ED). Comparing the isovalues at which the splitting into irreducible domains occurs and the shape of the resulting irreducible basins should provide a very unbiased way of confronting the RDG isosurfaces obtained from different ED’s. Such a detailed analysis was however delayed to a future work.

In section 2.4, it was explored in some detail to what extent the RDG-based NCI descriptor provides a complementary picture to that offered by QTAIM. In the context of the present work, it was possible to show, in few cases, that noticeable differences between the IAM and multipole derived RDG isosurfaces may be traced back to changes in the ED topology, in particular in the kind of pair of atoms linked by a bond path. Yet, a completely distinct BP description, as it is inherent to the “yes/no” language of the topological approach, usually translates in smoother and less clear-cut changes in the RDG isosurfaces, including change of colours in given regions and different preferential extensions of the surface (see for instance the case of the delocalized interaction between the H15 atom and the C2-N6 and S1-C2 bonds electron density distribution in famotidine).

In spite of the mentioned general differences between the IAM and multipolar isosurfaces, a one to one correspondence was generally found as for their capability of revealing the presence of a given NCI. However, the two resulting descriptions may be more or less alike depending on the nature of the

interaction. When van der Waals-like isosurfaces are considered, like for instance those relating facing molecules along the *c* axis in Austdiol, a close similarity is often observed. In such a case, the ED distribution of each of the interacting molecules, especially when their centres of mass are far apart in the crystal, 'sees' the atoms of the other as they were spherical. In other words, in the intermolecular region the deformation ($|\geq 1$) multipoles do not contribute significantly to the ED distribution, that is therefore reasonably approximated by the IAM description (provided the atoms have monopole populations close to the atomic ones). For stronger and more directed interactions like the HB's, the situation changes due to the increasing limitations of the IAM density in reproducing the correct ED curvatures as the strength of the H...Acceptor interaction increases. In turn, this may result in a reversed λ_2 sign. As a matter of fact, the IAM-isosurface size depends just on the interaction geometry, since it is essentially the latter that determines the ED distribution within a system made up by non-interacting atoms. Actually, the details of the electronic rearrangements accompanying the formation of HB's are lost in the IAM picture. Obviously, the NCI isosurfaces cannot overcome this simplification, even though they may be able to partly recover some of the lost ED features as second-order effects, at least if they significantly reflect into the corresponding packing geometries. For example, if the C-H... π interaction in benzene (Figure 2.17) is considered, a large RDG surface appears that encompasses the whole region above the 6-membered ring. The latter bears some analogy with the multipole-derived surface as the H2 atoms is nearly at the same distance with respect to the C atoms of the facing aromatic ring. However, it is significantly broader in space, almost flat, fairly less structured and exhibiting alternating regions of positive and negative λ_2 values. All the problems sketched above are expected to increase for the interactions involving significant ED rearrangement, as in this case the ED pictures provided by the multipole and IAM models necessarily diverge. Indeed, IAM-derived RDG iso-surfaces are not able to recover the relatively localized nature of the strongest S11...H18A interaction in famotidine, even though a somewhat attractive ($\rho(r)\text{-sign}(\lambda_2) < 0$) contribution appears just between facing S11 and H18A atoms.

At the multipolar level, stronger interactions are characterized by small, disc-shaped RDG domains, whereas weaker and weaker interactions are progressively denoted by broader, multiform RDG domains, and possibly including more than one critical point (at the RDG isovalues of 0.4-0.6 selected in this paper). This overall picture is less sharp and partly lost using the IAM ED's that are always broader and less structured. In particular, it may become difficult to assess the correct hierarchy among a series of related NCIs.

As a general conclusion, our results question the ability of the simpler IAM ED model to provide an accurate picture of the multifaceted NCI landscape in complex materials and biological polymers such as DNA fragments and proteins. As for the latter, we envisage that the use of multipolar density databanks, when carefully tuned to model the ED of the building blocks of biological systems [80], could provide an alternative and more viable route for applying the NCI descriptor also to this fascinating world.

2.7 'NCImilano' A CODE FOR THE STUDY OF NON-COVALENT INTERACTIONS BASED ON THE ELECTRON DENSITY

In this section, the code 'NCImilano' [33] will be presented. The latter is able to compute the NCI descriptor (presented in section 2.2) over a grid of points in the real space. In turn, the resulting grid files can be read in input by other freely available programs, such as VMD [81] or Molliso[82], to produce insightful 3D images. Another similar program ("NCI plot") was already introduced by Contreras-García et al. [38] and, in a later stage, incorporated into the code "critic"[83], that it is currently interfaced with various plane wave quantum mechanical codes. Our program should be attractive for the X-ray charge density community, as it can deal with gas-phase or solid-state ED's as evaluated by popular multipolar and Gaussian-based quantum mechanical computational platforms. More in detail, it can read grid files produced by XD2006[35], TOPOND [69] (that in turn is interfaced to CRYSTAL [68]), and GAUSSIAN 03/09 [84]. Moreover, 'NCImilano' is also able to calculate properties directly from the GAUSSIAN wavefunction file and to compute energy density grid files (see Section 2.7.1 below for a discussion about the use of this quantity).

The code is written in FORTRAN90 language. We provide different executable files for different operative systems (unix 32/64 bit, windows 32/64 bit). No machine libraries are required to run the program ('static' option of the compiler). To be run, the program requires files generated by XD2006, GAUSSIAN or TOPOND codes (see *infra*). A formatted ASCII input file containing specific instructions is also needed. We make available a template for this file, whereas specific details on how it should be filled in can be found in the manual.

The program is divided into three modules (Fig. 2.29). Each of them carries out a specific calculation. The first one ('properties from wavefunction') computes grid files in 'cube' format of several properties from the wavefunction file produced by GAUSSIAN. The second part ('topond to cube') converts the grid files written by TOPOND into the 'cube' format, to be read by the third part of the program. The last module ('RDG, $\rho \cdot \text{sign}(\lambda_2)$ and Abramov's energies') allows the user to calculate all the properties for the NCI investigation presented above (Section 2.7.3), except energy densities from the wavefunction, which are calculated in the first module (presented in section 2.7.1). Every time the program is run, it prints an output file which summarizes all the active commands, along with the values of the integrated properties over the volume enclosed by RDG isosurfaces (see Section 2.7.3). In the following paragraphs, the features of the three program modules are given.

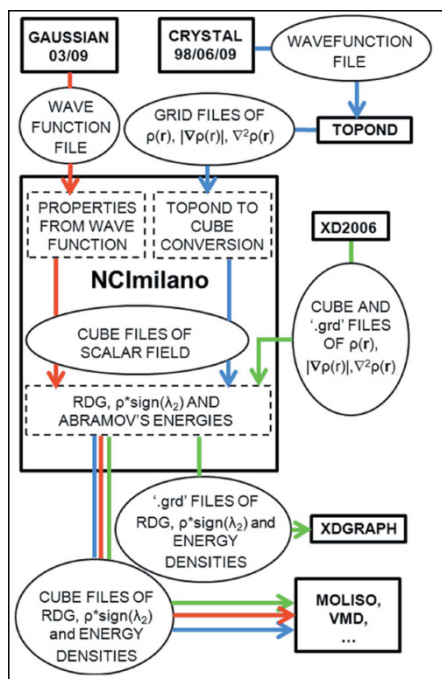


Figure 2.29 Flow chart illustrating the features of NCI milano. Solid squares are used to indicate programs, whereas dashed squares represent module or routines of a particular code. Circles correspond to files whose associated arrows indicate the program from which they are produced and the ones which read them as input.

2.7.1 PROPERTIES FROM THE WAVEFUNCTION

This module produces grid files in ‘cube’ format of various scalar fields from the gas-phase wavefunction file. The user is allowed to select the center of the grid, its dimensions and grid step, the latter two quantities defining the total number of grid points and the sampling accuracy. Output grid files are written in cube format. NCI milano requires just the formatted input file and the wavefunction. Although the present release of the code is able to read just the formatted ‘wfn’ file as provided by the GAUSSIAN program, the main computational routine is completely general. Therefore, our code can be easily implemented to deal with wavefunction files produced by every non-periodical quantum chemical code that uses Gaussian basis sets. As for the calculation of various molecular orbital contributions to specific properties at each point, the same strategy as implemented in the PROAIM [85] code has been employed.

The properties computable by this module are $\rho(\mathbf{r})$, $|\nabla\rho(\mathbf{r})|$, $\nabla^2\rho(\mathbf{r})$, the latter being the ED Laplacian [26], and the total Energy Density $H(\mathbf{r})$, together with its potential ($V(\mathbf{r})$) and kinetic ($G(\mathbf{r})$) contributions. The possibility of calculating energy densities has been introduced with the aim of using them as a quantity to be mapped onto RDG isosurfaces. In the original recipe of the RDG-based NCI descriptor, the signed $\rho(\mathbf{r})$ was mapped onto low-RDG isosurfaces. However, other choices of the scalar field to be plotted onto the RDG surfaces are obviously possible. We propose here to use the Energy Density. First and foremost, it is a quantum-mechanical well-rooted quantity, as its integration over the whole space gives the electronic energy of the system. Furthermore, it avoids a distinction between ‘attractive’ and ‘repulsive’ interactions, which is always arbitrary [31]. Finally, the possibility of partitioning the total energy into potential and kinetic contributions helps in distinguishing more neatly the specific nature of different NCI, and to study how a given type of NCI is influenced by different chemical or crystalline environments.

We made available in the program the possibility of calculating energy densities from the gas phase wavefunction. When the wavefunction is not available, such as in the case of experimentally-driven ED’s, the code uses the approximate functional introduced by Abramov [86] (see section 2.7.3) to provide an estimation of the kinetic energy density in the low-ED regions of the unit cell. An example of energy density mapped onto RDG isosurfaces is reported in Fig. 2.30. It can be seen how the decomposition into kinetic

and potential contributions allows to characterize different C-H...C contacts in solid benzene, one of which is associated to a CH... π interaction (these interactions were already extensively discussed in sections 2.4.3, 2.5.3 and 2.6.4). In general, when the corresponding RDG isosurfaces are considered, the total energy density, $H(\mathbf{r})$, is positive and close to zero (Fig. 2.30a). Nevertheless, the smaller isosurface (fig. 2.30b, 2.30c), displays higher $G(\mathbf{r})$ and $|V(\mathbf{r})|$ contributions than the larger one, emphasizing the different nature and localization extent of the two interactions. A more detailed investigation about the use of energy density as a quantity to be mapped onto RDG isosurfaces will be performed in the future.

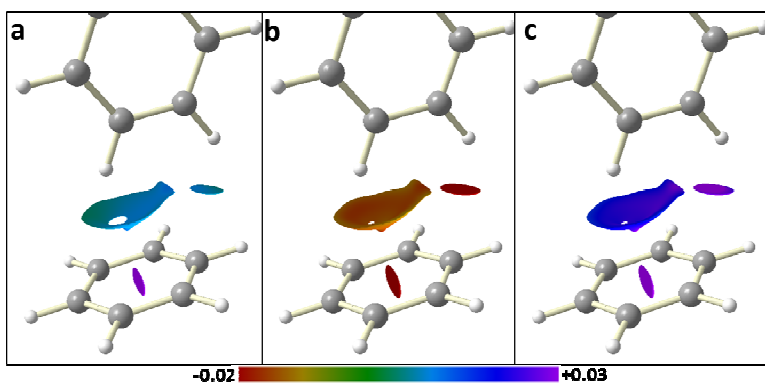


Figure 2.30 0.6 RDG isosurfaces with energy densities mapped onto them for a molecular pair of benzene molecular crystal. a) total energy density b) kinetic energy density c) potential energy density. The color scale for Energy density [au] is shown below the picture

According with other popular codes for the ED topological analysis [69,85,87], we compute $G(\mathbf{r})$ as:

$$G(\mathbf{r}) = \frac{1}{2} \sum_{i=1}^N \alpha_i |\nabla \varphi_i(\mathbf{r})|^2 \quad \text{eq. 2.11}$$

φ_i being the i -th Natural Orbitals and α_i its occupation number. The potential energy density is calculated through the virial theorem in its local form [26](eq. 2.12):

$$V(\mathbf{r}) = \frac{1}{4} \nabla^2 \rho(\mathbf{r}) - 2G(\mathbf{r}) \quad \text{eq. 2.12}$$

Eventually, the total energy density is obtained by summing the potential and kinetic terms.

2.7.2 TOPOND TO CUBE CONVERSION

This section is designed to convert grid files calculated from TOPOND into the standard cube format, to be used as input to the third module of the code (seeSection 2.7.3).TOPOND reads the periodical wavefunction printed by CRYSTAL and calculates several topological properties from the ED-derived scalar and vector fields [69]. In particular, TOPOND can write two and three dimensional grid files of $\rho(\mathbf{r})$, $|\nabla \rho(\mathbf{r})|$ and $\nabla^2 \rho(\mathbf{r})$. Due to translational and point symmetry invariance relationships, in a crystal there are several possible valid choices of atoms defining the asymmetric unit. In other words, there is not an unequivocal set of atomic coordinates to be written in the TOPOND grid files. Therefore, the latter do not contain any information on atomic positions and NCImilano reads the atomic coordinates of the asymmetric unit from the regular ASCII CRYSTAL output file. Then, the user can decide which and how many asymmetric units will be written into the cube file by specifying the corresponding symmetry operations in the main input file.

Note that this choice determines which atoms can be visualized when RDG isosurfaces will be plotted by a suitable program.

2.7.3 RDG, $\rho \cdot \text{sign}(\lambda_2)$ AND ABRAMOV'S ENERGIES

In this module, the quantities RDG, $\rho(\mathbf{r})\text{sign}(\lambda_2)$ and energy density calculated using Abramov's functional [86] (hereinafter "Abramov's energies") are evaluated starting from existing grid files of $\rho(\mathbf{r})$, $|\nabla\rho(\mathbf{r})|$ and $\nabla^2\rho(\mathbf{r})$.

Actually $|\nabla\rho(\mathbf{r})|$ and $\nabla^2\rho(\mathbf{r})$, can be computed by our code using the 'central difference method', [88] (equations 2.13a and 2.13b), with all variables being defined as double-precision reals:

$$f'(x) = \frac{-f(x+2h)+8f(x+h)-8f(x-h)+f(x-2h)}{12h} \quad \text{eq. 2.13a}$$

$$f''(x) = \frac{-f(x+2h)+16f(x+h)-30f(x)+16f(x-h)-f(x-2h)}{12h^2} \quad \text{eq. 2.13b}$$

where h is the grid step. The same numerical recipe is also used to calculate the ED Hessian matrix from which eigenvalues are obtained, included λ_2 . Such a method has been tested [89] for ED derivatives of several systems: it has been reported a practically non-existent error for first and pure second derivatives using a 0.005 a.u. grid step when double precision variables are used (as in our code). However, since both 2.13a and 2.13b require the evaluation of the function at two neighboring points, the ED Hessian matrix cannot be calculated at the grid boundary. Therefore, the program sets to zero the Hessian-related quantities at the grid border. This choice avoids singularities and at the same time does not affect the accuracy of the computed quantities within the space enclosed by the isosurface.

RDG can be calculated at all the points of the input grids through equation 2.3. Since RDG is low for both covalent and non-covalent interactions, the user can define an ED range to single out just NCI [24]. A similar cutoff can be applied to $\rho(\mathbf{r})\text{sign}(\lambda_2)$, so that only certain kind of interactions are investigated. For example, by considering just negative signed ED values, non-bonded contacts are excluded [24]. In addition, a spatial cutoff can be applied to keep some regions out from the analysis. In all the points outside the ED or spatial ranges defined by the user, the RDG is set to an arbitrarily large value (10^{10}), so that they are excluded from the computation of any reasonable isosurface.

Regarding the evaluation of the kinetic energy density, when the system wavefunction is not available (as in the case of experimental ED studies), equation 2.11 cannot be employed. Anyhow, according to Abramov [86], an approximate expression for directly computing $G(\mathbf{r})$ from ED distributions is:

$$G(\mathbf{r}) = \frac{3}{10} (3\pi^2)^{\frac{2}{3}} \rho(\mathbf{r})^{5/3} + \frac{(\nabla\rho(\mathbf{r}))^2}{72\rho(\mathbf{r})} + \frac{1}{6} \nabla^2\rho(\mathbf{r}) \quad \text{eq. 2.14}$$

Once $G(\mathbf{r})$ is available, potential and total energy densities can be obtained as reported in Section 2.7.1 above. It should be stressed that such an approximation is acceptable, in terms of accuracy[90], just when $\rho(\mathbf{r})$ is quite low, *i.e.* it is not suitable to compute $G(\mathbf{r})$ in regions of space where covalent interactions are significant. Nevertheless, as NCI necessarily dominate the low-ED regions, this approach should in our case be reliable enough.

It should be noted that it is also possible, in principle, to implement the calculation of RDG, $\rho(\mathbf{r})\text{sign}(\lambda_2)$ and Abramov's energies directly from wavefunction or multipolar parameter files. However, the choice of calculating these quantities from grid files has the advantage of providing an interface with all the codes

able to deal with theoretical and experimental ED's. At the moment, allowed input formats are 'cube' and XD2006 / TOPOND grid files, but other formats can be straightforwardly implemented as well. In particular, when XD2006 'grd' grid files are read in, the program outputs grids in both 'cube' and 'grd' formats. The latter can be given as input to XDGRAPH, the graphical routine of the XD program package, to easily build two and three dimensional plots of the quantity that is being studied. Moreover, this format choice allows one to directly apply the RDG-based NCI descriptor to promolecular ED distributions, if desired, as the corresponding grid files can be obtained from both XD2006 and CRYSTAL (through the code TOPOND). Eventually, as entries in cube files are written with six digits, the truncation error on input quantities is negligible. Last but not least, calculations in double precision guarantee that the truncation error on the calculated quantities is also negligible.

The program also prints the volume of RDG isosurfaces and the integrated value of ED, $\rho(r)\text{sign}(\lambda_2)$ and Abramov energies over regions of space enclosed by 10 specific RDG isovalues. The latter range from 0.1 to 1.0, at steps of 0.1, as RDG values considered to build isosurfaces in NCI studies are usually comprised between 0.3 and 0.7. Moreover, it is possible to print a file where (signed) ED and RDG are evaluated at every point in the input grid file. In this way, it is possible to build RDG vs (signed) ED plots as those shown, in paragraph 2.4 and 2.5.

REFERENCES

- [1] J. D. van der Waals (1873) *Ph.D. Thesis*, University of Leiden, Netherlands
- [2] J. Cerný, P. Hobza. *Phys. Chem. Chem. Phys.* (2007) 9, 5291
- [3] a) G. R. Desiraju (1989) *Crystal Engineering, The Design of Organic Solids*. Amsterdam: Elsevier b) A. Gavezzotti (2007). *Molecular Aggregation. Structure Analysis and Molecular Simulation of Crystals and Liquids*. Oxford: Oxford University Press
- [4] a) M. R. Caira *Topics in Current Chemistry; Design of Organic Solids* (1998) 198, 163-208 b) L. Lo Presti, R. Soave, M. Longhi, E. Ortoleva. *Acta Cryst.*(2010) B66, 527
- [5] A. Gavezzotti, G. Filippini. *J. Am. Chem. Soc.* (2005) 117, 12299
- [6] C.-A. Palma, M. Cecchini, P. Samorì. *Chem. Soc. Rev.* (2012) 41, 3713.
- [7] A. J. Stone (2002) *The Theory of Intermolecular Forces*, Oxford University Press, Oxford.
- [8] E. Arunan, G. R. Desiraju, R. A. Klein, J. Sadlej, S. Scheiner, I. Alkorta, D. C. Clary, R. H. Crabtree, J. J. Dannenberg, P. Hobza, H. G. Kjaergaard, A. C. Legon, B. Mennucci, D. J. Nesbitt. *Pure Appl. Chem.* (2011) 83, 1637
- [9] V. Bertolasi, P. Gilli, V. Ferretti and G. Gilli. *Acta Cryst.* (1998). B54, 50
- [10] J. J. Novoa, F. Mota. *Chemical Physics Letters* (2000) 318, 345
- [11] S. Tsuzuki, A. Fujii. *Phys. Chem. Chem. Phys.*(2008) 10, 2584
- [12] F. A. Quirocho, N. K. Vyas. *Nature*(1984) 310, 381
- [13] T. E. Clark, M. Makha, A. N. Sobolev, S. J. Dalgarno, J. L. Atwood and C. L. Raston. *Cryst. Growth Des.*(2007) 7, 2059
- [14] IUPAC. *Compendium of Chemical Terminology*, 2nd ed. (the "Gold Book"). Compiled by A. D. McNaught and A. Wilkinson. Blackwell Scientific Publications, Oxford (1997). XML on-line corrected version: <http://goldbook.iupac.org> (2006-) created by M. Nic, J. Jirat, B. Kosata; updates compiled by A. Jenkins. ISBN 0-9678550-9-8. doi:10.1351/goldbook
- [15] R. E. Rosenfield Jr, R. Parthasarathy, J. D. Dunitz. *J. Am. Chem. Soc.* (1977) 99, 4860-4862
- [16] P. Politzer, J. S. Murray, T. Clark. *Physical Chemistry Chemical Physics* (2013), 15(27), 11178-11189
- [17] M. Brookhart; M. L. H. Green, G. Parkin. *Proceedings of the National Academy of Sciences of the United States of America* (2007), 104(17), 6908-6914
- [18] P. Hobza. *Phys. Chem. Chem. Phys.*(2008) 10, 2581-2583
- [19] K. Müller-Dethlefs, M. Sander and E. W. Schlag. *Z. Naturforsch.* (1984) 39a, 1089
- [20] D. A. Beattie, R. J. Donovan. *Prog. React. Kin.*(1998) 23, 281
- [21] see, for example: S. J. Grimme. *Comput. Chem.* 2006, 27, 1787
- [22] R. Sedlak, T. Janowski, M. Pitonak, J. Rezac, P. Pulay, P. Hobza. *J. Chem. Theory Comput.*(2013) 9(8), 3364
- [23] M. A. Spackman, J. McKinnon, D. Jayatilaka. *CrystEngComm* (2008) 10, 377

-
- [24] E. R. Johnson, S. Keinan, P. Mori-Sanchez, J. Contreras-Garcia, A. J. Cohen, W. Yang, *J. Am. Chem. Soc.* (2010) 132, 6498
- [25] G. Saleh, C. Gatti, L. Lo Presti, J. Contreras-Garcia. *Chem. Eur. J.* (2012) 18, 15523
- [26] R. F. W. Bader (1990) *Atoms In Molecules: A Quantum Theory* Oxford: Clarendon Press
- [27] G. Saleh, C. Gatti, L. Lo Presti. *Comput. Theor. Chem.* (2012) 998,148
- [28] W. Koch, M. C. Holthausen (2001) *A Chemist's Guide to Density Functional Theory. Second Edition* WILEY-VCH Verlag GmbH, D-69469 Weinheim (Federal Republic of Germany)
- [29] a) A. Zupan, J. P. Perdew, K. Burke, M. Causà. *Int. J. Quantum Chem.* (1997) 61, 835-845 b) A. Zupan, K. Burke, M. Ernzerhof, J. P. Perdew. *J. Chem. Phys.* (1997) 106, 10184
- [30] C. Gatti. *Zeitschrift für Kristallographie* (2005) 220, 399-457
- [31] R. F. W. Bader. *Chem. Eur. J.* (2006) 12, 2896
- [32] T. Ziegler, A. Rauk. *Theor. Chim. Acta* (1977) 46, 1.
- [33] G. Saleh, L. Lo Presti, C. Gatti, D. Ceresoli. *J. Appl. Cryst.* (2013) Accepted
- [34] N. K. Hansen, P. Coppens. *Acta Cryst.* (1978) A34, 909-921
- [35] A. Volkov, P. Macchi, L. J. Farrugia, C. Gatti, P. Mallinson, T. Richter, T. Koritsanszky, XD2006 - A Computer Program Package for Multipole Refinement, Topological Analysis of Charge Densities and Evaluation of Intermolecular Energies from Experimental and Theoretical Structure Factors, 2006. See also <http://xd.chem.buffalo.edu/>
- [36] A. D. Becke, *J. Chem. Phys.* 1993, 98, 5648-5652
- [37] R. Krishnan, J. S. Binkley, R. Seeger, J. A. Pople, *J. Chem. Phys.* 1980, 72, 650-654
- [38] J. Contreras-Garcia, E.R. Johnson, S. Keinan, R. Chaudret, J-P. Piquemal, D.N. Beratan, W. Yang, *J. Chemical Theory and Computation* (2011) 7, 625
- [39] Giacovazzo, C., Monaco, H. L., Artioli, G., Viterbo, D., Ferraris, G., Gilli, G., Zanotti, G., Catti, M. (2002) *Foundamentals of Crystallography. Second Edition*. Edited by C. Giacovazzo. New York: Oxford University Press
- [40] L. Lo Presti, R. Soave, R. Destro. *J. Phys. Chem B* (2006) 110, 6405
- [41] H.-S. Bürgi, S. C. Capelli, A.E. Goeta, J. A. K. Howard, M.A. Spackman, D.S. Yufit. *Chem. Eur. J.* (2002) 8, 3512
- [42] J. Overgaard, D. E. Hibbs. *Acta Cryst.* (2004) A60, 480
- [43] Diamond 3.2h, Copyright (c) 1997-2012 Crystal Impact GbR, Bonn Germany, by Klaus Brandenburg.
- [44] G. R. Desiraju, A. Gavezzotti *Acta Crystallogr.* (1989) B45, 473
- [45] F. H. Allen, O. Kennard, D. G. Watson, L. Brammer, A. G. Orpen, R. J. Taylor. *Chem. Soc. Perkin Trans. II* (1987) S1
- [46] A. Ø. Madsen. *J. Appl. Cryst.* (2006) 39, 757
- [47] P. Munshi, A. Ø. Madsen, M. A. Spackman, S. Larsen, R. Destro. *Acta Cryst. Sect. A* (2008) 64, 465
- [48] D. E. Hibbs, C. J. Austin-Woods, J. A. Platts, J. Overgaard, P. Turner. *Chem. Eur. J.* (2003) 9, 1075

-
- [49] F. L. Hirshfeld. *Acta Cryst. Sect. B* (1971) 27, 769
- [50] U. Koch, P. L. A. Popelier. *J. Phys. Chem.* (1995) 99, 9747
- [51] J. F. Dobson, K. McLennan, A. Rubio, J. Wang, T. Gould, H. M. Lee, B. P. Dinte. *Aust. J. Chem.* (2001) 54, 513.
- [52] L. Lo Presti, R. Soave, M. Longhi, E. Ortoleva, *Acta Crystallogr. Sect. B* (2010) 66, 527.
- [53] L. Lo Presti, A. Ellern, R. Destro, B. Lunelli. *J. Phys. Chem. A* (2009) 113, 3186.
- [54] B. Civalleri, C. M. Zicovich-Wilson, L. Valenzano, P. Ugliengo. *CrystEngComm* (2008) 10, 405-410.
- [55] D. S. Sholl, J. A. Steckel (2008) *Density Functional Theory: A Practical Introduction*, John Wiley & Sons, Inc., Hoboken, New Jersey, USA, pag. 29.
- [56] See ref. 3b, Chapt. 12, and references therein.
- [57] M. J. Allen, D. Tozer. *Journal of Chem. Phys.* (2002) 117, 11113.
- [58] R. F. W. Bader. *J. Phys. Chem. A* (2009) 113, 10391.
- [59] R. F. W. Bader. *J. Phys. Chem. A* (2010) 114, 7431.
- [60] M. Nishio. *Phys. Chem. Chem. Phys.* (2011) 13, 13873.
- [61] C. Gatti, *Structure & Bonding* (2012) 147, 193.
- [62] B. Hegedus, P. Bod, K. Harsanyi, I. Peter, A. Kalman, L. Parkanyi, *Journal of Pharmaceutical and Biomedical Analysis* (1989) 7, 563.
- [63] G. Gilli, P. Gilli, *J. Mol. Struct.* (2000) 552, 1.
- [64] a) A. Savin, B. Silvi, F. Colonna, *Can. J. Chem.* (1996) 74, 1088. b) M. Catalayud, J. Andrés, A. Beltrán, B. Silvi, *Theor. Chem. Acc.* (2001) 105, 299.
- [65] R. Destro, R. Soave, M. Barzaghi, L. Lo Presti, *Chem. Eur. J.* (2005) 11, 4621.
- [66] T. A., Keith, R. F. W. Bader, Y. Aray, *Int. J. Quant. Chem.* (1996) 57, 183.
- [67] A. M. Pendas, E. Francisco, M. A. Blanco, C. Gatti. *Chem. Eur. J.* (2007) 13, 9362.
- [68] R. Dovesi, V. R. Saunders, C. Roetti, R. Orlando, C. M. Zicovich-Wilson, F. Pascale, B. Civalleri, K. Doll, N. M. Harrison, I. J. Bush, P. D'Arco, M. Llunell, *CRYSTAL06 User's Manual*, University of Torino, Torino, Italy, 2006
- [69] C. Gatti, *TOPOND98: an electron density topological program for system periodic in N (N=0-3) dimensions*, User's Manual, CNR-ISTM, Milano, Italy, 1999
- [70] M. A. Spackman. *Chemical Physics Letters* (1999) 301, 425.
- [71] C. Gatti, E. May, R. Destro, F. Cargnoni. *J. Phys. Chem. A* (2002) 106, 2707.
- [72] R. F. Nalewajski (2012) *Electron Density as Carrier of Information*, in: R. F. Nalewajski (Ed.), *Perspectives in Electronic Structure Theory*, Springer, Dordrecht-Heidelberg-London- New York, pp. 415-452.
- [73] R. F. Nalewajski, E. Świtka. *Phys. Chem. Chem. Phys.* (2002) 4, 4952.
- [74] R. F. Nalewajski, E. Świtka, A. Michalak. *Int. J. Quantum Chem.* (2002) 87, 198.
- [75] S. Kullback, R. A. Leibler. (1951) 22, 79.

-
- [76] R.F. Nalewajski, E. Broniatowska. *J. Phys. Chem. A* (2003) 107, 6270.
- [77] C.E. Shannon (1948) *A mathematical theory of communication*, Bell System Tech J 27 379-423 and 623-656.
- [78] M. Hô, V.H. Smith, D.F. Weaver, C. Gatti, R.P. Sagar, R.O. Esquivel. *J. Chem. Phys.* (1998) 108, 5469.
- [79] R. Ponc, C. Gatti. *Inorg. Chem.* (2009) 48, 11024.
- [80] C. Jelsch, S. Domagała, B. Guillot, D. Liebschner, B. Fournier, V. Pichon-Pesme, C. Lecomte, *Frontier Applications of Experimental Charge Density and Electrostatics to Bio-macromolecules*, in: C. Gatti and P. Macchi (Eds.), *Modern Charge Density Analysis*, Springer, Dordrecht-Heidelberg-London- New York, 2012, pp. 527-552.
- [81] Humphrey, W., Dalke, A. & Schulten, K. *Journal of Molecular Graphics* (1996) 14, 33.
- [82] Hübschle, C. B. & Luger, P. *J. Appl. Crystallogr.* (2006) 39, 901.
- [83] A. Otero-de-la-Roza, E. R. Johnson, J. Contreras-García. *J. Phys. Chem. Chem. Phys.* (2012) 14, 12165.
- [84] Frisch, M. J., Trucks, G. W., Schlegel, H. B., Scuseria, G. E., Robb, M. A., Cheeseman, J. R., Scalmani, G., Barone, V., Mennucci, B., Petersson, G. A., Nakatsuji, H., Caricato, M., Li, X., Hratchian, H. P., Izmaylov, A. F., Bloino, J., Zheng, G., Sonnenberg, J. L., Hada, M., Ehara, M., Toyota, K., Fukuda, R., Hasegawa, J., Ishida, M., Nakajima, T., Honda, Y., Kitao, O., Nakai, H., Vreven, T., Montgomery, J. A. Jr, Peralta, J. E., Ogliaro, F., Bearpark, M., Heyd, J. J., Brothers, E., Kudin, K. N., Staroverov, V. N., Kobayashi, R., Normand, J., Raghavachari, K., Rendell, A., Burant, J. C., Iyengar, S. S., Tomasi, J., Cossi, M., Rega, N., Millam, J. M., Klene, M., Knox, J. E., Cross, J. B., Bakken, V., Adamo, C., Jaramillo, J., Gomperts, R., Stratmann, R. E., Yazyev, O., Austin, A. J., Cammi, R., Pomelli, C., Ochterski, J. W., Martin, R. L., Morokuma, K., Zakrzewski, V. G., Voth, G. A., Salvador, P., Dannenberg, J. J., Dapprich, S., Daniels, A. D., Farkas, Ö., Foresman, J. B., Ortiz, J. V., Cioslowski, J. & Fox, D.J. (2009). Gaussian 09, Revision A.1 Gaussian, Inc., Wallingford CT, 2009
- [85] F. W. Biegler-König, R. F. W. Bader, T.-H. Tang. *J. Comput. Chem.* (1982) 3, 317; AIMPAC download page: <http://www.chemistry.mcmaster.ca/aimpac/imagemap/imagemap.htm>
- [86] Y. A. Abramov. *Acta Cryst.* (1997) A53, 264.
- [87] Barzaghi, M. (2002) *PAMoC (Version 2002.0)*, Online User's Manual CNR-ISTM, Institute of Molecular Science and Technologies. Milano, Italy; <http://www.istm.cnr.it/pamoc/>
- [88] C.F. Gerald, P. O. Wheatley (1989). *Applied Numerical Analysis*. Reading, MA: Addison-Wesley
- [89] A. Volkov, C. Gatti, Y. Abramov, P. Coppens. *Acta Cryst.* (2000) A56, 252.
- [90] O. Galvez, P. C. Gomez, L. F. Pacios. *Chem. Phys. Lett.* (2001) 337, 263.

Chapter III: Using the Source Function to detect electron delocalization effects

3.1 INTRODUCTION

In the previous chapter the issue of using experimentally-derived ED to investigate a fundamental chemical paradigm such as the non-covalent interactions was discussed. In this chapter, we will face the topic of whether ED distribution is able to give a description of another cornerstone of chemistry: the electron delocalization.

According to the Union of Pure and Applied Chemistry (IUPAC), the concept of ‘electron delocalization’ in theoretical organic chemistry indicates a “redistribution of the valence shell electron density throughout a molecular entity as compared to some localized models (individual atoms in their valence states, separated bonds or fragments)” [1]. However, this definition is obviously not free of controversies. In particular, it makes explicit reference to a model, hence the arbitrariness in the choice of the model unavoidably makes the definition rather ambiguous. Thus, as well as many other paradigms of chemistry, the concept of ‘electron delocalization’ (and the consequent antonym: ‘electron localization’), on the one hand cannot be uniquely defined but, on the other hand, it is essential for the description of many chemical phenomena. Among the latter, concepts on which chemistry itself was built, such as covalent bonds, electron pairs, aromaticity (see *infra*) etc. are intimately related to electron localization/delocalization. Generally speaking, electron delocalization is not an observable (in the quantum mechanical sense) but its consequences are. In other words, the presence of electron delocalization cannot be directly measured, but it reveals itself in several chemical phenomena which can be detected experimentally. Indeed, magnetic properties of the molecules, such as the NMR chemical shift of protons [2], are routinely exploited to detect electron delocalization in π -conjugated systems. There exist also several other experimental techniques which can be used to investigate electron delocalization, *e.g.* magnetic coupling constant [3,4,5,6] and the Fermi contact term [7,8,9]. Moreover, indications of electron delocalization are sometimes obtained also from experimental outcomes of routinely employed analytical techniques such as high-energy UV and Raman spectra [10,11,12]. Last but not least, electron delocalization (and especially aromaticity) imply a modification of bond lengths and therefore every experimental technique which can lead to the determination of the molecular structure is able to give important hints related to the presence of electron delocalization in certain situations. From the energetic point of view, instead, a quantitative measure of the enthalpy change associated to electron delocalization phenomena is obtained from the evaluation of heats of hydrogenation of aromatic compounds [13]. The latter, process, indeed, is exothermic for isolated double bonds, while when conjugation is present, the process becomes less energetically favorable (even endothermic when aromaticity pattern is broken, as in the reaction benzene \rightarrow cyclohexadiene) [13].

From a theoretical point of view, the very fact that electron delocalization is not an observable brings two important consequences. On the one hand, it means that there are no experimental techniques which can directly measure the electron delocalization and because of that theoretical investigations are without any doubts necessary for the study of this phenomenon. On the other hand, the lack of experimental counterpart makes it impossible to find a unique, universally accepted recipe to measure electron delocalization. For this very reason, a plethora of theoretical approaches have been developed to investigate this phenomenon. A quick overview of the most important theoretical approaches which are usually employed to describe electron delocalization will be given in section 3.1.1, while in section 3.1.2 the attempts made so far to use ED distribution to detect electron delocalization will be briefly reviewed.

3.1.1 ELECTRON LOCALIZATION/DELOCALIZATION FROM THE WAVEFUNCTION

Within the framework of Molecular Orbitals (MOs) approach, there exist several techniques based on transformation of the so-called 'canonical orbitals' in order to obtain 'chemically meaningful' orbitals. In particular, the latter are obtained by applying to the natural orbitals a unitary transformation, that is a transformation which allows to pass from one MO representation to another without altering the property of the wavefunction, including the ED distribution and the total energy. When applying this kind of techniques to investigate electron delocalization, one usually aims at obtaining a localized set of MO which should, in principle, be localized in those regions of space associate to atomic cores, bonding electron pairs (*i.e.* electrons associated to chemical bonds) and lone pairs [14,15,16]. However, it often happens that the localization process is not perfect and several localized MOs still occupy common region of molecular space [17]. Among the techniques which exploit MO transformations to obtain chemically meaningful orbitals, the one which is probably the most largely exploited nowadays is the so-called Natural Bond Orbital (NBO) approach [18,19]. The philosophy behind NBO is somewhat different from the techniques described above, as it is based, rather than on unitary transformation, on a process of mixing of occupied and virtual orbitals to obtain the NBOs. Although this technique has been successfully used to investigate electron delocalization and aromaticity [20,21], it must be pointed out that the energy obtained from the occupied NBO is often lower than the energy of the wavefunction from which NBOs were obtained, and mixing between occupied and virtual NBO space has to be carried out in order to recover the correct total energy. Because of this, the chemical picture obtained using NBO has been object of controversies in several cases (*e.g.* about the origin of rotation barrier in ethane [22]).

Besides the methods based on MOs, it is worth mentioning that also wavefunctions obtained through Valence Bond approach have been used to describe electron localization/delocalization by investigating the weights of the most relevant resonance structures [23].

The study of electron localization/delocalization can be also carried out independently from the method from which the wavefunction is obtained, and several approaches exist for this purpose. Being independent from the method used to obtain the wavefunction, this class of methods is expected to pinpoint the physical origin of the chemical phenomena under investigation. One of the oldest method to localize electrons in a given region of space is the so-called loge theory [24,25]. Within this approach, the real space is divided into regions (loges) where there is a maximum probability of finding a given number of electrons. Furthermore, the whole (molecular) space can be divided into best-loges, the latter being the ones which give the most probable division of space into regions containing a given integer numbers electrons. Such real-space partitioning is obtained by minimizing the so-called missing information function [24,25]. Although the loge theory is quite old, the idea of partitioning the space into regions which has a maximum probability of finding integer number of electrons has not yet been abandoned, as testified by recently developed theories following this very idea [26].

The methods exploiting the pair density (eq. 3.2) are nowadays the most commonly employed theoretical approaches to investigate electron delocalization. The reason behind this is that the definition of electron delocalization is inherently tied to the concept of electron pairing (originally introduced in the popular model of Lewis [27]), which is in turn embodied in the pair density. Indeed, this function contains all the information on the correlated motion of a pair of electrons, as due to Fermi (exchange) and Coulomb correlation (see *infra*). In the following, a definition of pair density will be given and the close relationship between the pair density and the delocalization extent of electrons will be explained through the concept

of Fermi hole [28]. The latter is an important quantity related to the pair density and extensively used to study electron delocalization.

The (spinless) second order density matrix is by definition obtained from the integration of the wavefunction, through the following expression:

$$P_2(\mathbf{r}'_1, \mathbf{r}'_2; \mathbf{r}_1, \mathbf{r}_2) = \frac{N(N-1)}{2} \int \psi^*(\mathbf{r}'_1, \mathbf{r}'_2, \dots, \mathbf{r}'_N) \psi(\mathbf{r}_1, \mathbf{r}_2, \dots, \mathbf{r}_N) d\mathbf{r}_3 d\mathbf{r}_4 d\mathbf{r}'_3 d\mathbf{r}'_4 \dots d\mathbf{r}_N d\mathbf{r}'_N \quad \text{Eq. 3.1}$$

By taking the diagonal elements of the second order density matrix, one obtains the pair density:

$$P_2(\mathbf{r}_1, \mathbf{r}_2) = P_2(\mathbf{r}_1, \mathbf{r}_2; \mathbf{r}_1, \mathbf{r}_2) \quad \text{Eq. 3.2}$$

$P_2(\mathbf{r}_1, \mathbf{r}_2)$ represents the probability of finding two electrons simultaneously located at \mathbf{r}_1 and \mathbf{r}_2 . The pair density can be conveniently split in two terms:

$$P_2(\mathbf{r}_1, \mathbf{r}_2) = \frac{1}{2} [\rho(\mathbf{r}_1)\rho(\mathbf{r}_2) + \Gamma_{XC}(\mathbf{r}_1, \mathbf{r}_2)] \quad \text{Eq. 3.3}$$

The first part represents the pair density one would obtain if the positions of the various electrons were independent from each other. Note the parallelism with probability theory: this term represents the probability of having two events whose outcomes are not correlated, *i.e.* the final probability is simply the product of the probabilities of the two events. The term Γ_{XC} , *i.e.* the so-called exchange-correlation density, incorporates the non-classical effects due to electron correlation and it represents the decreasing of the pair density with respect to the first term of equation 3.3 due to the correlated motion of electrons. Indeed, Γ_{XC} can be seen as a measure of the degree to which density is excluded at \mathbf{r}_1 because of the presence of an electron at \mathbf{r}_2 . In fact, the latter concept is usually defined by considering the Fermi Hole [28]:

$$h_{r_2}(\mathbf{r}_1) = \rho(\mathbf{r}_1) - \frac{2P_2(\mathbf{r}_1, \mathbf{r}_2)}{\rho(\mathbf{r}_2)} \quad \text{Eq. 3.4}$$

where $h_{r_2}(\mathbf{r}_1)$ is the Fermi hole. The latter is a non-positive quantity and it highlights, for single-determinant methods*, those regions of space where there is a decrease of ED caused by the Pauli repulsion between ED at \mathbf{r}_1 and the reference electron at \mathbf{r}_2 . From eqs. 3.3 and 3.4 one can immediately see how the Fermi hole is closely related to the exchange correlation-density: when the former goes to zero, so does the latter. With respect to Γ_{XC} , Fermi hole has the advantage of being defined in real space, therefore allowing an easy-to-catch investigation of electron localization/delocalization. As nicely illustrated by Bader *et al.* [29], the charge of an electron is spread out in a manner described by its Fermi hole and, as a consequence, the localization of Fermi hole in a particular region of space is a necessary and sufficient condition for an electron to be localized in such region. In other word, when the Fermi hole of an electron is delocalized over a certain region of space, so is the electron itself. This concept can be nicely illustrated by using the words of Bader *et al.*: "The Fermi hole is an electron's doppelgänger- it goes where the electron goes and vice-versa" [29]

* For explicitly correlated wavefunctions, eq. 3.3 include also the effect of Coulomb repulsion, which is the electron correlation between electrons of opposite spin. Coulomb correlation is completely neglected in the Hartee-Fock method. In many DFT functional, the effect of the Coulomb hole are implicitly included, but since the second-order density matrix is not defined in Kohn-Sham wavefunction, none of the equations 3.1-3.4 can be rigorously applied.

In this brief discussion it was illustrated how information about electron delocalization can be directly extracted from the electron pair density through the definition of the exchange-correlation density, Γ_{xc} . As a matter of fact, there exist many techniques which exploit the exchange-correlation density to gain insights into chemical bonding mechanism, such as the Electron Localization Function (ELF) [30], the Electron Localizability Indicator [31] and the Domain Averaged Fermi Hole [32], to name just a few. A measure of the number of electron pairs shared by two atoms can be obtained from the so-called Delocalization Index (DI) [33]. The latter will be used in our investigation as a reference quantity for the measure of electron delocalization. The philosophy behind DI is that, when double integration of Γ_{xc} over two atomic basins is performed, the resulting number represents the number of electron pairs shared by these two atoms:

$$\delta(\Omega_A, \Omega_B) = -2 \iint_{\Omega_A, \Omega_B} \Gamma_{xc}(\mathbf{r}_1, \mathbf{r}_2) d\mathbf{r}_1 d\mathbf{r}_2 \quad \text{Eq. 3.5}$$

Note that, also in this case, there is a close parallelism with statistics and, in particular, with multivariate analysis. Indeed, eq. 3.5 is nothing else than the covariance between two sets of data, the latter being in this case the population of electrons in two atomic basins. In other words, delocalization index represents the correlation of electron population between two atomic basins.

When the double integration of eq. 3.5 is performed over the same basin, one obtains the Localization Index (LI). LI denotes the number of electrons localized in a given atomic basin. From a statistical point of view, LI is the variance of atomic electron population and it represents the fluctuation of electron population in a given atomic basin.

The definition of DI intrinsically relies on the partition of molecular space into atomic regions. The use of zero-flux surfaces defined in QTAIM [34] bears many advantages (definition of virial theorem, univocally defined atomic kinetic energy, decomposition of every quantum mechanical observable in atomic contributions, etc.) and for this reason DI is usually calculated considering QTAIM partitioning. The use of DI integrated over QTAIM basins is nowadays spread throughout the literature dealing with chemical bonding investigation, and remarkable results have been obtained, which truly allowed to gain more insights into chemical bonding mechanism. The interested reader can find an overview of that in ref. 35.

3.1.2 ELECTRON LOCALIZATION/DELOCALIZATION THROUGH THE ELECTRON DENSITY DISTRIBUTION

The investigation of chemical paradigms through the use of ED bears many advantages, already discussed in the first chapter of this thesis. As explained in the previous paragraph, the presence of electron delocalization naturally manifests itself in the second-order density matrix. ED, being obtained from the one-electron density matrix, does not contain any *explicit* information about the electron pairing mechanism. However, it is well known that all the ground state properties of a system are determined by its ED distribution [36]. Because of that it is reasonable to assume that, although electron delocalization is not an observable (see previous sections), ED should embody features which allow one to measure electron localization/delocalization of electrons*.

* The effect on the electron density and related topology upon inclusion of static and/or dynamic correlation into the wavefunction has been carefully documented in the literature (see C. Gatti, P. J. MavDougall, R. F. W. Bader J. Phys. Chem (1988)88,3792)

Regarding electron localization, Bader [29] has shown that ED distribution contains information on the position of localized electron pairs (bonding and lone pairs) and that their geometry is in accordance with the Valence Shell Electron Pair Repulsion (VSEPR) model [37], a cornerstone theory of structural chemistry. In particular, the electron pairs of VSEPR manifest themselves in minima of ED Laplacian (*i.e.* regions where ED is maximally concentrated). This approach has been successfully used to investigate important chemical phenomena (*e.g.* the ED changes in urea crystal due to intermolecular interactions [38]). The VSEPR model has been extensively used by chemists to predict the molecular geometry of main group elements [37]. Therefore, the fact that ED Laplacian provides a physical basis for such model is a noteworthy example of the wealth of information contained in the ED distribution. In addition, Bader *et al.* [29] demonstrated that in many cases ED Laplacian and ELF fields are homeomorphic. This homeomorphism establishes a physical link between the portrayal of electron localization obtained from ED Laplacian and the one derived from electron pair density. Being able to provide significant insights into the physics behind chemical bonding, QTAIM has played a major role in the ED-based investigation of electron delocalization. In particular, there have been many attempts to correlate the latter with the properties at BCPs [39]. Generally speaking, it is well-known that, as far as chemically similar bonds are compared, the ED value at BCP (ρ_{BCP}) is directly (exponentially) proportional to the bond strength [40], and several attempts have also been made to try to relate ρ_{BCP} with bond order [41]. Because of this, ρ_{BCP} has been used to detect the presence of π electron conjugation. Indeed, when a single bond is conjugated with one (or more) adjacent double bond(s), its bond order increases (leading to bond order values falling between one and two). The presence of π conjugation can be detected even more efficiently by considering the ED curvatures at BCP. More in details, the quantity used to detect π conjugation is the so-called ellipticity, which is defined as:

$$\varepsilon = \left| \frac{\lambda_1}{\lambda_2} \right| - 1 \quad \text{Eq. 3.6}$$

where λ_1 and λ_2 are the negative curvatures at BCP. Ellipticity is to be understood as a measure of the departure from cylindrical symmetry of ED around BCP. For a bond having a significant π contribution, the eigenvector (L2) associated to the smallest curvature λ_2 will lie perpendicular to the π nodal plane. Along such direction, in fact, ED must decay slower with respect to the direction of L1 (*i.e.* the eigenvector associated with λ_1), where the π contribution is null. Because of this, Bader suggested that the ellipticity at BCP provides a quantitative measure of the π character of a given bond [42]. In particular, for π conjugated bonds, the L2 axis are all parallel throughout the chain of bonds involved in the conjugation pattern. This approach has been widely used to investigate π conjugation. Nevertheless, it presents several drawbacks. The first is that it only allows to study π delocalization (the only exception being, to the best of our knowledge, the study of cyclopropane where σ delocalization could be investigated [43]), which, although very important especially for aromaticity, is far from covering all the types of electron delocalization. Moreover, ε is obtained as a ratio of two curvatures and it is hence a quantity very sensitive to variation in ED distribution. Therefore, the same conclusions drawn above for the anticipated experiment-theory disagreement in the location of maxima of ED Laplacian holds true for ellipticity. Last but not least, large ellipticity values may have nothing to do with π orbitals, *e.g.* in those cases where the molecular geometry is such that one of the bond paths is near to get broken (that is the ED topology is near to the so-called ‘catastrophe points [34]’)

A powerful and very promising ED-based tool which mirrors the localization extent of chemical bonds is the Source Function (SF) [44]. A more detailed description of this quantity is given in the next section.

The approaches which exploit QTAIM to investigate electron delocalization are not limited to the few properties discussed before, although the latter certainly represent the most widely used methods. The interested reader is referred to ref. 39 for an exhaustive overview of the study of electron delocalization using scalar fields (including ED).

3.1.3 THE SOURCE FUNCTION AND ITS USE TO DETECT ELECTRON DELOCALIZATION

Bader and Gatti showed [44] that the ED at a point r in a system can be viewed as consisting of contributions from all the other points r' of the system itself through the following equation:

$$\rho(\mathbf{r}) = -\frac{1}{4\pi} \int \frac{\nabla^2(r')}{|\mathbf{r}-\mathbf{r}'|} d\mathbf{r}' \quad \text{Eq. 3.7}$$

The point r is usually defined as the *Reference Point* (RP), while the integrand is defined as the Local Source LS(\mathbf{r},\mathbf{r}'). In equation 3.7, the term $(4\pi|\mathbf{r}-\mathbf{r}'|)^{-1}$ is a Green's function or an influence function, [45] and it represents the effectiveness of how the cause $\nabla^2\rho(\mathbf{r}')d\mathbf{r}'$ contributed to determine the effect $\rho(\mathbf{r})$. In other words, the cause-effect relationship depends on the reciprocal of the distance between the element of Laplacian of the density $\nabla^2\rho(\mathbf{r}') d\mathbf{r}'$ and the point of interest given by r .

It is important to note that eq. 3.7 has a close similarity with the well-known Poisson equation for electrostatic potential (eq. 3.8),

$$\varphi(\mathbf{r}) = -\frac{1}{4\pi} \int \frac{\rho(r')}{|\mathbf{r}-\mathbf{r}'|} d\mathbf{r}' \quad \text{Eq. 3.8}$$

where $\varphi(\mathbf{r})$ represents in this case the electrostatic potential at r . This parallelism is helpful to obtain an intuitive interpretation of eq. 3.7: the ED Laplacian determines the ED at a point in the system in the same way as the charge determines the electrostatic potential.

A step further which offers a chemically meaningful perspective is obtained by dividing the integration of LS into the atomic basins defined by QTAIM (*i.e.* the zero flux surfaces described in chapter I). In this way, the ED at the RP may be equated to a sum of atomic contributions, each of which is termed Source Function (SF) of the atom A to the point r :

$$\rho(\mathbf{r}) = -\frac{1}{4\pi} \sum_A^{Nat} \int_{\Omega_A} \frac{\nabla^2(r')}{|\mathbf{r}-\mathbf{r}'|} d\mathbf{r}' = -\frac{1}{4\pi} \sum_A^{Nat} S(\mathbf{r},\Omega_A) \quad \text{Eq. 3.9}$$

This partitioning into atomic regions allows one to obtain the contribution of each atom in determining the ED at the RP. Given that contributions from each atom sum up to the value of ED at RP, the SF contributions are usually expressed as percentage contribution through the following expression:

$$SF\%_A = \frac{S(\mathbf{r},\Omega_A)}{\sum_B^{Nat} S(\mathbf{r},\Omega_B)} \quad \text{Eq. 3.10}$$

Regarding the choice of chemically meaningful RPs, when one wants to investigate chemical bonding, BCPs are usually taken as the least biased choice. However, other choices are possible (*see infra*). The investigation of SF contributions to BCP is able to provide precious information which are usually not easily obtainable from ED distribution. SF contributions are related to the nature and strength of a given interaction. As a general rule, the higher is the contribution from the two bonded atoms to their BCP, the

stronger is the interaction. $S\%$ contributions, on the other hand, give information about the localized character of a given interaction: when the two bonded atoms display a high $S\%$ value to the BCP connecting them (fairly close to 100%), it means that the interaction is strongly localized, and *vice-versa*.

Given that several mistakes regarding the interpretation of SF results appeared in literature [46], a point needs to be stressed here. Atomic contribution of eq. 3.9 does not represent a direct donation of ED from the atom to the RP, but rather an *influence*, in the same way as a charge determines the electrostatic potential (see eq. 3.8). Therefore, caution needs to be taken when interpreting the results, as the extraction of chemical information from the SF should always remind such relationship.

SF approach has been extensively used in literature to gain insights into chemical bonding mechanisms. Seminal works dealing with application of SF to paradigmatic examples of chemical interactions have been published [47]. For hydrocarbons, it was shown that both SF and $SF\%$ contributions increase with increasing bond order. SF was also demonstrated to be able to mirror the 3c-2e character of bonds such as the prototypical one of B_2H_6 . Furthermore, SF has been used to explore the chemical transferability of functional group on a new perspective [48]. When applied to H bonds, SF was proved to be able to discriminate (through the contribution to the HB BCP of H, acceptor and donor atoms) among the various HB categories proposed by Gilli and Gilli [49]. Moreover, the sum of the contributions of the three atoms (donor + hydrogen + acceptor) displays a correlation with the HB strength and therefore with its energetics. Last but not least, it is worth mentioning the results of the application of SF to Metal-Metal and Metal-Ligands bonds [50]. By exploring the SF contributions of ligands and metal atoms at various BCPs, interesting parallelisms with common chemical thinking have been recovered. For example, it was shown how the SF is able to distinguish between the delocalized character of Metal-Ligand and Metal-Metal bond and the localized nature of intra-ligand bonds such as CO bond in Metal Carbonyl systems. A remarkable result of all the investigations above reported, and particularly so for the latter, is that for most of the considered cases the picture of bonding obtained from SF closely follows the trends obtained from pair-density based descriptors such as DI [33]. Although no direct physical relationship exists between, for example, DI and SF, the fact that the latter leads to the same bonding picture as the former puts forward the SF as an ideal approach for the ED-based study of electron delocalization.

Indeed, encouraging preliminary results were already obtained by Gatti [47] in the study of π delocalization. In particular, he investigated the SF contributions for the series of systems showing increasing conjugation, namely: cyclohexene, cyclohexadiene and benzene. This investigation was triggered by a previous work of Macchi and Farrugia [51], in which they explored the orbital-decomposed SF contributions for several systems. From the latter investigation, it was concluded that “ π -electron delocalization in the benzene ring is not manifest in the SF when the RP is taken at the CC bcp”. This conclusion was based on the fact that orbitals having π symmetry give a null SF contribution when RP is taken in the orbital nodal plane. Conversely, one should always bear in mind that σ and π distributions are not independent one another. Rather, as pointed out by Bader *et al.* [42], they are self-consistently interrelated and indeed one can anticipate that, although π orbitals do not give direct contribution to the RP when the latter lies in the nodal plane, some small effects are still detectable due to the influence of π orbitals on the σ distribution. In the preliminary investigation reported in ref.47, it was indeed shown that this is the case for the series cyclohexene-cyclohexadiene-benzene. Furthermore, when the RP is shifted away from the BCP in a direction where the π orbitals give direct contribution, conjugation effects become more evident.

Following the results of Gatti's preliminary investigation, Monza et al. [52] carried out a systematic study of several aromatic and conjugated hydrocarbons using SF approach. In particular, they considered as RPs

both the BCP and a point shifted by 1 a.u.* along the direction of the ED Hessian eigenvector L2 associated with the second greatest eigenvalue. Indeed, as explained before when ellipticity was discussed, such eigenvector is the one which points towards the direction of the π orbital distribution (hence perpendicular to the molecular plane when simple aromatic molecules are considered). The systems investigated were, in addition to the series of 6 member rings cited above, several poly-aromatic hydrocarbons, namely: naphthalene (along with its hydrogenated derivatives, in which the conjugation pattern of one ring is interrupted), anthracene, phenantrene and biphenyl. The main results of their investigation are explained in the following. For the series cyclohexene-cyclohexadiene-benzene, it was shown that the SF% contributions to the double bond from the atoms forming such bond decreases with increasing conjugation. The opposite is true for the SF% contribution from the other atoms of the ring, i.e. their contributions increases in the series cyclohexene-cyclohexadiene-benzene. This trend, besides being in agreement with the picture obtained using DI [52], is also in accordance with common chemical thinking. From the investigation on polycyclic aromatic hydrocarbons, Monza *et al.* concluded that the mutual influence of each benzoid ring to all others, despite being a subtle effect, is clearly revealed by SF [52]. They also proposed a new local aromaticity index defined in terms of SF contributions. Such index shows an excellent correlation with the FHDD index [53], which is based on DI. Generally speaking, DI and SF approaches show the same trend for all the interaction investigated by Monza *et al.*, confirming therefore the SF as an ideal tool to study electron delocalization using an experimentally derived quantity. Last but not least, they showed that SF description of aromaticity is quantitatively invariant with respect to the use of different Hamiltonian and/or different basis sets.

In the next sessions, the results regarding the application of SF to experimentally-derived ED distribution of some molecular crystals will be presented. In particular, we explored the ability of SF to detect electron delocalization from experimentally derived ED distribution obtained through multipolar refinement against single crystal X-ray diffraction datasets. The experimentally derived results were also compared with the ones from DFT periodical calculations.

The rest of the chapter is divided as follows: In section 3.2 an overview of the test cases chosen for our investigation and the methods used to obtain ED and SF results will be illustrated. In section 3.3, the results are reported, while conclusions will be drawn in section 3.4.

3.2 TEST CASES: DESCRIPTION, MULTIPOLAR REFINEMENT, *AB-INITIO* CALCULATIONS AND SOURCE FUNCTION EVALUATION

3.2.1 CHOSEN TEST CASES AND REASONS BEHIND THE CHOICE

The conditions an X-ray diffraction dataset has to satisfy to be considered as a good candidate to obtain a reliable experimentally derived ED distribution were already reported in Chapter II. In this case, obviously, the test case systems were chosen among those molecular crystals which show interesting features for electron delocalization (rather than considering their NCI, as done in chapter II). Good-quality X-ray diffraction data were already published for two very simple aromatic molecules: benzene and naphthalene.

* This is an arbitrary value chosen as a benchmark. The reason behind this choice is that it is close to the maximum of the π density calculated by Monza *et al.* to be 1.05 au for benzene

These two systems were hence included in the test case set. In fact, these two paradigmatic examples of aromatic molecules offer the possibility of exploring the ability of SF to detect electron delocalization (and eventually to obtain a measure of their aromaticity) at the experimental level. Moreover, the same systems were investigated in the seminal work by Monza *et al.* [52], hence their study allows us to explore whether the results obtained from an ideal model like the theoretically derived ED *in-vacuo* is actually reproducible when real systems are investigated. In other words, since the advantage of the SF approach for the investigation of π delocalization and to aromaticity lies in the fact that it is based on an observable and measurable quantity, it is of paramount importance to explore whether the conclusion drawn in ref. 52 hold true when experimentally derived ED distribution are considered. A certain degree of discrepancy between experimentally-derived SF values and the ones from *in-vacuo* theoretical calculations can be anticipated, since the former were obtained in solid state through the use of a multipolar model. It must be pointed out, however, that the perturbation on molecular ED distribution of benzene and naphthalene due to the intermolecular interactions is expected to be small, since the latter (typically C-H \cdots C, H \cdots H and C-H \cdots π) are not strong enough to significantly perturb the π delocalization pattern. Regarding the bias introduced by the use of a multipolar model, this issue was already investigated by Lo Presti and Gatti [ref]. They showed that the projection onto multipolar model does not significantly influence SF% contribution at BCPs of the investigated systems, the only exception being the Metal-Metal bond of bis(pentacarbonylmanganese). The differences caused by the multipolar model are expected to be small also in this case, although the theory-experiment comparison reported here represents an extension of the work of Lo Presti and Gatti, since RPs other than BCPs will be considered (namely the points along the eigenvector L2). While the inclusion in the test case set of simple molecules is important for the reasons explained so far, it is essential to consider also a bigger, more complicated system, to challenge the ability of SF to describe electron delocalization in non-ideal cases. The molecular crystal chosen for this purpose is the 8'-benzhydrylidenamino-1,1'-binaphthyl-2-ol (hereinafter BAB, scheme 3.1) which contains as many as 58 atoms in the asymmetric unit (236 electrons) and is therefore rather challenging both from both theoretical and experimental point of view. The inclusion of this system into the test case set offers several interesting additional opportunities, explained in the following:

- BAB contains benzene-like and naphthalene-like rings (scheme 3.1). Therefore the SF contributions of the atoms and bonds of such ring can be compared to the experimental results obtained from benzene and naphthalene molecular crystals. This is a key step, because it represents a comparison between results obtained from ED distributions coming from experiments carried out at completely different operative conditions (temperature, beam intensity, crystal size, data collection strategy, multipolar model etc.). The stability of SF results against the use of different datasets would lead to the conclusion that the results obtained in this work on benzene and naphthalene can be safely used as a benchmark for future experimentally-based investigations of electron delocalization.
- All the aromatic rings mentioned above are substituted in one or more positions (see scheme 3.1). This gives us the chance to explore how the substitution influences the delocalization pattern of the neighboring bonds. Possibly, a step further in the investigation of the substituent effect might be obtained by evaluating the SF-based aromaticity indicator for the different substituted rings. This last step, however, is not part of the investigation reported in this dissertation and it will be explored in future works.
- BAB is characterized by the presence of several (formally) single bonds positioned between bonds having π character. This means that there are a number of bonds which might display

conjugation effects. As explained in the previous sections, there is not a 'universal' technique which can define whether an allegedly single bond is conjugated with the neighboring bonds. On the other hand, DI offers a measure of the electron sharing between distant bonds and will therefore be used in this work as a reference quantity to measure conjugation effect. Indeed, when distant atoms display a DI value significantly different from zero, it means that a certain degree of delocalization is taking place between them. In the case of π systems, this fact can be used to measure the degree of conjugation.

In summary, three molecular crystals were chosen as test cases for the experimentally based investigation of electron delocalization: benzene, naphthalene and BAB (scheme 3.1). In the next sections, details regarding the multipolar refinement, *ab-initio* calculations and SF evaluation are reported.

3.2.2 MULTIPOLAR MODEL

In this section, an overview of the molecular crystals chosen as test cases will be given, with particular emphasis on the multipolar model used to obtain experimental ED distribution. All the multipolar refinements were carried out with XD2006 [54].

BENZENE

For benzene, the dataset taken from Bürgi *et al.* [55] already illustrated in chapter II was used here. Initially, the same refinement strategy was used. A close inspection of the results obtained from such model, revealed that two bonds were characterized by an unexpectedly low ellipticity. In particular, while for benzene an ellipticity value comprised between 0.15 and 0.25 is expected [52] due to the significant π character of its bonds, we found for two of them (related by symmetry) a value of only 0.02. For this reason, we tried to use a multipolar model in which hexadecapole populations were not refined. With the latter model, reasonable ellipticity values were obtained for all the bonds. Ellipticity and ρ_{BCP} values for the two models are reported in Table 3.1. Note that the introduction of hexadecapoles in the multipolar model affects only subtle features of ED distribution, as confirmed from the fact that ρ_{BCP} is much less affected by the introduction of hexadecapoles with respect to ellipticity. As a matter of fact, ellipticity values undergo dramatic changes, as ellipticity is very sensitive to the method adopted to obtain ED distribution and hence this quantity cannot be considered as an optimal indicator of electron delocalization (not only for this reason, as pointed out in section 3.1). Note that for the model without hexadecapoles the ellipticity is the same for all bonds, which is a reasonable result considering that no strong NCIs able to significantly distort the molecular π cloud are present in this crystal system (see chapter II).

Table 3.1 Experimentally derived ED at BCP (ρ_{BCP}) and ellipticity (ϵ) values at C-C BCPs of benzene molecular crystal for two different multipolar models. Only the three symmetry independent C-C bonds are considered. e.s.d.'s on ellipticity cannot be calculated using XD2006 and therefore they are not reported.

	$\rho_{\text{BCP}}[\text{e}/\text{\AA}^3]$			ϵ		
	C1-C2	C2-C3	C1-C3'	C1-C2	C2-C3	C1-C3'
H-model	2.24(1)	2.28(1)	2.22(2)	0.02	0.14	0.16
O-model	2.26(2)	2.28(2)	2.21(2)	0.23	0.23	0.23

To test the stability of the SF against the use of different multipolar refinements, both models have been used to calculate SF. The models with and without hexadecapoles will be referred to, in the discussion, as H-model and O-model, respectively. Statistical agreement factors for the two models are reported in Table 3.2, while all the other details about the diffraction dataset were already reported in chapter II (section 2.4.3).

Table 3.2 Agreement factors from least-square refinement for the two different multipolar models of benzene molecular crystal.

	H-model	O-model
Refinement against	F^2	F^2
$R(F^2)$	0.0240	0.0395
$R_w(F^2)$	0.0337	0.0474
GOF	1.0435	1.4466

NAPHTHALENE

Low temperature X-ray diffraction data for naphthalene molecular crystal were measured by Oddershede *et al.* [56]. They performed a careful analysis of datasets measured at different temperatures (100, 135, 170 and 205 K) and compared the multipole populations obtained in the various refinements to establish whether the static electron density was actually deconvoluted from thermal motion. Indeed, if a good deconvolution of ED and thermal motion is achieved, the multipole populations are expected to be independent from the temperature and only ADPs should undergo variation with temperature. From this careful analysis, they concluded that the deconvolution was successful for all the datasets measured below 200 K. According to the original paper, we performed the multipolar refinement against the structure factors measured at 135 K, as the latter is the most precise dataset (according to R_{int}).

Naphthalene crystallizes in the space group $P2_1/c$ with half of the molecule in the asymmetric unit. As a result, the unit cell contains only two molecules. Relevant data for the dataset used for the refinement are reported in Table 3.3.

Table 3.3 Most relevant data for the X-ray diffraction dataset of naphthalene molecular crystal

space group	T [K]	wavelength [\AA]	$\sin(\theta_{\text{max}}/\lambda)$	R_{int}
$P2_1/c$	135	0.71073	1.14	0.0274

We took from the original work geometry and ADPs without refining them. The latter were obtained also for hydrogen atoms through a sum of rigid-body contributions obtained from ADPs of Carbon atoms (the analysis was carried out with the program THMA11 [57]) and the correction for internal motion obtained from *ab-initio* calculations [56]. Regarding the multipolar populations, we refined those which were refined in the original paper, *i.e.* up to $l=3$ for C atoms and up to $l=2$ for H atoms. Also contraction/expansion coefficients were refined (two coefficients, *i.e.* one for the core and one for the valence, for each atom type). Final agreement indices are reported in Table 3.4

Table 3.4 Agreement indices from least-square refinement of multipolar model for naphthalene molecular crystal

Refinement against	F^2
Number of data	4368
Included in the refinement	3658
$R(F^2)$	0.0165
$R_w(F^2)$	0.0239
GOF	0.9214

(±)-8'-BENZHYDRYLIDENEAMINO-1,1'-BINAPHTYL-2-OL (BAB)

BAB crystallizes in the space group $P2_1/c$ with four molecules per unit cell. The X-Ray diffraction dataset for this compound was measured by Farrugia *et al.* [58]. They carried out a detailed study of several properties of this crystal system such as intra- and inter- molecular NCIs and π -conjugation (by means of QTAIM [34]). Regarding the latter, for several allegedly conjugated bonds a plot of ellipticity along the whole bond path was considered*. This analysis and the results obtained from it in the original paper will be considered when discussing the results of SF for the conjugated bonds. The most relevant data regarding the crystal system and the measured data set are reported in Table 3.5

Table 3.5 Most relevant data for the X-ray diffraction dataset of naphthalene molecular crystal

space group	T [K]	wavelength [Å]	$\sin(\theta_{max}/\lambda)$	R_{int}
$P2_1/c$	100	0.71073	1.079	0.036

In the multipolar model published by Farrugia *et al.*, the ADPs were obtained through a careful refinement procedure in which extensive chemical constraints were employed in the initial stages [58]. ADPs for hydrogens, instead, were obtained with the software SHADE [59]. Regarding expansion/contraction parameters k and k' , one set of parameters (one for each multipole) for each atom type can by default be refined in XD2006 [54]. Farrugia *et al.*, instead, allowed the multipole refinement of more degrees of freedom by further dividing the k and k' of each atom according to its connectivity. This led to the refinement of 6 k/k' sets of parameters for C atoms and 2 sets for H atoms. More in details, they divided the atoms of *BAB* according to their connectivity. Regarding our multipolar refinement, we kept geometry and ADPs fixed at the published values [58]. We split k/k' parameters according to the original paper and refined multipoles up to hexadecapoles for C, N and O atoms and up to quadrupole for H. For C atoms, we did not refine those multipoles which break the mirror plane of aromatic rings, according to the strategy employed in the original paper [58]. Probably due to the complexity of the system, it was not possible to obtain the convergence in the least-square refinement when all the parameters were refined

* The analysis throughout the bond path is more informative with respect to the simple evaluation of ellipticity at BCP, especially for polar bonds

simultaneously. We overcame this problem by performing a block-refinement in which we optimized multipole populations at fixed k -parameters and then k -parameters at fixed multipole coefficients. After 6 steps, all the parameters were not changing more than their own s.u., hence we considered the least-square procedure converged. As to the data included in the refinement, we applied the same cutoff as in the original work: only structure factor having $I/\sigma(I) > 3$ ($F > 1.5\sigma(F)$) were included in the least-square procedure. Final agreement indices are reported in Table 3.6.

Table 3.6 Agreement factors from least-square refinement of multipolar model for *BAB* molecular crystal

Refinement against	F^2
Number of data	23246
Included in the refinement	19691
$R(F^2)$	0.0198
$Rw(F^2)$	0.0288
GOF	1.6916

3.2.3 THEORETICAL CALCULATIONS

To have a benchmark to compare experimental results, we performed fully-periodical *ab-initio* calculations (with the code CRYSTAL06 [60]) at the B3LYP/6-311G**[61,62] level of theory*. The geometry was kept fixed at the best experimental estimate. At the moment in which this thesis is being written, the periodical wavefunction of BAB has not been obtained yet, due to the fact that this system contains many symmetry-independent atoms and because great care is required to obtain convergence in the SCF procedure. Different numerical techniques to obtain convergence are being tested.

As explained in section 3.1.1, DI will be used in this work as a reference quantity to measure electron delocalization [63]. For benzene and naphthalene, we calculated them from *in-vacuo* wavefunction at optimized geometry, as it was done in ref 52. For BAB, instead, we kept the geometry fixed at the experimental one, and, besides for the calculation of DIs, BAB wavefunction will be used in a few cases as a theoretical benchmark for the valuation of SF^\dagger . This calculation was performed with GAUSSIAN09 [64] at the same level of theory of ref. 52, namely B3LYP/DZVP2 [65,61]. DI's were evaluated with PROAIMV [66].

3.2.4 BASIN INTEGRATION AND SOURCE FUNCTION EVALUATION

According to the work of Monza et al. [52], we evaluated SF contribution of the various atoms considering as RPs the BCPs of the investigated bonds and the points shifted along L2 by 1 au (in both directions, therefore in total we considered 3 RPs for each bond considered). From an operative point of view, we performed a BCP search for the bonds under investigation, obtaining the topological properties at the BCPs, including eigenvector directions. Then we calculated the position of the points at ± 1 au along L2 (for bonds having π character these two points are expected to be located above and below the π nodal plane) and,

* due to the difficulties encountered in the convergence of SCF for BAB, the most external function for O and N atoms of BAB were shrunk by a factor 1.44

† To the best of our knowledge, there are no code to calculate delocalization indices from periodic wavefunction obtained with Gaussian basis set. However, DIs and ED distribution for covalent bonds are expected not to be influenced by the surrounding molecules, especially considering the absence of strong intermolecular interactions. Therefore for the calculation of DIs and SF contributions, the use of *in-vacuo* wavefunction can be considered as good approximation to the periodical one

besides using them as RPs, we calculated the ED in such points. The latter step is necessary to obtain SF% values (see eq. 3.10). Atomic basin integrations and evaluation of SF contributions were performed with XDPROP [54] routine, TOPOND [67] and a modified version [68] of PROAIM [66] for the density obtained from XD2006, CRYSTAL06 and GAUSSIAN09, respectively. The sampling accuracy for the evaluation of atomic properties is defined by two angular (θ and ϕ) and one radial parameters. For theoretically derived ED, when not otherwise stated, the number of points used are 64,48 and 120 for ϕ , θ and radial coordinate, respectively. For the integration performed with XDPROP, instead, 972 angular and 400 radial points were used (Gauss-Chebyshev radial quadrature technique [69] was used). For the integration of experimental ED and ED from *in-vacuo* calculations, β -spheres (*i.e.* the part of the basin for which the integration is performed without evaluating the integration ray, which is fixed at the value of the sphere radius, and by using a small number of angular points since the electron distribution within β -spheres is supposed to deviate slightly from spherical symmetry) were automatically determined by the integration software. For the integration of ED from periodical wavefunction, the β -sphere was set roughly to the value of nearest BCP. For the experimentally derived multipolar ED, only the multipoles centered on atoms belonging to the molecule under investigation will be considered. This choice is reasonable considering the discussion given in section 2.4.1 of this dissertation.

There exist several methods to establish a posteriori accuracy of the integration. Here three indicators will be considered: the molecular charge (which should be 0 for all the systems here considered*), the Lagrangian integrated over atomic basins[†] (values below 10^{-3} a.u. are considered as a good result) and the difference between ED at a RP and the sum of SF contributions of all atoms at such RP. In Table 3.7, values for these indicators are reported for all the systems investigated and for both experimental and theoretical ED (both *in-vacuo* and periodical. In the case of BAB, only the results for *in-vacuo* calculations are reported)

Table 3.7 Error in the reconstruction of ED (third column), total molecular charge (fourth column) and Lagrangian integrated over atomic basins (fifth column) for all the systems considered. For the SF% error and Lagrangian averaged value over all integrated atomic basins is reported, while the maximum value is reported in brackets. For L, absolute value is considered.

method	system	err SF%tot (max)	total charge	L (max)
experimental	benzene ^a	0.10(0.21)	9.5E-4	3.4E-4(1.1E-3)
	naphthalene	0.37(0.69)	1.8E-2	5.5E-4(2.2E-3)
	BAB	0.73(3.93)	2.7E-2	4.1E-4(3.4E-3)
<i>in-vacuo</i> DFT	benzene	0.60(0.98)	-5.1E-4	2.7E-4(7.6E-4)
	naphthalene	0.14(0.24)	4.2E-3	2.7E-4(8.0E-4)
	BAB	4.78(11.42)	7.1E-3	2.4E-4(1.5E-3)
periodic DFT	benzene	- ^b	6.2E-6	2.4E-4(4.4E-4)
	naphthalene	-	3.5E-3	7.1E-4(1.1E-3)

^a H-model was considered; ^b in periodic systems, the correct evaluation of this term would require the calculation of the so-called 'atomic surface term' [47], which is not yet implemented in TOPOND.

Generally speaking, the values reported in the table above seem to indicate a negligible error in the integration process. However, there is one exception: the error on the reconstruction of ED at the various RPs is quite high for the *in-vacuo* calculation on BAB. On the other hand, the error on the total charge and the average L values are rather small. To estimate whether the discrepancy in the SF reconstruction of ED in BAB significantly affects the SF results, we performed an additional integration with increased number of grid points (96, 64 and 140 points for ϕ , θ and radial, respectively) and compared the resulting SF

* In molecular crystals, charge transfer between molecules can take place only if there is more than one molecule in the asymmetric unit

[†] Lagrangian is defined as $L(\Omega) = -1/4 \nabla^2 \rho(\Omega)$. For a atomic basins defined in QTAIM, L is supposed to be zero

contributions with the ones obtained with the smaller grid described above. Considering, for each RP, only those atoms which contribute at least 1% to its ED, the average of the relative differences in SF contribution is as low as 0.3%*. In addition, the use of a finer grid does not significantly improve the error in the reconstruction of ED obtained with the coarse grid (the one leading to the values reported in table 3.7)†. For all these reasons, it can be safely concluded that the error due to the integration process is negligible for BAB as well as for all the other systems considered in this discussion. The error in the reconstruction of ED at RPs of BAB, in fact, is probably caused by the presence of number of atoms far away from the RP, which give a very small SF contribution to the ED. The integration error on those atoms is likely to be greater in percentage and therefore lead to a greater error in the reconstruction of ED at BCP.

3.3 RESULTS

3.3.1 BENZENE

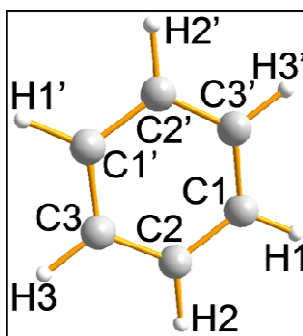


Figure 3.1 Atomic numbering for benzene molecule. The atom labeled with ‘ symbol are the ones which does not belong to the asymmetric unit in the molecular crystal.

The experimentally derived SF% contributions for benzene atoms are reported in Table 3.8, while atom labels are reported in Fig 3.1. Results for the two different multipolar models (see previous section) are considered. According to ref 52, the SF contributions to a given bond are divided according to the ‘topological’ distance from the bond itself: *ba* stands for ‘bonded atoms’ and is the contribution of the two atoms forming the bonds, *nn* stands for nearest neighbors and it is calculated by summing up the contributions from the atoms bonded to the two atoms forming the bonds (two in the case of benzene), while *others* is the contribution from all other carbon atoms of the system (*i.e.* the remaining two atoms). Note that only three bonds were considered as only half a molecule is symmetry-independent

*in other words, for those contributions which are greater than 1%, we calculated the relative difference as $(SF\%[\text{old grid}] - SF\%[\text{new grid}]) / SF\%[\text{old grid}]$. The average of this value calculated for all the RPs considered in this work is 0.3%

†With the finer grid, the average error in the ED reconstruction is 4.8%, while the maximum error is 11.5%

Table 3.8 SF% contributions for the experimentally derived ED distribution of benzene molecular crystal

H-model						
	BCP			OOP ^a		
	SF%ba	SF%nn	SF%others	SF%ba	SF%nn	SFothers
C1-C2	86.0	5.0	1.3	71.8	9.6	2.7
C2-C3	86.4	4.9	1.3	73.4	8.9	2.7
C1-C3'	86.1	5.1	1.3	72.6	9.3	2.7
average (esd ^b)	86.2(2)	5.0(1)	1.29(3)	72.6(8)	9.3(6)	2.7(2)
O-model						
	BCP			OOP ^a		
	SF%ba	SF%nn	SF%others	SF%ba	SF%nn	SFothers
C1-C2	86.0	5.3	1.5	73.4	9.6	3.1
C2-C3	86.5	5.1	1.5	73.9	9.4	3.1
C1-C3'	86.1	5.3	1.6	73.3	9.7	3.1
average(esd ^b)	86.2(2)	5.2(1)	1.53(2)	73.5(3)	9.5(2)	3.1(1)
B3LYP/DZVP2, <i>in-vacuo</i>						
	SF%ba	SF%nn	SF%others	SF%ba	SF%nn	SFothers
C-C (D _{6h})	84.3	5.3	1.5	72.2	9.1	2.6

^aThese are the contributions to the RP shifted by 1 au along L2. The average between the values above and below the molecular plane are reported; ^besd represents the standard deviation of the average over the six C-C bonds

From the values reported in the table above, several interesting conclusions can be drawn. The first is that an excellent agreement with the results reported in ref. 52 is achieved, the only exception being the SF%_{ba} contributions, for which the agreement is anyway still good. It is worth stressing that such an agreement is found even though the values reported in ref. 52 were obtained from *in-vacuo* calculations, while the results presented here are the outcome of experimentally derived multipolar model in the solid state. Therefore it seems that, at least for the benzene molecule, the results of SF approach to electron delocalization are almost independent from the method used to obtain ED distribution and barely affected by the crystal field effects. In addition, by comparing the values relative to the two different multipolar models it can be immediately seen that the two different models are in close agreement and therefore they lead to the same picture of delocalization. This means that the results are barely influenced by the multipolar refinement strategy adopted. Nevertheless some trends can be noticed. The inclusion of hexadecapole leads to a better agreement for the Out Of Plane (OOP) contributions (*i.e.* those for the RPs shifted along L2) at the expenses of the agreement for SF% contributions at BCP. On the other hand, it seems that the O-model better describes the uniformity of the molecular π cloud, as measured by the deviation of each individual SF% contribution from their average value (a measure of such deviation is given by the e.s.d. values reported in the table).

Although the agreement between experimentally derived results and the ones from *in-vacuo* calculations can be considered satisfactory, a non-negligible difference was found for the SF%_{ba} contributions to BCP for both the multipolar models considered. A better understanding of this difference can be obtained by considering the results of periodical calculations, reported in Table 3.9.

Table 3.9 SF% values from periodical B3LYP/6-311G** calculations at experimental geometry of benzene molecular crystal. Averaged values over the 6 C-C bonds are reported. The values in brackets refer to the standard deviation of the average.

BCP			OOP		
SF%ba	SF%nn	SF%others	SF%ba	SF%nn	SFothers
84.68(8)	5.10(1)	1.33(2)	71.35(8)	8.79(3)	2.54(4)

SF%_{ba} values reported in table 3.9 are much closer to the results calculated from *in-vacuo* wavefunction than to the ones obtained from experimentally-derived multipolar model. This fact rules out the possibility that the differences between results from *in-vacuo* wavefunction and from experimental ED are caused by the crystalline environment or by the (slightly) different geometries (namely the experimental one and the theoretically optimized *in-vacuo* geometry). The two remaining reasons which may explain this difference are either the projection onto multipolar model or the effect of random errors in the experimental dataset. The latter possibility however, can be safely excluded due to the low R_{int} (0.0258) value obtained for the dataset. Thus, the discrepancy on SF%_{ba} values are likely to be caused by the projection onto multipolar model. The higher SF%_{ba} obtained from the multipolar model seems to be an overaccumulation of ED onto the interatomic axis. This hypothesis is confirmed by the value of ρ_{BCP} for multipolar ED (table 3.1), which are significantly greater than the one obtained from *ab-initio* calculation (results reported in table 3.1 are to be compared with an average value of ρ_{BCP} of 2.03 and 2.07 for *in-vacuo* B3LYP/DZVP2 and periodical B3LYP/6-311G** calculations, respectively)

3.3.2 NAPHTHALENE

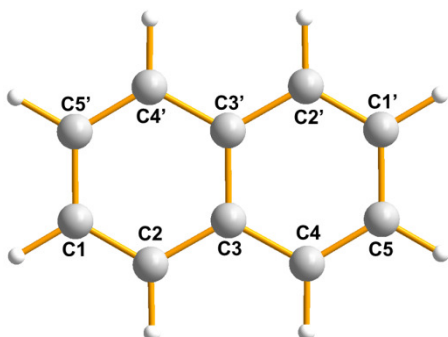


Figure 3.2 Atomic numbering for naphthalene molecule. The atoms labeled with ' symbol are the ones which does not belong to the asymmetric unit in the molecular crystal.

The atom numbering for naphthalene molecule adopted in this work is reported in Fig. 3.2. Note that in crystal only half molecule is symmetry-independent, while the molecule *in-vacuo* has D_{2h} symmetry with only 4 out of the 10 C-C bonds being symmetry independent. SF% contributions for naphthalene are reported in Table 3.10, along with delocalization indices for *in-vacuo* calculation (D_{2h}). Although the point-group symmetry is lower for the molecule in crystal, bonds which are symmetry-related *in-vacuo* shows

almost identical bond lengths and SF%_{ba} contributions* in crystal. Their average value is therefore considered when discussing the various SF contributions.

Table 3.10 SF% contributions for naphthalene. For SF and bond length, each row is divided as follows: the first line refers to the value from experimentally derived multipolar ED, the second to periodical calculation at experimental geometry (B3LYP/6-311G**) and the third to the *in-vacuo* calculations (B3LYP/DZVP2, geometry optimized in D_{2h} symmetry). For solid state results, the average value is reported for those bonds which are symmetry equivalent *in-vacuo* (D_{2h}). An average value is reported also for OOP contributions (*i.e.* the average is calculated including also SF% contributions below and above the molecular plane). Esd in the evaluation of the average are reported in parenthesis. In some cases, esd. was calculated for a set containing only two data (e.g. for the OOP contributions of C3-C3') and therefore, in general, no statistical meaning should be attributed to esd. Rather, they are shown to give an indication of the differences among the values used to evaluate the average.

Bond(s)	SOURCE FUNCTION						bond length ^a [Å]	DI ^b (non-bonded)
	BCP			OOP				
	SF%ba	SF%nn	SF% others	SF%ba	SF%nn	SF% others		
C1-C2/ C5-C4 ^c	86.27(3)	4.21(5)	2.37(6)	73.62(5)	7.26(10)	4.76(11)	1.374	1.49 (0.138)
	85.44(7)	4.19(1)	2.19(1)	73.27(13)	6.98(1)	4.24(2)	"	
	85.3	4.4	2.3	74.2	7.2	4.3	1.380	
C1-C5'	84.34	5.83	1.92	69.58(14)	10.50(12)	3.88(5)	1.416	1.29 (0.143)
	83.61	5.75	1.71	69.38(11)	10.09(1)	3.36(1)	"	
	83.7	5.9	1.9	70.4	10.1	3.7	1.424	
C2-C3/ C3-C4 ^c	83.05(21)	7.32(12)	3.18(2)	67.20(37)	12.87(23)	6.46(4)	1.417	1.25 (0.184)
	82.65(20)	7.04(4)	2.89(1)	67.13(10)	12.15(5)	5.77(1)	"	
	82.5	7.3	3.0	68.3	12.2	5.9	1.427	
C3-C3'	81.58	9.80	3.29	64.40	17.31	6.53	1.422	1.22 (0.230)
	81.20	9.49	2.88	64.47(4)	16.54(4)	5.63(<1)	"	
	81.2	9.8	3.2	65.4	16.6	6.0	1.434	

^a Atomic positions were not refined hence e.s.d. could not be calculated. When SF contribution for some bonds is reported as average, so is the bond length ^b DI are calculated from *in-vacuo* wavefunction. For a given bond A-B, the number in parenthesis is the sum of all the DIs between A and the C atoms bonded to B and between B and C the atoms bonded to A^c These two bonds are considered equivalent

The SF% contributions obtained from different methods (experimental, *in-vacuo* wavefunction and periodic wavefunction) display in general a very good agreement among each other. However some features are worth of being discussed separately. For SF%_{ba} contributions, the fact that experimental values are somehow greater than theoretical ones, while *in-vacuo* and periodic wavefunction are in excellent agreement confirms the trend already hypothesized in the case of benzene, namely that the multipolar model leads to an enhanced accumulation of charge in the internuclear axis. Regarding the agreement among the various models, it must be pointed out that the trends of SF% contributions in passing from benzene and naphthalene reported in ref. 52 is recovered using experimentally-derived ED distribution.

As for the physical picture sketched by SF, naphthalene can be seen as formed by two fused benzene-like rings and for this reason it is particularly interesting to compare the results reported in Table 3.10 with the ones of benzene. This comparison, indeed, allows to explore –from the SF point of view– how the

* The two couples of bonds in question are C1-C2/C4-C5 and C2-C3/C3-C4 and the differences in bond length are 0.0002 Å and 0.0006 Å, respectively (standard deviations cannot be estimated since geometry has not been refined but usually they are in the order of 0.001 Å). The difference in SF% ba contributions is 0.04 % and 0.31%.

delocalization pattern of one ring is influenced by the presence of another ring. Looking at the $SF\%_{ba}$ contributions, one notices that they are all but one lower than in benzene. What just stated is true also when DIs between bonded atoms in naphthalene and benzene are compared (DI of benzene *in-vacuo* at the B3LYP/DZVP2 level of theory is 1.39). Therefore, it can be concluded that for these bonds SF is able to mirror the (slightly) different degree of electron sharing. The comparison with benzene for the *nn* contributions is not straightforward due to the fact that in naphthalene some bonds have more than two nearest neighbor atoms (a thorough discussion is reported in ref.52). The most peripheral bonds, namely C1-C2 and C1-C5' (and their symmetry equivalents) however, have the same number of nearest neighbors as in benzene and the comparison may shed light on the influence of the second ring on the delocalization pattern. Regarding C1-C2, one of its nearest neighbor atoms has a different connectivity with respect to benzene, namely it is bonded to three carbons rather than two carbon and an hydrogen. This different bonding scheme is clearly reflected in $SF\%_{nn}$ contributions: for C1-C5' $SF\%_{nn}$ is higher than in benzene, reflecting somehow a higher degree of delocalization, while for C1-C2 such contribution is lower than in benzene. Such lowering of SF contribution is due to the smaller contribution of the C3 atom (*i.e.* the one bonded to two carbons, see Fig. 3.2), which is for experimental results as low as 1.96 (while the contribution of the other nearest neighbor atom, C5' it is 2.28). The lowering of SF% contribution of a carbon atom when its hydrogen is substituted with another atom is often observed and it will be explored in more details in paragraph 3.3.3. As for C1-C5', the nearest neighbor atoms have the same connectivity as benzene. Nevertheless, the $SF\%_{nn}$ contributions for C1-C5' are higher. This fact is an indication of the greater electron delocalization, with respect to benzene, taking place in one ring of naphthalene because of the presence of the adjacent ring. In the last column of Table 3.10, the values reported in brackets represent an estimation of the degree of delocalization between the atoms forming each bond and the adjacent atoms (see the caption of table 3.10 for the rigorous definition). In the matter in question, the value for C1-C2 is the sum of the DIs C1-C3 and C2-C5', while the value for C1-C5' is the sum of DIs C1-C4 and C2-C5'. The DI latter value is lower with respect to the former, therefore also in this case DIs give a confirmation of the bonding picture obtained from SF.

Regarding the $SF\%_{others}$ contributions, their physical significance was already discussed in ref. 52. Due to the agreement between experimental SF contributions and SF contribution reported in such work, the same conclusions hold true for the experimental picture and this topic will not be commented here any further.

3.3.3 8'-BENZHYDRYLIDENEAMINO-1,1'-BINAPHTYL-2-OL

BENZYL RINGS

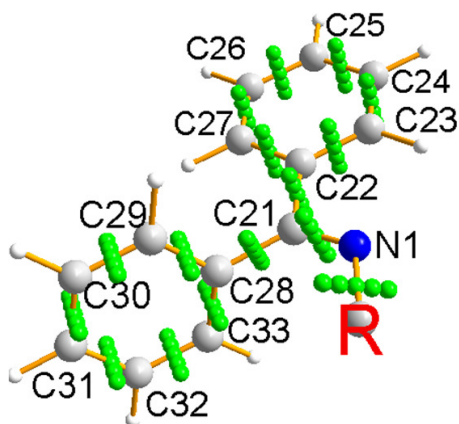


Figure 3.3 Atomic numbering for the benzyl rings of *BAB*. The green spheres are placed along L2 eigenvectors each 0.5 au (from -1 au to +1 au with respect to the BCP) to show the direction of the eigenvectors associated with each bond. “R” is a label used to indicate the rest of the molecule (not shown here for the sake of clarity)

In Figure 3.3, the atomic numbering for the two benzyl rings of *BAB* is reported, along with the direction of the eigenvectors L2 for all the covalent bonds. To distinguish the two rings in the discussion, they will be referred to using the first and the last name of the composing atom (C22...C27 and C28...C33). Both the two benzyl rings have one atom which is bonded to the bridging atom C21, which, in turn, forms a double bond with the nitrogen atom. The fact that the two benzene-like rings are substituted in one position is expected to (slightly) perturb their delocalization pattern but, at the same time, one can reasonably assume that the two rings maintain their aromatic identity. This assumption is reflected in the SF picture (Table 3.11): the SF% contributions of the various atoms are alike to the ones of benzene but the contributions of the substituted atoms is lower. This finding is in accordance with the fact that the substituting atom, namely a carbon, is more electronegative than hydrogen and hence it exerts a greater electron withdrawing effect. This, in turn, leads to a deformation of ED distribution of the substituted atom. The latter, indeed, is expected to accumulate more ED in the bond with the substituting atom and, as a consequence, its SF contribution to the bonds of the ring will be lower.

Table 3.11 SF% contributions for the two benzyl rings of BAB. The averaged values are evaluated excluding the substituted atoms (C22 and C28), whose contributions are reported separately. esd are reported in brackets.

	BCP	+1au	-1au
RING 1 (C22-C27)			
SF% ba, average	86.6(4)	72.6(3)	71.7(1.6)
SF% nn, average	5.1(1)	9.1(2)	8.9(4)
SF% others, average	1.4(1)	2.8(2)	2.6(3)
SF% ba C22	84.9	69.0	68.7
SF% nn C22	4.6	7.5	7.5
SF% others C22	1.1	1.9	1.9
RING 2 (C28-C33)			
SF% ba, average	85.7(7)	72.5(7)	71.5(1.6)
SF% nn, average	5.1(3)	8.9(3)	8.9(4)
SF% others, average	1.4(2)	2.7(4)	2.6(3)
SF% ba C28	84.2	69.4	69.1
SF% nn C28	4.6	8.1	8.1
SF% others C28	1.1	2.1	2.1

From Table 3.11, one can indeed see that the contributions to the various RPs from the two substituted atoms is lower than the average contributions for the remaining atoms of the ring. This difference is significant also in terms of esd, since the difference between the SF% contributions of the substituted atoms and the average values for the ring is greater than 3 e.s.d.'s for most of the values reported in Table 3.11. On the other hand, the two substituted rings maintain their aromatic identity: the SF contributions of substituted atoms are lower than in benzene but still much closer to values of benzene than to the values obtained for systems showing a lesser degree of conjugation, such as cyclohexadiene or cyclohexene (as an example, one may consider the 'SF%other' contributions to the BCP: 0.0 for the former and 0.7 for the latter. For a full comparison, see ref. 52). The results for the averaged contributions of the non-substituted atoms for benzyl rings in BAB are in excellent agreement* with the values found for benzene molecular crystal (and, by extension, with the theoretically derived results *in-vacuo*), despite the fact that the two have been obtained from experiments carried out in completely different conditions. This is an important result because it demonstrates that the SF is an extremely stable descriptor for the ED-based investigation of electron delocalization. Indeed, it is not significantly influenced neither by the quality of the dataset, nor by the choice of the multipolar model (the latter point was demonstrated in the section 3.3.1).

* A note regarding OOP contributions is in order here. The agreement between the results obtained for benzene and the results for the two benzyl rings of BAB is better for the SF% contributions at +1 a.u. with respect to the contributions at -1 a.u. . In addition, the latter show, in general, much higher esd's with respect to the former. The reason for this is unknown so far and it deserves further investigations.

NAPHTHYL RINGS

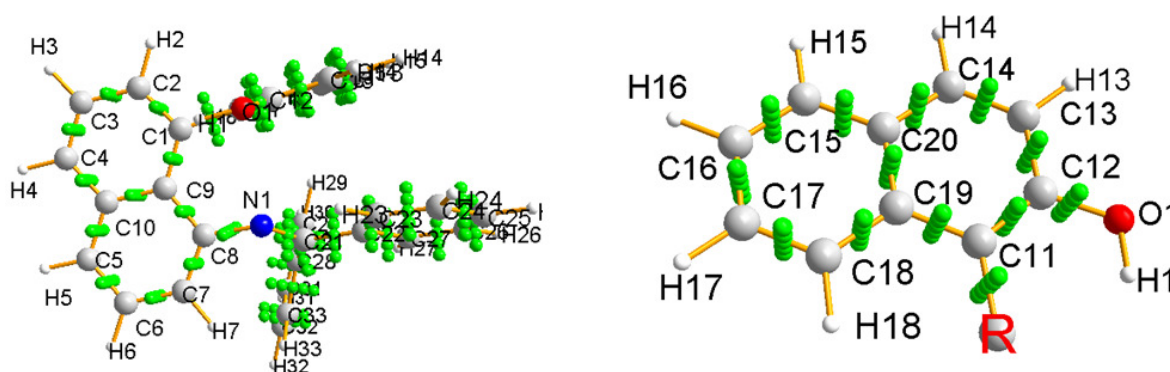


Figure 3.4 Atomic numbering for the naphthyl rings of *BAB*. Green spheres are placed along L2 eigenvectors each 0.5 au (from -1 au to +1 au with respect to the BCP) to show the direction of the eigenvectors associated with each bond. “R” is a label used to indicate the rest of the molecule (not shown here for the sake of clarity)

BAB molecule contains two doubly-substituted naphthalene-like rings: in the present discussion they will both be referred to as ‘naphthyl’ ring, although one of them is technically a naphthylol ring (following the convention used for benzyl rings, naphthyl ring will be labeled as C1...C10 and C11...C20). Their atomic numbering and the direction of L2 eigenvectors for the C-C bonds is reported in Figure 3.4. As for benzyl rings, also in this case we found that substituted C atoms show a lowering of SF% contribution to the bonds of the ring. Accordingly, the contributions for the substituted atoms will be discussed separately. SF% contributions for the non-substituted C atoms of the two naphthyl rings are reported in Table 3.12. The SF% contributions to those bonds which are symmetry-equivalent in isolated naphthalene (D_{2h}) are reported in the table as a unique, averaged value, in the same way as it was done for naphthalene molecular crystal (see previous section).

Table 3.12 SF% contributions for the two naphthyl rings of *BAB*. The averaged values are evaluated excluding the substituted atoms, whose contributions are in table 3.13. esd are reported in brackets. Regarding the meaning, see Table 3.10. Note that, to allow an easier comparison with table 3.10, there is a correspondence between the order in which the various atomic contributions are reported and the positions of the various bonds (compare the entries with Fig. 3.4 and 3.2).

NAPHTHYL RING (C1...C10)				
bonds	BCP		OOP	
	SF%ba	SF%nn	SF%ba	SF%nn
C1-C2/C7-C8/C5-C6/C3-C4	86.8(6)	4.17(3)	74.5(1.2)	7.2(1)
C2-C3/C6-C7	85.0(7)	5.78(0)	70.7(<1)	9.7(<1)
C1-C9/C9-C8/C5-C10/C4-C10	83.1(2)	7.12(7)	68.1(2)	11.3(1)
C9C10	81.7	9.79*	65.5	17.1*
NAPHTHYLOL RING(C11...C20)				
bonds	BCP		OOP	
	SF%ba	SF%nn	SF%ba	SF%nn
C15-C16/C13-C14/C11-C12/C17-C18	86.1(1)	4.1(2)	74.5(7)	7.0(5)
C16-C17/C12-C13	85.0	5.8	71.3(2)	10.4(<1)
C15-C20/C14-C20/C11-C19/C18-C19	83.2(1)	7.0(3)	68.2(2)	12.2(4)
C19/C20	81.3	9.8	64.2	17.6

The SF% values reported in Table 3.12 display a very good agreement with the results obtained for naphthalene molecular crystal. More importantly, the trends of SF% contributions in passing from benzene to the various bonds of naphthalene reported in ref. 52 and confirmed at the experimental level from the data of benzene and naphthalene molecular crystals (compare tables 3.8 and 3.10) are recovered in passing from benzyl to naphthyl rings of BAB (when non-substituted bonds are considered). This represents a further confirmation of what concluded in the discussion about the benzyl rings, *i.e.* that the experimental conditions do not significantly influence the values of SF% contributions. In light of this corroboration, it must be pointed out that the three systems considered so far are very different from a crystallographic point of view. In particular, it is worth stressing this difference by taking a closer look at the differences between the conditions of, for example, the benzene and BAB experimental determinations. Benzene crystallizes with only 6 symmetry-independent atoms and its geometry and thermal motion had been determined through a careful refinement exploiting a dataset from neutron diffraction (therefore only 87 parameters had to be included in the multipolar refinement). In addition, a careful analysis of ADPs, which included also a comparison with vibrational frequencies obtained from *ab-initio* calculation, was carried out in order to ensure a complete deconvolution of thermal motion from static ED distribution. As a result, the latter was determined in extremely accurate way, as confirmed by the fact that it was possible to use such ED distribution to calculate values of Electric Field Gradient and molecular quadrupole moment which were in quantitative agreement with other experimental measurements [55]. The geometry, thermal motion and ED distribution of BAB, on the other hand, were obtained from an X-ray diffraction experiment only. BAB crystallizes in a unit cell as large as 2284.1 \AA^3 which contains as many as 58 symmetry-independent atoms, which leads to 1066 parameters to be refined, and for this reason BAB can be considered as a quite challenging system for the experimental determination of ED distribution from X-ray diffraction. Although the multipolar refinement for BAB was carried out in a meticulous way as well, the experimentally derived ED distribution of BAB is necessarily significantly less precise (and probably also less accurate) than the one of benzene. The lower precision is also reflected in the higher SF% values esd's for benzyl rings of BAB with respect to benzene (one should also take into account that for the former system only 4 of the 6 bonds were considered, as the substituted atoms were excluded from the evaluation of averaged SF% contributions). Similar conclusions apply to the comparison between BAB and naphthalene. Nevertheless, a quantitative agreement was found between naphthyl rings of BAB and naphthalene and between benzyl rings of BAB and benzene. Since this correspondence involves four comparisons of two different functional groups (naphthyl and benzyl) and three different crystal systems, every hypothesis of fortuitous agreement (*e.g.* compensation of errors) can be ruled out. As a result, it is reasonable to conclude that the stability of SF-based approach to the study of electron delocalization is a general rule. This puts forward the SF as an ideal tool for the experimental ED-based study of electron delocalization.

The fact that the two naphthyl rings are substituted in two positions allows to investigate the substituent effect from the point of view of SF, as it was done for the benzyl rings. A very convenient way to analyze the effect of the substitution is obtained by exploiting the fact that some atoms are, in term of SF contribution, nearly equivalent. More in details, it was shown in this and the previous sections that those atoms which are symmetry related in isolated D_{2h} naphthalene give similar SF% contributions also in crystalline naphthalene and in the naphthyl rings of BAB, despite they are formally non-equivalent by symmetry*. Therefore, the effect of substitution can be seen by comparing the SF% contribution to a given

* although the contribution from each single atom is not shown in this dissertation, the fact that the esd's reported in Tables 3.10 and 3.12 are reasonably small is a proof of the fact that the contribution used to evaluate the average are similar among each other

bond from the substituted atom with the SF% contribution to the same bond from a non-substituted atom which would be symmetry-equivalent in D_{2h} naphthalene. The latter will be referred to as ‘reference atoms’ corresponding to a given substituted atom (e.g. the atom C4 is the reference atom corresponding to C1). The SF% contributions of substituted atoms and the ones of corresponding reference atoms are reported in Tables 3.13 and 3.14 for C1...C10 and C11...C20 rings, respectively. Since the substituent effect can be considered as a rather subtle feature of ED distribution, the theoretically derived SF% contributions* are also reported in order to have a corroboration of the picture obtained from experiment.

The ring C11...C20 is substituted in two positions –in *meta* with respect to each other- by a carbon atoms and an hydroxyl group. By contrasting the SF% contributions from a substituted atom with the contributions from its corresponding reference atoms, it can be immediately seen that the substitution leads to a lowering of SF% contributions of the substituted atoms to the bonds of the naphthyl ring. This is true for both the contributions to the nearest RPs (*i.e.* the RPs of the two C-C covalent bonds involving the substituted atom) and the ones far away. The lowering of SF% is seen even more clearly when the OOP contributions are considered, in accordance with the fact that the substitution causes a perturbation in the π delocalization pattern of the naphthyl ring.

Table 3.13 SF% contributions for the substituted atoms of the naphthyl ring C11...C20 of BAB. The contributions at +1.a.u and -1 a.u. are reported in brackets. See the main text for the definition of “reference contributions”. Experimental and theoretical (B3LYP/TZVP) results are reported in the first and second row, respectively.

contributions of substituted atoms		reference contributions	
atom/bond	SF%	atom/bond	SF%
C11/C19C20	2.1(3.6;3.6) 2.1(3.4;3.4)	C14/C19C20	2.4(4.3;4.3) 2.4(4.1;4.1)
		C15/C19C20	2.4(4.4;4.4) 2.5(4.1;4.2)
		C18/C19C20	2.5(4.4;4.4) 2.4(4.0;4.0)
<hr/>			
C11/C11C19	40.6(32.1;32.7) 40.6(33.5;33.2)	(C14/C14C20)	42.1(35.3;35.5) 41.7(34.9;33.2)
		C15/ C15C20	42.2(35.4;35.5) 41.8(35.0;34.9)
		C18/ C18C19	41.8(34.3;34.4) 41.6(34.6;34.9)
<hr/>			
C12/C12C13	40.5(31.9;31.5) 39.7(31.5;31.9)	C13/C12C13	41.7(35.3;35.0) 42.0(35.8;34.7)
		C16/C16C17	41.9(35.3;35.3) 41.7(35.2;35.2)
		C17/C16C17	43.0(36.1;35.9) 41.6(35.0;34.9)
<hr/>			
C12/C13C14	1.8(2.9;2.9) 2.0(3.0;3.0)	C17/C15C16	2.2(3.8;3.8) 2.4(3.9;3.9)
		C16/C17C18	2.4(4.2;4.2) 2.4(3.9;3.9)

* Isolated BAB, B3LYP/DZVP2

The naphthyl ring C1...C10 is also substituted in two positions (C1 and C8), and the substituent atoms are an sp^2 hybridized carbon and an iminic nitrogen (Fig. 3.4). The study of the substitution effect in this ring is particularly interesting since the two substituted atoms are in positions which would be symmetry-equivalent in D_{2h} naphthalene and for this reason they share the same reference atoms. Hence, this particular situation allows to make a comparison between the different effect of the two substituting atoms, namely the carbon and the nitrogen. Generally speaking, SF% contributions of substituted atoms is lower than the one of their corresponding reference atoms (Table 3.14) therefore validating the trend already seen for benzyl rings and for the C1...C10 naphthyl rings. By comparing the contribution of C1 and C8 to the various bonds, one may notice that the ones of C8 are always lower (although the difference for RPs of bonds which do not directly involve these two atoms is quite small). As a matter of fact, C8 is substituted by a nitrogen, while C1 is substituted by a carbon. Therefore, it seems that there is a correspondence between the electronegativity of the substituting atom and the lowering of SF%. This fact gives more credit to the hypothesis sketched in the previous section when discussing the effect of the substitution on benzyl rings, *i.e.* that the smaller contribution of the substituted atoms is caused by the fact that the substituent atom is more electronegative than hydrogen. This in turn, causes a deformation of ED distribution due to the electron-withdrawing effect of the more electronegative substituting atom.

Table 3.13 SF% contributions for the substituted atoms of the naphthyl ring C1...C10 of BAB. The contributions at + 1.a.u and -1 a.u. are reported in brackets. See the main text for the definition of "reference contributions"

contributions of substituted atoms		reference contributions	
atom/bond	SF%	atom/bond	SF%
C1/C1C9	40,8 (33,2;33,1)	C4/C4C10	42,3(35,4;35,2)
	40,6(33,1;32,7)		41,9(35,0;34,9)
C8/C8C9	40,5(32,4;32,7)	C5/C5C10	41,9(35,0;35,1)
	39,6(31,2;31,6)		41,7(35,2;35,2)
C1/C1C2	41,6(34,7;34,9)	C4/C3C4	43,3(36,7;36,8)
	41,7(35,4;35,0)		42,9(37,0;37,1)
C8/C7C8	41,4(34,5;34,6)	C5/C5C6	43,4(36,3;36,4)
	40,7(34,0;33,7)		42,7(37,3;37,3)
C1/C2C3	2,5(4,5;4,5)	C4/C2C3	2,9(5,2;5,2)
	2,6(4,3;4,3)		3,0(5,1;5,1)
C8/C6C7	2,5(4,5;4,4)	C5/C6C7	2,9(5,2;5,2)
	2,4(4,0;4,0)		3,0(5,1;5,1)
C1/C9C10	2,0(3,4;3,4)	C4/C9C10	2,5(4,4;4,3)
	2,0(3,3;3,3)		2,5(4,2;4,1)
C8/C9C10	1,9(3,2;3,1)	C5/C9C10	2,4(4,3;4,2)
	1,9(3,1;2,9)		2,5(4,2;4,1)

All the trends discussed so far for the substituent effect are exactly reproduced when theoretically-derived ED distribution is considered, confirming the reliability of the experimental results also in this case.

Whether the lowering in the SF% contribution of substituted atoms is due only to the enhanced electronegativity of atoms linked to the substituted carbons (hence electron charge is subtracted from the substituted C atom) or whether such enhanced electronegativity also induces an electron delocalization decrease inside the ring can be definitively established by considering the DIs. In particular, it is interesting to compare the DIs between atom pairs involving the substituted atoms with the atom pairs which would be symmetry equivalent in D_{2h} naphthalene (the latter will be called, in the present discussion, 'reference values', in a similar way to what was done for SF results), *e.g.* $DI(C8,C6)$ vs $DI(C5,C7)$. Since those two values are expected to be very close each other in absence of substituting atoms (since so are SF contributions, see discussion above), this comparison should be able to single out the effect of substitution on delocalization. In figure 3.5 some relevant values of DI reported. For the C1...C10 ring (Fig. 3.5a) the DI involving atoms C1 and C10 are always lower than their reference counterpart, and this is true no matter whether the DI is calculated between bonded or non-bonded atoms. The only exception is represented by the DI involving the two central atoms C9 and C10. Indeed, the values of $DI(C1,C10)$ and $DI(C8,C10)$, *i.e.* the ones concerning the substituted atoms, are almost equal to their corresponding reference values, namely $DI(C4-C9)$ and $DI(C5-C9)$ (the difference is too small to draw any conclusion from it). This might be caused by the fact that the atom C9, which is involved in both the reference couples, is situated in between the two substituted atoms, and might therefore be affected by the substitution as well. The lowering of DI between couples involving substituted atoms with respect to the corresponding reference values is found in the C11...C20 ring as well. Also in this case, however, there is an exception, *i.e.* that $DI(C12,C14)$ is not lower than its references values, namely $DI(C17,C15)$ and $DI(C16,C18)$. Since the latter two values are alike to each other, the origin of this unexpected similarity should be sought in the feature of the C12,C14 couple. Indeed, the same value in isolated naphthalene (C1-C3 in fig. 3.5c) is higher than all the three values mentioned above. In general, this fact deserve further investigations. All in all, despite the presence of two outliers values, the majority of the DI values calculated corroborates the substitution effect seen in the SF picture, namely a lowering of the electron delocalization between the substituted atoms and the rest of the ring. Therefore, despite the fact that SF is obtained from ED distribution only, it seems (once again) able to mirror the effect of electron delocalization.

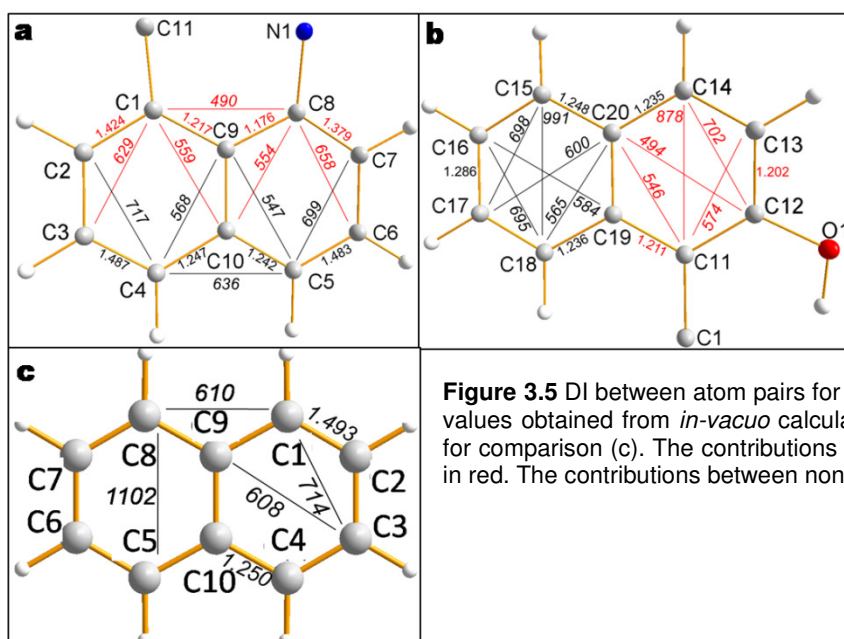


Figure 3.5 DI between atom pairs for the two naphthyl rings of BAB (a,b). The values obtained from *in-vacuo* calculations on naphthalene are also reported for comparison (c). The contributions involving substituted atoms are reported in red. The contributions between non-bonded atoms are multiplied by 10^4

CONJUGATED BONDS

As explained in section 3.2.1, the chemical connectivity of BAB offers an interesting case for the study of conjugation. From Fig. 3.3 and 3.4, one can see that there are several formally single bonds located between π bonds. This fact enabled us to explore the ability of SF to reveal the conjugation in this system from experimentally derived ED. In particular, the bonds C21-C22 and C21-C28 (see Fig. 3.3) are especially apt for this study since they link the N1-C21 double bond with the two benzyl rings. In addition, one of the rings (the C22...C27) lies in the same plane as the nodal plane of the π cloud of N1-C21^{*}, while the other ring (the C28...C33) is oriented perpendicular to it. For this reason, C21-C22 is expected to have a certain π character due to conjugation effects, while C21-C28 is not. From Fig. 3.3 it can be noticed that, as expected, the eigenvectors L2 of the bonds of the benzyl ring C22...C27 lie roughly parallel to the ones of the bonds C21-C22 and C21-N1, while the eigenvectors of the ring C28...C33, instead, are almost perpendicular to them. In this section, the ability of SF to discriminate between allegedly conjugated and single bonds (namely C21-C22 and C21-C28) will be explored.

Before looking at the SF results, it is worth taking a closer glance to the two bonds under investigation from other points of view. The interatomic distances of the two bonds are not very different from each other: 1.4974(2)Å and 1.4877(2)Å for C21-C28 and C21-C22, respectively. In addition, even the shortest between those two bonds is significantly longer than the average bond length for a conjugated C-C bond situated between an aromatic and an iminic group[†] [70]. Therefore, if a conjugation effect is present, it is not very strong. On the other hand, only C21-C22 displays a significant ellipticity (0.11), while ED at the C21-C28 BCP is almost spherically distributed (its ellipticity is as low as 0.01). A measure of the degree of conjugation can be obtained from the evaluation of DIs[‡]. Indeed, conjugation is expected to rise the DI value between non-bonded atoms as it happens in benzene and cyclohexadiene, where the DI between two carbon atoms in *meta* position (for cyclohexadiene the two atoms at the extremities of the allyl fragment are considered) is 0.075 and 0.072, respectively. Delocalization indices among atoms C21, C22, C28 and N1 are reported in Table 3.15

Table 3.15 DI between formally single bonds of BAB

AB→	C21C22	C21C28	C22N1	C28N1
δ (AB)→	1.014	0.958	0.100	0.096

The DI values reported in the table above indicate that there are more electrons delocalized between C22 and N1 than between C28 and N1. The difference, however, is as low as 4%. Therefore, as already hypothesized on the basis of bond lengths and ellipticities, there is a conjugation effect taking place on the C21-C22 bond, but such effect is not very strong, as it can be concluded from the fact that it has an only marginal repercussion on both molecular geometry and DI. It is interesting at this point to see whether and how the (slightly) different bonding situation of C21-C22 with respect to C21-C28 is reflected in the ED distribution. SF% values for the contribution at the C21-N1 bond are reported in table 3.14

^{*}The orientation nodal plane of the π orbital can be inferred by looking at the eigenvectors L2 reported in Fig. 3.4

[†]The average value for carbon-carbon bond in the group C_{aromatic}-C=N-C is 1.476 Å and 1.491 Å for conjugated and non-conjugated bonds, respectively.

[‡]calculated from *in-vacuo* B3LYP/DZVP2 wavefunction at the experimental molecular geometry.

Table 3.14 SF% contributions to the N1C21 double bond from the atoms of the two benzyl fragments bonded to C21. First line refers to exptl. results, while the second to theoretical ED obtained through B3LYP/DZVP2 (gaussian09) at crystal geometry

atom	SF% to N1C21 BCP	SF% to N1C21 at +1au	SF% to N1C21 at -1au
C22	1.6	2.5	2.6
	1.8	2.9	2.9
C28	1.5	2.3	2.6
	1.6	2.5	2.6

Although the conjugation effect is weak, it is clearly reflected by the SF% value. In particular, the contribution at the N1-C21 BCP and at the associated OOP points is higher for C22 than for C28, the former being the atom involved in the conjugated bond. Although the difference in SF% contribution is quite small, it must be pointed out that the same trend is obtained for both experimental and theoretical results. This confirms that the agreement with the picture provided by DI is not fortuitous but rather it is due to the difference in the ED distribution of the two bonds caused by the presence of conjugation effect. As a further confirmation, it is worth noticing that in the original paper by Farrugia *et al.* [58], it was reported that the ellipticity plots in the neighborhood of BCPs indicate that C21-C22 bond displays a significant π character, while C21-C28 does not. However, differently from SF, ellipticity plots do not allow a quantitative measurement of conjugation.

Although in the Table above the conjugation effects are investigated through the contribution from the atoms of the allegedly conjugated bond to the π bond, one may in principle reverse the situation and explore the conjugation effect by considering the contributions from the atom involved in the π bond to the BCP and OOP points of the supposedly conjugated bond. However, one should bear in mind that when a bond does not have π character at all (therefore ED is cylindrically distributed in the neighborhood of the BCP), the L2 direction cannot be associated with any particular physical meaning anymore. The OOP SF% contributions, therefore, lose their physical meaning as well. On the other hand, it is worth noticing that the N1 contribution at the BCP is slightly higher for the C21-C22 bond than for C21-C28 (5.44% VS 5.31% for experimentally derived results, 5.83% and 5.81% for the theoretical ones). This fact can be interpreted as an indirect sign of the more conjugated character of C21-C22, *i.e.* the higher contribution of N1 at C21-C22 BCP with respect to C21-C28 BCP is due to σ - π interdependency. In other words, the contribution from π orbitals is null at BCP, but the increased π character of the bond affects in turn the σ orbitals, leading to the increased contribution reported above (see ref. 52). Clearly, since the conjugation effect is small (see discussion above), the indirect effect is even smaller and therefore the difference in SF% contribution from N1 to the two BCPs is very small as well.

As a general guideline, we advise, when exploring the possible π conjugation effects, to look at the contributions from the two atoms involved in the supposedly conjugated bond to the π bonds which give rise to the conjugation effects.

3.4 CONCLUSIONS AND OUTLOOKS

In this chapter, results of the study of electron delocalization by means of the Source Function (SF) were presented. In particular, experimentally-derived ED was obtained from previously published single-crystal

X-ray diffraction datasets for three test cases, namely: benzene, naphthalene and 8'-benzhydrylideneamino-1,1'-binaphthyl-2-ol (BAB) molecular crystals. We explored the SF% contributions of the various atoms to the BCPs ED and to the ED at points shifted by 1 au along the second ED-Hessian eigenvector (*i.e.* the one associated with the second greatest eigenvalue), since such points are located in a region where there is a large contribution to ED from π orbitals [52]. For benzene and naphthalene, the ability of SF to detect electron delocalization from an ED obtained from *in-vacuo* calculations was already demonstrated by Monza *et al.* [52]. The results presented here are in close agreement with the ones obtained from *in-vacuo* calculation, demonstrating the stability of SF against the model used to obtain ED. For benzene, two different multipolar models were tested and they both led to the same picture, indicating that the choice of refinement strategy does not alter the SF description. For naphthalene, a correlation between SF contributions from distant atoms and DI between non-bonded atoms was shown. Regarding BAB, three main features were explored, namely: i) the SF% contribution of naphthyl and benzyl fragments, to be compared with results obtained from naphthalene and benzene; ii) the effect of substituent atoms on the SF picture, and iii) the ability of SF to detect subtle effects of π conjugation. The results for naphthyl and benzyl rings were calculated by excluding the contributions of substituted atoms and a very good agreement, both in SF contributions trends and in their absolute values, was found with the values obtained for benzene and naphthalene. The importance of this comparison lies in the fact that the agreement was found between ED distribution obtained from experiments carried out in different conditions and on different crystal systems, hence showing that SF description is also stable against the use of different datasets. The effect of substitution on aromatic rings was investigated by comparing the SF% contribution of the substituted atoms with the ones of the other atoms of the ring. It was shown that substitution leads to a lowering of SF%, both for theoretical and experimental ED distribution. In particular, the specific atom connectivity of BAB allowed us to compare the effect of the atoms bonded to the aromatic ring, namely H, C(sp²) and N. It was shown that SF% contributions of the substituted C atom decreases in passing from H to C and from C to N. This scale is in accordance with the electronegativity of the substituent atom and led us to hypothesise that the diminishing of SF contributions upon substitution is due to the electron withdrawing effect of the substituent atom. In general, the lesser degree of electron delocalization between the substituted atoms and the rest of the ring is confirmed by the DI values. Regarding conjugation, two bonds are particularly interesting for this investigation, as they both link an iminic group with the two benzyl rings of BAB. They are characterized however, by different torsion angles $C_{\text{aromatic}}-C=N-C$: in one case the angle favours conjugation, while in the other case it does not. By looking at bond lengths and DIs, it was shown that a conjugation effect is present, but its effect is small. SF is able to recover even this subtle feature. In particular, the contribution to the C=N bond from the C atom involved in the conjugated bond is slightly higher than the contribution of the C atom of the non-conjugated bond.

As a general conclusion, the investigation presented in this chapter puts forward SF as an ideal tool for the ED-based study of electron delocalization (and related phenomena), due on one hand to its stability against the method used to obtain ED and on the other hand to its remarkable ability in mirroring the changes in ED distribution caused by electron delocalization.

The next step in this investigation will be the application of the aromaticity index defined by Monza *et al.* [52] to experimentally-derived ED distributions.

REFERENCES

- [1] IUPAC. Compendium of Chemical Terminology, 2nd ed. (the "Gold Book"). Compiled by A. D. McNaught and A. Wilkinson. Blackwell Scientific Publications, Oxford (1997). XML on-line corrected version: <http://goldbook.iupac.org> (2006-) created by M. Nic, J. Jirat, B. Kosata; updates compiled by A. Jenkins. ISBN 0-9678550-9-8. [doi:10.1351/goldbook](https://doi.org/10.1351/goldbook). Although the IUPAC definition cited previously is the most recent and one, it must be mentioned that it exists another definition of "delocalization". However, the latter is more specific and regards mainly the electron delocalization associated to π conjugation (see: *PAC*, 1994, 66, 1077 on page 1104 of the IUPAC gold book cited above)
- [2] R. H. Mitchell. *Chem. Rev.* (2001), 101, 1301
- [3] J.E. McGrady, T. Lovell, R. Stranger. *Inorg. Chem.* (1997) 36, 3242.
- [4] H. Chevreau, I. d. P. R. Moreira, B. Silvi, F. Illas. *J. Phys. Chem. A* (2001) 105, 3570.
- [5] J. Cabrero, C.J. Calzado, D. Maynau, R. Caballol, J. P. J. Malrieu. *Phys. Chem. A* (2002) 106, 8146.
- [6] N. Suaud, A. Gaita-Arinò, J.M. Clemente-Juan, E. Coronado. *Chem. Eur. J.* (2004), 10, 4041
- [7] A. Soncini, P. Lazzeretti. *J. Chem. Phys.* (2003) 119, 1343.
- [8] C. F. Matta, J. Hernandez-Trujillo, R. F. W. Bader. *J. Phys. Chem. A* (2002) 106, 7369.
- [9] J. E. Gready, T. Hambley, K. Kakiuchi, K. Kobiuro, S. Sternhell, C. W. Tansey, Y. Tobe. *J. Am. Chem. Soc.* (1990), 112, 7537.
- [10] R. Dabestani, I. N. Ivanov. *Photochem. Photobiol.* (1999) 70, 10.
- [11] J. T. Hupp, R. D. Williams. *Acc. Chem. Res.* (2001) 34, 808.
- [12] A. V. Szeghalmi, M. Erdmann, V. Engel, M. Schmitt, S. Amthor, V. Kriegisch, G. Nöll, R. Stahl, C. Lambert, D. Leusser, D. Stalke, M. Zabel, J. Popp. *J. Am. Chem. Soc.* (2004) 126, 7834.
- [13] J. Sharman. *JACS* (1939) 115(9), 3527
- [14] C. Edmiston, K. Ruedenberg. *Rev. Mod. Phys.* (1963) 35, 457.
- [15] S. F. Boys. *Rev. Mod. Phys.* (1960) 32, 296.
- [16] J. M. Foster, S. F. Boys. *Rev. Mod. Phys.* (1960) 32, 300.
- [17] R. Daudel, M. E. Stephens, E. Kapuy, C. Kozmutza. *Chem. Phys. Lett.* (1976) 40, 194.
- [18] J. P. Foster, F. Weinhold. *J. Am. Chem. Soc.* (1980) 102, 7211.
- [19] A. E. Reed, L. A. Curtiss, F. Weinhold. *Chem. Rev.* (1988) 88, 899.
- [20] G. P. Bean. *J. Org. Chem.* (1998) 63, 2497.
- [21] N. Sadlej-Sosnowska. *J. Org. Chem.* (2001) 66, 8737.
- [22] F. M. Bickelhaupt, E. J. Baerends, *Angew. Chem., Int. Ed.* (2003) 42, 4183.
- [23] see, for example: J. Gerratt, D. L. Cooper, P. B. Karadakov, M. Raimondi. *Chem. Soc. Rev.* (1997) 87.
- [24] R. Daudel, R. F. W. Bader, M. E. Stephens, D. S. Borrett. *Can. J. Chem.* (1974), 52, 1310.
- [25] R. Daudel, H. Brion, S. Odier. *J. Chem. Phys.* (1955) 23, 2080.
- [26] O. M. Lopes Jr., B. Braïda, M. Causà, A. Savin *Advances in the Theory of Quantum Systems in Chemistry and Physics Progress in Theoretical Chemistry and Physics* Volume 22, 2012, pp 173-184
- [27] G. N. Lewis. *J. Am. Chem. Soc.* (1916) 38, 762.
- [28] E. Wigner and F. Seitz. *Phys. Rev.* (1933) 43, 804.
- [29] R. F. W. Bader, S. Johnson, T.-H. Tang. *J. Phys. Chem.* (1996) 100, 15398.
- [30] A. D. Becke, K. E. Edgecombe. *Journal of Chemical Physics* 1990, 92.
- [31] M. Kohout *Faraday Discuss.*, (2007) 135, 43.
- [32] R. Ponc. *Journal of Mathematical Chemistry* (1998) 23, 8.
- [33] X. Fradera, M. A. Austen, R. F. W. Bader. *J. Phys. Chem. A* (1999) 103, 304.
- [34] R. F. W. Bader (1990) *Atoms In Molecules: A Quantum Theory* Oxford: Clarendon Press
- [35] J. Poater, M. Duran, M. Solà, B. Silvi. *Chem. Rev.* (2005) 105, 3911.
- [36] P. Hohenberg, W. Kohn, *Phys. Rev.* (1964) B864, 136.

- [37] R. J. Gillespie, D. Humphreys, C. Baird, E. A. Robinson *Chemistry* (1990) Allyn & Bacon.
- [38] C. Gatti, V. R. Saunders, C. Roetti *J. Chem. Phys.* (1994) 101, 10686.
- [39] G. Merino, A. Vela, T. Heine *Chem. Rev.* (2005) 105, 3812.
- [40] E. Espinosa, E. Molins, C. Lecomte. *Chemical Physics Letters* (1998) 285, 170.
- [41] see, for example: P. Roversi, M. Barzaghi, F. Merati, R. Destro *Can. J. Chem.* (1996) 74, 1145.
- [42] R. F. W. Bader, T. S. Slee, D. Cremer, E. Kraka. *J. Am. Chem. Soc.* (1983) 105, 5061.
- [43] D. Cremer, E. Kraka, T. S. Slee, R. F. W. Bader, C. D. H. Lau, T. T. Nguyendang, P. J. MacDougall. *J. Am. Chem. Soc.* (1983) 105, 5069.
- [44] R. F. W. Bader, C. Gatti, *Chem. Phys. Lett.* (1998) 287, 233.
- [45] G. Arfken, in *Mathematical Methods for Physicists*, 3rd edn, Academic Press, Orlando Florida, 1985, p. 897
- [46] S. Grabowsky, T. Schirmeister, C. Paulmann, T. Pfeuffer, P. Luger. *J. Org. Chem.* (2011) 76, 1305.
- [47] C. Gatti, *Structure & Bonding* (2012) 147, 193.
- [48] C. Gatti, F. Cargnoni, L. Bertini. *J. Comput. Chem.* (2003) 24, 422.
- [49] G. Gilli, P. Gilli *Journal of Molecular Structure* (2000) 552, 1.
- [50] C. Gatti, D. Lasi. *Faraday Discussions* (2007) 135, 55.
- [51] L. J. Farrugia, P. Macchi. *J. Phys. Chem. A* (2009) 113, 10058.
- [52] E. Monza, C. Gatti, L. Lo Presti, E. Ortoleva. *J. Phys. Chem. A* (2011), 115 (45), 12864.
- [53] C. F. Matta, J. Hernandez-Trujillo *J. Phys. Chem. A* (2003) 107, 7496.
- [54] A. Volkov, P. Macchi, L. J. Farrugia, C. Gatti, P. Mallinson, T. Richter, T. Koritsanszky, XD2006 - A Computer Program Package for Multipole Refinement, Topological Analysis of Charge Densities and Evaluation of Intermolecular Energies from Experimental and Theoretical Structure Factors, 2006. See also <http://xd.chem.buffalo.edu/>
- [55] H.-S. Bürgi, S. C. Capelli, A. E. Goeta, J. A. K. Howard, M. A. Spackman, D. S. Yufit. *Chem. Eur. J.* (2002) 8, 3512.
- [56] J. Oddershede, S. Larsen *J. Phys. Chem. A* (2004) 108, 1057.
- [57] E. Huber-Buser. Organic Chemistry Laboratory, Swiss Federal Institute of Technology, Zurich, Switzerland, 1988
- [58] L. J. Farrugia, P. Kočovský, H.-M. Senn, S. Vyskočil. *Acta Cryst.* (2009) B65, 757.
- [59] A. Ø. Madsen. *J. Appl. Cryst.* (2006) 39, 757.
- [60] R. Dovesi, V. R. Saunders, C. Roetti, R. Orlando, C. M. Zicovich-Wilson, F. Pascale, B. Civalleri, K. Doll, N. M. Harrison, I. J. Bush, P. D'Arco, M. Llunell, *CRYSTAL06 User's Manual*, University of Torino, Torino, Italy, 2006.
- [61] A. D. Becke, *J. Chem. Phys.* 1993, 98, 5648.
- [62] R. Krishnan, J. S. Binkley, R. Seeger, J. A. Pople, *J. Chem. Phys.* 1980, 72, 650-654.
- [63] Note that the second-order density matrix is not available for DFT wavefunction. We calculated them with the formalism used for Hartree Fock wavefunction (formally exact for such wavefunction):
$$DI(\Omega_A, \Omega_B) = 2 \sum_{k,l} S_{kl}(\Omega_A) S_{kl}(\Omega_B)$$
Where $S_{kl}(\Omega_A)$ is the overlap matrix between k -th and l -th molecular orbitals integrated over the atomic basin Ω_A . Although the use of this formalism for DFT molecular orbitals (so-called Kohn-Sham orbitals) is not rigorously exact, Poater *et al.* [J. Poater, M. Solà, M. Duran, X. Fradera. *Theor Chem Acc* (2002) 107:362] showed that DI calculated in this way display the same trend as the ones calculated from Hartree Fock wavefunction (in general, the DI calculated from DFT tends to overestimate electron delocalization).
- [64] Frisch, M. J., Trucks, G. W., Schlegel, H. B., Scuseria, G. E., Robb, M. A., Cheeseman, J. R., Scalmani, G., Barone, V., Mennucci, B., Petersson, G. A., Nakatsuji, H., Caricato, M., Li, X., Hratchian, H. P., Izmaylov, A. F., Bloino, J., Zheng, G., Sonnenberg, J. L., Hada, M., Ehara, M., Toyota, K., Fukuda, R., Hasegawa, J., Ishida, M., Nakajima, T., Honda, Y., Kitao, O., Nakai, H., Vreven, T., Montgomery, J. A. Jr, Peralta, J. E., Ogliaro, F., Bearpark, M., Heyd, J. J., Brothers, E., Kudin, K. N., Staroverov, V. N.,

-
- Kobayashi, R., Normand, J., Raghavachari, K., Rendell, A., Burant, J. C., Iyengar, S. S., Tomasi, J., Cossi, M., Rega, N., Millam, J. M., Klene, M., Knox, J. E., Cross, J. B., Bakken, V., Adamo, C., Jaramillo, J., Gomperts, R., Stratmann, R. E., Yazyev, O., Austin, A. J., Cammi, R., Pomelli, C., Ochterski, J. W., Martin, R. L., Morokuma, K., Zakrzewski, V. G., Voth, G. A., Salvador, P., Dannenberg, J. J., Dapprich, S., Daniels, A. D., Farkas, Ö., Foresman, J. B., Ortiz, J. V., Cioslowski, J. & Fox, D.J. (2009). Gaussian 09, Revision A.1 Gaussian, Inc., Wallingford CT, 2009
- [65] N. Godbout, D. R. Salahub, J. Andzelm, E. Wimmer. *Can. J. Chem.* (1992) 70, 560.
- [66] Available from Prof. R. F. W. Bader's Laboratory, McMaster University, Hamilton, ON, Canada L8S 4M1; <http://www.chemistry.mcmaster.ca/aimpac/>.
- [67] C. Gatti, *TOPOND98: an electron density topological program for system periodic in N (N=0-3) dimensions*, User's Manual, CNR-ISTM, Milano, Italy, 1999
- [68] Gatti, C. Unpublished result (available upon request)
- [69] J. M. Perez-Jorda, A. San-Fabian, F. Moscardo. *Comp. Phys. Comm.* (1992) 70, 271.
- [70] F. H. Allen, O. Kennard, D. G. Watson, L. Brammer, A. G. Orpen, R. J. Taylor. *Chem. Soc. Perkin Trans. II* (1987) S1.

Chapter IV: chemical bonding in coordination polymers



1.1 INTRODUCTION

The topic that will be faced in this chapter is the investigation of chemical bonding in Coordination Polymers (CPs) through the analysis of their experimental ED distribution. In particular, accurate X-ray diffraction datasets have been measured for two simple CPs, namely $\text{Co}(\text{HCOO})_2(\text{H}_2\text{O})_2$ and $\text{Cu}(\text{HCOO})_2(\text{H}_2\text{O})_2$ (in the rest of the discussion these compounds will be simply called ‘Co formate’ and ‘Cu formate’). It is worth pointing out that, while in the two previous chapters of this dissertation new applications of ED-based descriptors were carried out, the main focus of this investigation will be *the use* of ED-based descriptors to understand the chemical bonding in the two compounds mentioned above. The experimental part of this work was carried out in the Department of Chemistry of the Aarhus University (Aarhus, Denmark)

4.1.1 COORDINATION POLYMERS

When organic moieties and metal atoms (or cluster) crystallize together, they give rise to materials displaying a wealth of remarkable properties particularly useful in chemistry, physics and potentially even in everyday life (see *infra*) [1]. Such kind of materials are generally referred to as Coordination Polymers (CoPs*), although in some specific cases they are called Metal Organic Framework (MOF) (the boundary between these two definitions was not clear until August 2013, *i.e.* when IUPAC established official definitions for the terms: coordination polymer, coordination network and metal-organic framework [2]). In the last two decades, the research in this field has undergone a tremendous growth [3], and new applications of this kind of materials are likely to be discovered in the near future. A brief overview of the properties and (potential) applications of CoPs is given in the following.

- **CATALYSIS.** The application in catalysis of materials often requires a high porosity and therefore this kind of application is, by definition [1], associated to MOF. However, a few examples are known in which the catalytic process is taking place on the surface of CoPs (an example is the compound $\text{In}_2(\text{OH})_3(1,4\text{-bdc})_{1.5}$ [4])
- **CHIRALITY** Although the possibility of creating chiral CoPs is intriguing in its own, the research in this field is mainly aimed at the creation of materials to be used for enantiomeric separation. An example is reported in ref 5
- **ELECTRICAL CONDUCTIVITY.** This property is certainly not one of the main focuses of the research in the field of CoPs, as short M-M contacts are required in order to obtain a significant electrical conductivity, and generally in CoPs metal centers are completely surrounded by organic ligands. However, some effort has been put in this direction and materials with anisotropic conductivity of magnitude comparable to that of metals have been synthesized [6]
- **LUMINESCENCE** CoPs displaying luminescence have the advantage, with respect to their molecular counterpart, of having higher thermal stability. Moreover, different metals can be coordinated to the ligands to tune the emission wavelength. Cadmium-based compound seems to be the most promising CoPs for luminescence applications, and investigation in this direction are being carried out [7]
- **MAGNETISM** Due to the presence of metal centers, many CoPs are characterized by magnetic ordering (ferro-, antiferro- or ferri- magnetic), which usually occurs at low temperature. The interest in this field

* The simple acronym “CP” is avoided since already used in the previous chapters to define Critical Points

is triggered by the possibility of creating light-weight magnets [8]. Therefore, this research field is mainly directed towards the discovering of materials having a high ordering temperature, as close as possible to the ambient conditions.

- **SPIN CROSSOVER** some investigations are being carried out [9] to explore the possibility of finding CoPs which display the ability of undergoing spin-transitions induced by temperature or by pressure. The aim is to find bistable systems which show the hysteresis phenomenon, possibly in a temperature range not too far from the ambient one. Such kind of materials would have several useful applications, *e.g.* temperature sensors or information storage.

The aforementioned properties are the ones which have been the subject of the major part of investigations in the last years. Clearly, many other properties can be attributed to CoPs and the field is in continuous development. From the discussion above, it should result clear that CoPs are going to play a fundamental role in material science. Therefore, a deep understanding of the chemical bonding in this class of materials is of paramount importance to gain insights in the structure-properties relationship and eventually also in the self-assembly processes which lead to the formation of certain kind of CoPs rather than others.

The aim of the project presented in this chapter is indeed the analysis of chemical bonding in the $M(\text{HCOO})_2(\text{H}_2\text{O})_2$ class of compounds, whose components -namely 3d transition metals, water and formic acid- are ubiquitously found in CoPs. A general description of structure and magnetic properties of the compounds investigated in this chapter is given in the next section.

4.1.2 3d METAL FORMATE DIHYDRATE $M(\text{HCOO})_2(\text{H}_2\text{O})_2$: STRUCTURE AND MAGNETIC ORDERING

An interesting feature of the family of compounds $M(\text{HCOO})_2(\text{H}_2\text{O})_2$ (where M is a metal) is the fact that when the metal belongs to the 3d transition series from d^5 to d^{10} (*i.e.* $M=\text{Mn,Fe,Co,Ni,Cu,Zn}$), isostructural crystals are formed. In particular, they all crystallize in the space group $P2_1/c$ with 4 formula units in the unit cell [10]. In these compounds, there are two symmetry-independent metal centers, located in the special positions (in particular M(1) and M(2) are in Wyckoff positions 2a and 2d, respectively). One of them (labeled as M(1) in this work) is coordinated to six formate moieties, while the second (labeled as M(2) in this work) is surrounded by two formate and four water molecules (Figure 4.1). All in all, both metal centers are coordinated to a slightly distorted octahedrons formed by six oxygen atoms. The two symmetry independent formate molecules form bridges between two metal atoms. In particular, one of these two formate linkers act as a bridge between M(1) and M(2), while the second connects two symmetry-related M(1) atoms (figure 4.1). The overall crystal packing pattern is depicted in Figure 4.1: Metal centers M(1) are connected to four M(1) and two M(2), while atoms M(2) are only connected to two M(1) centers (this is because M(2) are coordinated to four water molecules, which act as terminal ligands).

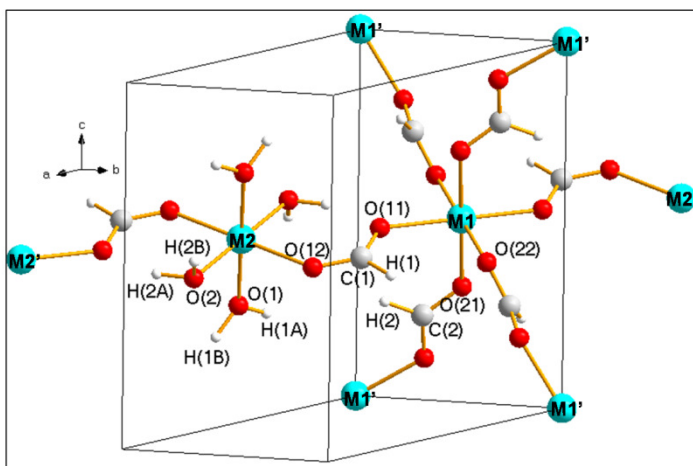


Figure 4.1. Representation of a selected portion of the crystal structure of the family of compounds $M(\text{HCOO})_2(\text{H}_2\text{O})_2$ ($M = \text{Mn, Fe, Co, Ni, Cu, Zn}$). For organic ligands, only the ones belonging for the asymmetric unit are labeled, while for the metals, the non-symmetry independent atoms are labeled with the symbol " ' ".

The compounds investigated in this work are the ones containing copper and cobalt. The electronic structure of both metal atoms are characterized by partially filled d shell and because of that, they are paramagnetic. In addition, they show some degree of magnetic ordering at very low temperature.

The Cobalt compound undergoes a phase transition causing magnetic ordering below 5.1 K [11]. In particular, adjacent Co(1) atoms (*i.e.* Co(1) atoms which are linked by a formate molecule) are ordered antiferromagnetically [12]. Directly linked Co(1) and Co(2) centers instead are ordered ferromagnetically. This magnetic ordering gives rise to two canted magnetic sublattices. Because of that, a net magnetic moment is obtained despite the antiferromagnetic ordering. Regarding the Cu formate, despite magnetic susceptibility [13] and heat capacity [14] were measured at different temperatures, no general agreement was reached regarding the magnetic structure. The detailed discussion about the data which were used to establish the magnetic structure of Cu compound is beyond the purpose of this dissertation and the interested reader is referred to refs 13, 14, 15,16 and 10. We just point out that in refs 15 and 16 authors concluded in favor of a ferromagnetic ordering and because of that we decided to model the crystal as ferromagnetic in the theoretical calculations (see section 4.4).

4.2 CRYSTALLIZATION AND X-RAY DIFFRACTION: OBTAINING THE EXPERIMENTAL ELECTRON DENSITY OF $\text{Co}(\text{HCOO})_2(\text{H}_2\text{O})_2$ AND $\text{Cu}(\text{HCOO})_2(\text{H}_2\text{O})_2$

4.2.1 FROM SYNTHESIS TO FINAL DIFFRACTION PATTERN: EXPERIMENTAL PROCEDURE

The crystals of Cu and Co formates have been obtained following the same procedure, described in the following. Metal-acetate compounds are dissolved into a solution of water and ethanol. The resulting solution is then poured onto a layer of formic acid giving rise to the formation of crystals at the interface

due to the diffusion process* [10]. The crystals formed in this way are usually plate-shaped, probably due to the method used to synthesize them. To obtain samples suitable for the ED distribution determination, several batches were scrutinized with the aim of finding crystals of appreciable thickness (the ideal thickness was around 0.2-0.3 mm, *i.e.* slightly smaller than the diameter of X-ray beam). However, the other two dimensions of the thick crystals chosen as possible candidates were often too large to fit the X-ray beam. Therefore, they were cut with a sharp blade. Eventually, three crystals for each compound were chosen as possible candidates for the final data collection and mounted on a thin glass fiber using epoxidic glue. For each of those crystals, a preliminary data collection at ambient temperature was carried out. Subsequently, the best sample of each compound was used for the final data-collection (pictures of the final crystals are reported in Fig. 4.2).

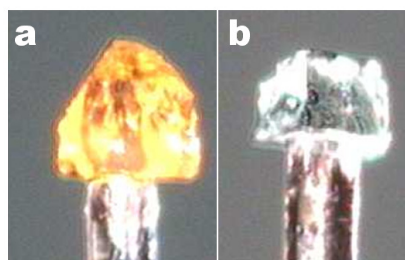


Figure 4.2. Photo of the crystals used for the low-temperature X-ray data collection. a) cobalt b) copper

The criteria considered to choose the final samples were, besides the absence of twinning phenomena, R_{int} (the smaller the better) and the average intensity of structure factors (the higher the better). The diffractometer used for all the data collections reported in this chapter was a Oxford Diffraction (now Agilent Technologies UK Ltd.) SuperNova system located at the Department of Chemistry, Aarhus University. For the final, low-temperature data collection, the samples were flash cooled at 100(1) K using a liquid nitrogen cryostream system (from Oxford Cryosystems).

The strategy for data collection was calculated using the program CrysAlisPro [17]. The latter allows the user to set some parameters for the data collection such as the desired total duration of the experiment, the completeness and the average intensity. Then, the collection strategy (*i.e.* the position of the diffractometer axis and the exposition time during the experiment) is calculated accordingly, based on the information arising from a preliminary data collection[†]. For both Co and Cu formate, we set the experiment in such a way to obtain a high average redundancy and a 100% completeness up to 1.32 in $\sin\theta/\lambda$. As for the average redundancy, it was set to 16 for Cu formate and 14 for Co formate (the former crystal had a stronger scattering power with respect to the latter, therefore it was possible to aim for an even higher average redundancy and at the same time keep a reasonable duration of the experiment, which was in both cases about 10 days long).

The program package CrysAlisPro was also used to integrate the intensity under the diffraction peaks and to correct the resulting reflections for polarization and Lorentz effect [18]. The same program package (in particular ABSPACK program was used) was exploited to apply a correction factor which takes into account the lowering of measured intensities due to adsorption phenomena. In particular, a numerical Gaussian grid method based on the indicization of the faces of the sample (the latter are defined by the user with an

* Such crystals were synthesized in the department of Chemistry of the university of Aarhus (Denmark)

[†] Clearly, at the end of the experiment, the average intensity and redundancy may slightly differ from the programmed values, since the calculation of the strategy is based on the examination of a small (therefore not very accurate) diffraction pattern coming from the preliminary data collection.

ad-hoc graphical subroutine) was employed. Finally, the program SORTAV [19] was used to merge equivalent reflections (number of reflections before and after the merging process are reported in Tables 4.1 and 4.2 for Cu and Co formate, respectively) and produce the final file containing Miller indices, F^2 and $\sigma(F^2)$ for each structure factor. Only reflections measured at least three times were considered in the merging procedure. In the next two sessions, a detailed description for the two multipolar models used for Co and Cu compounds is reported.

4.2.2 MULTIPOLAR REFINEMENT OF $\text{Cu}(\text{HCOO})_2(\text{H}_2\text{O})_2$

The structure of the compound was solved using the program SHELX [20]. The latter was then used to perform the spherical atom refinement to obtain an initial estimation of atomic positions and thermal motion. The resulting structure was used as starting geometry in XD2006 [21]. The atomic Scattering Factors were taken from the databank of Su, Coppens and Macchi (see ref. 21) and corrections for anomalous dispersion as well as for (isotropic) extinction were applied to the model. For all the refinement steps described in the following, the least-squares procedure was stopped when the maximum shift/s.u. among all the refined parameters was lower than 10^{-6} . In the first step, only atomic positions and thermal motion were refined*, including in the least-squares procedure only the data having $\sin\theta/\lambda > 0.8$ †. The position of hydrogen atoms were modified after each cycle so that the distance from the nearest (bonded) atom equals the average X-H neutron distance [22]. Anisotropic thermal motion parameters were refined for heavy atoms, while for hydrogen atoms the isotropic thermal parameter was kept fixed at 1.5 times the value of the atom to which they are bonded‡. In the successive steps, the populations of the multipoles were refined, increasing in each step the maximum angular momentum of the multipoles (from $l=0$ to $l=4$). For hydrogen atoms, only monopole and dipole populations were refined. Odd order multipoles are not allowed for Cu atoms (due to the fact that they lie in a special position, see paragraph 4.1.2), therefore they were not refined. Once all the multipole populations have been refined, the expansion/contraction parameters k and k'^{\S} were refined too (one for each atom type, excluding H atoms for which such parameters were kept fixed at the default values**). To improve the description of the ED distribution on the two metal centers, an attempt was made to refine different k and k' parameters for the two Cu atoms. The refinement of two different k' , however, led to serious convergence issues and therefore only one k' parameter for both metals was refined (it was nevertheless possible to refine two different k for the two metal centers). In the final refinement step, all the parameter refined previously (geometry, ADPs of heavy atoms, multipole population and k/k' parameters) were refined together. Note that all the measured reflections were included in the refinement††. Relevant data regarding the crystal system, the data collection and the multipolar model are reported in Table 4.1.

* The two metals atoms lie in a special position (see section 4.1.2) and therefore their position was not refined.

† high angle data are not affected by the aspherical features of the atomic scattering factor, therefore this choice allows one to obtain a starting geometry which is not biased by the –not yet refined- aspherical features

‡ Only for the sake of calculating the thermal motion of H, the so-called Uiso value was used as value for the thermal motion of heavy atoms

§ We remind the reader that k parameter modifies the core density, while k' acts on the deformation density, *i.e.* on the multipoles

** Since neither position nor thermal motion of hydrogen atoms were refined, the introduction a fine feature such are the expansion/contraction parameters would not make any sense

†† actually those very, very weak reflections which, due to non-perfect estimation of the X-ray detector background signal, had negative intensity were excluded from the refinement. They were 363 in total

Table 4.1 Relevant data relative to the X-ray diffraction experiment on the Cu formate.

Formula	Cu(HCOO) ₂ (H ₂ O) ₂
space group	P2 ₁ /c
T [K]	100 (1)
a, b, c cell edges [Å]	8.4930(<1),7.0828(1),9.4259(1)
β[°]	97.079(1)
Wavelength [Å]	0.71073
ρ _{calc} [g cm ⁻³]	1.863
μ [mm ⁻¹]	2.00
integrated reflections (unique)	159505 (10925)
sinθ/λ max [Å ⁻¹] (completeness)	1.35(99.8%)
R _{int}	2.93%
N refined parameters	346
R(F ²), wR(F ²)	0.0129,0.0363
Gof	0.9704

RELIABILITY OF THE FINAL MODEL

A multipolar model is considered reliable when one can reasonably assume that there are no systematic errors and that the random errors -which are always present in an experimental determination of a quantity- do not significantly affect the final result. There are many criteria to establish the reliability of the multipolar model. In general, they are based on diverse ways to analyze the difference between the structure factor calculated from the multipolar model and the measured ones. An overall measure is given by the values of R(F²), which are certainly good for the system here considered (see table 4.1). A closer inspection can be obtained by considering the residual density map, which is the (fast) Fourier transform of the difference between measured and calculated structure factors [18]. The highest peaks are reported in table 4.2.

Table 4.2. List of the strongest residual peaks of the fast Fourier transform of the difference between observed and calculated structure factors for Cu formate [e Å⁻³]

+0.51	+0.50	+0.36	+0.32	-0.29	-0.27	-0.27	-0.25
-------	-------	-------	-------	-------	-------	-------	-------

Form this table, one may notice that the two highest peaks are significantly stronger than all the other. They are situated far from atomic position, and precisely they are both in the neighborhood of the Co(2)-O(12) bond*. However, it must be pointed out that the magnitude of the highest and lowest peaks of residual density is comparable to the values obtained for similar compounds [10]. Therefore, one can generally conclude that the residual peaks analysis does not indicate the presence of systematic errors, especially considering the very high resolution of the data included in the refinement (Table 4.2)[†]. The residual density maps in the planes containing the copper atoms and the coordinating oxygen atoms are reported in Figure 4.3.

* Such peaks are partially visible in fig. 4.2.

[†] It must be pointed out that, as customarily done, only data having $I/\sigma(I) > 3$ are included in the evaluation of the residual map (where $\sigma(I)$ is the standard deviation associated to the measured intensity)

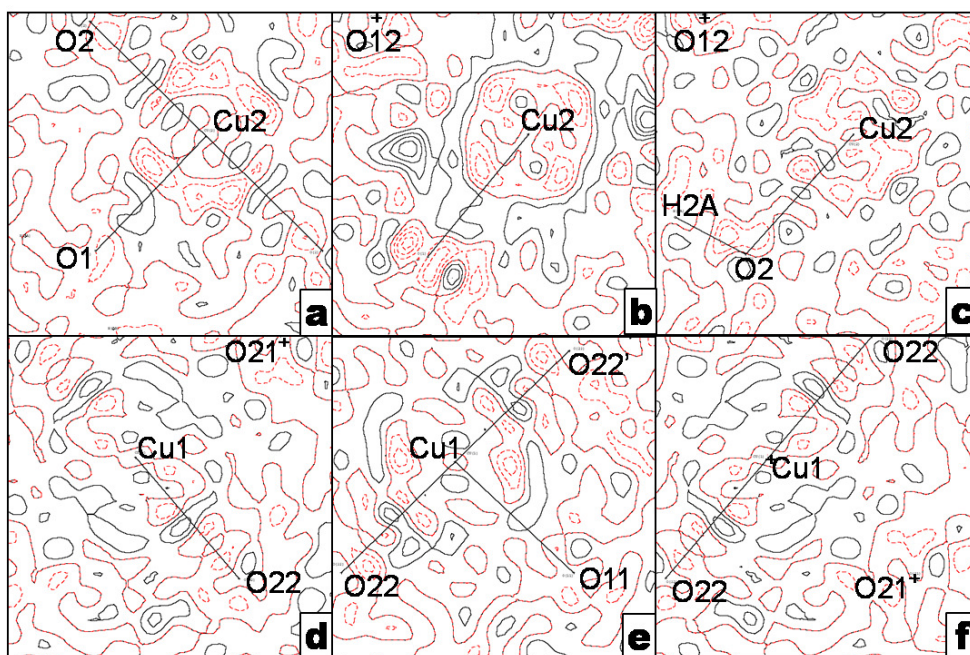


Figure 4.3 Residual density maps in the plane containing the three symmetry-independent atoms labeled in each panel (atoms which do not belong to the asymmetric unit are labeled with the symbol “ ‘ ”). Note that solid straight lines indicates those bonds which are contained in the plane of the plot and which are not longer than 2.3 Å. Contour lines are $\pm 0.1 \text{ e } \text{Å}^{-3}$. Positive and negative contours are indicated by black solid and red dotted, respectively.

Aside from the presence of the peaks discussed above, the map can be considered rather flat and featureless, which is a further indication of the absence of systematic errors in the multipolar model. The normal probability plot (DR plot) is a graphical technique which may be used to assess whether a set of data follows a normal distribution. Points obtained from a normal distribution should lie on a straight line as the one depicted in fig. 4.4a. Deviation from normal distribution leads to the appearance of points significantly away from such line, although deviation in the extremities are quite common for experimental data (severe deviations from a normal distribution would causes departure from the straight line also near the center of the plot, see paragraph 4.2.3). The normal distribution plot for the dataset of Cu formate is reported in fig. 4.4a. Although a significant deviation can be seen in the left part of the plot, the rest of the points perfectly lie on the diagonal and therefore such dataset can safely be considered free from systematic errors.

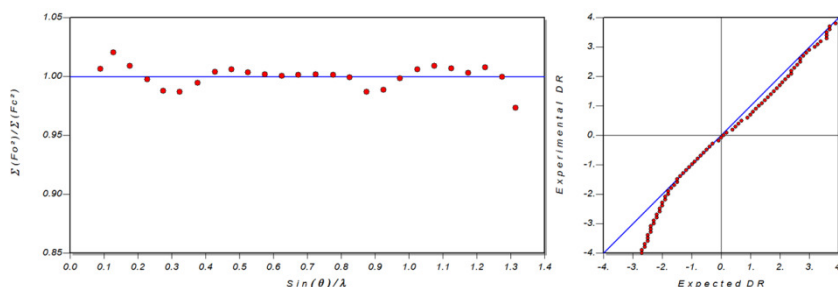


Figure 4.4 Right: DR data plot. Left: difference between calculated (from the multipolar model) and observed structure factors at different resolutions for the Cu formate.

Finally, the plot of the difference between observed and calculated structure factors (figure 4.4b), gives a further confirmation of the fact that our multipolar model is able to give a good fitting of the measured data at all resolutions.

4.2.3 MULTIPOLAR REFINEMENT OF $\text{Co}(\text{HCOO})_2(\text{H}_2\text{O})_2$

For the Co formate, the same refinement strategy adopted for the Cu compound was used, including the use of all the measured data. However, the results of the least-squares process gave several indications of a bad data fitting. In particular, quite high residual density peaks were obtained (the strongest peaks were $+1.508/-1.090 \text{ e } \text{\AA}^{-3}$). In addition, the normal probability plot revealed severe deviations from the ideal straight distribution, hence a great departure from normal distribution of the dataset can be inferred (fig 4.5a). A closer inspection revealed that the multipolar model was not able to fit the data at very high resolution (above 1.25\AA^{-1} in $\sin\theta/\lambda$), as can be seen from the plot reported in fig. 4.5b. Therefore we concluded that those data were severely affected by random errors (probably due to their low intensity*) and we excluded them from the multipolar refinement.

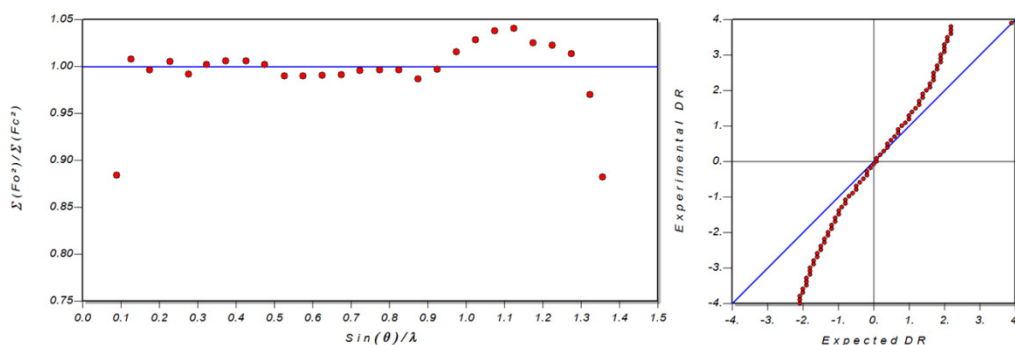


Figure 4.5. DR plot (right) and difference observed-calculated for the structure factors at different resolutions (left) for the refinement of Co formate carried out using the whole collected dataset.

More in details, we excluded from the refinement all the data having a resolution higher than 1.25\AA^{-1} and all the data having an $I/\sigma(I)$ ration smaller than 1 (*i.e.* all those data whose intensity is smaller than their own standard deviation). The application of such cutoff drastically improved the quality of the fitting. The residual density peaks in this new model range from $+0.38$ to $-0.25 \text{ e } \text{\AA}^{-1}$. Regarding the multipolar model, it must be pointed out that, differently from the Cu formate, neither in the initial refinement (the one including all the data), nor in the final one was it possible to refine different k and k' parameters for the two metal hence only one k and one k' parameter was considered for Co atoms. The residual density map is rather flat and featureless (figure 4.6). The DR plot (fig. 4.7a) has a distribution similar to the one already obtained for Cu formate, therefore the same conclusions hold true for the Co compound.

* As a comparison, the average intensity of the data in the resolution range $1.06-1.35 \text{\AA}^{-1}$ in $\sin\theta/\lambda$ is 3.7 and 31.0 for Cobalt and Copper compound, respectively.

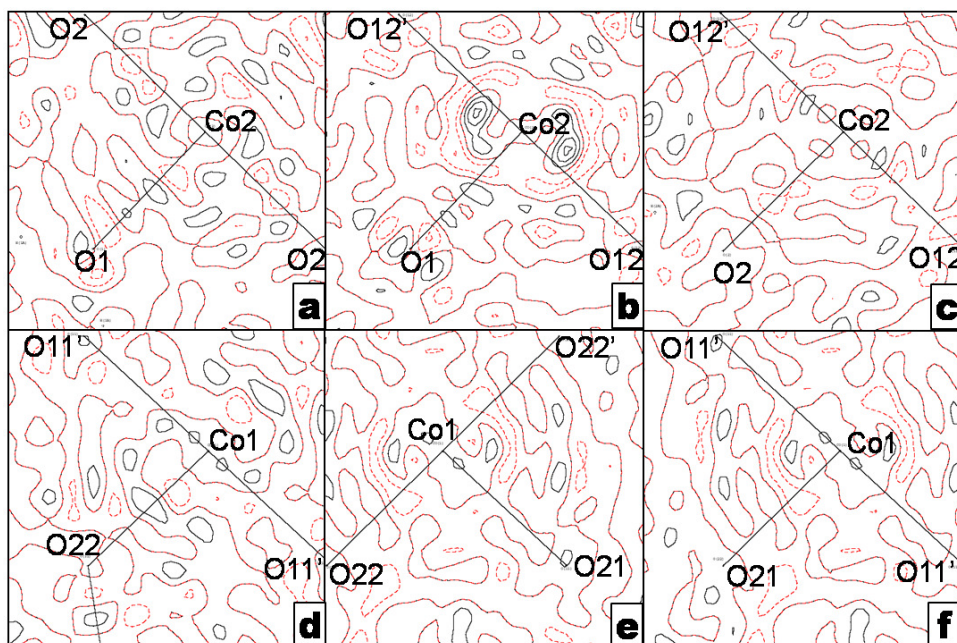


Figure 4.6 Residual density maps in the plane containing the three symmetry-independent atoms labeled in each panel (atoms which do not belong to the asymmetric unit are labeled with the symbol “'”). Note that solid straight lines indicates those bonds which are contained in the plane of the plot and which are not longer than 2.3 Å. Contour lines are $\pm 0.1 \text{ e } \text{Å}^{-3}$. Positive and negative contours are indicated by black solid and red dotted, respectively.

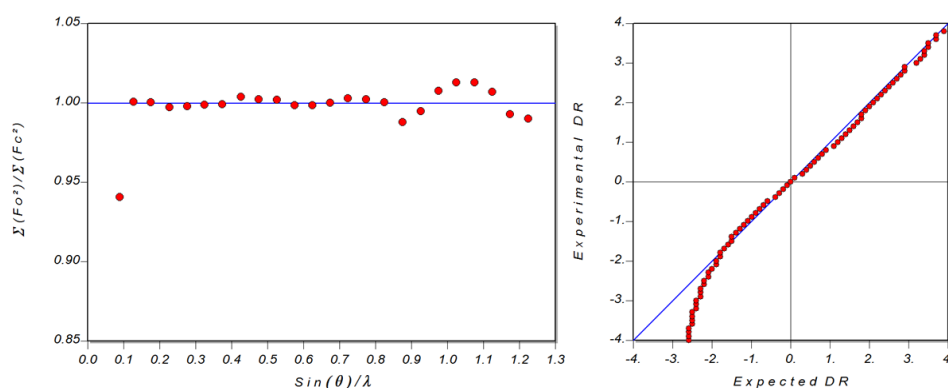


Figure 4.7 Right: DR data plot. Left: difference between calculated (from the multipolar model) and observed structure factors at different resolutions for the Co formate.

Finally, a plot of the difference between calculated and measured structure factors against the data resolution is reported in Fig. 4.7b. This plot indicates an overall good agreement between the model and the measured data for all the resolution range included in the least-squares procedure. Note that this plot shows substantially improvement with respect to the one reported in fig. 4.5b.

Relevant data regarding the crystal system, the data collection and the multipolar model are reported in Table 4.3. The very low R-factor reported in such table represent a further confirmation of the good fitting of the multipolar model to the dataset when the abovementioned cutoff is applied.

Table 4.3 Relevant data relative to the X-ray diffraction experiment on the Co formate. The values regarding the agreement indices between observed and measured structure factors (the last two lines of the table) refers to the model in which the cutoff was applied to the data included in the refinement (see main text)

Formula	Co(HCOO) ₂ (H ₂ O) ₂
space group	P2 ₁ /c
T [K]	100 (1)
a, b, c cell edges [Å]	8.6611(<1), 7.1249(<1),9.2784(1)
β[°]	97.413(1)
Wavelength [Å]	0.71073
ρ _{calc} [g cm ⁻³]	1.819
μ [mm ⁻¹]	1.57
integrated reflections (unique)	167517 (12602)
sinθ/λ max [Å ⁻¹] (completeness)	1.35 (99.3 %)
R _{int}	2.84%
N refined parameters	352
R(F ²), wR(F ²)	0.0138,0.0349
Gof	1.0239

4.3 EXPERIMENTAL RESULTS

In this section, the results obtained from the X-ray diffraction experiments (namely crystal geometry and ED-based descriptors analysis) are presented. Particular attention will be given to the M-O bonds characterization.

4.3.1 Co(HCOO)₂(H₂O)₂

GEOMETRY

As for all the other compounds of the M(HCOO)₂(H₂O)₂ family [10], in the Co formate the coordination sphere of the two unique Cobalt atoms display some significant deviation from octahedral symmetry. When the angles are considered (Table 4.4), one notice immediately that the coordination sphere of Co1 shows a greater departure from octahedral geometry with respect to the atom Co2.

Table 4.4 O-Co-O angles in Co formate. Note that for each metal center only the three symmetry-independent angles are reported. Standard deviations in brackets.

O11-Co1-O22	92.608(5)
O11-Co1-O21	93.541(6)
O21-Co1-O22	90.400(6)
O12-Co2-O1	89.964(9)
O1-Co2-O2	91.322(6)
O12-Co2-O2	89.474(7)

Regarding bond distances (see Table 4.5, second column), they are all significantly different among each other (this of course holds true only for the three symmetry-independent ones). However, the Co2-O1 bond is significantly shorter than the remaining two symmetry independent bonds, namely Co2-O12 and

Co2-O2. Regarding the formate linkers, the C-O bond lengths (Table 4.6, second column) are all quite similar to each other and slightly longer than the C-O distance found in the isolated molecule (*i.e.* 1.2466 Å [23]). Finally, the geometry of the two water molecules with respect to the Co2 center is quite different. This can be seen by calculating the angle between the plane containing the three atoms of the water molecule and the line joining Co2 and the oxygen atom of the water*. While for the water 2 (*i.e.* the water containing the atom O2), such angle is 55.5°, perfectly in line with an hypothetical approach of the water molecule through one of its lone pairs†, the angle calculated for water 1 (*i.e.* the water containing the atom O1) is as low as 9°. This means that the atom Co2 and the three atoms forming the water molecule 1 lie almost in the same plane. The reason for this unexpected geometrical arrangement may be sought in the type of Co-O1 interaction as well as in the HB network. Indeed, regarding the latter, it must be pointed out that there is a network of quite strong O-H...O HBs involving the water molecules and the oxygen atoms of the formate linkers (table 4.7). Being a structural feature, the presence of such HB network is common to all formates in the isostructural series of formate Mn-Zn (see section 4.1.2), although the strength of the HB bonds may be different in the various compounds.

Table 4.5 Co-O distances and bond critical points properties in Co formate. Note that for each metal center only the three symmetry-independent bond lengths are reported. Standard deviations in brackets. λ 's indicate the eigenvalues of the ED Hessian matrix at BCP (in other words they represent the magnitude of the main curvatures of ED at BCP)

bond	d_{A-B} [Å]	ρ_{BCP} [e/Å ³]	$\nabla^2 \rho_{BCP}$ [e/Å ⁵]	d_{BCP-A} [Å]	d_{BCP-B} [Å]	λ_1 [e/Å ⁵]	λ_2 [e/Å ⁵]	λ_3 [e/Å ⁵]
Co1-O11	2.1300(1)	0.421(4)	6.316(4)	1.052	1.078	-1.75	-1.73	9.80
Co1-O21	2.0913(1)	0.453(4)	7.186(5)	1.036	1.055	-1.89	-1.79	10.87
Co1-O22	2.0627(1)	0.494(4)	7.807(5)	1.019	1.044	-2.23	-2.07	12.11
Co2-O1	2.0463(2)	0.503(6)	8.331(7)	1.013	1.033	-2.29	-2.15	12.78
Co2-O2	2.1219(1)	0.429(4)	6.354(5)	1.046	1.076	-1.81	-1.75	9.91
Co2-O12	2.1460(1)	0.399(4)	5.937(4)	1.060	1.086	-1.60	-1.56	9.10

Table 4.6 C-O distances and bond critical points properties in Co formate. ϵ represents the ellipticity. Standard deviations in brackets.

bond	d_{A-B} [Å]	ρ_{BCP} [e/Å ³]	$\nabla^2 \rho_{BCP}$ [e/Å ⁵]	ϵ [e/Å ⁵]
C1-O11	1.2619(2)	2.62(3)	-18.3(2)	0.08
C1-O12	1.2574(2)	2.58(2)	-16.7(2)	0.04
C2-O22	1.2581(2)	2.52(2)	-11.9(1)	0.06
C2-O21	1.2540(2)	2.55(2)	-9.2(1)	0.08

Table 4.7 Hydrogen bonds distances and bond critical points properties in Co formate. Standard deviations in brackets. Since H positions were not refined (see paragraph 4.2), standard deviations are not reported for geometrical parameters

D-H...O [Å]	$d_{H...O}$ [Å]	angle _{DHO} [deg]	ρ_{BCP} [e/Å ³]
O2-H2A...O11	1.797	157.6	0.19(2)
O2-H2B...O22	1.784	173.7	0.16(2)
O1-H1A...O21	1.769	175.7	0.16(3)
O1-H1B...O11	1.740	177.1	0.17(2)
C1-H1...O1	2.875	163.0	0.02(<1)

* Note that this angle is equivalent to the θ angle defined in scheme 2.4 (section 2.4.4) when the S...S NCI geometry have been discussed.

† According to VSEPR, the vector joining the oxygen atom center with the lone pair should form an angle of approximately 54.5° (=109/2) with the plane containing the three atoms of the molecule

ELECTRON DENSITY DISTRIBUTION

As stated in the introduction, the main goal of this investigation is to gain insights into the chemical bonding in the class of compounds $M(\text{HCOO})_2(\text{H}_2\text{O})_2$, where M is Cobalt in the present case. According to QTAIM [24], chemical interactions are characterized by the presence of Bond Paths, and information about the interaction under investigation can be extracted from the calculation of several properties at the BCP. Regarding the Co-O interactions, the ED at BCPs (table 4.5) is, as expected, lower than the values which are typically found in covalent organic bonds (see, for example the C-C bonds investigated in chapter III). The Laplacian of ED is positive, due to the dominance of the positive curvature parallel to the BP (λ_3) over the two negative ones (λ_1 and λ_2). Although positive value of ED-laplacian has been associated to closed-shell interactions [25], it is nowadays well known that for interactions involving metal atoms positive values of ED Laplacian can be found also in those cases where the interaction has some partial covalent character (see, for example [26]). All in all, however, the ED values at BCPs lie in the typical range observed for metal-organic interactions with no significant covalent character. The comparison among the BCPs of the six symmetry independent Co-O bonds reveals the expected trends, *i.e.* the bonds having shorter Co-O distance have higher values of $\rho(r)$, $\nabla^2\rho(r)$ and curvatures at BCP (table 4.5). As for the latter, in passing from weaker to stronger interactions, λ_3 grows faster than the other two curvatures, leading to the observed increase in the values of ED Laplacian. For all what was said so far, it can be straightforwardly concluded that, in the present case, only a limited amount of information can be extracted from analysis of ED properties at the BCP. Therefore, other ED-based tools have to be employed to gain real insights into the Co-O interactions (see *infra*). For the BCPs of the C-O bonds within the formate linkers (table 4.6), ED and ED Laplacian lie in the ranges typical for values of covalent polar bonds (see, for example, ref [27]). In particular, ellipticities are significantly different from zero, indicating therefore a partial double bond character. The remaining BCPs found in this compound are the ones related to C-H bonds and to the HBs. As for the latter, the geometry and ED at BCP for O-H...O interactions are reported in table 4.7. From such table, it can be seen that the values of ED at BCP is typical of quite strong HBs [28]. Because of that, for the $\text{Mn}(\text{HCOO})_2(\text{H}_2\text{O})_2$ it was hypothesized that these interactions may even play a role in the magnetic ordering of the compound. Theoretical calculations will be carried out in order to establish, through the analysis of the spin density and related quantities, whether this is the case for the compounds here investigated.

Regarding the Co-O bonds, a step further in the understanding of their physical origin can be obtained by analyzing the distribution of ED concentration and depletion regions in the valence shell of the metal [29]. The latter is formed by 4s and 3d electrons. Since the former orbitals are by definition spherically symmetric, the analysis of Valence Shell Charge Concentrations (VSCCs, *i.e.* the minima of ED Laplacian*) of the metal centers may give precious information concerning the occupancy and orientation of d orbitals. The same analysis, when carried out on oxygen atoms, allows one to infer their hybridization (see also the discussion at the beginning of paragraph 3.1.2). Regarding the latter, the VSCC analysis reveals the expected hybridization state for oxygen atoms (figure 4.8), namely sp^2 (*i.e.* three minima, one for the double C-O double bond and two for the lone pairs) for the oxygen atoms of the formate linkers and sp^3 (four VSCCs, two for bonds and two for lone pairs) for the ones of water.

* Rigorously speaking, the term 'VSCC' is often used in literature to indicate those regions of the valence shell where the ED-laplacian is negative (which include the ED-laplacian minima). In this dissertation, however, the term VSCC will be used –for sake of brevity– to denote the ED-laplacian minima

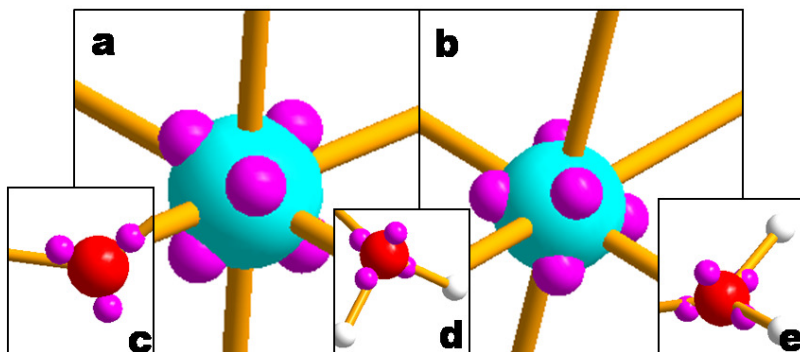


Figure 4.8 VSCCs (violet small spheres) on atoms: a) Co2 b) Co1 c) O12 d) O2 e) O1. Bonds to neighboring atoms are indicated by yellow lines

All such oxygen atoms display one charge concentration directed towards the metal. This is also true –quite unexpectedly– for the water1 (fig. 4.8e), whose tetrahedral arrangement of the VSCC is therefore distorted (see the discussion above for the orientation of this molecule with respect to Co2). On the other hand, the VSCCs of both Co atoms are directed away from the Co-O bond, as often found for metal-ligands bonds. In summary, VSCC of the oxygen atoms point in between the VSCC (*i.e.* towards regions of charge depletion) of the metal (fig. 4.8a-b). This kind of interaction, usually referred to as “key-lock” [29], indicates that the electrostatic contribution plays a dominant role. In particular, energy stabilization is mainly obtained through the breaking of degeneracies of d orbitals described in the well-known Crystal Field Theory (CFT) [30]. According to CFT, for a Cobalt in an octahedral environment, two of the three orbitals having t_{2g} symmetry (namely d_{xy} , d_{yz} and d_{zx}) are expected to be doubly occupied, while the remaining t_{2g} orbital and the two e_g (namely $d_{x^2-y^2}$ and d_{z^2}) should be occupied by only one electron* (figure 4.9a, up). In the case of the so-called ‘low-spin’ configuration, which is unlikely due to the nature of the ligands [30], t_{2g} are doubly occupied while the remaining electron goes into one of the e_g orbitals (figure 4.9a, down). Both these electronic configurations, however, are at odd with the disposition of the VSCC showed in figure 4.8. Indeed, the preferential occupation of t_{2g} orbitals must manifest itself through the presence of eight VSCC directed toward the vertices of a cube, while an occupation of two out of three t_{2g} orbitals must lead to VSCC resembling the vertices of a parallelepiped [31]. Instead, in the present case the VSCC on both metal atoms have an overall octahedral disposition, which is typical of a preferential occupation of e_g orbitals [31]. Since it is reasonable to assume that in this system a donation/back-donation mechanism, if present, is not strong enough to perturb the disposition of VSCC of the metal center[†], the latter is most likely the result of a d orbital occupation which is reversed with respect with what would be expected on the basis of CFT. In particular, one can explain the observed VSCC distribution by hypothesizing a d orbitals scheme in which the z Cartesian axis is directed toward the faces of the octahedral coordination (fig 4.9b). Within this orientation, the crystal field stabilization energy would be obtained by doubly occupying the e_g orbitals (*i.e.* the ones pointing away from the ligands) leading to the observed octahedral distribution of VSCC (fig. 4.9 c). The occupation of d orbitals can be obtained from experimental ED distribution (in particular from the population of even-order multipoles) as shown by Holladay et al. [32]. Obviously, the orbitals population

* Note that such description refers to a ideal octahedral environment, while the coordination sphere of the Co is slightly distorted (see geometry description). The departure from the perfect octahedral symmetry causes a further splitting of the energy levels. However, when the distortion is not strong (as in the present case), the d orbitals occupation is expected to follow anyway CFT rules

[†] this assumption is justified by the SF contributions, see *infra*, which indicate that the covalent component of Co-O bonds is not significant More importantly, confirmation is also obtained from theoretically-derived results, see section 4.4.

depends on the orientation of the Cartesian reference system. By orienting the Cartesian axis towards the ligand, the 'conventional' CFT picture is obtained (*i.e.* preferential occupation of t_{2g} orbitals). However, there are less subjective methods to orient the axis, *e.g.* by maximizing or minimizing the population of certain orbitals. When this procedure is applied in order to maximize the population of e_g orbitals, the resulting Cartesian axis are oriented almost exactly towards the observed VSCC (Cartesian axis oriented in this way are represented in figure 4.9b, along with the resulting orbital population).

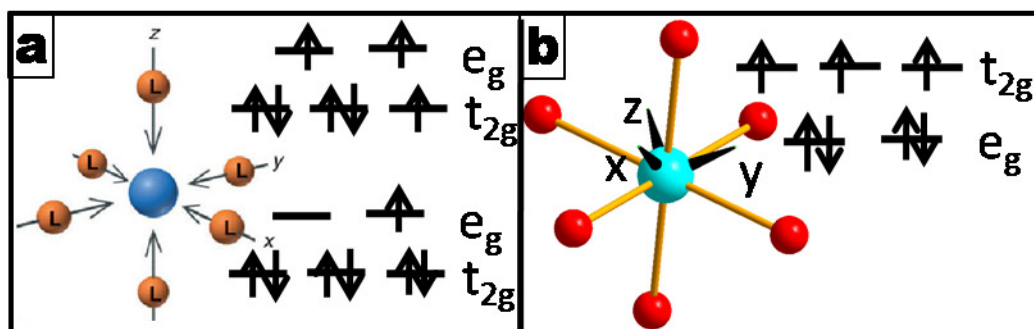


Figure 4.9 a) coordinate system and d orbital occupancies (up: high-spin configuration; down: low spin configuration) coordination in the crystal field theory b) system and d orbital occupancies in the proposed model. Note that the orientation of axis is also the one obtained from experimentally-derived d orbital populations when the e_g occupancy is maximized

Table 4.8 experimentally-derived d orbitals occupancy (see main text for details) expressed as percentage of the total d orbitals population.

	d_{z^2}	d_{xz}	d_{yz}	$d_{x^2-y^2}$	d_{xy}
Co1	0.225	0.178	0.190	0.237	0.170
Co2	0.219	0.186	0.186	0.255	0.155

Although this cannot be considered as a definitive proof of the proposed d orbital scheme, it is certainly a hint in that direction. Being orbitals an object intrinsically related to the wavefunction, theoretical calculations are needed in order to definitively establish whether the d-orbital scheme proposed here is correct. Some preliminary results are reported in section 4.4. The MO picture as well as the spin density distribution obtained for a model compound $\text{Co}_2(\text{HCOO})_7(\text{H}_2\text{O})_4$ confirm the hypothesis proposed here for the d orbital occupancy of metal centers. The unusual orbital picture described above is of paramount importance not only for the implication in inorganic chemistry as an exception to the CFT, but even more importantly because it may lead to an explanation of the magnetic ordering observed for the Co formate (see paragraph 4.1).

Regarding the properties of atomic basins as defined by QTAIM [24], atomic charges and volumes are reported in table 4.9. Worth of noticing is the fact that both cobalt atoms display a similar charge, and that the latter is significantly lower than the formal value of +2. The charge of oxygen atoms, on the other hand, has a value greater than unity. Such high values are not surprising, as charges around -1 are often found of organic oxygen atoms in neutral organic molecules (see, for example, ref. 27). On the other hand, it can be seen that the overall charge of formate moieties (-0.7 and -0.8) is lower than the formal -1 value while the water molecules are almost neutral. Therefore, the picture offered by QTAIM consists in a separation of charge between formate linkers and metal centers which is lower than the one expected on the basis of formal atomic charges.

Table 4.9 charge and volume of the atomic basins defined in QTAIM for the symmetry-independent atoms of Co formate

Atom	charge	volume(au)	atom	charge	volume(au)
Co(1)	1.23	10.54	C(1)	1.78	7.12
Co(2)	1.30	10.85	C(2)	1.61	8.44
O(11)	-1.33	15.10	H(1)	0.23	6.18
O(12)	-1.38	17.93	H(2)	0.31	5.97
O(21)	-1.35	16.50	H(1A)	0.64	1.99
O(22)	-1.35	17.08	H(1B)	0.67	1.80
O(1)	-1.24	18.87	H(2A)	0.65	1.63
O(2)	-1.16	18.45	H(2B)	0.67	1.87

The integration over QTAIM atomic basins allows one to calculate the Source Function (SF) contributions at BCPs, in order to see the chemical bond from an additional perspective. For the Co-O bonds, the bonded atoms (Co+O) contribute to roughly 60% of the density at BCP (examples for two Co-O bonds –one involving water and another involving a formate linker- are reported in fig. 4.10^{*}). Such values are typical for metal-organic interactions [33]. In general, the higher is the SF% contribution from the bonded atoms to the ED at BCP, the more covalent is the bond, being higher than 80% for typical open-shell organic bonds (see, for example, the C-C bonds of benzene, chapter II and III). Therefore, SF picture indicates that the Co-O bonds of the Co formate do not have a strong covalent character. Regarding the remaining atoms of the system, other significant contributions to the Co-O BCP are given by the atoms covalently bounded to the O atoms, namely H atoms for water and OHC group for formate linkers (fig. 4.10a). For the latter, by summing up the contributions from the whole molecule, one obtains a value of 45%. Similarly, H atoms contribution to 10% to the H₂O-Co BCP leading to a value of 47% for the water whole molecule (fig. 4.10b). Generally speaking, for a given Co-O interactions, the only significant SF% contributions come from the metal center and from the molecule coordinated to it, the contributions of the remaining atoms of the system being very small. Thus, the picture of Co-O bonds offered by SF points towards an interaction between the metal atom and the ligand as a whole rather than the somehow more localized interaction between oxygen and cobalt. Indeed, for the Co-O BCPs of this system, the sum of the contributions of metal and ligands ranges from 70% to 80% of the total ED, a value which is comparable to that obtained for two covalently bonded atoms at their BCP. As a final comment regarding SF results, we note that for C-O bonds of formate moieties, a significant contribution comes from the O atom not directly involved in the bond, mirroring the expected (π) electron delocalization taking place within the OCO fragment (see chapter III).

* The SF contributions for the 6 symmetry-independent Co-O bonds are very similar (within 3%) and they are not all reported for sake of brevity. The contributions for the water1 are slightly higher, being 33.6%, 39.1%, 4.9% and 4.5% for Co, O1, H1A and H1B, respectively

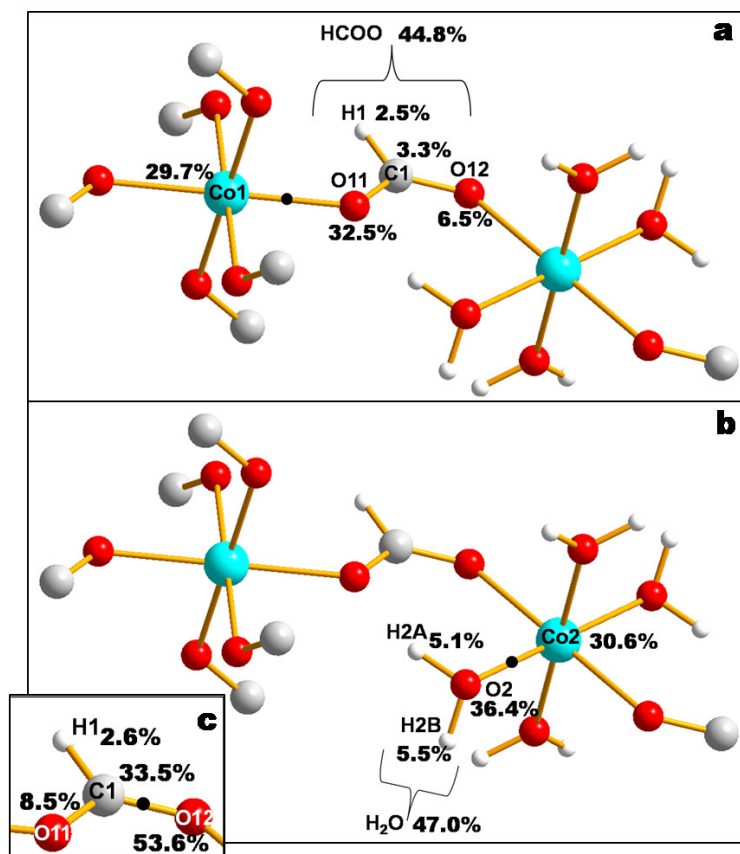


Figure 4.10 Source Function contributions to some relevant BCPs in Co formate (reported as percentage of the total ED at BCP). BCPs used as reference points are indicated by black dots. For each reference point, only values higher than 3% are reported

4.3.2 $\text{Cu}(\text{HCOO})_2(\text{H}_2\text{O})_2$

GEOMETRY

The Cu compound $\text{Cu}(\text{HCOO})_2(\text{H}_2\text{O})_2$ has the same atom connectivity as Co formate (see the discussion regarding the isostructural series $\text{M}(\text{HCOO})_2(\text{H}_2\text{O})_2$). A peculiar feature of the Cu compound is the fact that both metal centers display two (symmetry-related) bonds which are significantly longer than the remaining four (table 4.11). In other words, the octahedral coordination undergoes an elongation along one direction (conventionally the z one). This is due to the well-known Jahn-Teller (JT) effect [34], *i.e.* the stabilization of the system obtained by removing the degeneracy* of orbitals (the e_g ones when an octahedrally coordinate d^9 metal is considered, as in this case). Although the JT effect affects both metal centers, the Cu2-O12 bond is significantly longer than Cu1-O21, indicating that such effect is stronger for the atom Cu2. Regarding the remaining 4 symmetry-independent Cu-O bonds, it is worth noticing that they are all significantly shorter and stronger than in the Co compound.

As for O-Cu-O angles, the octahedral coordination of the Cu atoms is also distorted (table 4.10). While for the metal center Cu1 the distortion is similar to the one found for Co formate, the atom Cu2 displays a greater angular departure from ideal octahedral values.

* Although in this case, due to the departure from octahedral symmetry, there is 'nearly-degeneration' of orbitals

Table 4.10 O-Cu-O angles in Cu formate. Note that for each metal center only the three symmetry-independent angles are reported. Standard deviations in brackets

O11-Cu1-O22	92.499(6)
O11-Cu1-O21	92.340(6)
O21-Cu1-O22	90.553(6)
O12-Cu2-O1	90.529(8)
O1-Cu2-O2	89.332(6)
O12-Cu2-O2	93.471(6)

The JT distortion has in turn a repercussion on the geometry of the formate linkers (note that the two symmetry-independent elongated Cu-O bonds involve the two symmetry-independent formate moieties, *i.e.* each formate molecule has one oxygen involved in the JT distorted bond with the metal). Indeed, both the symmetry-independent formate linkers have one of the C-O bonds significantly longer than the other (table 4.12). For both the formate linkers, the shorter bond is the one involving the oxygen atom which form the JT distorted bond with the metal. Considering that in the Co formate all the C-O bonds have a bond length slightly greater than in gas phase (see section 4.3.1), it can be hypothesized that the interaction of the oxygen of the formate with the metal center leads to a weakening of the C-O bond. This fact may be explained by assuming the presence of a (although weak) back-donation from the d orbital of the metal to the π^* orbital of the formate. Theoretical calculations will be carried out in order to gain a deeper understanding into the type of Cu-O interaction which leads to the observed geometry.

Regarding the water molecules, in the Cu compound one of the two symmetry-independent ones is tilted with respect to the 'ideal' geometry which would allow the water to approach the metal through a lone pair. A similar situation was already found for the Co formate (see previous section). However, this effect is less pronounced for Cu formate with respect to the Co compound. Indeed, the angles between the O-Cu vector and the plane containing the water molecule are 28.5 and 53.5 for water1 and water2, respectively (the angle for water 1 is as low as 9° for Co formate).

Table 4.11 Cu-O distances and bond critical points properties in Cu formate. Note that for each metal center only the three symmetry-independent bond lengths are reported. Standard deviations in brackets. λ 's indicate the eigenvalues of the ED Hessian matrix at BCP (in other words they represent the magnitude of the main curvatures of ED at BCP)

bond	d_{A-B} [Å]	ρ_{BCP} [e/Å ³]	$\nabla^2\rho_{BCP}$ [e/Å ⁵]	d_{BCP-A} [Å]	d_{BCP-B} [Å]	λ_1 [e/Å ⁵]	λ_2 [e/Å ⁵]	λ_3 [e/Å ⁵]
Cu1-O11	2.0069(1)	0.502(5)	9.064(6)	1.022	0.986	-2.48	-2.38	13.93
Cu1-O21	2.3336(1)	0.232(2)	3.819(2)	1.180	1.154	-0.90	-0.88	5.59
Cu1-O22	1.9666(1)	0.556(5)	10.337(7)	1.003	0.963	-2.77	-2.62	15.73
Cu2-O1	1.9526(2)	0.551(6)	10.245(9)	0.981	0.971	-2.55	-2.35	15.15
Cu2-O2	2.0048(2)	0.524(6)	8.921(8)	1.018	0.988	-2.72	-2.50	14.14
Cu2-O12	2.3931(2)	0.211(2)	3.269(2)	1.203	1.191	-0.80	-0.75	4.81

Table 4.12 C-O distances and bond critical points properties in Cu formate. ϵ represents the ellipticity. Standard deviations in brackets

bond	d_{A-B} [Å]	ρ_{BCP} [e/Å ³]	$\nabla^2\rho_{BCP}$ [e/Å ⁵]	ϵ
C1-O11	1.2761(2)	2.50(2)	-20.9(1)	0.14
C1-O12	1.2457(2)	2.73(2)	-25.2(1)	0.04
C2-O22	1.2750(2)	2.47(2)	-14.7(1)	0.05
C2-O21	1.2430(2)	2.72(2)	-23.7(1)	0.02

ELECTRON DENSITY DISTRIBUTION

ED and curvatures for the Cu-O BCPs are reported in table 4.13. The bonds which are elongated due to JT effect (hereinafter 'JT bonds') display, as expected, lower ED and curvatures at BCP. The remaining Cu-O BCPs show an ED higher with respect to the Co-O bonds (table 4.11), in accordance with the fact that the latter are longer and hence presumably weaker. The same holds true for C-O bonds in formate linkers: the C-O bonds opposite to the JT bonds, *i.e.* the longest ones, are characterized by lower ED. Regarding NCI, the HB network in the Cu compound is generally stronger (see ED at BCPs in table 4.13) than in Co formate, as can be seen by H...O distances and ED at corresponding BCPs. In particular, the O1-H1B...O12* is significantly stronger than the remaining HBs. In addition, this bond constitutes the only direct bridge between Cu metal centers (M2 centers are not directly linked one another, see section 4.1). For these reasons, it may be hypothesized that this bond is playing an important role in the magnetic ordering of Cu formate. Theoretical calculations will be carried out to establish whether this is actually the case.

Table 4.13 Hydrogen bonds distances and bond critical points properties in Co formate. Standard deviations in brackets. Since H positions were not refined (see paragraph 4.2), standard deviations are not reported for geometrical parameters

D-H...O[Å]	d _{H...O} [Å]	angle _{DHO} [deg]	ρ _{BCP} [e/Å ³]
O2-H2A...O11	1.770	167.5	0.18(2)
O2-H2B...O22	1.801	172.7	0.16(2)
O1-H1A...O21	1.746	168.7	0.15(3)
O1-H1B...O12	1.688	170.4	0.23(2)
C1-H1...O1	2.575	158.7	0.05(1)

The VSCC distribution on the Cu₂ atom is in agreement with the expected JT d⁹ configuration, *i.e.* four minima in between the four closest ligands and two additional ones along the direction of the longer JT bonds (although the latter are slightly tilted, see fig. 4.11a). For Cu₁, instead, only four VSCCs were found, the ones along the JT bonds being lacking (fig. 4.11b). For this metal center, the JT bond is shorter than for Cu₂ (table 4.11) which indicates that the splitting of e_g orbitals is more effective in Cu₂ with respect to Cu₁. This, in turn, leads to a greater accumulation of ED in d_{2z} orbitals in Cu₂ with respect to Cu₁ (see *infra*), which explains why the VSCCs along the JT bonds were found in the former but not in the latter. The VSCC distribution of oxygen atoms of water ligands deserves some comments. In the 'geometry' section it was discussed how the orientation of water₁ molecule does not allow the oxygen to face one of its lone pairs toward the Cu atom without inducing a significant distortion of its VSCCs with respect to the ideal VSEPR [35] tetrahedral distribution. Although this distortion was found for the Co compound, this is not the case for the Cu formate. Indeed, none of the VSCCs of water₁ is directed towards the metal, and their spatial distribution is still mostly tetrahedral (figure 4.11e). Regarding the VSCC of the formate moieties, both the symmetry-independent O atoms involved in the JT bonds display 4 ∇²ρ minima (figure 4.11). Their distribution, however, is not tetrahedral and generally different between O₁₂ and O₂₁. The reason for this unexpected VSCC distribution is not clear and a comparison with theoretically-derived ED will be carried out to exclude the possibility of an artifact caused by the use of the multipolar model. The remaining oxygen atoms of the formate molecules have the expected sp²-like distribution already found for the Co compound.

* acceptor atom belongs to the asymmetric unit at 1-x, -0.5+y, 0.5-z

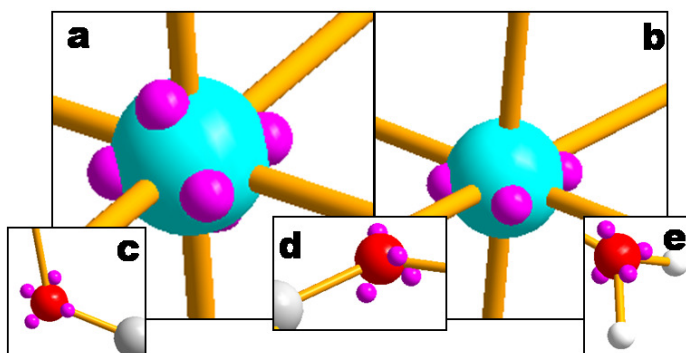


Figure 4.11 VSCCs (violet small spheres) on atoms: a) Cu2 b) Cu1 c) O12 d) O21 e) O1. Bonds to neighboring atoms are indicated by yellow lines

A quantitative measure of the different extent to which JT effect affects the electron distribution of the two Cu atoms can be obtained by looking at the experimentally derived d-populations obtained through the method proposed by Holladay *et al.* [32]. To have an unbiased comparison of the e_g population between the two metal centers, the coordinate system which minimize the e_g population is considered. The d orbital populations are very similar, but it can be noticed that, as expected, the d_{z^2} population is (slightly) higher for the Cu2 atom (table 4.15), a confirmation of the stronger JT effect with respect to Cu1.

Table 4.15 Experimentally-derived d orbitals occupancy (see main text for details) expressed as percentage of the total d orbitals population.

	d_{z^2}	d_{xz}	d_{yz}	$d_{x^2-y^2}$	d_{xy}
Cu1	0.208	0.204	0.216	0.146	0.226
Cu2	0.219	0.209	0.215	0.140	0.217

Regarding the integral properties, atomic charges and volumes are reported in Table 4.16. Although the formal charge of metal centers in the $M(\text{HCOO})_2(\text{H}_2\text{O})_2$ isostructural series is +2, the values obtained for Cu atoms are close to unity. Overall, the formate linkers have roughly the same charge as in the Co compound, namely -0.65 and -0.79. Note that in both cases the formate moiety linking the two symmetry equivalent M1 (M=Co,Cu) centers has a less negative charge than the one linking the two symmetry-independent metal centers. This is in accordance with the fact that the M2 center is surrounded by only two negatively charged formate linkers (the remaining four water fragments are formally neutral) and therefore the latter are able to withdraw more charge from M2 than from M1, which is coordinated to six formate moieties. Regarding the water ligands, it is worth mentioning that in this case the water2 has a significant positive charge (+0.25), differently from what observed in the Co compound, where both water molecules are substantially neutral.

Table 4.16 charge and volume of the atomic basins defined in QTAIM for the symmetry-independent atoms of Cu formate

Atom	charge	volume(au)	atom	charge	volume(au)
Cu(1)	1,08	9,65	C(1)	1,57	7,00
Cu(2)	1,19	10,21	C(2)	1,59	6,97
O(11)	-1,25	14,37	H(1)	0,24	6,05
O(12)	-1,22	17,28	H(2)	0,28	5,92
O(21)	-1,30	16,50	H(1A)	0,69	1,52
O(22)	-1,36	16,20	H(1B)	0,63	2,28
O(1)	-1,27	18,20	H(2A)	0,64	1,74
O(2)	-1,09	17,97	H(2B)	0,71	1,70

The SF contributions for the C-O bonds and for the shortest Cu-O bonds follow the same pattern observed for the Co compound* and will not be commented here any further. Regarding the JT bonds, the SF contributions for one of them is reported in figure 4.12†. It can be seen that the two bonded atoms (namely Cu and O) give a contribution which is roughly halved with respect to the value obtained for Co-O and the remaining Cu-O bonds, indicating that the JT bonds basically have a closed shell nature. As for the rest of the system, there is an increase in the SF% contributions of the remaining atoms of the formate moiety to the BCP of JT bonds and, as a result, the contribution from the whole formate ligand is similar to that obtained for Co-O bonds. Therefore, concerning the formate linker participating in the JT bond, SF indicates that the interaction is due to the whole formate fragment, in the same way as it was observed for the other M-O bonds. The different character of the M-O bonds, on the other hand, is indicated by a lower SF contribution from the two bonds forming the bond path (namely Cu and O).

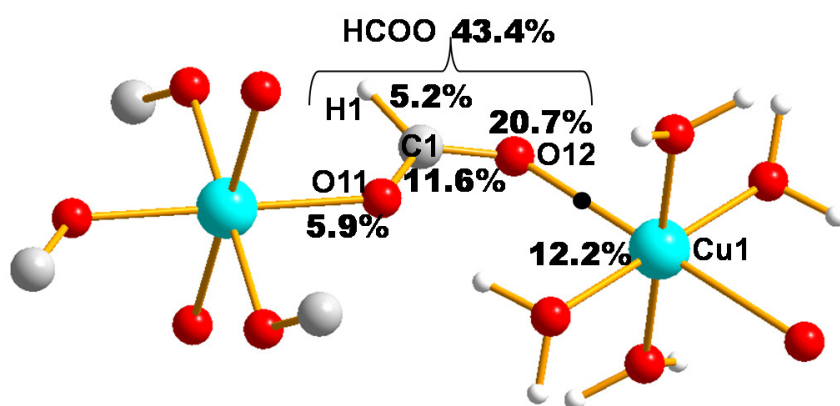


Figure 4.12 Source Function contributions (expressed as percentage of the total ED at BCP) for one of the JT bonds in Cu formate

4.4 THORETICAL CALCULATIONS: OUTLOOKS AND PRELIMINARY RESULTS

Although experimental ED have been obtained from good quality X-ray diffraction datasets, some approximation are intrinsically used both in the treatment of experimental data (*e.g.* thermal diffuse scattering is often neglected, as in this case [18]) and in the model used to obtain the ED distribution (*e.g.* the multipolar expansion centered on rigid pseudo-atoms [36]). For these reasons, the comparison with theoretical results is highly desirable in order to have trustable results on which reliable conclusions may be

* The Cu-O bonds (excluding JT ones) are shorter and have higher ED at BCP with respect to the Co-O bonds. Therefore, as expected, they are characterized by a higher contribution from the bonded atoms. In particular, we obtained SF% contribution from the bonded atoms of 70.8%, 73.3%, 72.2% and 72.0% for the Cu1-O11, Cu1-O21, Cu2-O1 and Cu2-O2 bonds, respectively.

† As it was done for Co-O bonds, only one example is reported here for sake of space. The SF% contributions for the other symmetry-independent JT bond is similar (within 3%)

drawn*. Even more importantly, the wavefunction grants access to those quantities which are not accessible from the ED distribution only (*e.g.* the spin density distribution). The calculation of periodical wavefunctions is the ideal approach to reproduce the properties of crystals (indeed this is what has been done for the investigations reported in chapter II and III to have a theoretical counterpart of the experimentally-derived ED). For the $M(\text{HCOO})_2(\text{H}_2\text{O})_2$ compounds, we performed unrestricted DFT (B3LYP [37]) periodical calculations at the experimental geometry using a triple zeta basis set optimized for periodical wavefunctions [38] using the code CRYSTAL06 [39]. As for the initial guess, we set ferromagnetically coupled metal centers for the Cu formate, while for Co compound we started from an antiferromagnetically coupled guess according to the experimental data (see section 4.1). In both cases we encountered many problems in the SCF procedure. In particular, the convergence process was very slow, and hundreds of SCF cycles were needed to reach a ΔE (*i.e.* the difference in energy between an SCF cycle and the following one) lower than 10^{-6} . For the Co compound, the convergence was even slower due to the fact that to model the antiferromagnetic coupling the symmetry of the system needs to be lowered (in particular, two asymmetric units are to be considered as the symmetry independent entity). For the Cu compound, we tested different computational approaches, including the use of different Hamiltonian and the optimization of atomic positions, but none of them led to an appreciable improvement in the convergence rate of the SCF procedure. Less accurate basis sets were also tested without any success. The slow convergence observed is not simply due to the complexity of the system but rather to problems in the SCF procedure implemented in CRYSTAL to obtain the periodical wavefunction of these systems. Indeed, the ED distribution around the metal centers appears to be unphysical. In particular, the ED laplacian has two positive and two negative lobes for both the symmetry-independent metal centers, and very similar distributions were obtained for both the Cu and the Co compound (figure 4.13), despite the fact that their d orbitals population is substantially different.

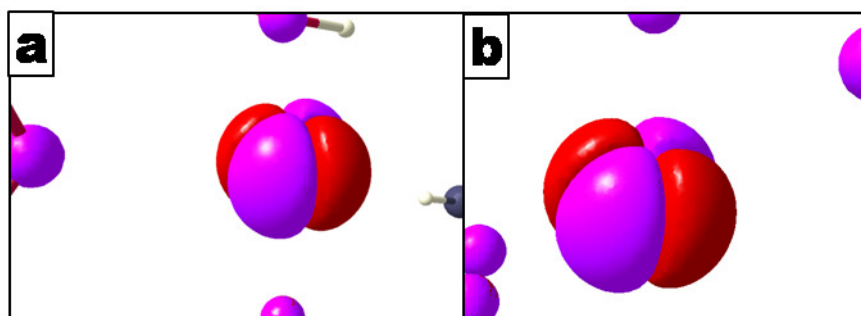


Figure 4.13 examples of ED-laplacian isosurfaces (+40 a.u., violet and -40 a.u., red) in the periodical wavefunction of Cu2 in Cu formate (a) and Co1 in Co formate (b). Note that, despite the two metals have different d orbital populations, the isosurfaces look almost identical.

Considering that the only aspherical features in the valence shell of 3d metals are due to the d orbitals population[†], such shape cannot be associated to any distribution of electrons into the d orbitals. Last but not least, the corresponding VSCC are in complete disagreement with the experimentally-derived results and with the one obtained from the model compound of Co formate (see *infra*). Note that similar results were obtained using HF as well as DFT (B3LYP and PW exchange-correlation functional were tested) Hamiltonians. As a future perspective of this work, we will eventually try to tackle the problem using a

* Clearly, the vice versa is true: theoretical approaches include approximations as well (mainly due to the necessity of approximating the electron-electron interaction in the Hamiltonian), therefore the comparison with experimental ED distribution provides a confirmation of theoretical results

[†] This is true when there are no strong covalent bonds involving the metal, as in the system studied here

completely different computational approach, namely the 'plane wave' method, which is expected to overcome the difficulties related to the use of Bloch functions involving atom centered Gaussian basis sets.

To reproduce the properties of a crystal, a valuable alternative to the periodical wavefunction is the so-called 'embedded cluster approach'. In particular, we built a model compound formed by the two symmetry-independent metal centers and all the ligands forming their coordination sphere (figure 4.14). The extremities of the formate linkers which are not bonded to the metals were 'saturated' with point charges to simulate the effect of the metal atoms not explicitly included in the calculation (their charge is +2, *i.e.* the formal charge of the metal). The geometry considered was the experimentally-derived one and the calculation was carried out at the B3LYP/6-311G** level of theory. Although probably too simplified to accurately describe properties intrinsically related to the periodic nature of the system (*e.g.* the magnetic ordering), the model compound is expected to be a good approximation of a periodical wavefunction when ED-related features (such as the VSCCs) are investigated. In addition, the analysis of MO features and spin density distribution which lead to the calculated ED is expected to provide valuable insights into chemical bonding of the investigated compound(s).

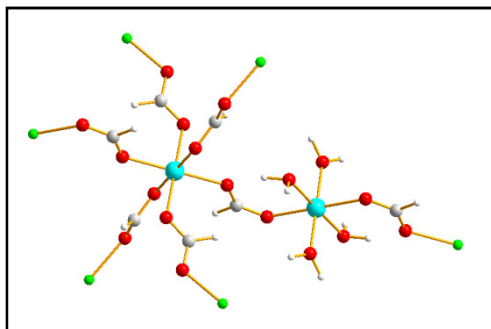


Figure 4.14 Model compound used to simulate the crystalline state of Co formate. Green spheres represents +2 point charges. The bond length are kept fixed to the experimental estimate.

In the following, the preliminary results for the Cobalt compound will be reported. In particular, we used the model compound to gain more insights into the d orbital occupation of the Co atoms, whose experimentally derived ED distribution showed some unexpected features (section 4.3.1). More in details, it was hypothesized a scenario in which the axis of the coordinate system are directed away from the ligands and the e_g orbitals are doubly occupied while the remaining three (alpha) electrons fill the three t_{2g} orbitals. Before discussing the results which may give additional proofs to such unconventional orbital picture, it must be pointed out that the VSCC distribution of Co atoms in the model compound is in agreement with the experimentally derived one. Namely, an octahedral distribution of VSCCs was found (an example is reported in fig. 4.15 as high value laplacian isosurfaces), although slightly tilted with respect to the experimental distribution presented in section 4.4.

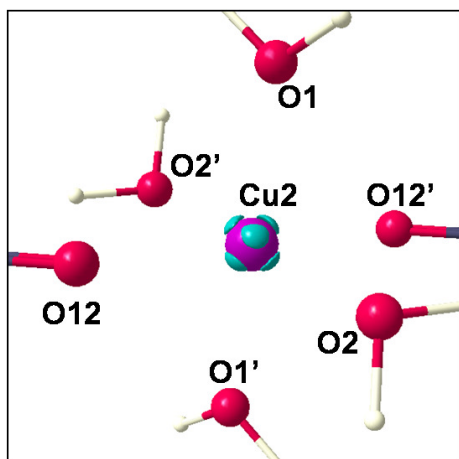


Figure 4.15 ED-laplacian isosurfaces (light blue. Isovalue value: $-40 \text{ a.u.} = 964 \text{ e}/\text{\AA}^5$) for Co2 in the model compound represented in fig. 4.14. Atoms not belonging to the asymmetric unit are labeled with the “ ’ ” symbol

The good agreement obtained constitute a solid basis which allows us to use the model compound to gain additional insights into the VSCC distribution experimentally found. The most important quantity not accessible from X-ray diffraction experiment which can confirm the hypothesized orbital picture is the spin density. Indeed, considering that a uniform occupation of t_{2g} orbitals must give rise to a cubically shaped density, a cubically shaped spin density distribution is expected to be found for a d-orbital occupancy as the one depicted in fig. 4.9 d-e. This is exactly what we found, as can be seen from figure 4.16a. The faces of the cubes, which correspond to the direction of the Cartesian axis of the reference system*, are directed towards the VSCCs, in accordance with the proposed model for the d-orbitals occupancy/orientation. A further proof of the proposed model for the d orbital population may be sought in the shape MO. Although the latter are usually delocalized through the whole system, we plotted the beta orbitals having a large contribution on the metal. Among them, we found two orbitals having a d_{z^2} -like shape entered on the two metal centers (figure 4.16 b-c). In an unrestricted calculation, the doubly occupied orbitals are expected to be the only ones having a beta contribution. The two orbitals depicted in figure 4.16 not only have a shape reminding d_{z^2} but, in addition, they are exactly oriented towards the z axis of the Cartesian reference system of the proposed model. In conclusion, the model system considered here have a VSCC distribution on metal centers which is in good agreement with the experimentally derived one. The plots of spin density and MO confirm the proposed model for the d orbitals occupation/distribution.

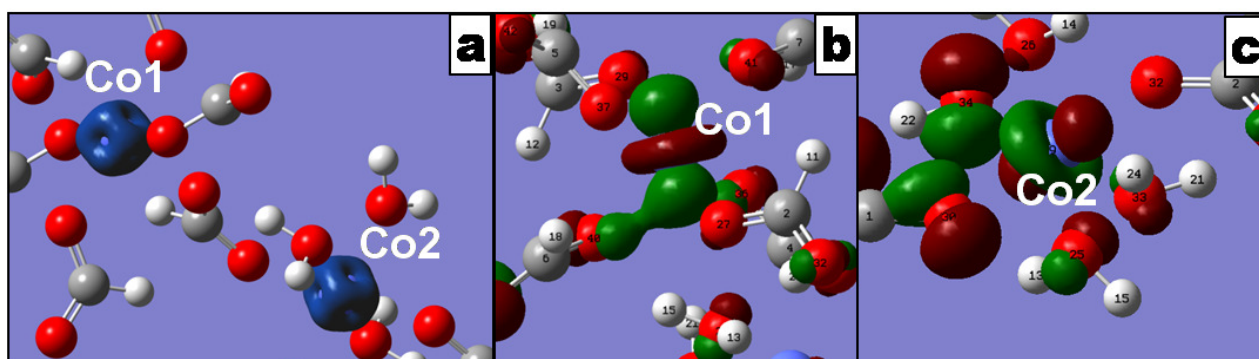


Figure 4.16 a) 0.02 a.u. spin density isosurface (blue) in the model compound. b,c) 0.05 isosurfaces of two selected beta orbitals (positive=green, negative=brown)

* As shown in ref. 31, t_{2g} orbitals give a cubically-shaped density distribution whose faces are perpendicular to the Cartesian axis

4.5 CONCLUSIONS

In this chapter, the chemical bonding in the isostructural coordination polymers $\text{Cu}(\text{HCOO})_2(\text{H}_2\text{O})_2$ and $\text{Co}(\text{HCOO})_2(\text{H}_2\text{O})_2$ was investigated by means of ED-based descriptors applied to experimentally-derived ED distribution. Crystals of the investigated compounds were synthesized from solution and the best samples were cut to make them fitting the X-ray beam of the diffractometer exploited to carry out the X-ray diffraction experiment. After some preliminary data collections, the best crystal of each compound was cooled down to 100 K and low-T X-ray diffraction reflections were measured up to a high resolution with a rather high redundancy. The dataset was used to obtain the experimental ED through a multipolar model, whose reliability was established through a careful analysis employing several techniques. For the Co compound it was necessary to exclude from the refinement all the reflections at very high resolution in order to achieve a trustworthy multipolar ED distribution. The resulting geometry and ED distribution were investigated to gain insights into the chemical bonding of Co and Cu formate.

In both compounds, the metal centers are coordinated to six oxygen atoms forming a distorted octahedral arrangement. In the case of Cu formate, two (collinear) M-O bonds on each metal center are significantly elongated with respect to the remaining bonds. This fact can be easily explained through the Jahn-Teller effect. The analysis of C-O distances of the formate linker and the comparison with bond length *in-vacuo* indicates that the closer is the terminal oxygen to the metal center, the longer is the corresponding C-O bonds. This C-O elongation, however, is small. Generally speaking, this effect may be due to an -although weak- back-donation mechanism from the metal to the π^* orbitals of the formate. However, theoretical calculations are needed in order to have a reliable proof of this hypothesis.

Regarding ED distribution, Bond Path examination suggests that the M-O interaction is mainly electrostatic (as confirmed by VSCC and Source Function analysis, see *infra*), although a certain degree of covalency cannot be ruled out. The evaluation of properties at M-O bond critical points clearly mirrors the weaker character of the Cu-O bonds distorted by the Jahn-Teller effect. Source Function (SF) contributions at bond critical points were evaluated and carefully investigated. For M-O bonds, the contribution of the bonded atoms is lower than 60% of the total ED at the M-O bond critical point (and even lower than 35% for the bonds elongated due to the Jahn-Teller effect). According to literature, this indicates that M-O bonds do not have a significant covalent character (though it does not exclude the presence of some secondary donation/back-donation mechanisms). For all M-O bonds, we found that a significant SF contribution to their bond critical points comes from all the atoms of the fragment whose oxygen atom takes part in the bond. By summing up the contribution of the whole fragment one obtains similar values of SF% contribution from the fragment independently from the type of metal center (Cu or Co) and independently from the type of fragment (water or formate). This total contribution varies only slightly with the M-O distance. As for the charges, metal atoms display values lower than the formal charge (+2), which is counterbalanced by the charge of the formate linkers (as a consequence, water moieties are basically neutral). All in all, integral properties indicate that the M-O bonds should be considered as an interaction between the metal atom and the whole fragment with which they interact. The examination of Valence Shell Charge Concentrations (VSCCs) provides precious information on the hybridization of the oxygen atoms and on the d orbital distribution of the metal atoms. Generally speaking, VSCC analysis indicates that the interaction is of 'key-lock' type, where the electrostatic plays the dominant role. However, the case of cobalt is particularly interesting, as an octahedral distribution of charge concentration regions was found, which is not in agreement with the d orbital occupation which can be derived from well-known crystal field

theory. We proposed a model reversed with respect to the conventional crystal field theory. In the proposed model, e_g and t_{2g} orbitals are doubly and singly occupied, respectively. This model is in agreement with the experimentally-derived d orbital populations obtained from the method of Holladay [32]. To obtain a conclusive evidence of such model, and in general to retrieve important information which are not directly obtainable from the ED distribution only, we tried to perform periodical DFT calculations. However, severe convergence problems were met which led to unphysical results. Neither the change of Hamiltonian and basis set nor the optimization of the structure could overcome such problem. The reason for this have still to be identified and further investigations in this direction will be carried out. To look for a confirmation of the proposed model for d orbital configuration of Co atoms, we carried out *in-vacuo* calculations on a rather big cluster embedded in point charges, which should properly simulate the local properties of the solid state (this is obviously true only far from the boundaries, but we built the cluster in such a way to explicitly consider the full coordination sphere of the two symmetry-independent metal atoms). Confirmation of the proposed model for d orbital occupation were found both in molecular orbital analysis and – most importantly- in the spin density distribution.

REFERENCES

- [1] C. Janiak *DaltonTrans.*(2003) 14, 2781.
- [2] S. R. Batten, N. R. Champness, X.-M. Chen, J. Garcia-Martinez, S. Kitagawa, L. Öhrström, M. O’Keeffe, M. Paik Suh, J. Reedijk *Pure Appl. Chem.* (2013) 85(8), 1715.
- [3] S. Kitagawa, R. Kitaura, S.-I. Noro *Angew. Chem. Int. Ed.* (2004) 43, 2334.
- [4] T. Sawaki and Y. Aoyama, *J. Am. Chem. Soc.*, (1999) 121, 4793.
- [5] J. S. Seo, D. Whang, H. Lee, S. I. Jun, J. Oh, Y. J. Jeon K. Kim *Nature* (2000) 404, 982.
- [6] see, for example: A. Aumüller, P. Erk, G. Klebe, S. Hünig, J. U. von Schütz H.-P. Werner *Angew. Chem., Int. Ed. Engl.* (1986) 25, 740
- [7] see, for example: J.-C. Dai, X.-T. Wu, Z.-Y. Fu, C.-P. Cui, S.-M. Hu, W.-X. Du, L.-M. Wu, H.-H. Zhang R.-Q. Sun *Inorg. Chem.* (2002) 41, 1391.
- [8] C.-T. Chen and K. S. Suslick *Coord. Chem. Rev.* (1993) 128, 293.
- [9] C. Janiak, T. G. Scharmann, J. C. Green, R. P. G. Parkin, M. J. Kolm, E. Riedel, W. Mickler, J. Elguero, R. M. Claramunt, D. Sanz *Chem. Eur. J.* (1996) 2, 992.
- [10] M. R. Jorgensen (2011) PhD thesis, University of Aarhus, Denmark
- [11] M. Matsuura, H. W. J. Blote and W. J. Huiskamp *Physica* (1970) 50, 444.
- [12] H. Yamakawa, M. Matsuura *J. Phys. Soc. of Japan* (1976) 41(3), 798.
- [13] R. B. Flippen, S. A. Friedberg *Journal of Chemical Physics* (1963) 38, 2652.
- [14] P. Burlet, J. Rossatmignod, M. Matsuura *Journal De Physique Lettres* (1979) 40, 455.
- [15] M. R. V. Jørgensen (2006). B.Sc. Report, Aarhus University.
- [16] M. Matsuura, K. Takeda, T. Satoh, Y. Sawada, J. M. Machadod *Solid State Communications* (1973) 13, 467
- [17] Agilent Technologies UK Ltd. CrysAlisPro, 171.34.44; Agilent Technologies UK Ltd.: Berkshire, U.K., 2010.
- [18] Giacovazzo, C., Monaco, H. L., Artioli, G., Viterbo, D., Ferraris, G., Gilli, G., Zanotti, G., Catti, M. (2002) *Foundamentals of Crystallography. Secon Edition*. Edited by C. Giacovazzo. New York: Oxford University Press

-
- [19] R. H. Blessing. *J. Appl. Crystallogr.* (1997) 30, 421.
- [20] G. M. Sheldrick *Acta Crystallogr., Sect. A: Found. Crystallogr.* (2008) 64, 112.
- [21] A. Volkov, P. Macchi, L. J. Farrugia, C. Gatti, P. Mallinson, T. Richter, T. Koritsanszky, *XD2006 - A Computer Program Package for Multipole Refinement, Topological Analysis of Charge Densities and Evaluation of Intermolecular Energies from Experimental and Theoretical Structure Factors*, 2006. See also <http://xd.chem.buffalo.edu/>
- [22] F. H. Allen, O. Kennard, D. G. Watson, L. Brammer, A. G. Orpen, R. J. Taylor. *Chem. Soc. Perkin Trans. II*(1987) S1
- [23] We obtained this value from a highly accurate (CCSD/cc-pVTZ) in-vacuo calculation carried out with GAUSSIAN (see ref. 64 of chapter III)
- [24] R. F. W. Bader (1990) *Atoms In Molecules: A Quantum Theory* Oxford: Clarendon Press
- [25] Bianchi, R.; Gervasio, G.; Marabello, D. *Inorg. Chem.* (2000), 39, 2360.
- [26] C. Gatti, D. Lasi *Faraday Discuss.* (2007) 135, 55.
- [27] G. Saleh, R. Soave, L. Lo Presti, R. Destro *Chem. Eur. J.* (2013) 19, 3490
- [28] G. Gilli, P. Gilli *Journal of Molecular Structure* (2000) 552, 1
- [29] F. Cortés-Guzmán, R. F.W. Bader *Coordination Chemistry Reviews* (2005) 249 (5), 633.
- [30] U. Muller *Inorganic Structural Chemistry* John Wiley and sons , Ltd (2006)
- [31] Y. Saito *inorganic molecular dissimetry* (1979) Springer-Verlag (Berlin and New York)
- [32] Holladay P. Leung, P. Coppens *Acta Cryst.* (1983) A39,377
- [33] C. Gatti, *Structure & Bonding* (2012) 147,193
- [34] H. Jahn and E. Teller *Proceedings of the Royal Society A* (1937).161 (905), 220.
- [35] R. J. Gillespie, D. Humphreys, C. Baird, E. A. Robinson *Chemistry* (1990) Allyn & Bacon
- [36] C. Gatti and P. Macchi (Eds.), *Modern Charge Density Analysis*, Springer, Dordrecht-Heidelberg-London- New York, 2012
- [37] A. D. Becke, *J. Chem. Phys.* 1993, 98, 5648-5652
- [38] M. F. Peintinger, D. V. Oliveira, T. Bredow *Journal of Computational Chemistry* (2013) 34(6) 451.
- [39] R. Dovesi, V. R. Saunders, C. Roetti, R. Orlando, C. M. Zicovich-Wilson, F. Pascale, B. Civalleri, K. Doll, N. M. Harrison, I. J. Bush, P. D'Arco, M. Llunell, *CRYSTAL06 User's Manual*, University of Torino, Torino, Italy, 2006

V Concluding remarks

Electron Density (ED) represents the probability of finding an electron in a point of space. Its importance lies in the fact that it is a quantity defined in real space (therefore easier to deal with compared to the wavefunction) and at the same time all the properties of a system can in principle be derived from it, as demonstrated by the Hohenberg-Kohn theorem. In addition, electron density can be experimentally obtained through X-ray diffraction experiments. It therefore plays the important role of a measurable quantity directly linked to the quantum world. Although the recipe to exactly derive chemical properties from electron density distribution is not known, there exist in literature many approaches which associate certain features of ED with chemical concepts (*e.g.* chemical bonds, electron delocalization, non-covalent interactions, lone-pairs, *etc.*), *i.e.* through the use of the so-called 'ED-based descriptors'. The work presented in this thesis aims at exploring new applications of recently proposed ED-based descriptors. Particular emphasis is put on the use of experimentally derived results.

A new descriptor (the "NCI descriptor") for the study Non-Covalent Interactions (NCIs) was recently proposed. Such descriptor makes use of the Reduced Density Gradient (RDG) to build isosurfaces which can be exploited to detect and characterize the various NCIs of a system. In this work, we applied such descriptor for the first time to experimentally-derived ED of three molecular crystals, carefully chosen as test cases: austriol, benzene and famotidine. We analyzed the results of the application of the "NCI descriptor" on a broad range of hydrogen bonds, from very weak to strong. General rules concerning the description of this kind of interaction in the "NCI descriptor" framework were sketched. Van der Waals interactions, which play a fundamental role in the crystallization of organic molecules, are very difficult to be detected in the ED distribution. We demonstrated the ability of "NCI descriptor" to highlight those regions of space between molecules which are interacting mainly through van der Waals interactions. The isosurfaces obtained in the "NCI descriptor" framework for less common interactions such as C-H \cdots π and H \cdots H were also investigated and characterized. We carried out also a systematic comparison between the picture offered by the Quantum Theory of Atoms in Molecules (QTAIM) and the one from the "NCI descriptor". The two approaches turned out to be complementary as the former has the advantage of being able to give a quantitative measure of the interaction strength but, on the other hand, the "NCI descriptor" is able to overcome the difficulties of QTAIM in correctly retrieving the delocalized character of certain interactions, *e.g.* the C-H \cdots π ones. To assess the reliability of the experimentally-derived results we compared them with the results obtained from fully-periodical DFT calculation. With the exception of a single interaction among the many investigated, the comparison showed a very good agreement between experimental and theoretical picture. Since in one of the original papers about the "NCI descriptor" it was claimed that when the latter is applied to the Independent Atom Model (IAM, that is the ED distribution obtained by superimposing ED of spherical, isolated atoms centered at the nuclear positions), a picture similar to the one derived from the quantum-mechanically derived ED distribution is obtained. To explore to what extent IAM is able to recover the features of "NCI descriptor" isosurfaces obtained using the "true" ED, we carried out a systematic comparison between the results obtained from IAM and the experimentally-derived ones. As a general trend we found that the ED distribution obtained from IAM is systematically more uniform and less structured. In general, IAM is unable to recover the fine details of the ED in the intermolecular region, since it lacks (by definition) the ED reconstruction caused by chemical interactions. Besides investigating the differences between experimentally and IAM derived isosurfaces, we also provided a rationale for such differences in terms of topological properties of ED. Despite we found that IAM and "true" isosurfaces differ systematically in shape, it must also be pointed out that IAM is able to detect all the interactions found using the "true ED". In order to carry out the all abovementioned investigations involving the "NCI descriptor", we developed a software, called "NCImilano", able to

calculate all the quantities needed for the evaluation of the “NCI descriptor” starting from experimental and/or theoretical (both periodical and *in-vacuo*) ED distribution. In addition, we implemented the evaluation of energy density, whose suitability as a quantity to be used for the investigation of NCIs will be explored in the future. For those cases where wavefunction -which is needed to exactly evaluate energy density- is not available, as in the case of ED derived from experiment, we implemented the Abramov’s approximation to calculate energy density directly from ED distribution. The error introduced by the use of such approximation is small in those regions characterized by low ED, as indeed are the regions where “NCI descriptor” isosurfaces appear.

Electron delocalization is a fundamental concept of chemistry involved in the definition of cornerstone notions of chemistry such as covalency and aromaticity. The definition of electron delocalization is intrinsically related to the second-order density matrix. However, ED distribution is influenced by the extent to which electrons are delocalized in a given system, as can be demonstrated through numerous examples. We exploited the Source Function (SF) as a tool to detect electron delocalization. SF is an ED-based descriptor and as such can be applied to experimental results. We carried out an investigation to explore the ability of SF to detect electron delocalization using experimentally derived ED distribution of three molecular crystals: benzene, naphthalene and 8'-benzhydrylideneamino-1,1'-binaphthyl-2-ol (BAB). The latter system is particularly interesting because it contains substituted benzyl and naphthyl rings. For both benzene and naphthalene, an excellent agreement between theoretically and experimentally derived results was found, attesting therefore the stability of the SF approach against the method used to obtain ED distribution. Such congruity regards not only a quantitative agreement found for the various SF contributions, but in addition the previously published trends obtained in passing from benzene to the various bonds of naphthalene were recovered using experimentally-derived ED. For benzene, two different multipolar models were tested and they substantially led to the same results. Hence, we could conclude that the SF picture is not significantly influenced by the multipolar model adopted to treat the X-ray diffraction data (provided a reasonably good model is considered). Regarding BAB, we also found a remarkable agreement between the non-substituted bonds of the benzyl rings and benzene and between the non-substituted bonds of the naphthyl rings and naphthalene. Since the ED distribution for the three considered molecular crystals was obtained from X-ray diffraction experiments carried out in substantially different conditions, the agreement found represents a further proof of the stability of the SF approach in the study of π electron delocalization. More in details, such agreement led us to conclude that the experimental conditions do not significantly influence the obtained results. As for the substituted atoms of the various rings, we explored how the substitution (with respect to benzene/naphthalene) influences the SF picture. We found that the substitution causes a lowering of the SF contribution of the substituted carbon atom to the ring bonds, this effect being stronger for more electronegative substituent atoms. Such effect complies with common chemical intuition and it is confirmed by the results obtained from the delocalization index. Finally, we demonstrated the ability of SF to detect subtle conjugation effects by comparing the results of two formally single C-C bonds situated in between bonds with π character. The π character of one of those two bonds seems to be stronger, as measured by bond length and delocalization index: this slight difference is detected by SF. Overall, SF was demonstrated to be an extremely powerful tool for the ED-based study of π electron delocalization, being able to detect even subtle delocalization features and being, in addition, remarkably stable against changes in the experimental conditions, multipolar model, and being even able to give a quantitative experiment-theory agreement.

All in all, the two investigations mentioned above demonstrated ED to be a very useful quantity to study chemical paradigms when appropriate descriptors are employed, even for those phenomena which scarcely influence the ED distribution such as the non-covalent interactions.

In the last part of the work presented in this thesis, the experience gained in the ED-based study of chemical phenomena was put into practice by investigation of chemical bonding in coordination polymers. In particular, the isostructural compounds $\text{Co}(\text{HCOO})_2(\text{H}_2\text{O})_2$ and $\text{Cu}(\text{HCOO})_2(\text{H}_2\text{O})_2$ were examined. These compounds, despite their structural simplicity, have many features which are found in most of the coordination polymers, namely the presence of ubiquitously found ligands such as formate and water, the magnetic ordering of the metal centers, the presence of both bridging and terminal ligands *etc.* . Therefore it is expected that a study of the physical origin of their properties, from the simple ones like the packing geometry to the more complex like the magnetic ordering, may shed light on some characteristic which are common to many coordination polymers. Crystals of the investigated compounds were synthesized at the University of Aarhus and the best samples were exploited to carry out very accurate X-ray diffraction experiments, from which ED distribution for both compounds was obtained. The focus of this investigation was put on the M-O interactions, which was studied by means of a number of tools, including careful geometry analysis, investigation of the ED distribution in the QTAIM framework, and the application of the Source Function . All in all, it was concluded that the metal-ligand interactions in the studied compounds has mainly electrostatic origin but, on the other hand, we noticed that some of the results point towards the presence an -although weak- donation/backdonation mechanism for these interactions. In the Cu compound, the effect of Jahn-Teller distortion was clearly detected in the crystal structure and in the topological features of ED distribution. For the Co compound, a violation of the classical crystal field theory d orbitals population was experimentally detected and confirmed theoretically by means of calculations on an appropriate model compound. So far, despite several attempts were made (trying different approaches within the formalism of periodical gaussian calculations), it was not possible to obtain a reliable periodical wavefunction. This work, however, is still in progress, and further studies are needed in order to obtain a complete picture of the chemical bonding on the investigated compounds.

ACKNOWLEDGMENTS (RINGRAZIAMENTI)

(English translation below)

In una tesi di dottorato è d'uopo ringraziare i propri relatori, e questo rende i ringraziamenti, in un certo senso, meno 'sinceri'. Per questo ho deciso di iniziare la parte dei ringraziamenti in questo modo: per sottolineare che il mio ringraziamento per i miei due relatori, il Dott. Leonardo Lo Presti ed il Dott. Carlo Gatti, viene dal cuore. Il Dott. Leonardo Lo Presti mi ha seguito sin dalla mia tesi di laurea, mi ha insegnato molto ed è sempre stato paziente e gentile con me. Molte delle cose che so sulla cristallografia (e non solo) le devo a lui, alla sua competenza ed alla sua dote nel trasmettere conoscenza alle giovani menti. Il Dott. Carlo Gatti ... beh, basterebbe il nome per esprimere la fortuna che ho avuto nel poter lavorare con lui. Nonostante ciò, vorrei aggiungere che anche lui mi ha seguito con estrema pazienza (ed, anche se superfluo sottolinearlo, estrema competenza) per tutto il periodo del mio dottorato. Non c'è una singola cosa di cui mi posso lamentare nei loro confronti per questi tre anni (spero tanto sia lo stesso per loro nei miei confronti).

Un altro ringraziamento speciale va al Center for Materials Crystallography. Non solo per aver pagato la mia borsa di dottorato, ma in generale per avermi dato la possibilità di condurre il mio dottorato in un ambiente di ricerca internazionale e stimolante. In particolare, i 'CMC meeting' sono stati sempre

un grande stimolo a progredire grazie allo scambio di conoscenza con i membri degli altri laboratori CMC. Ringrazio in particolare il Prof. Bo Iversen, sia in quanto leader del progetto CMC, sia per avermi dato la possibilità di spendere sei mesi del mio dottorato presso i suoi laboratori all'università di Aarhus. Riguardo a ciò, vorrei ringraziare Mette S. Schmökel e Jacob Overgaard per il loro prezioso aiuto nella parte sperimentale del mio lavoro.

Infine, ringrazio tutti i giovani scienziati con cui ho avuto modo di condividere diverse idee durante il dottorato: Ahmed Orlando, Emanuele Monza, Davide Ceresoli, Mattia Sist, Mette S. Schmökel, Jacob Overgaard, Maja Kruger Thomsen, Solveig R. Madsen, Jacob Hej, Mads Jorgensen. Spero di non aver dimenticato nessuno.

Non mi è mai piaciuto mettere nei ringraziamenti di un lavoro scientifico anche persone a cui sono grato 'nella vita', quindi non lo farò nemmeno ora (anche perché se no la lista sarebbe infinita). Chi ha fatto parte della mia vita ha la mia stima e lo sa, non servono parole su di una tesi per ricordarlo.

In a PhD thesis it is customary to thank the supervisors, and this makes the acknowledgment, somehow, less 'sincere'. That's why I decided to open the acknowledgment part in this way: to point out that my gratitude to my supervisors, Dr. Carlo Gatti and Dr. Leonardo Lo Presti, 'comes from the heart'. Dr. Leonardo Lo Presti has been supervising me since the beginning of my MSc thesis and he has always been kind and patient to me. Most of the things I know about crystallography (and not only) were taught to me by him, thanks to his expertise and his ability in transmitting knowledge to young minds. Regarding Dr. Carlo Gatti ... well, mentioning his name should be enough to express how lucky I have been in having the possibility of working with him. Nevertheless, I'd like to point out that he has also been patient (and, needless to say, professional) during the whole period of my PhD. When I look back at these three year of PhD, there isn't a single thing regarding my supervisors which I can complain about (and I deeply hope it's the same for them about me).

Another special thank goes to the Center for Materials Crystallography. Not only for having funded my PhD, but also for having given me the possibility of carrying it out in an international and stimulating environment. In Particular, the CMC meetings had been an important incentive in helping me to become a better scientist thanks to the knowledge exchange with the rest of the CMC laboratories. A special thanks goes also to Prof. Bo Iversen, not only as the leader of the CMC project, but also for having given me the possibility of spending six months of my PhD in his lab in Aarhus. Concerning that, I'd like to thank also Mette Schmökel and Jacob Overgaard for their precious help in the experimental part of my work.

Last but not least, I want to thanks all the young scientists with whom I could share my mind during the PhD: Ahmed Orlando, Emanuele Monza, Davide Ceresoli, Mattia Sist, Mette S. Schmökel, Jacob Overgaard, Maja Kruger Thomsen, Solveig R. Madsen, Jacob Hej, Mads Jorgensen. I hope I haven't forgotten anyone.

I've always thought that in a scientific work I don't like to thank people to whom I'm thankful 'in life', therefore I'm going to avoid it here as well (also because it would take forever). People who took part in my life have my respect and they know that, there is no need of words on a PhD thesis to remember it.